UNIVERSITY OF SOUTHAMPTON

SCHOOL OF PHYSICS AND ASTRONOMY
FACULTY OF ENGINEERING, SCIENCE AND MATHEMATICS

Diffractive encoding of microparticles for application to bead-based biological assays

Sam William Birtwell

Thesis submitted for the degree of Doctor of Philosophy

March 2008

UNIVERSITY OF SOUTHAMPTON

ABSTRACT

FACULTY OF ENGINEERING, SCIENCE AND MATHEMATICS
SCHOOL OF PHYSICS AND ASTRONOMY

Doctor of Philosophy

DIFFRACTIVE ENCODING OF MICROPARTICLES FOR APPLICATION TO BEAD-BASED BIOLOGICAL ASSAYS

by Sam William Birtwell

A new method for high-capacity encoding of microbeads that allows non-contact optical reading has been developed. In this new approach, a bead is encoded by a number of superimposed gratings with different periods manufactured on the surface of the bead, where each distinguishable tag has a unique combination of superimposed gratings. The tags are read optically at a distance, by detecting the diffraction pattern produced by the superimposed gratings. It has been demonstrated that the tagging method allows for millions of unique and distinguishable tags only a few tens of micrometers in size, when read by visible laser light. Using 2-dimensional superimposed gratings has been demonstrated to further increase the number of unique tags.

The tagging method was first demonstrated using chromium-on-glass libraries of tags manufactured by e-beam lithography. Two libraries containing tags with up to five superimposed gratings were fabricated, one containing 1-dimensional tags, and the other containing 2-dimensional tags. A laser reading system has been developed including a software package that automatically identifies individual tags in the library. Capacity for up 68000 unique 50μm long 1-dimensional tags and up to 10^8 unique $50 \times 50\mu$m 2-dimensional tags was demonstrated.

The diffractive tags were developed for biological, chemical and medical applications by manufacturing them from the polymer SU8, which is suitable for biochemical functionalisation. A nano-imprint process for creating diffractive tags in SU8 has been developed, that allows for high-throughput manufacturing. A library of 100 different tags were shown to produce high-quality diffraction patterns, recognisable in the laser reading system. Capacity for up to 10^4 unique 100μm long 1-dimensional tags and up to 10^8 unique $100 \times 100\mu$m 2-dimensional tags was demonstrated using this manufacturing method.

A version of the tagging technology based on holographic writing has been developed. Holograms of binary arrays of spots were written into SU8 doped with a photochromic dye. This version of the technology offers a number of potential advantages, including use of error-checking algorithms and smaller diffraction angles. Capacity for 10^{14} codes was demonstrated to be theoretically achievable on a $100 \times 100\mu$m tag. A laser reading system has been developed with a software package that automatically identifies individual holographic tags. Capacity for 10^{19} tags was demonstrated on bulk photochromic-doped SU8. A dry-etch based method was developed for manufacturing individual particles of SU8 doped with photochromic dye. Capacity for 512 tags has been demonstrated on a 500μm particle. Additionally, it was shown that tags written using this technique could be erased and re-written, which is the first demonstration of rewritable microbead tagging.

Contents

List of Figures

Acknowledgements

Firstly, I would like to thank my main supervisor Nikolay Zheludev, whose guidance and high standards have improved the quality of my research and writing immeasurably, and who spent a lot of time reading and criticising the many drafts of this thesis. I also thank my second supervisor Hywel Morgan for many fruitful discussions and helpful guidance, especially in the fabrication areas of the project, and for many helpful comments on this thesis.

I would also like to thank my colleagues in the 4G group, in particular; Gerasim Galitonov for imparting his knowledge of programming and electronics; Rohan Ranasinghe for help with any chemical knowledge I needed, and many useful discussion on DNA chemistry; Peter Roach for many helpful discussions on chemistry and biochemistry; Joseph She for his knowledge of immunology; Katie Chamberlain for fabrication assistance; and Shahanara Banu for her enormous efforts in the development of the fabrication processes required for this work. I would like in addition to thank Bruno Soares for reading and commenting on the finished thesis.

Finally, thanks to my friends and family for helping me escape from the rigours of writing when necessary. An extra special mention for Cat for being there when needed, for putting up with never seeing me while I was writing this thesis and for tolerating my permanently stressed state.

Chapter 1

Introduction and background

1.1 Biological assays

1.1.1 ELISAs and microarrays

In recent years, rapid advances in genomics and proteomics have produced demand for high throughput analysis of large numbers of biomolecules, in particular for application to medical diagnostics and drug discovery. For example, immunoassays require the identification of a large number of different antibodies that exist in blood or other samples obtained from a patient, in order to identify diseases [1]. Such identification is accomplished in routine clinical diagnostics by use of an Enzyme-Linked ImmunoSorbant Assay (ELISA) [1], which tests for the presence or absence of a certain antibody. A schematic outline of the principle of an example ELISA (known as an indirect ELISA) that might be carried out on a diagnostic sample, is shown in figure 1.1. An antigen (substance to which a specific antibody will bind) which binds to the target antibody of interest is coated on the inside of a well of a microtitre plate. A sample from a patient is added and any target antibody in the patient binds to the antigen. A 'detection antibody', which can bind to the target antibody and is linked to an enzyme, is then mixed with the sample. The detection antibody binds to the target antibody. The sample is then washed to get rid of non-bound detector antibody. A 'substrate' chemical is then added, which is a chemical that the enzyme can convert from a colourless to a coloured form. The colouring of the solution is then measured by spectrophotometry, indicating the quantity of target antibody present in the sample.

The disadvantage of a traditional ELISA is that the reaction is large-scale and only tests for a single antibody at a time. Multiple ELISAs may be performed in a

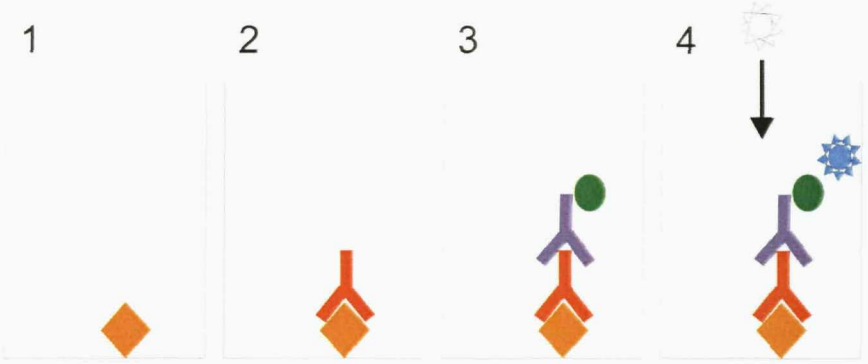

Figure 1.1: Schematic diagram showing the principle of an indirect ELISA. (1) Antigen (orange) corresponding to a particular target antibody is bound to a well of a microtitre plate. (2)A patient sample is added to the well, and any target antibody (red) in the sample binds to the antigen. (3)A detection antibody (purple) bound to an enzyme (green) is added to the well, and binds to target antibody. (4)A substrate (white) is added, which is converted by the enzyme to a coloured form (blue). The amount of colour therefore indicates the quantity of target antibody present in the sample

microtitre plate, which has a number of wells (typically between 6 and 1536 wells) which act as reaction vessels. A different antigen is bound to each well, and an ELISA carried out in each. The solution colouring in each well is measured on an automated 'plate reader', which performs spectrophotometry on each well in turn. In order to use a large number of wells, large volumes of sample from the patient are required.

Therefore testing for multiple antibodies is a time consuming process, and requires relatively large volumes of sample from the patient. The object of much current research in this field is "multiplexed" and high-throughput analysis of biomolecules. If we stay for the moment with the example of an immunoassay, the ideal case would be to have a system which tests for a large number of different antibodies all at once in a single, low-volume, patient sample. To do this, one needs to have a large number of different antigens, each of which will bind to one of the antibodies produced in response to a disease. These antigens need to be reacted at the same time with a patient sample: the particular antigens which bind to antibodies in the sample indicate which antibodies are present. The obvious question which arises from this is how can we tell which antigen in the mixture is which. The answer is to have some method of labeling the antigens, such that their identity may be quickly recognised by machine.

A well-developed method for this identification is the protein micro-array, which

has been used for 'micro-ELISAs' of cytokines [2] and immunoglobulin-E antibodies [3]. This is a plate of a material such as glass, which contains a square array of positions, each with a different antigen attached. The whole plate is reacted with an antibody-containing sample, and the antibodies in the sample bind only to their corresponding antigens. A detector antibody which can bind to all the target antibodies and which is linked to a fluorescent dye is added, and binds to all the plate positions to which target antibodies are attached, making them fluorescent. The fluorescent positions on the plate can be automatically identified by analysing a microscope image of the plate, and hence the antibodies present in the patient sample (and the corresponding disease(s) in the patient) can be identified. A simple example with four antigens reacted with a sample containing two different target antibodies is shown in figure 1.2(A) and (B).

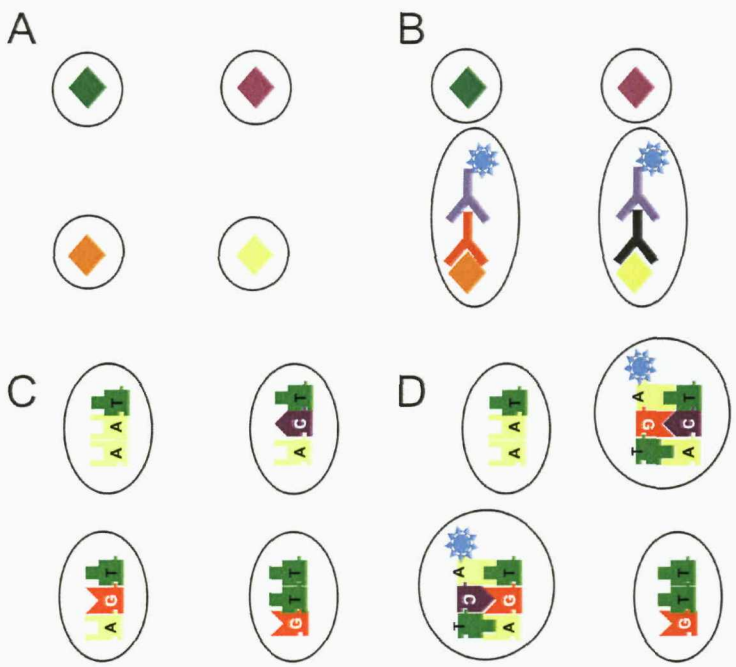

Figure 1.2: Schematic diagram showing the principle of a microarray used for immunoassay and DNA assay applications. (A)Different antigens (coloured diamonds) are attached to each of four sites on a microarray. (B)Target antibodies (red and black) bind to two of the sites, and a fluorescently labeled detector antibody binds to the target antibodies making the reacted positions fluorescent. The antigens at the fluorescent sites are identified by the (x,y) coordinates of the sites. (C)A similar arrangement of different 3-base oligonucleotides bind to two complementary fluorescently-labelled DNA sequences (D). The sequences are again identified by the (x,y) coordinates of the fluorescent array sites.

Similar microarrays manufactured by companies such as Affymetrix and Illumina

are also more routinely used for identification of DNA and RNA fragments in samples. Uses for this include; detection of DNA sequences that indicate the presence of bacteria and viruses (including genetic variants of more common types) [4]; measurement of gene-expression which allows investigation of cellular activity such as protein synthesis [5, 6], and can be used for diagnosis of diseases such as leukaemia [1]; detection of DNA methylation which affects gene expression and plays a part in diseases such as multiple sclerosis and diabetes [7]; and identification of indicators of genetic disease, such as the single-nucleotide polymorphism (SNP - a change in a single DNA base which causes disease) which causes cystic fibrosis [6]. A DNA microarray has a different DNA sequence (oligonucleotide) of the required length attached to each position on the plate. In a similar manner to the immunoassay microarray, fluorescently labeled oligonucleotides will only hybridise (chemically bind) to their complementary sequence on the microarray plate. Again specific sites will become fluorescent, allowing identification of the specific DNA sequences present in the sample. A simple example of four different 3-base DNA sequences binding to two target complementary sequences in a sample is shown in figure 1.2(C) and (D). Typically, DNA assays require a much higher level of multiplexing than immunoassays. An image of a real DNA microarray is shown in figure 1.3, showing the size of each individual site. It is currently possible to make arrays with several tens of thousands of sites [5], which require much smaller amounts of sample than a microtitre assay would.

1.1.2 Bead-based assays

Microarrays suffer from some disadvantages, including slow reaction kinetics [8], and problems with localization of the biomolecules bound to the chip. For this reason there has recently been a large amount of research interest in "bead-based" assays. Such assays use micrometre-sized solid particles (beads) as a platform for attachment of the detector biomolecules, for example antigens in an immunoassay. A number of particles are used, each one with a different antigen attached. The particles are then reacted in suspension in the sample under investigation, in the same manner as a microarray. Since positional encoding of the type used on the microarrays described above cannot be used on a suspension of particles, each particle must be somehow identifiable. The method of doing this is to 'tag' each particle with an identifying code which is somehow indicative of the molecule bound to its surface. An outline of this is shown in figure 1.4. After reaction the particles must be

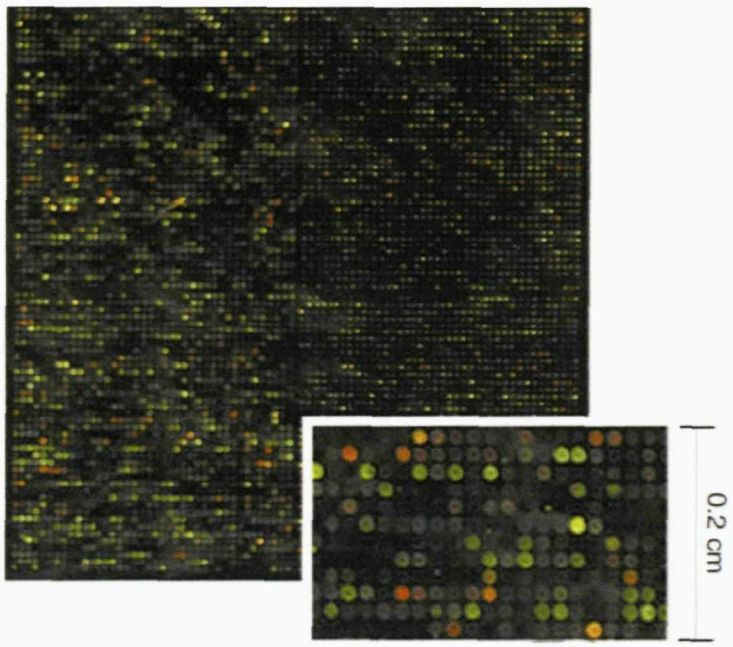

Figure 1.3: An example DNA microarray, using two fluorescent indicator dyes, Cy3 and Cy5, to differentiate samples taken from cells in two different activation states. (image taken from [5]).

analysed for (a)their fluorescence signal indicating the binding of (for example) an antibody from the sample, and (b)the code. The combination of these two will allow identification of the specific antibodies present in the sample. In addition to this kind of analysis, particles could be analysed in microfluidic systems, allowing for very high throughput analysis. Additionally, such a system allows particles to be directed after analysis into other reaction vessels depending on the results of fluorescence and code analysis. This may be useful for so called split-and-mix synthesis, in which compounds such as oligonucleotides are progressively and combinatorially synthesised (considered in more detail in section 4.1.2).

Having outlined the motivations behind developing bead-based assays, it has become apparent that there is a need for a method to encode microparticles. Such a method must be: readable by non-contact methods; suitable for encoding particles of tens of microns in size; unaffected by any reactions required for the biochemical parts of the assay; robust with low error rate; able to encode large numbers of particles, each with a unique code and implementable on materials which are compatible with biomolecule attachment. This thesis will present a particular method for encoding microparticles, based on modifying the particles so that they give a unique, machine

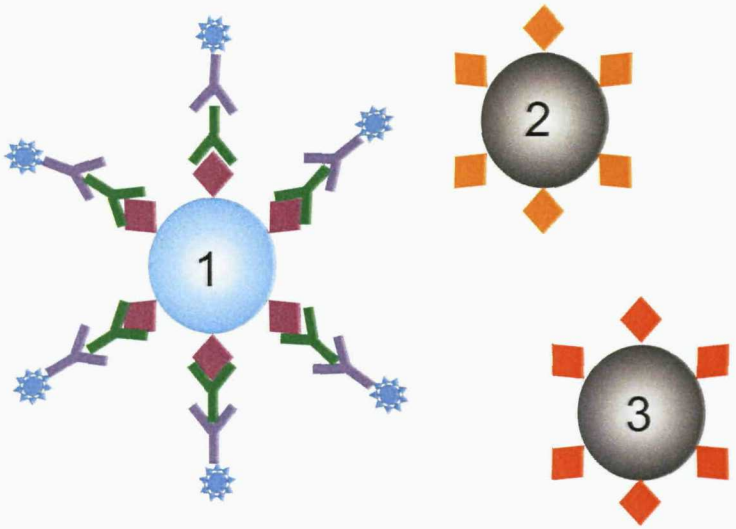

Figure 1.4: Schematic layout of a simple bead-based immunoassay. Three beads, each with a different antigen attached, are encoded with unique number indicative of the antigen on the surface. The beads are reacted with a sample containing a single type of target antibody, which binds to only one of the antigens. Fluorescently labeled detector antibody is then added which binds only to the target antibody. One of the beads becomes fluorescent after binding, and the number on the bead indicates the antigen on this bead, and hence the antibody in the sample.

readable diffraction pattern upon illumination with a laser beam. For the rest of this chapter, the circumstances and larger project within which this encoding technology was developed will be considered, followed by reviewing a number of existing methods of encoding microparticles which have been developed in recent years. Finally the concept of diffraction of light will be introduced, along with a generic explanation of how it may be used as an encoding technique, including a brief review of some existing technologies that make use of diffraction for data encoding purposes.

1.2 The 4G project

The work presented in this thesis was undertaken by the author as part of the 4G Basic Technology project at the University of Southampton. This is a project that was set up with the aim of investigating methods for practically realising high throughput bead-based assays. The project is highly multi-disciplinary, featuring contributions from researchers specialising in engineering, microfabrication, physics, chemistry and bioinformatics. One of the main original aims was to investigate the

possibility of using split-and-mix synthesis together with bead-based analysis to sequence the human genome in a high throughput manner using 16-base oligonucleotides. However, since the work of the bioinformatics part of the project showed that this was essentially impossible [9], the project has mainly concentrated on other uses of bead-based assays, such as SNP analysis, detection of virus and bacterium DNA and mutations, proteomic assays and immunoassays.

An outline of the structure of the 4G project is shown in the diagram in figure 1.5. Grayed out parts of the diagram indicate the work of other people and the rest constitutes the sections of the project undertaken mostly by the author. The project is essentially divided into four main areas. The first, is broadly described as bioinformatics and is now completed. This section of the project was mainly concerned with investigation of the feasibility of sequencing human, bacterial and viral DNA, using the kind of short oligonucleotides that may reasonably be attached to beads. Since it is no longer in existence, it is not shown on the diagram. The second section of the project ("Assay development") involves chemists who work on the attachment of DNA, proteins and antigens to the surface of the specific microparticles used in the project, together with performing assays using the encoded microparticles. In addition to this, part of this section is devoted to synthesising DNA on the surface of the microparticles, for possible applicability to split-and-mix synthesis. The third section of the project involves design and microfabrication of the microfluidic chips for transport of the particles during analysis, and integration of the fluidics into optical systems. In this part, high-speed software for reading the codes in flow is also developed. The final section is that with which the author was directly involved, which constitutes development of the encoding strategy for the microparticles, together with hardware and software for reading the codes and characterization of the encoded microparticles themselves once manufactured. Although the author was involved with fabrication of the codes, a large portion of the manufacturing was done by other people on the project. The parts directly contributed by the author are outlined in black in figure 1.5. There is however considerable overlap between the various areas of the project, with people contributing jointly to many areas.

1.3 Existing microparticle encoding technologies

In the years since the identification of the possibilities of bead-based assays, there have been a large number of proposed techniques for encoding beads to use in such assays [10]. Research in this area has been extensive, and this section will give

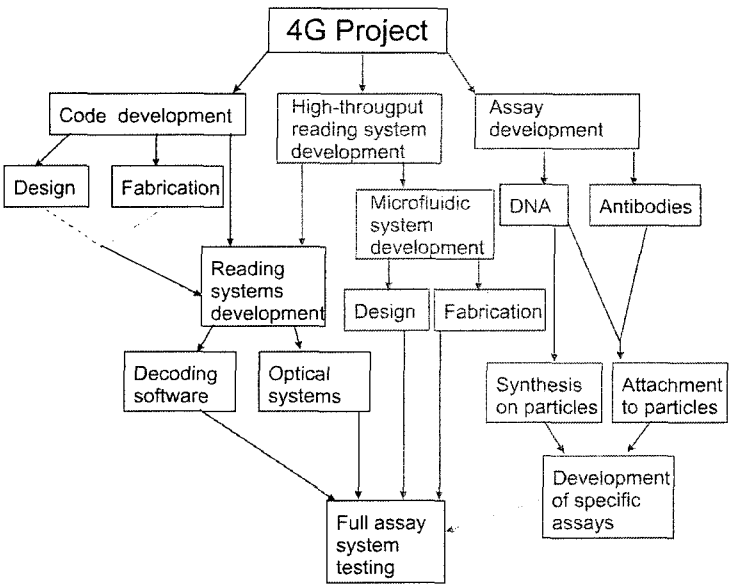

Figure 1.5: Diagram indicating the structure of the 4G project, showing the main overall areas of development.

an overview of the available microparticle encoding techniques, considering their advantages and disadvantages. The important points to consider when reviewing the encoding techniques are; the encoding capacity of each technique (how many molecules may potentially be identified using each technique, which determines the types of assays it can be used for); the simplicity of the manufacturing process (i.e. is it realistically possible to manufacture the number of encoded particles required for a particular assay); the simplicity of the reading system; robustness of the technique (i.e. how likely errors are to be made in the reading of the code); and the compatibility of the technique with other aspects of the assay, in particular the chemical processes that the particles will have to undergo (i.e. whether the particles can actually be used for their suggested applications).

1.3.1 Fluorescent dyed microspheres

The first and most well established encoding technique to be developed was the use of the specific emission spectrum of a polymer microsphere doped with a fluorescent dye. This is commonly achieved by soaking latex microspheres in organic solvent so that they swell, allowing dye molecules to enter the material via pores. When placed in an aqueous solution, the spheres shrink, trapping the dye molecules within the latex. Using a single dye at different concentrations, a multiplexed assay of six

different cytokines has been demonstrated [11]. The code is provided simply by the fluorescence intensity from each particle, read using a fluorescence activated flow-cytometer (FACS) which excites the dye with a laser emitting light of a wavelength within the absorption band of the dye, and detects the fluorescence emission from it. The particles flow in a stream past the excitation laser, allowing a large number of particles to be analysed based on the intensity of their emitted fluorescence. The results of statistical analysis of the particle fluorescence intensity is presented in the histogram in figure 1.6, showing good separation between the six fluorescence intensities, which allows each fluorescence intensity to be used as a unique code to identify the particles. There is, however, little scope for increased multiplexing using this technology, without introducing overlap in the populations.

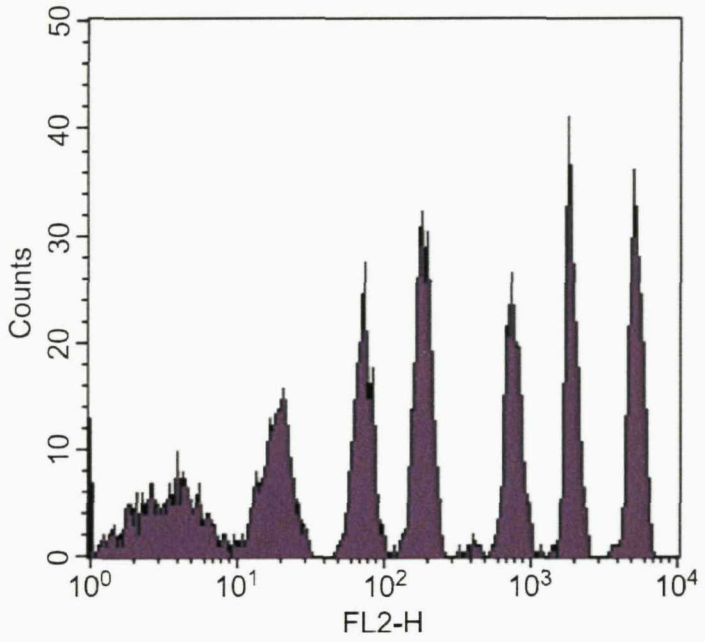

Figure 1.6: Histogram of particle population as a function of fluorescence intensity received in the detector of a flow-cytometer, for particles doped with six concentrations of a fluorescent dye. The lack of overlap between the six populations indicates that the six types of particle will be easily distinguishable (image taken from [11]).

Similarly encoded beads are used in commercially available bead based assay instruments, such as Luminex Corporation's xMAP technology [12]. This technology uses a proprietary method to uniquely encode each bead with a mixture of two fluorescent dyes, one with a red and one with an infra-red emission spectrum. The unique emission spectrum produced by a particular ratio of the two dyes serves as

the method for identification of a particle. The company advertises 100 unique codes being available using this method [12], and Luminex beads have successfully been used to detect eight different cytokines [13], and 11 singe-nucleotide polymorphisms (SNPs) of enzyme genetic material [14]. The xMAP technology was recently approved by the US Food and Drug Administration for clinical use as part of a system to identify 12 different viruses by analysis of their genetic material [15]. In all cases using the Luminex system, a green fluorescent dye is used to indicate binding of a molecule to the microparticles, so as not to interfere with the spectrum of the fluorescent code.

A similar approach is to use semiconductor quantum dots rather than organic fluorophores to fluorescently encode microparticles. These quantum dots are typically a core of cadmium selenide (CdSe) surrounded by a shell of zinc sulphide (ZnS) [16, 17, 18, 19]. The boundary between the two materials creates a potential which, due to the small size of the particle, confines the electron wavefunction, forcing it to exist only at discrete values. The electrons thus have discrete energy levels, and after excitation will emit a single wavelength of light, whose peak wavelength depends on the radius of the particle. The linewidth of the quantum dot emission is generally lower than organic dyes, and the peak wavelength of the emission may be tuned by varying the radius of the quantum dot, potentially allowing for a large number of individual emission wavelengths which could be used for microparticle encoding. In addition, the excitation spectrum of a quantum dot is typically very broad [16], allowing all of the different sized quantum dots to be excited with a single wavelength. Figure 1.7(B) indicates the narrow emission spectra of six different sized quantum dots, compared to the emission spectra of the two organic dyes rhodamine red and DsRed2, shown in figure 1.7(A). The quantum dots are seen to have much narrower emission lines than the organic dyes, allowing the potential for many unique fluorescence wavelengths to use for encoding. In addition, the black line in figure 1.7(B) shows the broad nature of the absorption spectra of the quantum dot with a 510nm emission peak wavelength, indicating the potential for exciting all sizes of quantum dots with the same wavelength. Figure 1.7(C) show the radius r in angstrom of the CdSe core of each of the six types of quantum dots, together with their corresponding emission peak λ in nm and a photograph of the emission from suspensions of each size under 365nm illumination.

Once quantum dots have been synthesised (see, for example [18, 21]), they may be incorporated into polymer microbeads to which biomolecules are then attached [17, 18, 20], or the quantum dots themselves may be functionalized for molecular

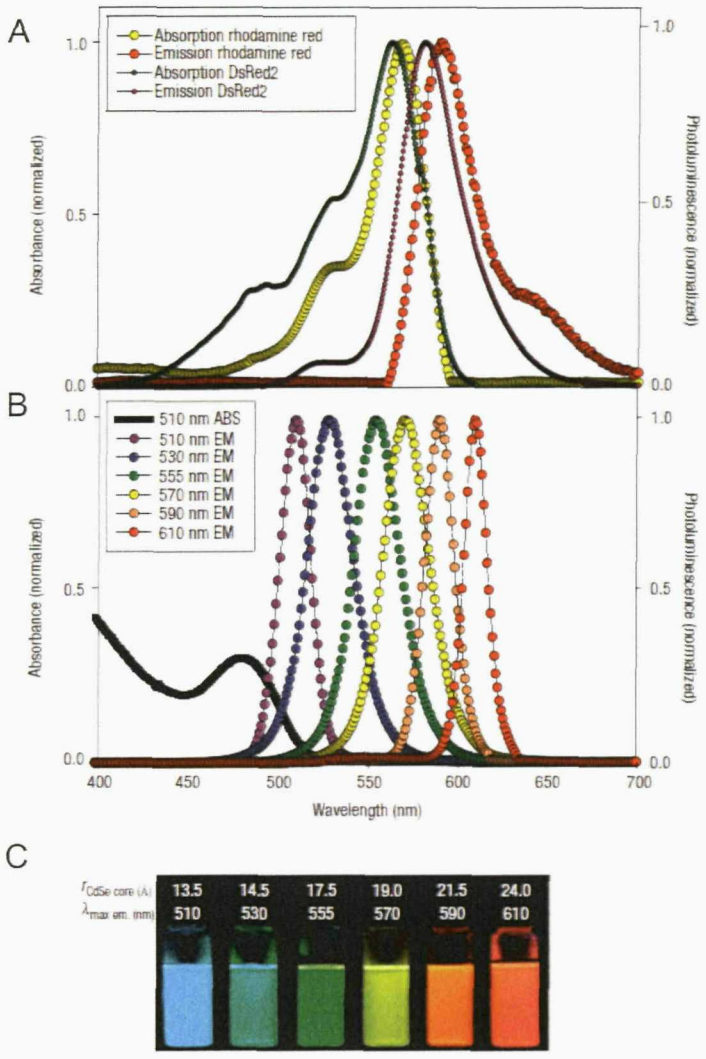

Figure 1.7: The emission spectra of six differently sized CdSe-ZnS quantum dots (B), compared to the emission spectra of two organic dyes, rhodamine red and DsRed2 (A). The black line in (B) shows the broad nature of the absorption spectrum of the quantum dots emitting at a peak wavelength of 510nm. The photograph in (C) shows an image of emission from each of the six quantum dots under 365nm illumination, together with their mean radius (figure taken from [19]).

attachment [19]. In addition to use of the emission wavelength difference as the code, multiple quantum dots may be embedded in a polymer microparticle in a precisely defined ratio, to create a larger number of unique emission spectra that act as a code [17, 18, 20]. One example is the embedding of quantum dots in polymer microspheres using a so-called "layer-by-layer" approach [17]. Layers of quantum dots are deposited in alternation with layers of polymer. By using different size quantum dots in different layers, the relative intensities of various parts of the microsphere emission spectrum change. A combination of intensity and wavelength values allows for a large number of codes, for example six different colours with six intensites could give about 40,000 codes [20]. The biological applicability of these particles was demonstrated by their use in a four-plex immunoassay. The small size of quantum dots means that they may be inserted into cells for multiplexed cell analysis [18]. Using different ratios of quantum dots, a 10-plex cellular assay was demonstrated, with the authors predicting the possibility of around 1000 codes using quantum dots with five different peak-wavelengths in four mixture ratios.

1.3.2 Patterned multi-wavelength fluorescence encoding

A technology with the potential for generating more unique codes than those described in the previous section, uses both the wavelength and *position* of a fluorescent dye as the code which identifies the microparticle. The particles are manufactured from multiple sections of aluminosilicate glass, doped with different rare-earth metal ions [22]. The barcodes were manufactured using a ribbon-fibre drawing method. To begin with, square 25 × 25cm glass blocks were prepared, doped with RE_2O_3 oxides of the rare-earth elements RE, where RE is either Dy (Dysprosium), Tm (Thulium), Tb (Terbium) or Ce (Cerium). These particular rare-earths were chosen due to their efficient visible emissions in the aluminosilicate matrix, their overlapping absorption spectra (for excitation purposes), and their non-interference with typical organic fluorescent markers used to indicate binding in a biological assay. Once the glass blocks were cast, they were drawn into 3.5 × 3.5cm glass canes and multiple canes doped with different glass were assembled in an order that defined a code. The cane assembly was fused in a graphite press at 900°C, and the whole fused assembly drawn into a ribbon fibre 20μm thick and 100μm wide. The ribbon fibre was then cut into 20μm sections using femtosecond laser pulses of wavelength 800nm and average power 100mW.

A false-colour fluorescence image of a selection of the resulting barcodes is shown

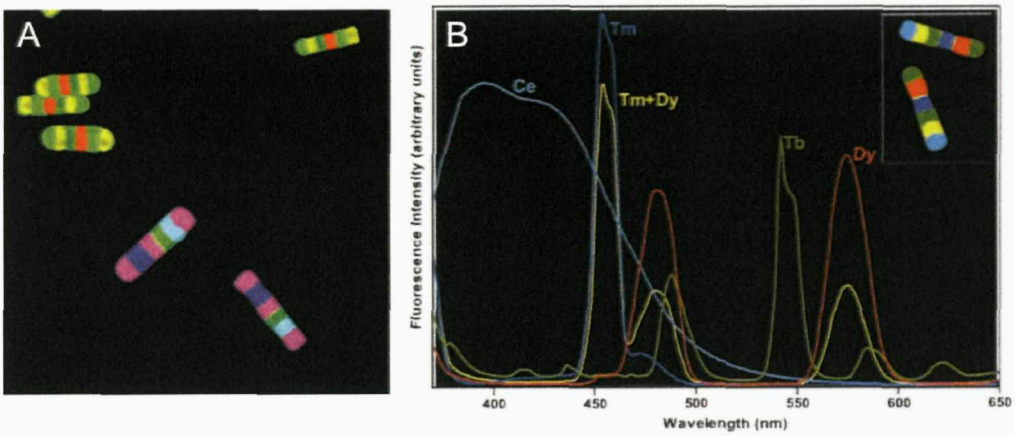

Figure 1.8: (A) A fluorescence false colour image of rare-earth doped glass encoded microparticles, showing two different codes. (B)The spectra of each element of a glass barcode, alongside two barcodes with each elemnt false coloured to match the spectra. Also included in (B) is the spectrum of a double-elemnt doped glass, which allows the colour palette to be increased compared to that available by doping with single rare-earth elements (figure taken from [22]).

in figure 1.8(A), together with the fluorescence spectra of each possible barcode element in figure 1.8(B). Using the six positions and four different rare-earth elements shown, the number of non-degenerate combinations (and hence the number of possible unique codes) is 2080. The authors also fabricated glasses doped with mixtures of two rare earth elements; the emission spectrum of the Tm + Dy combination is included in figure 1.8(B). Such two element combinations increase the colour palette to 9 and hence the number of codes 265,000. By extending the colour palette to include triple element combinations, the authors claim that $> 10^6$ codes would be theoretically achievable using this technique. The applicability of these glass microbarcodes to bead-based assays was shown by the successful demonstration of a 2-plex DNA assay.

Although the capacity for a large number of codes has been demonstrated with this technique, a significant disadvantage would appear to be the complex nature of the manufacturing process. A separate fibre ribbon has to be manufactured for each unique code required, resulting in a relatively time consuming manufacturing process in order to be able to use the technique for highly multiplexed assays.

1.3.3 Patterned metallic nanowires

A similar approach involves the use of nanowire barcodes manufactured from alternating sections of different metals, where the reflectivity, position and length of the metal sections combine to create unique codes [23, 24, 25]. The nanowires are manufactured [24], by electroplating alternating metal layers into an alumina template. The template was a commercially available alumina membrane with 200nm diameter pores, which was initially prepared by evaporating a silver layer onto one side as a conduction layer for the electroplating. Alternating layers of gold and silver where then electroplated to the required section lengths, in order to produce a code. The resulting nanowires were then removed from the template by dissolving the alumina in 3M sodium hydroxide.

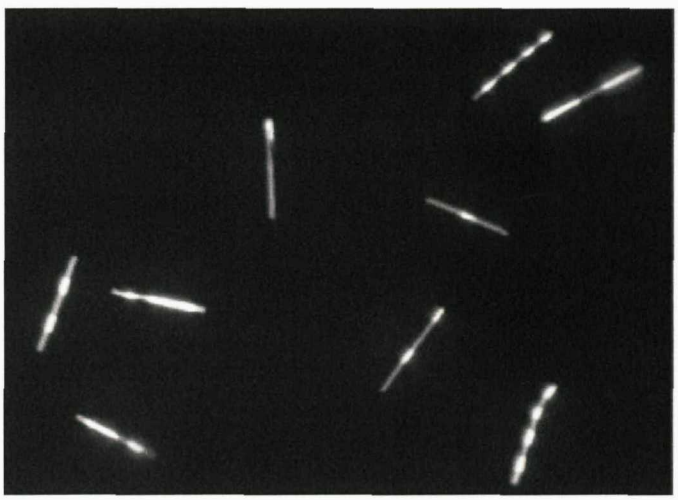

Figure 1.9: Optical micrograph of encoded metallic nanowires after release from their alumina electroplating template (figure taken from [24]).

A mixture of wires with different codes is shown in figure 1.9. The final nanowires are 200nm in diameter and approximately 4.5μm long. The code on a wire is binary with '0' bits represented by gold stripes of a fixed length and '1' bits by silver stripes of a fixed length [23]. The length of a stripe of a particular metal indicates how many of the same bit appear in sequence (e.g. '11' will appear as a silver stripe double the length of '1'). Readout of the code is accomplished by illuminating the nanowires with light of a wavelength for which one metal has a high reflectivity whilst the other has a low reflectivity. The code can then be automatically read from microscope images such as that shown in figure 1.9 by analysing the image

brightness along the wire's length.

The segment length used for each binary digit in figure 1.9 was 640nm, allowing 7 binary digits to be encoded, resulting in an encoding capacity of 80 unique codes (roughly half what is expected from binary considerations, as there is no indication of which direction the particles should be read). The minimum segment length obtainable corresponds to the Rayleigh resolution limit of the microscope system used to read the codes. The authors claim that for reliable readout the section length needs to be well above this diffraction limit, and give an example of a 6.5μm wire with 500nm segments, which allows 13 binary digits to be encoded, giving a capacity for 4160 unique codes. The nanowires have been functionalized for biochemistry and used to demonstrate a 2-plex immunoassay [23], and a 15-plex SNP assay [26].

1.3.4 Structurally patterned microparticles

A large number of technologies are based on encoding by microstructuring different materials, to create patterns which constitute a binary code. One such commercially available technology is the UltraPlex technology developed by SmartBead Technologies Ltd., a spin-out company of the University of Cambridge, UK [10, 27]. The codes used in this technology are manufactured from aluminium rods patterned with holes, defined and patterned by photolithography and dry etch methods. An example of a selection of such codes are shown in figure 1.10(A). The company offers a fully automated reaction and reading system for immunoassays, and around 100,000 codes are possible using this technology.

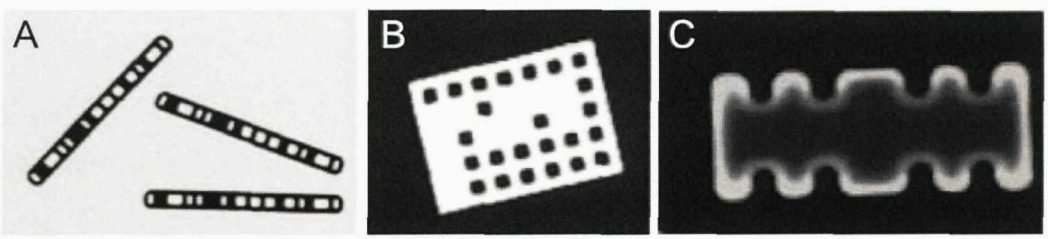

Figure 1.10: (A)Optical micrograph of encoded aluminium rods manufactured by SmartBead Technolgies, as used in their UltraPlex system (figure taken from [10]). (B)Optical micrograph of a 3DMS ImageCode. The L-shaped pattern of holes indicate the orientation, and the central holes constitute a binary code. (C)Optical micrograph of a 3DMS FloCode. The pattern of ridges along the edge is a binary code, read by recording the fluctuations of scattered laser light as the particle flows through a laser beam (figures taken from [28])

A similar technology developed by 3D Molecular Sciences Ltd. (3DMS, Cambridge, UK), involves the patterning of the epoxy photo-polymer SU8 [28]. They have developed two types of code, both defined and patterned using photolithographic selective cross-linking of the SU8. The first type, termed ImageCodes is designed to be read on a flat plat and are relatively large in size ($100 \times 100\mu$m). They are patterned with square arrays of holes, which represent binary digits making up a code. An example of an ImageCode is shown in figure 1.10(B). The L-shaped pattern of holes around the edge is used to identify the orientation of the particles, and the rest of the holes constitute the code used to identify the particles. The second type are designed to be read in a more-high throughput, flow-based system. An example is shown in figure 1.10(C). The codes have different patterns of ridges along both edges, which constitute the code. During reading, the particles flow past a laser beam, and the change in scattered laser light due to the ridges is monitored by a detector, allowing high-speed, automated reading of the code on the particle. The number of codes is quoted to be of the order of 10^6, although no detail is provided to justify these numbers. The attachment of DNA to the flow codes has been demonstrated, proving their compatibility with biochemical assays [28].

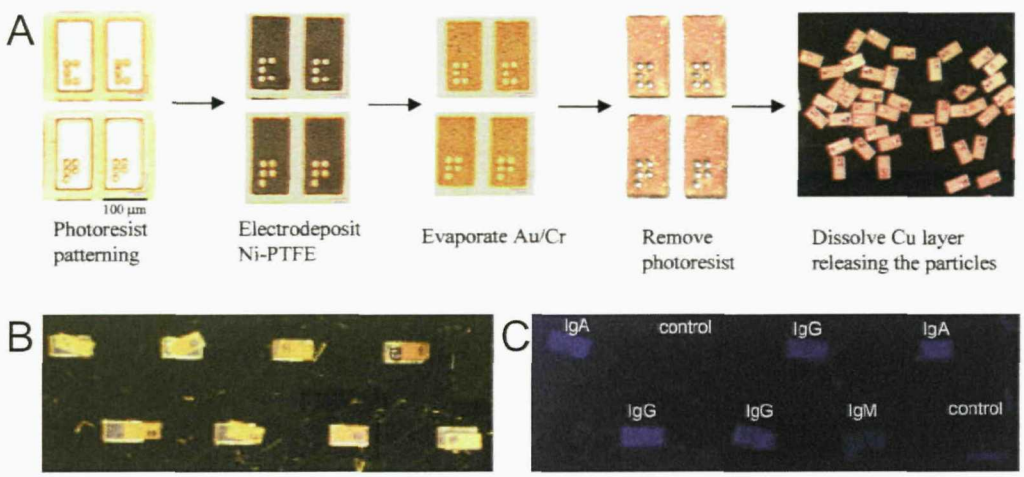

Figure 1.11: (A) particles are manufactured by first photolithographically patterning an SU8 mould on a glass substrate with a Cu sacrificial layer, into which alternating nickel and PTFE layers are deposited. The particles are coated with gold for biomolecule attachment, and lifted off by etching the Cu layer (figure taken from [29]). (B) Particles with three different codes are coated with IgA, IgG or IgM and a particle with fourth code remian uncoated and are used as a control. (C) A fluorescence image of the particles after reaction reveals little binding of the target analyte to the control particles (figures taken from [30]).

Another encoding technology based on patterning holes into particles to make

binary codes, has been demonstrated by using SU8 photopolymer moulds to manufacture patterned nickel particles [29]. The manufacturing process is shown schematically in figure 1.11(A): An SU8 layer was spun onto glass coated with a copper sacrificial layer, and the SU8 photolithographically patterned to form square wells (as moulds for the particles) with SU8 pillars to mould the code bits. Nickel and PTFE were electroplated in alternating layers of approximately $6\mu m$ thickness, followed by a chrome adhesion layer and then a gold coating. The SU8 was then removed, and the finished particles lifted off by etching the copper sacrificial layer. The resulting particles are of dimensions $100 \times 200\mu$m, with an $80 \times 50\mu$m array of up to 8 code spots, which can be made either present ('1') or absent ('0'), creating a binary code. This particular scheme can encode $2^8 = 256$ different microparticles, although increasing the number of bits would be possible, to create more unique codes. The gold layer is used due to its higher compatibility with chemical attachment than the nickel layers, with the nickel layers supplying mechanical stability.

The particles have been successfully used in a 3-plex immunoassay [30], the results of which are shown in figures 1.11(B) and (C). A selection of particles with three different codes 1.11(B) have either one of three antibody types (IgA, IgG or IgM) attached to the surface. A particles with a fourth code have no antibody attached, and are used as a control. A fluorescence microscope image of the resulting codes after incubation with antigens corresponding to each antibody is shown in figure 1.11(C). The lack of fluorescence on the control particles shows that little non-specific binding of the targets occurs. The particles were also used in a similar fashion in a 3-plex oligonucleotide hybridisation assay [31].

Pregibon *et al.* [32] recently demonstrated an encoding technology very similar to the 3DMS ImageCodes. However, a significant achievement of their work was the demonstration of encoding, analyte attachment to the beads and reading of the codes all within a microfluidic system. The method of manufacturing the encoded microparticles is shown in figure 1.12(A); two streams of the monomers of poly(ethylene glycol) (PEG) flow together down a microfluidic channel, remaining separate due to the laminar flow properties of microchannels. One stream contains fluorescently labeled monomers to form the code region while the other contains monomers with a biological probe (for example an oligonucleotide) attached, for use in an assay. The particles are defined and patterned using UV light passed through a mask and a reduction lens; regions of high UV intensity polymerize the monomers forming a solid particle from which the un-crosslinked monomer is subsequently rinsed, leaving holes signifying binary '1' digits. The resulting particles, shown in

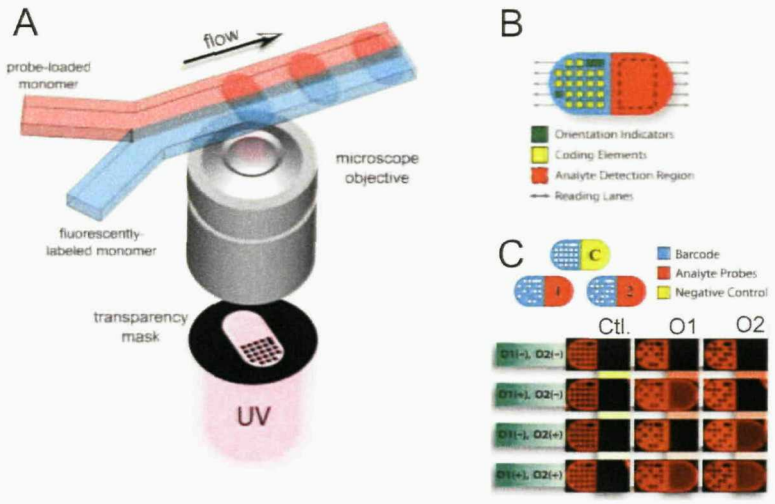

Figure 1.12: (A)Particles manufactured in-flow from the photo-polymer PEG. Two flow streams contain fluorescent labeled PEG for the code section of the particle and Peg with probe attached for the analyte section of the particle. (B)The resulting particles contain a code featuring orientation digits and the code digits themselves, and an analyte region, both of which are read along the lines defined by the arrows. (C)Three types of coded particle, allow the binding of different oligonucleotides O1 and O2 to be compared to a control region Ctl (figures taken from [32]).

figure 1.12(B), feature a coding region on one half of the particle, consisting of two orientation-identification elements and 20 digits of a binary code which may be made present ('1') or absent ('0') depending on the desired code. As a result the example presented here has the capacity for $2^{20} \approx 10^6$ unique codes. The region surrounding the holes representing the code digits is fluorescent, increasing the signal-to-noise ratio. The other half of the particle has the biological probe attached, for use in bead based assays using these particles.

The applicability of these particles to DNA hybridization assays was demonstrated by fabricating three types of particles with different codes; one type with oligonucleotide O1 in the analyte stream, one type with oligonucleotides O2 and one type with naked PEG containing no oligonucleotide as a control (figure 1.12(C)). All three types of particle were reacted with a solution containing no oligonucleotides (O1(-), O2(-)), a solution containing the fluorescently-labelled complementary oligonucleotide to O1 (O1(+), O2(-)), a solution containing the fluorescently-labelled complementary to O2 (O1(+), O2(-)), and a solution containing both fluorescently-labelled complementaries (O1(+), O2(+)). The results can be seen in the bottom part of figure 1.12(C): The control 'Ctl.' shows no increase in fluo-

rescence in the molecular-binding section of the particle, whilst the particles containing O1 and O2 show an increase in fluorescence in the solutions containing their respective complementary oligonucleotides, indicate binding of the complementary oligonucleotides to the particles. This demonstrates the use of the particles in bead based DNA-hybridisation assays. In addition, the authors demonstrate the use of more than two flow streams to create particles with multiple analytes in separate regions.

Two more technologies have been developed recently based on structuring of beads to provide a code. They are conceptually similar, and rely on the readout of the reflectance of optical [33] or radio-frequency (RF) [34] radiation in a flow device. The first type [33] are microbars of silicon $1000 \times 500 \times 100\mu$m defined photolithographically, and patterned with wet-etched aluminimium stripes which constitute the code. Two examples of the coded microparticles are shown in figure 1.13(A). The codes are read by flowing the particles through a microfluidic system past a 633nm laser beam focussed to a 50μm spot. The reflected light from the laser is read by a phototransistor, and an example readout of the detector from a particle is shown in figure 1.13(B). The aluminium has a higher reflectivity of the laser light than the silicon, allowing the aluminium areas to be identified from the reflectance readout. The microbars were successfully identified at flow rates of 10 cm s^{-1}.

The second type of flow-read reflectance codes consists of SU8 bars ($100 \times 20 \times 0.3\mu$m), with embedded aluminium strips, again defined and patterned photolithographically [34]. An example of such a code is shown in figure 1.13(C). The particles flow in a microfluidic system past a set of radio frequency (RF) generating/detecting electrodes. The reflectance of the RF field is detected, and the aluminium shows increased reflectance compared to the SU8, so that aluminium areas can be identified from the RF reflectance readout. Typical readouts for the codes '1100110011' and '0110110110' are shown in figure 1.13(D). Such a 10-bit code gives an encoding capacity of $2^{10} = 1024$ unique codes, with the authors claiming the possibility to decrease the bit-width by a factor of two, allowing for $2^{20} \approx 10^6$ unique codes. Flow rates of 10cm s^{-1} were demonstrated with successful readout, and binding of antibodies to the particles has been demonstrated.

1.3.5 Photobleached fluorescent microspheres

A microbead encoding method which involves patterning microspheres without structuring them, involves the writing of patterns by fluorescence photobleaching

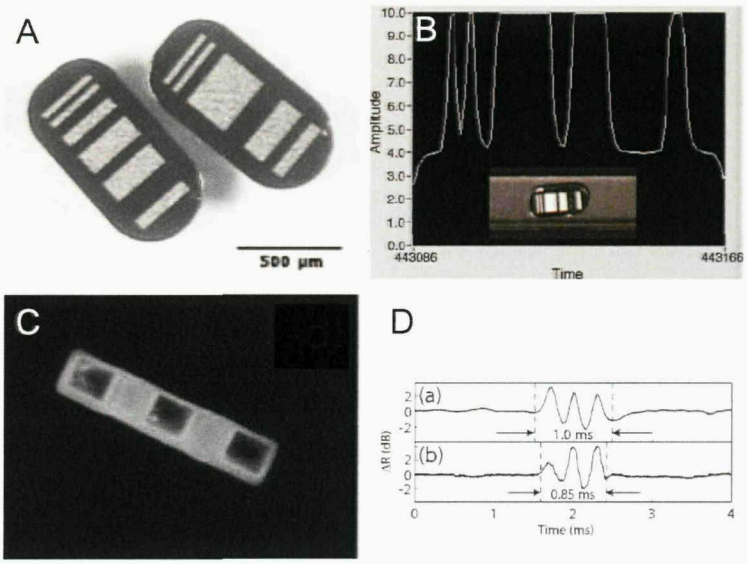

Figure 1.13: (A)Silicon microbars encoded with patterned aluminium. (B)Reflectance traces of 633nm laser light recorded from flowing silicon microparticles allow successful identification in flow speeds up to 10cm $s^{-}1$ (figures taken from [33]). (C)An SU8 microbar encoded with patterned aluminium. (D)RF reflectance traces allow identification of SU8 bars in flow at similar speeds to that recorded for the silicon bars(figures taken from [34]).

[35, 36, 37]. The particles were 45μm diameter polystyrene spheres doped with a specialized fast bleaching green fluorescent dye (N-(7-nitrobenz-2-oxa-1,3-diazol-4-yl)diethyl amine). The dye was bleached using light of wavelength 488nm from an 30mW argon-ion laser which was focussed by a 40$\times$ objective onto the sphere [37]. The laser was deflected by an acousto-optic modulator controlled by a computer, in order to be raster-scanned over the sphere, writing the desired pattern by photobleaching the fluorescent dye. The pattern could then be observed by illuminating the sphere with lower intensity light of the same wavelength (with power levels of 30μW), causing fluorescence to be excited in the non-bleached parts of the sphere, whilst the bleached parts remain dark. Some examples of codes written into spheres using this method are shown in figure 1.14. The codes are dark bars whose width and intensity constitute the code elements: partial photo-bleaching may be employed to adjust the fluorescence intensity in the code bars. An example of a two-level code (bleached/unbleached) is shown in figure 1.14(A), and a three level code (bleached/partially bleached/unbleached) example is shown in 1.14(B). Since the codes are written by scanning the laser beam over the sphere, the write time can be minimized by writing only in one dimension, creating what the authors term

'dot codes' (figure 1.14(C)). A cross section through this dot code is shown in figure 1.14(D) showing the distinguishability of the three bleaching intensity levels used. Using two intensities and three bar widths, the authors claim an encoding capacity of 4×10^6 unique codes, increasing to 10^8 with the use of three intensity levels.

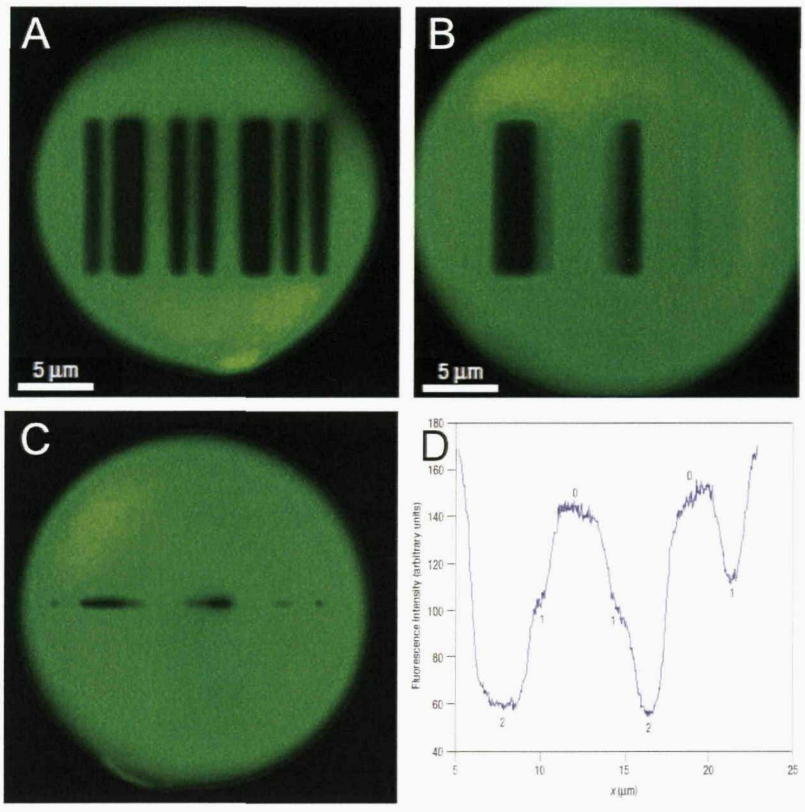

Figure 1.14: Codes written into fluorescent microspheres by photobleaching. Codes are written as bars of different width, and may be of two (A) or three (B) intensity levels. Write time is minimized by creating 'dot codes' (C), and a cross section through such a dot code (D) indicates the ability to distinguish the three fluorescence levels (figures taken from [37]).

A significant problem with the above technology is that the use of spherical beads means that the code is not necessarily oriented in the correct plane for reading, as the bead may easily rotate in all three dimensions. This problem was solved by using a 'layer-by-layer' approach to coating the microspheres with a material suitable for the attachment of antibodies/antigens [35, 36]. A layer of poly(allylamine hydrochloride) (PAH) is first deposited on the microspheres, followed by a layer of ferromagnetic chromium dioxide (CrO_2) nanoparticles of diameter less than 450nm. Another layer of PAH is deposited to trap the nanoparticles on the surface, followed

by more layers to which antibodies may be attached. A magnetic field is applied to the particles during writing, which permanently magnetizes the CrO_2 nanoparticles. On reading, a weaker magnetic field in the same direction causes the microspheres to rotate into the correct orientation for reading. Using the layer-by-layer coatings, the encoded microspheres have been successfully used in 3-plex immunoassays [36].

1.3.6 Raman spectroscopic encoding

A number of encoding technologies have been developed, that make use of codes based on Raman spectroscopy. The first of these are formed from aggregates of silver nanoparticles with organic molecules chosen for their specific Raman spectra [38], termed 'Composite Organic-Inorganic Nanoparticles (COINs)'. The particles are manufactured, as shown schematically in figure 1.15(A), by placing seed silver nanoparticles in a solution of silver nitrate and a Raman label. The silver particles grow in the solution and aggregate with the Raman labels to form the COINs. Some example COINs are shown in the TEM images in figure 1.15(B). Raman spectroscopy of the COINs reveals particular dominant peaks, whose Raman shift depends on the particular organic Raman label used (see figure 1.15(C)). The silver nanoparticles enhance these peaks via Surfaced-Enhanced Raman Scattering (SERS), phenomenon in which Raman signals from substances in close proximity to rough metal surfaces are increased. Inclusion of more than one organic Raman label results in a larger number of dominant peaks, allowing for more codes to be created (see figure 1.15(D)). The authors claim that with 50 Raman labels, whose Raman-shift peaks are separated by 15 cm^{-1}, of the order of millions of different codes are possible. Antibodies were conjugated to the COINs by adsorption, allowing them to be used in a demonstration of a 2-plex immunoassay.

A method has also been proposed that uses polystyrene beads, in which the styrene monomer is modified with a range of additional chemical groups in order to create unique features in the Raman spectra of the beads [39]. Each particular type of styrene monomer is given a binary digit (see figure 1.16(A)), and the presence or absence of this monomer results in the assignment of '1' or '0' respectively, to that particular digit. With the 6 different monomers used, up to $2^6 = 64$ beads may be uniquely encoded. To demonstrate the reading of the Raman-encoded beads, beads with 12 unique codes among them were randomly inserted into 100μm wells patterned by reactive-ion etching into a silicon carrier. The bead were inserted from a suspension in ethanol, using mechanical assistance to force beads into the

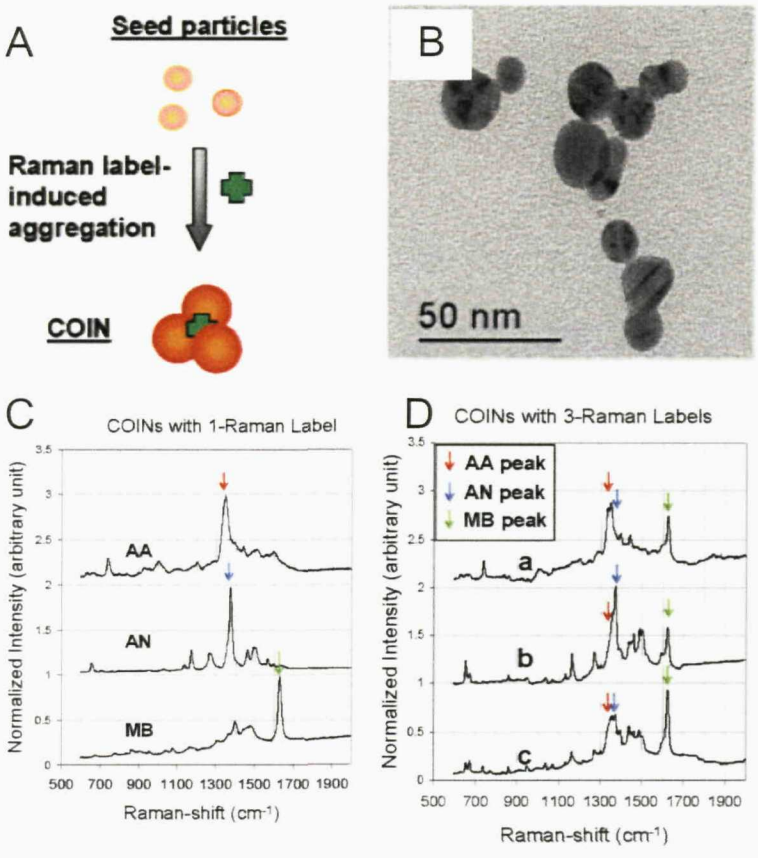

Figure 1.15: (A)Schematic diagram of the formations of the COIN aggregates. (B)TEM images of some COINs. (C)Raman spectra of COINs containing three different organic Raman labels 8-azaadenine (AA), 9-aminoacridine (AN)and methylene blue (MB). The spectra show the different positions of the dominant Raman peaks which may be exploited for encoding. (D)Raman spectra of COINs containing different ratios of all three Raman labels, showing how the varying relative heights of the dominant peaks can be used to create larger numbers of unique codes.(figures taken from [38]).

wells. An area of 48 beads was scanned using 110μm steps over the carrier (see figure 1.16(B)) taking a Raman spectrum at each step. Each bead is then uniquely associated with a Raman spectrum, as shown by the colour coding associating the beads in figure 1.16(C) with the spectra in figure 1.16(D). A deconvolution algorithm identifies which styrene monomers' signature peaks are present in each spectrum by comparison against a set of prerecorded spectra from each type of polystyrene [40], allowing a binary code to be associated with each bead. The deconvolution process took 15 minutes for the 48 beads, giving a readout rate of approximately 3 beads per minute. Attachment of peptides to the beads has been demonstrated

[40], showing no appreciable effect on Raman spectra, allowing the codes to be read after attchment of molecules the surface of the beads.

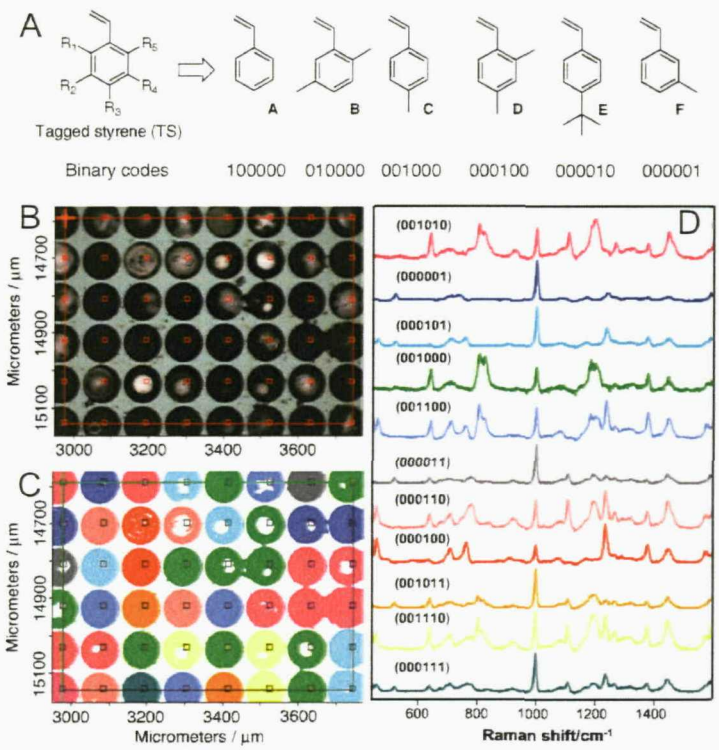

Figure 1.16: Polystyrene beads can be encoded by inclusion of styrene monomers with various additional side groups, with each type of monomer representing a binary digit (A). The beads are deposited in wells in a silicon carrier, which is scanned in 110μm steps and Raman spectrum collected at each step (B). Each bead (C) is associated with the correspondingly coloured Raman spectrum (D). A deconvolution algorithm then uses the presence or absence of each monomer signature in each spectrum to assign each bead a binary code (figures taken from [39]).

A third Raman based method uses a single dye with a characteristic Raman spectrum, whose various positions on a micron-length wire constitute the code [41]. The wires are manufactured using a process called 'on-wire lithography' [42]: Nanowires of nickel with pairs of gold segments (see figure 1.17(A), step 1) are synthesised by electroplating, in a similar manner to the nanowires described in section 1.3.3. After removal of the electroplating templates, the wires are deposited randomly on a surface and covered with evaporated silica. The wires are freed from the surface by sonication in ethanol, and the nickel etched away leaving arrays of gold nanodisk pairs held together by a silica 'backbone' (1.17(A), step 2). Raman-active dyes are then attached to the gold (1.17(A), step 3) [41], and the arrays are examined by

confocal Raman microscopy, which forms an image by scanning pixel-by pixel over the nanodisk array, recording the Raman spectrum between 139 and 2789 cm^{-1} at each point and integrating the Raman intensity over the whole spectrum to create the pixel intensity. The Raman signal is increased inbetween the gold disk pairs due to the higher dye concentration in these regions, as compared to other areas of the array, resulting in confocal Raman images of the type seen in figure 1.17(B) for the code 11111. The signal inbetween the disk pairs is further enhanced due to surface-enhanced Raman scattering. Disk pairs can be removed from the array to create 0 digits, allowing any 5-bit binary strings to be encoded with this method, as seen for some examples in figure 1.17 (C). The encoding capacity of these nano-disk arrays is then $2^5 = 32$ codes. Using this technology, DNA assays have been demonstrated by attaching Raman-labeled oligonucleotide sequences to the gold disks in place of the simple Raman labels. The encoding capacity can potentially be increased by using more disks in the array, and using a number of different Raman-active dyes, identified by filtering the Raman images according to the unique Raman properties of each dye.

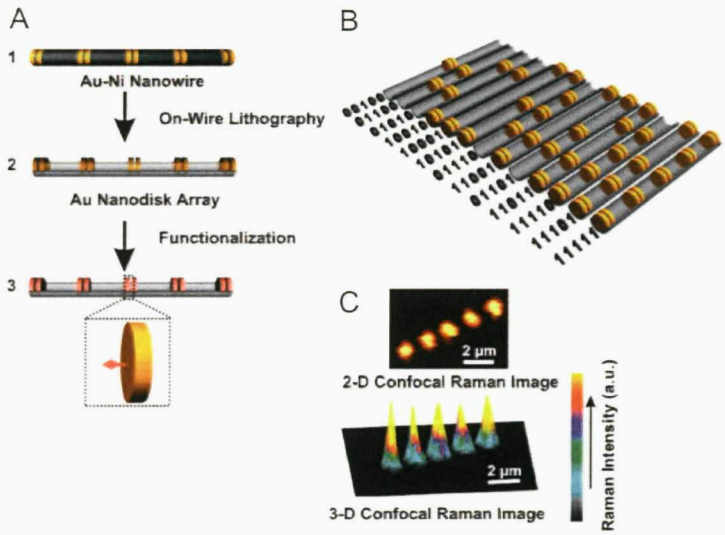

Figure 1.17: (A)Schematic diagram of the process for manufacturing nanodisk codes, for the example code 11111. Omission of any of the nanodisks change a '1' bit to a '0' bit, allowing creation of a large number of binary codes, as seen here for some examples (B). The codes are read by confocal Raman spectroscopy, which shows enhanced signal between the disk pairs, allowing the code to be identified by areas of strong Raman signal (figures taken from [41]).

1.3.7 Tag technology summary and discussion

This section has described a number of existing technologies, which are being developed to solve the problem of uniquely encoding large numbers of microparticles for use in bead-based biological assays. These are essentially divided into two main technologies: The first is spectroscopic encoding, in which the concentration of various molecules constitutes the code, where the various molecules are detected by UV-visible spectrophotometry or Raman spectroscopy; the second is graphical encoding, in which a pattern is encoded on the surface of the microparticle, and read directly using a microscope with attached CCD camera and machine vision software. There is some overlap between the two, in that some technologies make use of both graphical patterning and spectroscopic information.

In general, the purely spectroscopic methods have lower encoding capacities, and the use of intensity information for the more highly multiplexed fluorescence-based technologies may start to make them unreliable as the number of codes increases, due to spectral intensity variations. In addition, the use of fluorescence as an indicator is not particularly compatible with the use of fluorescent dyes to indicate analyte binding, which is a common technique in most biochemical assays. However, fluorescence based flow-cytometric assays technologies with approximately 100 unique codes are in commercial use, demonstrating that they have a promising and well-defined place for reliable assay encoding for applications with lower multiplexing requirements, such as many common immunoassays.

The graphical methods have the advantage of much higher encoding capacities (of the order of 10^6 unique codes). In addition, it is easy to implement binary encoding techniques featuring error detection mechanisms when using these graphical technologies. They also have the advantage of not requiring fluorescence as part of the encoding (although some of the technologies do), reducing interference with the binding indicators of the assay. The main disadvantage of many of the graphical methods is that to obtain large encoding capacities, the particles must generally be around 10 times larger than those used for fluorescence based technologies (i.e. dimensions of hundreds rather than tens of micrometres). In addition, creating an adequate signal to noise ratio between '1' and '0' bits often requires either a more complicated manufacturing process to incorporate high reflectivity elements into the microparticles (as in [33] and [34]), or the use of fluorescent dyes to create a bright background for dark code elements (as in [37] and [32]). There is also the potential that damage to the bars causes reading errors by removing or reducing the signal of some parts of the code. There is also little scope for coping with mis-orientation of

the particles, which may result in reading errors.

1.3.8 Diffractive encoding of microparticles

The work presented in this thesis investigates a method of encoding microparticles that retains the high encoding capacity and compatibility with fluorescent binding indicators that are the most useful features of the graphical encoding methods, while attempting to address some of the graphical methods' disadvantages. To do this, encoded patterns will still be created on the surface of the microparticles, but instead of reading them directly to obtain the code, the distribution of light diffracted by the patterns on the particles' surfaces will be detected and analysed. This method offers a number of advantages over graphical systems; principally that the code is projected from the particle, so that no additional optics are required for reading the tag. This simplifies the system, compared to the microscopy systems required to read graphical tags. This simplification makes the reading system for this tag more amenable to miniaturisation. In addition, the diffractive method's reliance on the periodicity rather than the absolute position of features on the tag's surface, makes this system more robust to tag contamination and breakage. To begin to understand how the diffractive method might work, some background on the phenomenon of diffraction will first be considered.

1.4 Diffraction

1.4.1 Introduction - the Huygens-Fresnel principle

In general, diffraction is a phenomenon that occurs when any wave encounters obstacles which either attenuate or vary the speed of the wave in a different manner to the surrounding medium. The effect is normally most pronounced when the obstacles are of only a few wavelengths in size. In this instance we only wish to consider visible light waves (with wavelengths of 400-700nm), and therefore the obstacles will have a different light absorption or refractive index than the surrounding medium, and will generally be of a size smaller than a few tens of microns. The obstacles could be arranged in a pattern, and the light diffracted by the pattern of obstacles will contain information about the dimensions of that pattern. The simplest way to visualize this, is to consider a *diffraction grating* which is an infinite (for the moment), mostly opaque object with periodic slits which transmit light. To visualize how the diffraction pattern of this grating is formed, we will use calculations

based on the Huygens-Fresnel Principle, which states that 'every unobstructed point of a wavefront, at a given instant in time, serves as a source of spherical secondary wavelets with the same frequency as that of the primary wave. The amplitude of the optical field at any given point is the superposition of all these wavelets, considering their amplitudes and relative phases' [43]. If we consider the slits as infinitesimal for the moment, when a plane wave of wavelength λ is incident on them, we may consider the grating as a series of point sources of spherical waves with wavelength λ, with the sources positioned along a straight line and spaced by distance a (see figure 1.18(A)). The distance a is usually known as the 'period' of the diffraction grating. The waves from all of the sources add up either constructively or destructively in different directions. The maximum intensity occurs at the angle θ when the phase of waves from one source differ by an integer number of wavelengths from the phase of all other sources. By considering the triangle $\triangle def$ in figure 1.18(A), it can be seen that this occurs when

$$a \sin\theta = m\lambda, \tag{1.1}$$

where m is an integer, i.e. $m = 0, \pm 1, \pm 2, ...$ Hence, the diffraction pattern of the array of slits is a series of high intensity beams (which can be represented by delta functions, as shown in figure 1.18(B)), traveling at angles θ defined by equation 1.1.

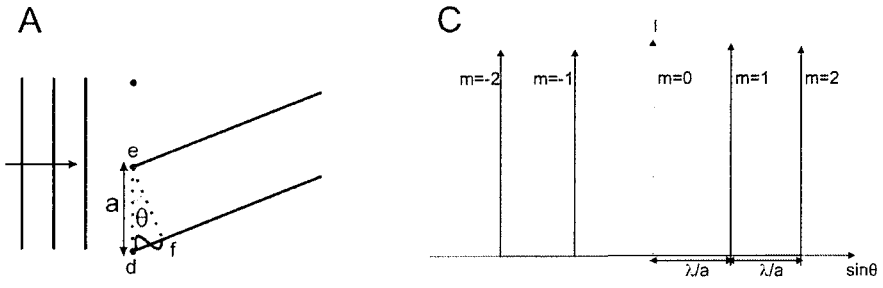

Figure 1.18: When a plane wave passes through an infinite-length array of infinitesimal slits of period a (A), diffracted maxima form when the waves from all slits have an integer number of wavelengths phase difference between them. The maxima appear as delta functions separated by λ/a in $\sin\theta$.

An infinite grating with slits of infinitesimal width is clearly not practical, so we need to consider what happens to the diffraction pattern when the grating has a finite length L and the slits have a finite width b. To see the effect that L has on the diffraction pattern, we start by considering what happens as the observation angle θ moves away from a maximum position. For an infinite grating, even a very small

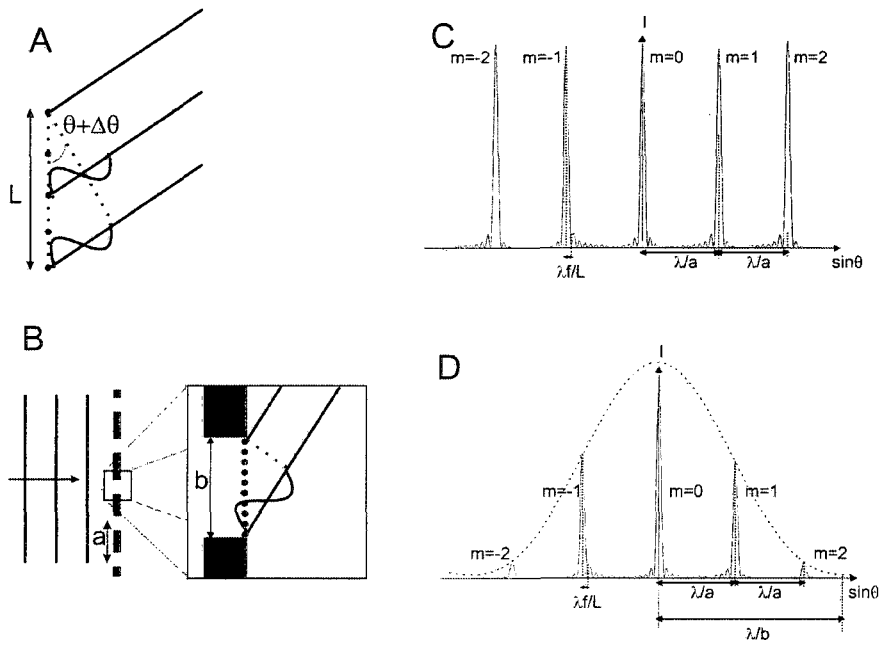

Figure 1.19: If the diffraction grating has a finite length L (A), the diffracted intensity falls to a minimum at $\sin(\theta + \Delta\theta) = \lambda/L$, giving the diffracted beams a larger width (B). Introducing a finite width b to the slits (C) gives a final form for a realistic diffraction grating, where the diffracted intensity of the maxima falls off according to the envelope defined by $\sin(\Delta\theta) = \lambda/b$ (D), shown here as a dotted line over the whole pattern.

change in θ immediately extinguishes the diffracted wave, as for each slit there will always be a slit somewhere else on the grating which has a wave π-radians out of phase with it, and therefore the light from all sources is completely canceled out. For a grating with finite length L, this complete cancelation only happens when the sources at either end of the grating are perfectly in phase, so that there are pairs all the way along the grating, separated by $L/2$ whose waves differ by $\lambda/2$. The first position at which this occurs next to a maximum at position θ, as shown in figure 1.19(A), is at the new position $\theta + \Delta\theta$ for which

$$\sin(\theta + \Delta\theta) = \frac{\lambda}{L}. \tag{1.2}$$

Up until this point the intensity drops off from the maximum, as more and more waves interfere destructively. In addition, as θ moves away from the minimum, a small proportion of the waves interfere constructively again, and in this manner a number of very weak subsidiary maxima are produced. The result is a diffraction pattern as seen in figure 1.19(B), with the principal maxima now spread out instead

of being infinitely thin δ-functions. The finite width b of the slits has a similar effect. We consider the slit to be made up of a large number of infinitesimal sources, as shown in figure 1.19(C). The intensity due to these sources falls to a minimum at $\sin(\Delta\theta) = \lambda/b$, which forms an envelope over the whole diffraction pattern, resulting in diffracted maxima with successively greater values of m being less and less intense, as shown in figure 1.19(D). The principal maxima of the diffraction pattern at values of θ that satisfy equation 1.1 are commonly called the diffracted orders of the grating, with $m = 0$ being the 0-order, $m = 1$ being the 1st-order, etc.

It should be clear that a set of diffraction gratings with different values of a can be uniquely identified from their diffraction patterns, as long as their diffracted orders are at different positions, so that they can be distinguished from each other. This sets the basis for an encoding system in which a grating of period a is illuminated with a plane wave, and its diffraction pattern observed on a flat plane parallel to the grating at some distance z from it. The period of the grating can be obtained by finding the angle θ for $m = 1$ using the separation of the peaks of the various diffracted orders together with the distance z. Equation 1.1 can then be used to recover a. Varying a changes θ, so we can create a number of codes using different values of a, which can be identified by their diffraction pattern. The diffracted orders with $|m| > 1$ can potentially also be easily eliminated from the diffraction patterns, as they are less intense than the $m = \pm 1$ orders, as seen in figure 1.19(D). This is exactly the basis that will be used for diffractive encoding of microparticles. The exact details of the encoding method are discussed in chapter 2. First, however, the phenomenon of diffraction needs to be considered in a more rigorous and generally applicable manner than that based on the Huygens-Fresnel principle, to provide some useful tools for formulating and investigating diffractive microparticle encoding techniques.

1.4.2 Fresnel and Fraunhofer diffraction

Mathematical formulations of the calculations of the forms of grating diffraction patterns based on the Huygens-Fresnel principle, can be found in references such as [43, 44, 45]. The formulation that is used to solve many types of diffraction problems is that of Kirchhoff, in which the wave equation of a spherical wave with wavelength λ emanating from a source P_1 and passing through an aperture in a perfectly absorbing infinite screen is solved with respect to the boundary conditions imposed by the aperture. This is done by considering an arbitrary aperture in such an opaque screen defined by the coordinates (x, y, z) and, using the geometry shown

in figure 1.20(A), the diffracted field $E(P_0)$ at a point P_0 with coordinates (x', y', z) is given by

$$E(P_0) = \frac{Ci}{2\lambda} \iint_A \frac{\exp(ik(r+s))}{rs} [\cos(\mathbf{n}, \mathbf{r}) - \cos(\mathbf{n}, \mathbf{s})] dS \tag{1.3}$$

where the integral is over the aperture A, C is a constant proportional to the strength of the source at P_1, $k = 2\pi/\lambda$, $\mathbf{r}$ is the vector connecting the source P_1 to a point on the aperture, $\mathbf{s}$ is the vector connecting the aperture point to the observation point P_0 and $\mathbf{n}$ is the normal to the aperture plane. The derivation of this is given in many standard texts (for example [44, 45]), and it is commonly referred to as the 'Fresnel-Kirchhoff diffraction formula'. Some problems with this formulation are that (i) it has been shown to be mathematically inconsistent in terms of its boundary conditions and (ii) it is only valid if the aperture is much larger than the wavelength (as it assumes the field immediately after the aperture is an exact geometrical shadow of the aperture and not disturbed by edge effects in any way) [44]. However, when considering only the diffracted intensity, the formulation and the common approximations to it (see below) have been shown to agree very well with experiment even with aperture sizes of around 1 wavelength, provided the diffraction pattern is observed at sufficiently large distances from the aperture [46, 47].

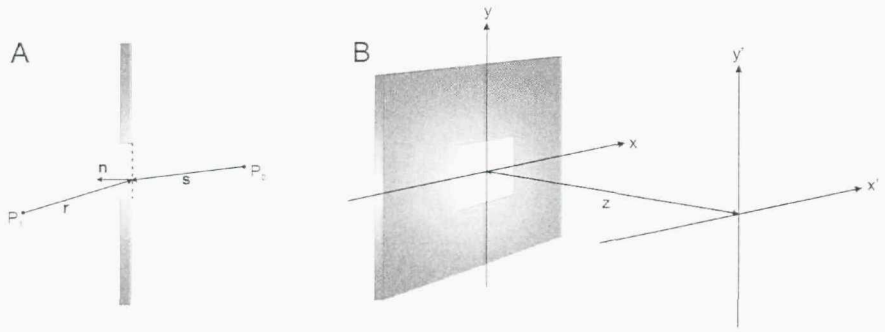

Figure 1.20: (A)The geometry used in the derivation of the Fresnel-Kirchhoff diffraction formula. Circular wavefronts emanate from point P_1, pass through the aperture, and are observed at point P_0. (B) Geometry used for the Fresnel and Fraunhofer approximations to the Fresnel-Kirchhoff formula. A plane wave passes through an aperture in the plane (x, y) and the diffraction pattern is observed in plane (x', y') a distance z from the aperture.

A number of approximations to the Kirchhoff formulation are made to solve certain types of problems. The most common being the Fresnel and Fraunhofer approximations, which apply when the source is a plane wave and the observation

plane is at a large distance from the aperture, relative to the wavelength of the light illuminating the aperture. To consider these approximations, we now use the geometry shown in figure 1.20(B): A plane wave illuminates an aperture in the plane (x, y), and the resulting diffraction pattern is observed in the plane (x', y'). The Fresnel approximation requires that the distance z between the two planes is large enough that the distance s from any point with coordinates (x, y) to any point with coordinates (x', y') can be approximated by the first two terms of its quadratic expansion, when written in terms of x, y, x', y' and z. The resulting expression [44] for the observed diffracted field amplitude $E(x', y')$ is

$$\begin{aligned} E(x',y') &= \frac{-i\cos\theta}{\lambda}\frac{C\exp(ikz)}{z}\exp\left[i\frac{k}{2z}(x'^2+y'^2)\right] \\ &\iint_{-\infty}^{\infty}\exp\left[i\frac{k}{2z}(x^2+y^2)\right]T(x,y)\exp(ik[xx'/z+yy'/z])dxdy \end{aligned} \tag{1.4}$$

where $k = 2\pi/\lambda$, θ is the angle between the aperture normal and a line from the aperture centre to the observation point, and $T(x, y)$ is a function which describes the transmission of the incident plane wave by the aperture (which could contain some structure, such as a grating, for example). The Fraunhofer approximation applies at even larger distances, and is that which we will use for diffraction calculations in this thesis. For the Fraunhofer approximation to be valid, the distance z should satisfy $z \gg k(x^2 + y^2)_{max}/2$ and the field $E(x', y')$ is then [44]

$$\begin{aligned} E(x',y') &= \frac{-i\cos\theta}{\lambda}\frac{C\exp(ikz)}{z}\exp\left[i\frac{k}{2z}(x'^2+y'^2)\right] \\ &\iint_{-\infty}^{\infty}T(x,y)\exp(ik[xx'/z+yy'/z])dxdy \end{aligned} \tag{1.5}$$

Apart from the factors preceding the integral, this is simply the Fourier transform of the aperture function, allowing the Fraunhofer diffraction patterns of objects which are not simply periodic (and therefore not easily analytically calculable) to be calculated on a computer using standard fast Fourier-transform (FFT) algorithms. Such FFT methods based on equation 1.5 will be used to simulate diffraction patterns throughout this thesis. The conditions for equation 1.5 to apply are also satisfied at any value of z, if a lens of focal length f is placed a distance f from both the diffracting object and the observation plane [44].

1.4.3 Diffraction from phase gratings

An alternative method of creating a diffraction grating, is to modulate the phase shifting properties of a structure, as opposed to the amplitude transmittance modulation considered in section 1.4.1. This is known as a phase grating, as diffraction from it depends upon the relative phase shift of light passing through, or reflected from, the grating features. Figure 1.21 (A) shows how a phase grating works; light passes through the entire grating, but is relatively phase shifted depending on the height D of the surface profile. For the purposes of calculating the diffraction patterns produced by such a grating (following Goodman [44]), it is treated as a flat surface, consisting of periodic regions which phase shift the light by different amounts. We consider the low points of the square profile to be zero phase shift, and the high points to be a relative phase shift ϕ of $\phi = -2\pi|n_1 - n_2|D/\lambda$ where n_1 is the refractive index of SU8 and n_2 the refractive index of the surrounding medium. The angular irradiance spectrum $I(\alpha)$ of such a grating is $I(\alpha) = F^{\star}(\alpha)F(\alpha)$, where $F(\alpha)$ is the Fourier transform of the spatial electric field distribution of the light immediately after passing through the grating, and $F^{\star}(\alpha)$ denotes the complex conjugate. For a phase grating of period a and aspect ratio $a/(a-b)$ this field is

$$F(\alpha) = \sum_{n=1}^{N} \int_{(n-1)a}^{(n-1)a+b} \exp\left[i2\pi \frac{\sin\alpha}{\lambda}\right] dx + \int_{(n-1)a+b}^{na} \exp\left[-i\phi\right] \exp\left[i2\pi \frac{\sin\alpha}{\lambda}\right] dx, \tag{1.6}$$

where as before $N \approx L/a$. The result is a diffraction pattern of similar form to that for an amplitude grating, with diffracted orders at angle α according to the equation $a\sin\alpha = m\lambda$ (figure 1.21 (B)). However, for a phase grating, the relative intensities among the various orders can be different to the amplitude grating case, depending upon the value of ϕ.

1.5 Existing diffraction-based encoding and sensing technologies

Diffraction-based encoding is already in use in optical communication systems, optical computing interconnects, information storage and sensing applications. In this section, some technologies that use diffractive methods for these purposes will be reviewed.

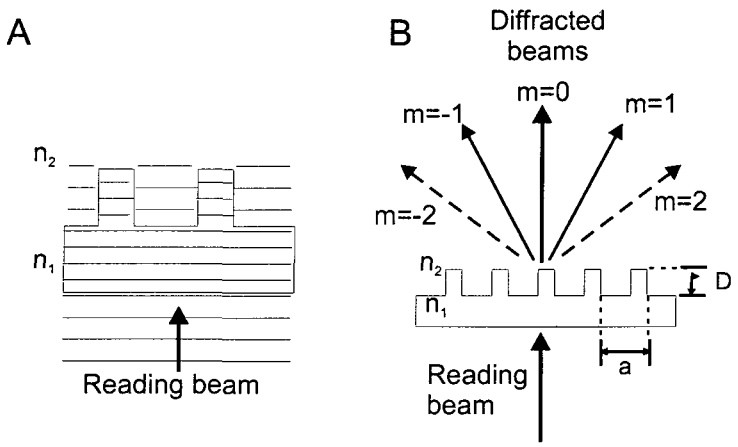

Figure 1.21: (A) A square profile grating consisting of ridges of height D on the surface of a material of refractive index n_1 is illuminated with a plane wave of wavelength λ. The grating shifts the phase of light traveling through the ridges with respect to that in the troughs. (B) The result is a series of diffracted beams in the same positions as for a similar amplitude grating, of the type considered in chapter 2.

1.5.1 Wavelength division multiplexing

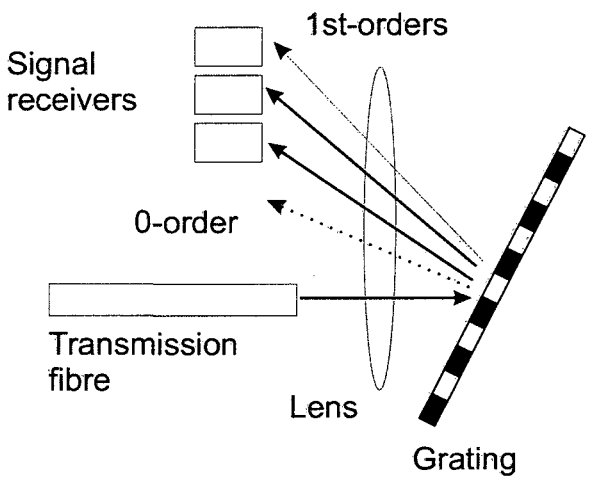

Figure 1.22: Schematic of a grating-based wavelength demultiplexer for optical fibre signals. Light from a fibre carrying multiple signal channels, each with a different wavelength, is diffracted from a grating. Detectors at the expected position of the first order for each wavelength receive the signals for each channel (image modified from [48]).).

Diffraction is used for encoding and de-coding signals in the well-established technology of optical fibre wavelength division multiplexing (WDM) [48]. In such a technology, multiple signals are sent at the same time down an optical fibre,

encoded with light of different wavelengths (each wavelength is termed a 'channel'). At the receiving end, the channels are separated using a diffraction grating, which disperses the light exiting the fibre, giving diffracted first orders at different angular positions for each channel (see figure 1.22. Two channels can be resolved if their wavelength difference is such that the angular positions of the first orders according to equation 1.1 are separated by more than the first order widths given by equation 1.2. This criterion sets the limit on the number of channels which can be encoded by this method in a single fibre (additional limits are set by factors such as signal degradation during transmission).

In order to obtain high channel capacities in WDM systems, the information not only needs to be decoded with a narrow wavelength range for each channel, but also *encoded* with a narrow range. Information is encoded for light based transmission systems using semiconductor waveguide lasers modulated according to the required signal. Diffractive encoding technologies have been developed that allow tuning of semiconductor lasers between multiple narrow wavelength bands [49, 50, 51, 52], allowing the use of WDM methods for systems with large numbers of wavelength channels. Typically, a narrow linewidth is obtained from such a laser using a Bragg mirror, which is grating of period a through which light is incident along the period driection. The reflectance of such a grating is confined to a narrow wavelength region, whose width is defined by the length of the grating in a similar manner to equation 1.2. This reflectance, combined with the cavity length of the laser, determines the wavelength output. In order to be able to tune the laser through multiple wavelengths, and thus transmit information in multiple wavelength channels, the cavity length must be tuned and, in addition, the Bragg mirror grating must be able to reflect multiple wavelength bands. To perform this function, the grating must have multiple periods.

The multiple period gratings are termed 'distributed Bragg reflectors (DBRs)', and laser making use of them are known as DBR lasers. A schematic of the structure of a typical DBR laser is shown in figure 1.23(A) [49]. The laser consists of a waveguide of semiconductor material with a gain section, a phase tuning section for changing the effective cavity length, and front and back DBR mirrors. The two DBRs have reflectance spectra with slightly different peak separations. To tune the laser, currents I_f and I_b are applied to the front and back reflectors, respectively, which shifts the spectra such that one peak from each reflector coincides in position with one peak from the other reflector. The reflectors are designed so that only one peak from each spectra coincides for a given current (see figure 1.23(B)). A current

I_p is then applied through the phase tuning section to set the cavity length to correspond to a mode with wavelength at the selected reflectance peak, producing lasing at the chosen wavelength. Since the light from the laser must travel through the reflectors, the length of the reflector gratings (and thus the width of the wavelength reflectance bands, as described above) is limited by the maximum signal reduction that can be tolerated, due to absorption in the grating regions.

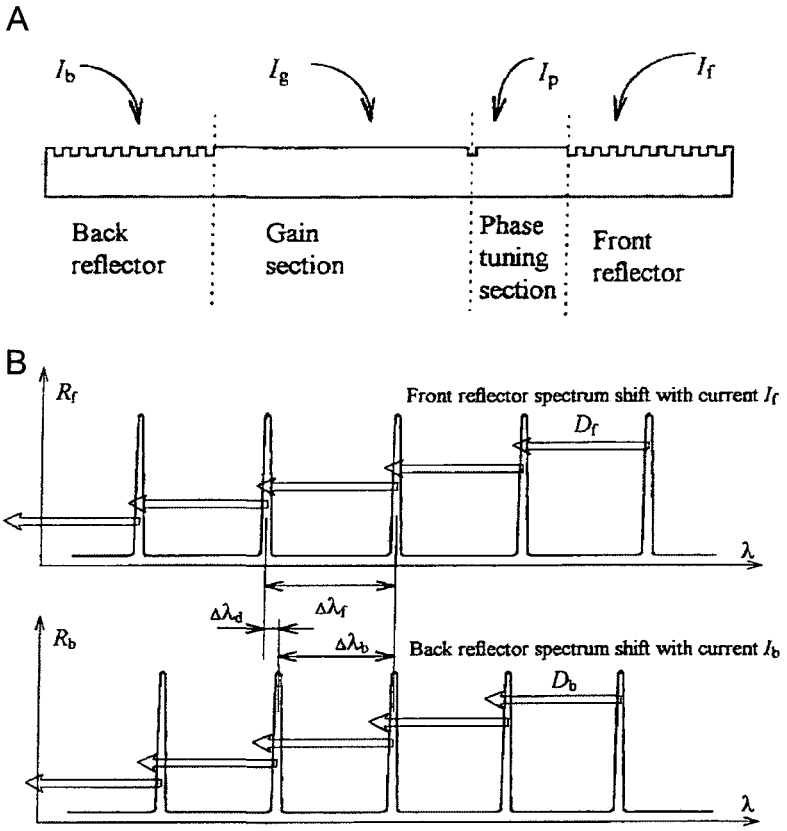

Figure 1.23: (A) The structure of a DBR laser, showing the reflector, gain and phase tuning regions, and the corresponding applied currents. (B)The spectra of the front and back reflectors are shifted by currents I_f and I_b, respectively, so that one peak of each of their respective reflection spectra coincide (figures taken from [49]).

A number of methods are used for creating multiple-period gratings in DBR semiconductor lasers. The three most widely used in devices are reviewed here: Sampled gratings (SGs), superstructure gratings (SSGs) and binary superimposed gratings (BSGs). An SG [50] is a grating which is periodically modulated so that it has a short grating section followed by a section with no grating, etc. Since the grating is formed by the multiplication of the unmodulated grating function and

the sampling function (figure 1.24(A)), the wavelength transmission spectrum is the convolution of that of the unmodulated gratings with that of the sampling function (figure 1.24(B)), due to the convolution theorem for Fourier transforms [44]. Thus there are multiple transmitted wavelengths, with transmitted intensities decreasing either side of the principle wavelength transmitted by the unmodulated grating. The intensity and position of each subsidiary transmission maximum is determined by the period of the sampling function. This technology has allowed for approximately 57nm tuning range with 14 wavelength channels [50], with power variation of around 3dB from centre to outlying channels.

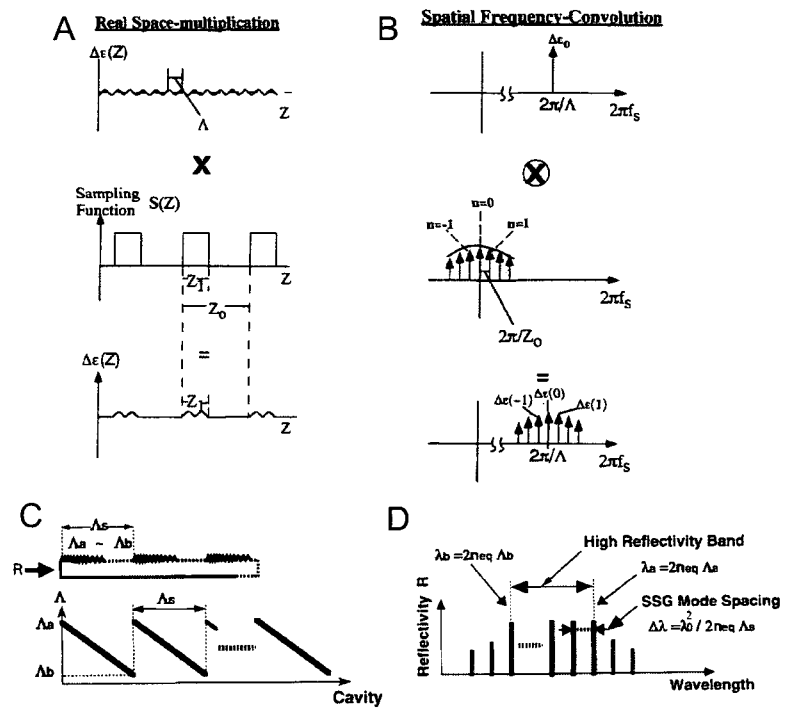

Figure 1.24: (A)The formation of a sampled grating by multiplication of an unsampled grating with a sampling function. (B)The resulting wavelength reflectance spectrum is formed by the convolution of the spectrum due to the unsampled grating, with the spectrum due to the sampling function (figure taken from [50]. (C)Formation of a superstructure grating by multiplying the grating period by a sawtooth function. (D)The resulting wavelength reflectance spectrum (figure taken from [51]).

Superstructure gratings [51, 52] have a continuously chirped grating period that varies linearly from a_1 to a_2, where $a_2 > a_1$ over a distance a_s, then reverts to a_1 and continues to cycle. This forms a grating with regions of continuously varying pitch, repeated with a large overall period a_s (the 'superstructure'). The principle is shown

in figure 1.24(C), together with the resulting wavelength transmittance spectrum in figure 1.24(D). The grating produces peaks of uniform intensity between wavelengths $\lambda_1 = 2n_{eq}a_1$ and $\lambda_2 = 2n_{eq}a_2$, spaced by $\delta\lambda = {\lambda_0}^2/2n_{eq}a_s$, where n_{eq} is the grating effective refractive index and $\lambda_0 = 2n_{eq}a_0$ is the wavelength transmittance due to the average grating period λ_0 [51]. Since the interactions between the various features can produce non-uniformity of the transmittance peaks, the relative phases of these features are adjusted by optimising the chirping function to produce peaks as uniform as possible [52]. Although more complex to design and manufacture than SGs, SSGs have the advantage of producing much higher uniformity (variation of around 0.8dB compared to 3dB) in the transmittance peaks. SSG devices have been demonstrated with around 60 wavelength channels over a 30nm wavelength tuning range [53].

A disadvantage of the superstructure grating is that many features of different size, some of them extremely small, must be accurately reproduced on the gratings, which is very demanding of the etch processes used to reproduce the gratings on the semiconductor waveguides. Binary superimposed gratings (BSGs) [49] offer sections of equal size which may be of one of two possible phases. The feature size is thus never less than some minimum value, which makes the fabrication processes more simple. The grating profile of a BSG is calculated by first forming a function $f(x)$ (where x is the coordinate describing distance along the length of the grating), which is the weighted sum of N sine waves with periods a_j corresponding to the desired wavelength reflectance peaks, given by

$$f(x) = \sum_{j=1}^{N} q_j \sin\left(\frac{2\pi}{a_j} + \Psi_j\right), \tag{1.7}$$

where q_j is a weighting factor and Ψ_j is the phase of each sine function. The resulting function $f(x)$ is then digitised into segments of length s, where each segment is given a phase value of $n(\lambda)+\Delta n/2$ if $f(s.[i-1/2]) > 0$, or $n(\lambda)-\Delta n/2$ if $f(s[i-1/2]) < 0$, where $i = 1, 2, 3...L/s$ for a grating of length L. Since this digitisation distorts the function $f(x)$, producing non-uniformities in the reflectance peaks, the peaks are optimised by adjusting q_j and Ψ_j for each sine wave making up $f(x)$. The result is reflectance spectrum with a band of uniform peaks (see figure 1.25) which is similar to that from an SSG. The grating however is much less difficult to fabricate, due a minimum feature size which is much more realisable with processes such as electron beam lithography. Although not as common in WDM systems as SSGs, lasers using BSG reflectors have been fabricated that demonstrate a tuning range of 24.5nm with

56 wavelength channels [54].

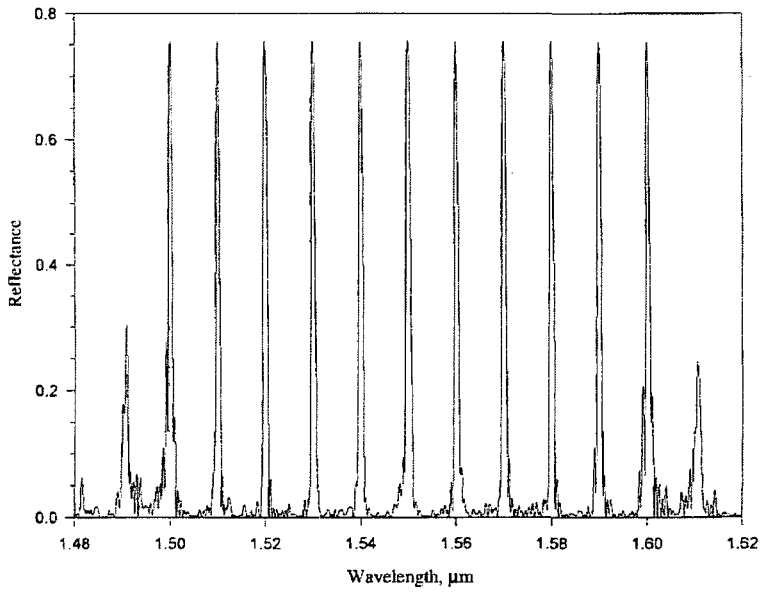

Figure 1.25: The wavelength reflectance spectrum of a binary superimposed grating (figure taken from [49]).

For an entire WDM system over long fibre transmission lines, extra noise can limit the number of channels available as compared to the number available from the laser. Currently around 40 different channels, each carrying data rates of approximately 40Gb s^{-1} are achievable over 10,000km distances, giving data rates of greater than 1Tb s^{-1} [55].

1.5.2 Diffractive multiple-beam generating elements and computer generated holograms

A great deal of research into diffractive structures has concentrated on the development of diffractive components for use as interconnects in optical computing systems. In particular, the development of elements for producing multiple beams from a single beam are important for distributing identical information throughout a system. Multi-beam elements may be required to produce beams of identical intensity (for example to distribute information to multiple parts of a computation system [56]), or to produce beams with a weighted distribution of intensities (particularly useful for optical neural network applications [57, 58, 59]).

As a result of the technological need for diffractive elements that produce multiple beams from a single incident light beam, there has been a large amount of research into methods for creating such elements. To be used for interconnects, such diffractive elements must be capable of producing an arbitrary number of beams as required, with as high diffraction efficiency as possible, and with the required intensity distribution for the particular application. The elements are usually based on phase- rather than amplitude-modulation due to the higher obtainable diffraction efficiencies, and are often binary-phase elements (each region of the element may have only one of two phase values) in order to simplify fabrication. For a 1D multi-beam array, methods such as those described above for DBRs can be used, as they will produce spatial diffraction patterns similar to their wavelength distribution patterns if they are constructed to be used with a single wavelength incident perpendicular, rather than parallel, to the grating plane. An additional method for creating 1D beam arrays is the Dammann grating [60]. A Dammann grating has a phase function $t(\xi)$ of the form shown in figure X, which is a single period of the grating. The grating is designed with the desired result that each of the N required diffracted orders have the same intensity. The intensity of 0 and nth desired order are given by [60]

$$\begin{aligned} u_0 &= 2\sum_{k=0}^{N}(-1)^k(\xi_{k+1}-\xi_k) \\ u_n &= \frac{1}{n\pi}\sum_{k=0}^{N}(-1)^k(\sin 2\pi n\xi_{k+1}-\sin 2\pi n\xi_k), \end{aligned} \tag{1.8}$$

where N is the number of transition points between phase levels and ξ_k denote the transition point positions. The amplitudes of each diffracted order are adjusted iteratively by a computer algorithm by adjusting the positions of each transition point, until uniformity in the diffracted orders has been obtained, to within some threshold. A similar grating may be constructed with phase functions in two perpendicular directions, to produce a 2-dimensional array of diffracted orders.

The Dammann method is somewhat restricted however in that diffraction efficiencies are limited to around 50% in the desired orders, the rest being distributed into other unused orders [61]. The Dammann grating is also limited to uniform arrays of diffracted orders: patterns with missing orders or orders of differing intensity cannot be constructed by this method [61]. Therefore, a number of methods have

been developed to produce diffractive optical elements which produce more general beam patterns for optical computing applications. The diffractive elements generated by these methods are often termed 'computer generated holograms' because their structure is generally no longer grating-like in appearance, and there is much more available freedom in the diffraction patterns that can be produced. Some commonly used methods for generating multi-beam arrays are outlined here. Although multi-beam arrays for encoding purposes have been considered so far, these methods are in fact designed to produce any arbitrary required output image. In all cases, they begin with a desired output image and attempt to create a hologram whose image output intensity distribution is as close as possible to the desired one.

The first of these methods is the direct quantization of an analytical hologram phase-function. This analytic function may be obtained by inverse Fourier transform of the required image field distribution, or calculating the result of the interference of the required image field with a plane reference wave [62] (which would be the hologram resulting from a Fourier interference based hologram formation method, such as that considered in chapter 4). This analytically obtained hologram phase-function is complex and continuously variable, and as a result would be almost impossible to fabricate by lithographic methods. Therefore, a number of methods can be used to quantise the phase-function into a finite number of pixels with a set number of possible phase levels [62, 63], producing a pattern that can be more easily fabricated. This quantisation process generally results in noisy reconstructed images, although the process is used for applications which require an approximation to a particular wavefront shape, rather than a particular image [63].

Another method of calculating pixelated CGHs is the iterative Fourier-Transform algorithm (IFTA, for holograms with Fraunhofer-region image reconstruction) [64, 65] and the closely-related iterative Fresnel algorithm (IFA, for holograms with Fresnel-region image reconstruction) [66]. A flow diagram of a generic IFTA is shown in figure 1.26. The algorithm starts by creating the image complex amplitude using a randomly generated phase distribution and the desired amplitude distribution. The image is then Fourier transformed (FT, generally by FFT) into the plane of the hologram. As it is a phase-only hologram, the amplitude of the complex field distribution across the hologram must be constant (to within some user-set tolerance). If it is, the process is terminated; if not, the constant amplitude is enforced over the hologram, the phase is kept, and the complex amplitude is inverse Fourier transformed (FT^{-1}) back to the image plane. There the phase is kept as the result from the FT$^-$1 calculation, and the amplitude is adjusted to that

desired in the image. The process is then repeated.

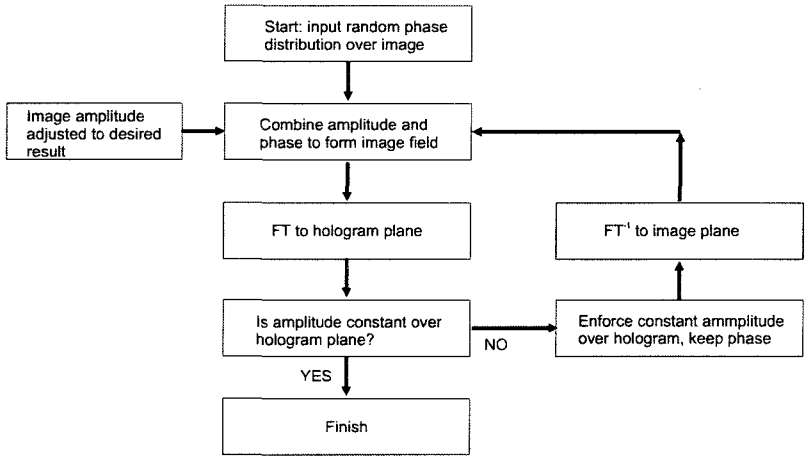

Figure 1.26: Flow diagram of a general iterative Fourier-transform algorithm for computer generated hologram calculation (figure modified from [66]).

The result as it stands does not produce the pixellated, phase discretised hologram required by manufacturing processes. The pixellation and finite phase levels are introduced as further constraints to the hologram along with the constant amplitude constraint, before the inverse Fourier transform back to the image plane [64]. However, once discretised, the IFTA algorithms tend to converge to local rather than overall optimum design [64], requiring a number of modifications to be introduced to the algorithm for calculation of pixellated holograms. One method of accomplishing this is "soft-quantization", in which only regions of the hologram phase distribution which are within a certain interval of one of the required phase levels are quantised. The size of the intervals are progressively increased with each iteration of the algorithm, until the whole hologram is quantised. Often, the continuous distribution is first optimised with one run of the algorithm, and then a second run performed to introduce the quantisation [64]. Other methods include allowing arbitrary light phase and/or amplitude in the diffraction space outside the image area, which reduces the severity of constraints on the process. Another method involves re-balancing high intensity and low intensity regions of the image after each iteration, improving output uniformity. In all cases however, introduction of binary phase (i.e. only two allowed phase levels, as is often desirable for manufacturing ease) produces many local optima, which the algorithm will often settle on, and binary phase holograms produced by IFTA methods are often very noisy as a result [64].

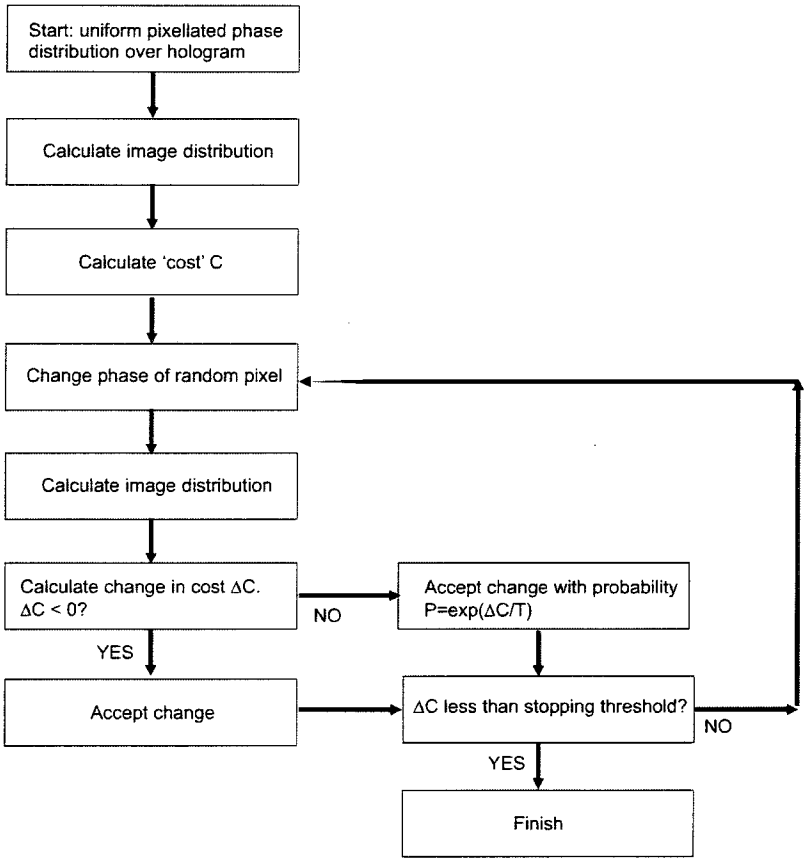

Figure 1.27: Flow diagram of a general simulated annealing algorithm for computer generated hologram calculation.

Finally, two alternative hologram generation methods will be considered, which can produce significantly higher quality holograms, particularly in the case of binary phase. These methods are based around building the hologram pixel-by-pixel, rather than quantising a continuous phase distribution. The first of these are termed "simulated annealing" algorithms. A flow diagram of such an algorithm is shown in figure 1.27 [61]. The algorithm begins by treating the hologram as an array of pixels, each with a random phase. The image intensity distrubution of this hologram is then calculated by calculating the intensity at each point $a_{x'y'}$ at coordinates (x', y') in the output plane as [61].

$$a_{x'y'} = \frac{1}{N^2} \sum_{x=0}^{N-1} \sum_{y=0}^{N-1} t_{xy} \exp\left(\frac{2\pi i(xx' + yy')}{N}\right) \tag{1.9}$$

where t_{xy} is the complex transmission function of the pixel at coordinates (x, y) in

the hologram plane. A "cost function", C is calculated as the squared difference between the desired and actual image intensity distributions. The phase of one pixel in the hologram is changed, and the difference ΔC between the previous and current cost function. If $\Delta C < 0$ the change is accepted, otherwise the change is accepted with a probability $P = \exp(\Delta C/T)$, where T is a fictitious "temperature". Once the change is accepted or rejected, another pixel is changed, and the algorithm continues through multiple iterations. The "temperature" T is slowly reduced throughout the running of the algorithm. Once a stopping condition is met (the ΔC is less than certain threshold), the algorithm is terminated. The "cooling" (annealing) process prevents the algorithm from settling in local optimum solutions, allowing it to reach a global optimum, allowing this algorithm to be used generation of high quality binary-phase holograms. A significant disadvantage of this method is the fact that it can require prohibitively long computing times [67].

The direct binary search (or direct search) algorithms [67, 68, 69, 70, 71] are similar to the simulated annealing method, but do not involve the use of a "cooling" process and so can have significantly reduced computing times. A flow diagram of this method is shown in figure 1.28. In a similar manner to the simulated annealing algorithm, the process is started with a pixellated hologram with arbitrary phase distribution among the pixels, subject to allowed phase levels. The cost C of the image intensity distribution is calculated, and then a phase level of one pixel is changed. If the new values of C is less than previous, the solution is kept, otherwise it is discarded. This process continues until a stopping criterion is met. In order to obtain good quality solutions, variants on this basic algorithm have been devised, with different methods of calculating C and different stopping criteria. Methods using the mean squared difference in intensity distribution between the calculated and ideal intensities converge quickly to local, not global, optima, requiring another method such as simulated annealing, or preconditioning using a method such as IFTA at the start of the algorithm to prevent this happening [68]. An alternative method [67] uses a cost function based on "state variable", of the form $C = -a\bar{I} + b\sigma_I$, where $\bar{I}$ is the average intensity of the image reconstructed from the hologram at each iteration, σ_I is the standard deviation of the image intensity and a and b are positive "cost balancing" parameters. The stopping criterion in this method is that the algorithm terminates when the estimated probability of a change being accepted (i.e. the probability of $\Delta C < 0$) is less than some user defined threshold. This allows holograms to be design that produce high quality images, without the long computing times required by simulated annealing algorithms.

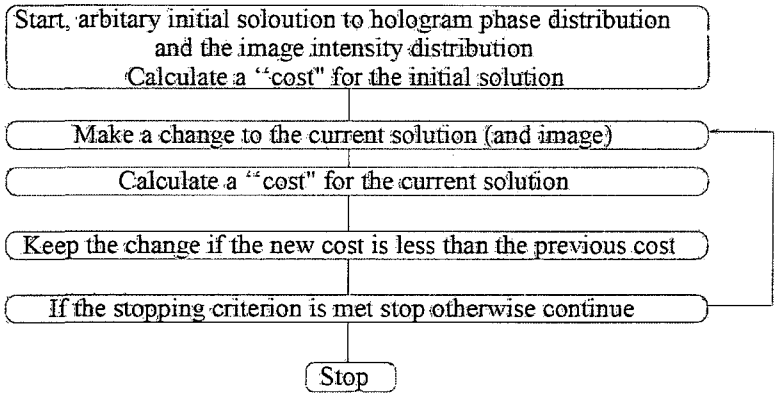

Figure 1.28: Flow diagram of a direct search algorithm for computer generated hologram calculation (figure taken from [67]).

1.5.3 Applications of computer generated holograms

As described briefly in the previous section, there are many technologies which make use of computer generated holograms, designed using the techniques described in the previous section. The Dammann method [60] was developed for fault removal in periodic masks, by placing the mask in front of the source illuminating a Dammann grating. The multiple diffracted images contain the correct periodic mask, spatially filtering out fault in the mask. Other applications include optical computing interconnects for parallel information transfer and optical neural networks, and optical security devices. Parallel information transfer applications require reasonably simple, uniform intensity beam arrays, for sending the same signal to multiple computing devices [56]. In addition, multi-beam elements have been used in the reverse process, to combine a number of signals for transport to a single detector [72, 73].

Optical neural networks [57, 58, 59] consist of light sources and detectors as the outputs and inputs, respectively, of the "neurons", together with weighted interconnects between the outputs and inputs. A layout of a typical optical neural network is shown in figure 1.29. The light sources (neuron outputs) are electrically connected each to one detector (neuron input). Each source is the n optically interconnected to every detector via beams of differing intensities produced by a computer generated hologram. Holograms for use in neural networks have been produced by preconditioned direct search [57] and simulated annealing [61]. The holograms may be pre-fabricated [57, 61] or displayed on liquid-crystal spatial light modulators [58, 59]. These neural networks have been demonstrated in network packet schedul-

ing (the switching of signal packets between source and destination) to perform at greater rates than electrical switches [58].

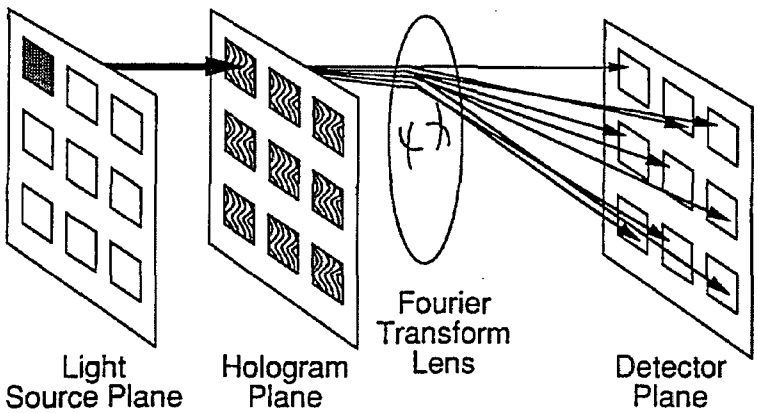

Figure 1.29: Layout of a typical optical neural network, in which light source form neuron outputs, detectors form neuron inputs and the inputs and outputs are interconnected by computer generated holograms that produce arrays of multiple, intensity weighted beams. (figure taken from [57]).

Security devices based on optical correlators have been developed [74, 75, 76], which make use of encrypted computer generated holograms. The encrypted hologram is designed to produce an unreadable image upon illumination, except when read in and optical correlator-based decryption device. To form an encrypted hologram, the image to be encrypted is overlayed with a pixellated mask of random phase, and the result is used to generate a CGH by a process such as simulated annealing [75]. The original image can only be recovered using a decryption device such as the one shown in shown in figure 1.30(A). The hologram is placed at the centre of a 4-f system, with a decryption key at the back focal plane of the first lens. The decryption key is the random phase mask used in the encryption process. The key is Fourier-transformed by the first lens, with the plane of the transform coinciding with the plane of the encrypted hologram. The cobined light distribution of the random phase mask FT and the encrypted hologram are then Fourier transformed to the front focal plane of the second lens, forming the decrypted image. An example image is shown in figure 1.30(B), with the corresponding encrypted hologram (figure 1.30(C)) and the decrypted image (figure 1.30(D)). An integrated optics device using micro-optic components has been demonstrated [74], as a practical miniaturised device using this decryption functionality for security applications.

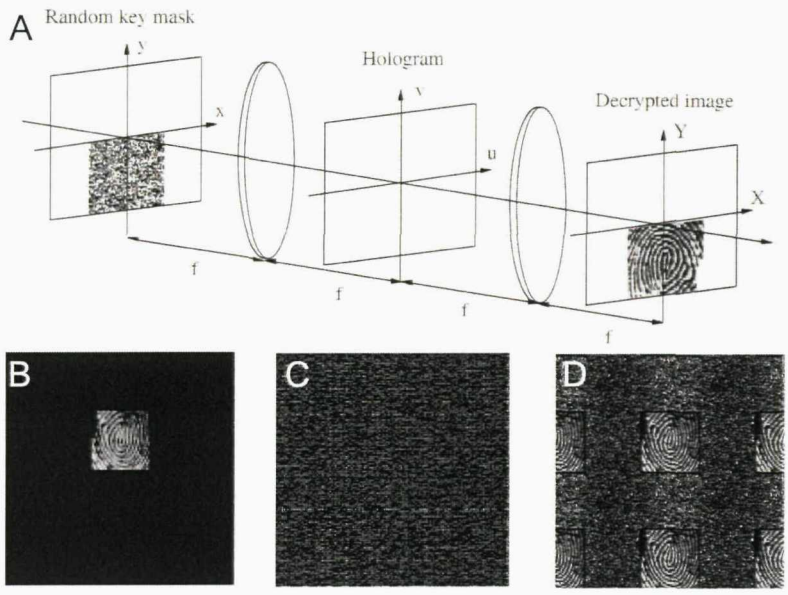

Figure 1.30: (A) Layout of an optical decryption system for encrypted holograms. (B)An example of an image to be encrypted. (C)The encrypted hologram designed from the image in (B). (D)Image decrypted from the encrypted hologram in (C). (figure taken from [75]).

1.5.4 Diffractive barcode scanner

Diffractive elements have also been used to create a passive-optics barcode scanner, i.e. one that requires no moving optical parts [77]. The optical layout of such a scanner is shown in figure 1.31. The scanning function is based around a tunable laser and a simple diffraction grating of a single period. When thelaser wavelength is tuned from λ_{min} to λ_{max}, the angle of the diffracted first order from the grating, θ_{out}, changes. The system is set up so that the angular change scans the first order across the barcode. Reflected light from the barcode is collected by a lens and focussed onto a photodiode, which feeds a readout of the reflected power to a computer for analysis of the code.

1.5.5 Holographic data storage

Diffractive structures, in the form of holograms, are also used in holographic data storage systems [78, 79, 80]. These are memories in which a number of 'pages' of data are written into photorefractive crystals as holograms formed by recording the interference pattern between the page data and a reference beam (see figure 1.32).

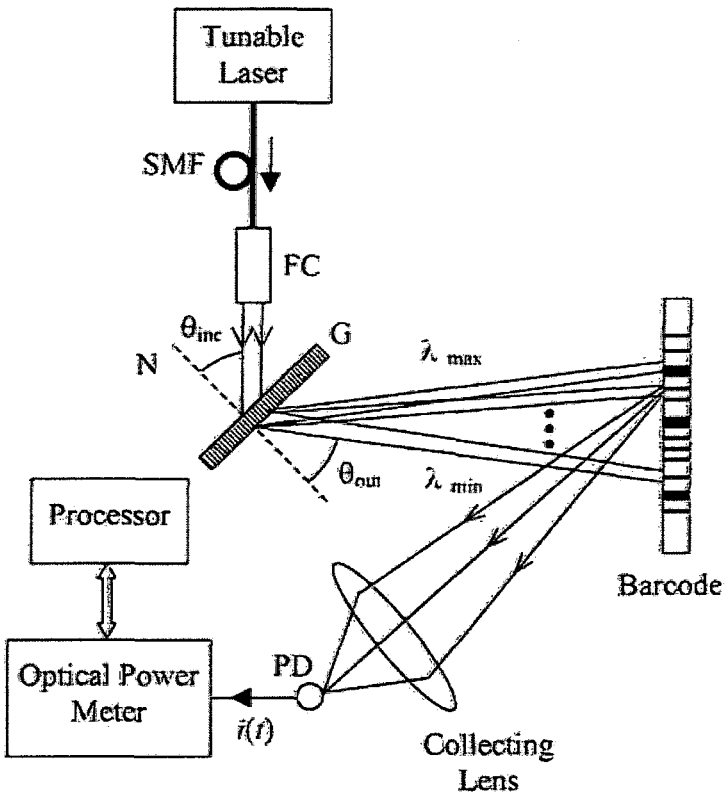

Figure 1.31: Optical layout of a diffractive optics barcode scanner, based around a diffraction grating (G) and a tunable laser. Tuning the laser wavelength from λ_{min} to λ_{max} changes the angle θ_{out} of the diffracted first order from the grating, scanning it over the barcode. (figure taken from [77]).

Using a number of different reference beam angles allows more than one page to be stored as overlapping holograms. Illumination with a beam at the same angle as the reference beam results in a diffracted image which is a reconstruction of the data page, where the page is effectively a patterning of the diffracted first order of the hologram. The number of resolvable pages that can be stored in the holographic storage system is again set by equations 1.1 and 1.2. More details of the mathematics and details of hologram formation will be considered in chapter 4.

1.5.6 Holographic chemical sensors

In addition, holograms are being developed for biochemical sensing applications. These include chemically sensitive substrates encoded with holograms, being developed by Smart Holograms Ltd., a spin-out company of Cambridge University [81].

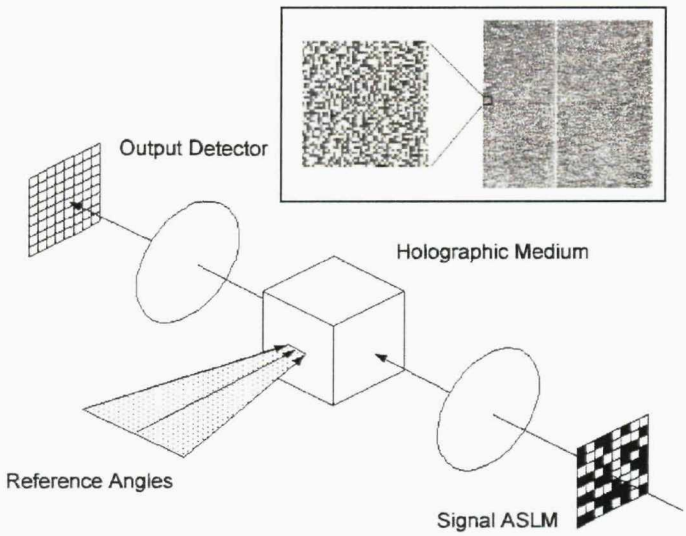

Figure 1.32: Schematic of setup for writing pixellated data from a spatial light modulator into a photorefractive crystal by interference with a reference beam to create a hologram. Reference beams at different angles allow multiple holograms to be superimposed. The same reference beams are diffracted from the holograms in readout, reconstructing the data. An example 1024×1024 pixel data page is shown in the inset, together with a magnified portion (images from [80]).

These holograms are made of a variety of polymers which swell upon being immersed in a target analyte. The polymers contain silver nitrate, into which holograms are written, which are then developed, leaving gratings made up of silver grains embedded in the polymer. The swelling has the effect of changing the spacing of the complex series of gratings making up the hologram. Considering a simple reflection grating (see figure 1.33(A)), when white light is incident on the grating at angle θ, light of wavelength λ is reflected back at angle $-\theta$, with λ set so that all parameters satisfy the Bragg equation $m\lambda = 2nd\sin\theta$ (which can be derived using a similar method to that used for equation 1.1), where m is an integer and n is the polymer refractive index. This selects the reflected wavelength depending on the spacing of the grating d, which changes as the polymer swells. Thus a change in colour of the diffracted image can be used as a quick method to signify pH change [82], as shown in figure 1.33(A). The pH sensitivity of these holograms is an order of magnitude greater than the most sensitive existing methods [82]. The holographic sensors can also be used to detect a variety of other analytes such as glucose, enzyme products and fermentation products [83], by using different polymers that swell in response to the conditions to be detected.

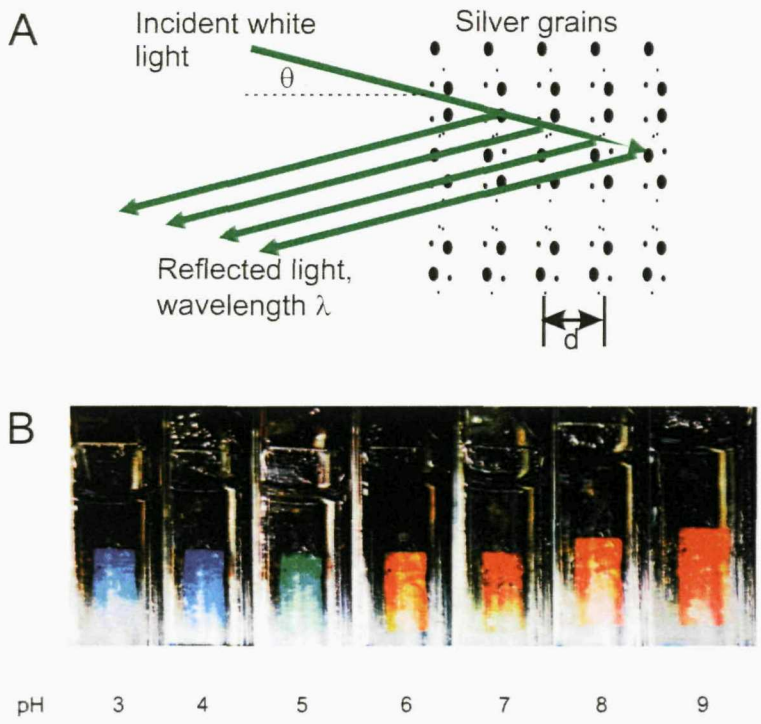

Figure 1.33: (A) The wavelength selectivity achieved by reflecting white light from a grating of silver grains with fixed spacing d. (B) Creating gratings in a polymer which swells in response to pH changes d as the pH changes, altering the reflected colour, thus allowing the grating to be used as a pH sensor (images from [82]).

1.6 Thesis synopsis

In the rest of this thesis a new technique for encoding microparticles will be described, based on reading diffraction patterns produced by unique structures fabricated on the surface of the particles. In chapter 2, the concept of using simple diffraction gratings, and more complex gratings with multiple periods, to uniquely encode microparticles is introduced. The large theoretical encoding capacity of these tags will be introduced, and the encoded gratings demonstrated experimentally using metal-on-glass gratings fabricated by e-beam direct-write lithography. In chapter 3, the steps required to make the technology suitable for implementation in bead based assays are described, including fabrication of the gratings on a bio-compatible polymer, and characterisation of the resulting diffraction patterns and the suitability for encoding. This characterization leads to a more realistic estimate for practically achievable encoding capacities using this technology. Chapter 4 introduces the concept of using holograms, which are more complex diffractive

structures, to encode particles, with the aim of overcoming some disadvantages of the simple grating technology. The concept of re-writeable codes will also be introduced in this chapter, together with the reasons for developing them. Finally in chapter 5, the conclusions which may be drawn on the technology detailed in the thesis are summarised, and options for further work in this area are described.

Chapter 2

Superimposed diffraction grating micro-tags

In this chapter, the simplest implementation of the diffractive microparticle encoding technique is introduced. In this implementation the pattern on the tag is simply a miniature diffraction grating, where information is coded in the pitch of the grating. The encoding capacity of such a tag can be greatly increased by fabricating more complex tags with several overlapping gratings on the surface.

To begin with, section 2.1, will consider how information can be encoded onto both 1 and 2 dimensional diffraction gratings, and how many codes are theoretically achievable. In section 2.2, the concept will be experimentally demonstrated by measurement of diffraction patterns from high-resolution gratings written by electron-beam direct-write lithography of chromium on a glass substrate. In section 2.3, we will consider undesirable features which appear in the diffraction patterns from the grating tags. The affect of these features on the encoding concept will be considered, together with solutions to the majority of problems that they cause.

2.1 Encoding concept

2.1.1 1-dimensional diffraction gratings

In a classical single diffraction grating, information can be encoded in the pitch or spacing of the grating, a. As we saw in chapter 1, when such a grating is illuminated with light at wavelength λ, for example at normal incidence, a series of diffracted beams of different order m is created in the far field (Fraunhofer) region, according to the equation $a \sin \alpha = m\lambda$. Here α is the angle of diffraction and m is the diffraction

order. Therefore, a measurement of the first order diffraction angle, at $m = 1$, gives direct information about the pitch of the grating a. This principle is shown in figure 2.1 (A). The number of distinguishable tags that can be manufactured depends on the ability to resolve a difference between two diffraction patterns. Two diffracted beams at diffracted angles α_1 and α_2 can be resolved if they satisfy the Rayleigh condition, i.e. if $|\alpha_1 - \alpha_2| \geq \Delta\alpha_1/2 + \Delta\alpha_2/2$, where $\Delta\alpha$ is angular width of the beam. The beam width $\Delta\alpha$ can be derived using similar principles to those used to derive equation 1.2, and is given by [43]

$$\Delta\alpha = \frac{\lambda}{Na\cos\alpha}, \tag{2.1}$$

where N is the number of periods in the grating of length L ($N \approx L/a$). Using this criterion it is possible to calculate the encoding capacity of diffractive barcodes consisting of a single grating for various values of the grating length, by calculating, for each value of L, the possible positions n_o of the first order diffracted beam (neglecting for the moment all diffraction orders above $m = 1$) between $\alpha = 0°$ and $\alpha = 90°$, seperated according to the Rayleigh criterion. Once the value of $\alpha + \Delta\alpha$ for a beam is greater than 90°, the calculation is terminated. The beam which extends beyond 90° is discounted, and the number of remaining beams gives the value of n_o for the particular value of L. This truncation of beams that extend beyond 90° accounts for the "jagged" appearance of all curves in figure 2.3. For this and all subsequent calculations, a value of $\lambda = 633$nm is used. The calculations were performed for value of L ranging from 1 to 100μm, in steps of 1μm. The encoding capacity of a single grating is then given by $c = n_o$. The results for this are presented in figure 2.3, curve (1).

2.1.2 Superimposing multiple grating periods

A much larger capacity of tag can be obtained if several gratings are superimposed on the particle. The particular method used in this work for superimposing multiple gratings is shown in figure 2.1(C). The superimposed grating is formed by multiplying the transmission function of the constituent grating transmission functions, which are made up of regions of zero transmission, and regions of one (100%) transmission. The result is a binary amplitude multi-beam grating. This combination method is simple and uses no optimisation of the grating profile, making it ideal for production of large numbers of prototype gratings. However, as will be discussed in subsequent parts of this chapter, the fact that no optimisation of the grating profile

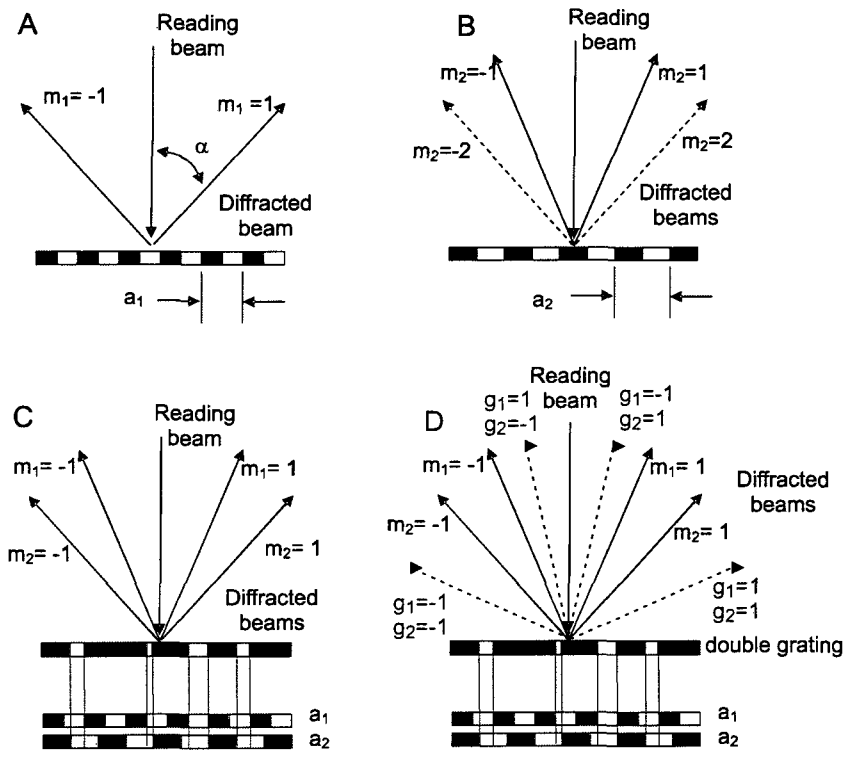

Figure 2.1: A) First order diffraction from grating with pitch a_1; B) first and second order diffraction from grating with pitch a_2; C) first order diffraction from combinatorial grating made by superposition of gratings with pitches a_1 and a_2; D) first and ghost order diffraction from the combinatorial grating.

is used has the disadvantage of introducing spurious features into the diffraction pattern of the gratings, which provide a limitation on the encoding capacity of this encoding technique.

A large number of other techniques exist for combining amplitude gratings, which can produce more ideal multiple beam diffraction patterns. One way to optimise gratings designed by a multiplicative method is to use the degree of freedom offered by the relative position of the constituent gratings with respect to each other. This modifies the relative phases of of the various components of the super imposed grating diffraction pattern, allowing diffracted order intensities to be adjusted. Many other possible methods have already been considered in section 1.5.2 in reference to phase gratings; methods such as BSG generation, in which the phase of various parts of the pattern is varied by translating the components of the binary grating, can be modified to be used for amplitude gratings of the type used here. In addition holography methods, as considered in section 1.5, have the opportunity to provide

even more optimal patterns, and one such method will be investigated in chapter 4.

2.1.3 Superimposed phase gratings

While amplitude gratings are used in this chapter to experimentally demonstrated the concept of superimposed grating diffractive microtags, it will be shown in chapter 3 that phase gratings are more useful for practical implementation of the tags on the surface of microparticles which are compatible with the necessary biochemistry. Superimposed phase gratings were designed for this work by simply taking amplitude grating calculated using the method in section 2.1.2, and substituting a phase shift of zero in regions with transmission 1, and phase shift of (ideally, although this is dependant on manufacturing accuracy) π in regions with transmission 0.

Similarly to amplitude gratings, the relative position of the constituent gratings can be adjusted to optimise order intensities. Phase gratings, in contrast to amplitude gratings, can also be stacked by algebraic addition rather than multiplication, with regions of phase shift 2π cycling back to zero, etc, which could help with grating optimisation. Additionally any of the methods considered in section 1.5.2 could also be used to provide more optimised multi-beam phase gratings.

We can use a fast Fourier transform algorithm to calculate the diffraction patterns from tags with various numbers of superimposed gratings, for different values of D. Here we use $n_1 = 1.6$ (the refractive index of SU8), as this is the material that will be used in chapter 3 for manufacture of phase gratings. The main difference caused by changing D is the relative intensity of the zero order compared to all other diffracted orders. In figure 2.2 (A) & (B), we see the diffracted angular intensity spectra for an example grating with period $a = 3.7\mu$m and $a/(a-b) = 3$, illuminated with a plane wave of wavelength $\lambda = 633$nm. The spectrum in (A) is for a grating with $D = 63$, while in (B) $D = 452$. I_0 is the value of the peak intensity of the zero order ($m = 0$) beam, and I_1 the peak intensity of the first order ($m = 1$) beams. Figure 2.2 (C) curve (1) shows the variation of the ratio I_0/I_1 of the zero order to first order intensity, as a function of D for such a single grating with $a = 3.7\mu m$ and $a/(a-b) = 3$ illuminated with a plane wave of wavelength $\lambda = 633nm$ in a vacuum ($n_2 = 1$). We can see that this ratio reaches a minimum at a certain value of D, which is the point at which $\phi = \pi$. At this point, $D = \lambda/(2|n_1 - n_2|)$, which for the parameters above gives $D = 452$nm. The spectra in figure 2.2 (B) is for a grating with D at this minimum point value, and we can see that the $m = 0$ beam intensity has fallen to around 1/6 of its intensity for a grating with $D = 63$

nm(figure 2.2 (A)). The light is instead diverted into the m=1 beams, which have risen to approximately 20 times their intensity for a grating with $D = 63$nm. Both effects contribute to the minimum value of $I_0/I_1 = 0.4$ seen on figure 2.2 (C) and (D) curves 1. The same calculations for water ($n = 1.33$) as the surrounding medium, gives a minimum at $D = 855$nm (see Figure 2.2 (D) curve (1)).

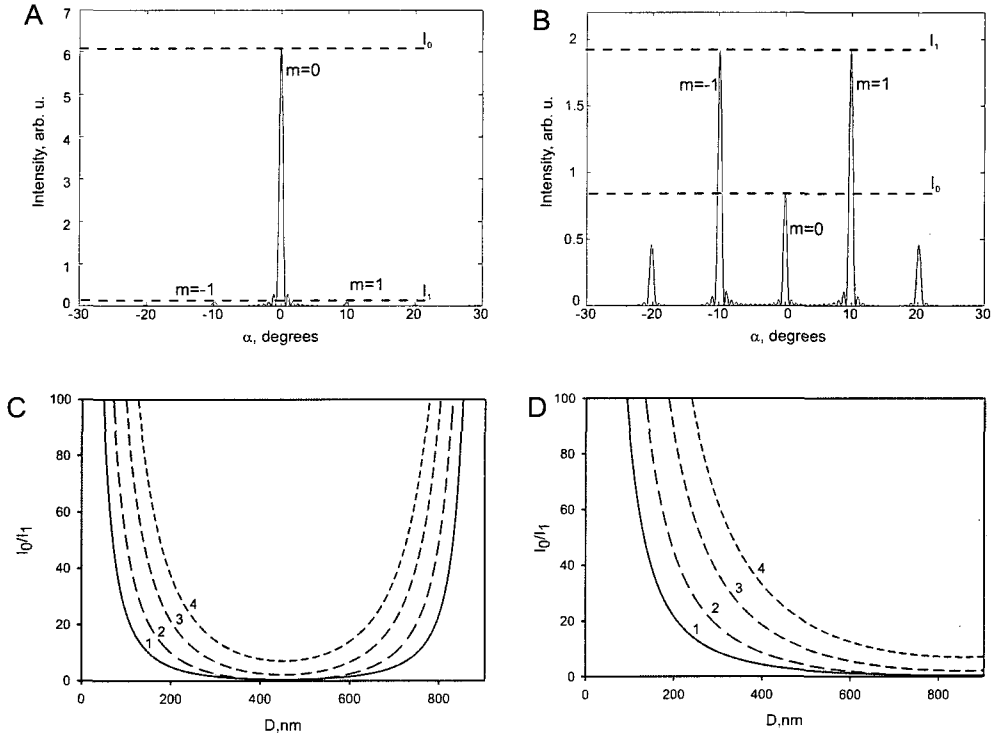

Figure 2.2: Example of calculated diffraction intensity profiles for a grating with $D = 63$nm (A) and $D = 452$nm (B) with incident wavelength $\lambda = 633nm$, showing a large difference in first order (I_1) and zero order (I_2) intensities. (C) & (D) The variation of the zero order to first order intensity ratio for SU8 tags with different numbers of superimposed gratings in air (C) and water (D), for different ridge depths D. The number of superimposed gratings on the tag is denoted by the number on each curve. All gratings profiles have $a/(a-b) = 3$.

For tags with 2, 3 and 4 superimposed gratings on the surface, the value of I_0/I_1 becomes larger for all values of D (examples shown in figure 2.2 (C)+(D), curves (2 - 4)), with each successive increase in the number of superimposed gratings. This mainly occurs because the intensity of the zero order is dependant on the ratio of regions with $\phi = 0$ to regions with $\phi = -2\pi|n_1 - n_2|D/\lambda$, which changes when multiple gratings are superimposed. This is a result of the encoding method, and optimisation could allow I_0/I_1 to reduced for multiple combined gratings. There

is also a faster deviation of the ratio from either side of the minimum point. The values given for superimposed gratings are the mean values of I_0/I_1 as there is some fluctuation of first order intensities for different first orders on each tag. The minimum point appears at the same value of D for all values of pitch a, and corresponds to $\phi = \pi$.

The importance of the calculations of I_0/I_1 is that a very intense zero order can cause scattering problems within the reading system, which can cause reading errors. In addition, more light in the code first order beams increases the ability to distinguish the code from any noise present. We would therefore ideally like phase grating tags to have the value of D which gives the minimum value of zero order intensity, and also the maximum amount of light diffracted into the first order beams. This is achieved by selecting the value $D = 452$nm for SU8 gratings in air, or $D = 855$nm for SU8 gratings in water, at which I_0/I_1 is a minimum for an illumination wavelength of $\lambda = 633$nm, as seen above.

2.1.4 Encoding capacity estimates for superimposed 1D gratings

Disregarding the effects of the grating combination method for the moment, a simple estimate of the encoding capacity of superimposed grating tags can be made by assuming each of the superimposed gratings can be considered to produce its own set of first order diffracted beams. In addition to the diffracted orders produced according to the equation $a \sin \alpha = m\lambda$, the superimposed gratings produce extra 'ghost' orders (see figure 2.1(D)), which are a due to the particular grating combination method used and are discussed in detail in section 2.3.2. These beams will eventually be seen to provide the limit on the number of gratings which can be superimposed using this particular method. If the tag has n_g superimposed gratings, the number of possible distinguishable codes c is then given by the number of possible combinations of n_g beams in the n_o possible positions, using the combinatorial formula $c = \frac{n_o!}{(n_o - n_g)! n_g!}$. This formula arises because each code diffracted first order is indistinguishable from the others: Hence if we have orders at positions 1, 2 and 3, this is indistinguishable from swapping the orders around in the same positions (e.g creating 3, 2, 1 or 2, 1, 3), so only the positions of the beams, not their sequence, is important. The results of calculations of the tag capacity for several superimposed gratings using this resolution criterion are presented by the solid curves (2)-(5), figure 2.3. The limit of $n_g = 5$ is chosen because it provides

enough tags on $100\mu m$ particle (around 10^9) to cover the whole human genome with 16-base oligonucleotides, which was part of the original aim of the project before it was shown to be impractical, as described in section 1.2. In practice, as shown in chapter 3, the maximum number n_{gmax} of superimposed gratings in the tag which can be distinguished reliably by diffraction is limited by the resolution δ of the tag's fabrication process and , more significantly, the interaction of the code orders with unwanted beams produced by this particular grating superimposing method.

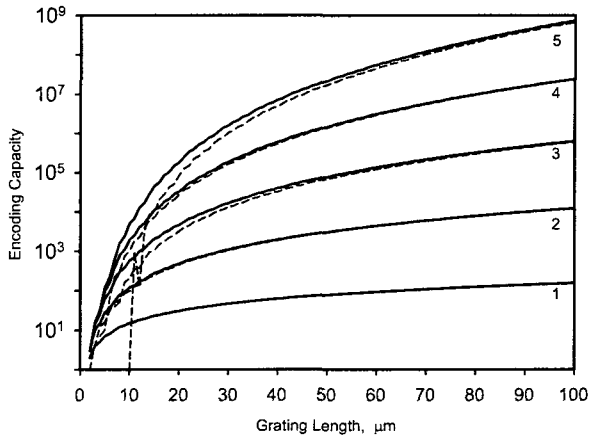

Figure 2.3: Encoding capacity of a diffractive bar-code tag as a function of the length of the tag for different numbers of superimposed gratings. The number on each curve corresponds to the number of superimposed gratings. Dashed lines show capacity after the elimination of tags with high intensity ghost beams, discussed in section 2.3.2.

2.1.5 2-dimensional gratings

To further increase capacity, '2-dimensional' tagging can be introduced, using diffractive elements created from two perpendicular gratings. An example of such a tag is shown in the inset to figure 2.4. The tags are read by the same method as the 1-dimensional tags, but now measuring the first order positions in the two perpendicular directions. The pitches of the two perpendicular gratings can be varied separately, and it is possible to have different numbers of superimposed gratings, n_{gx} and n_{gy}, in each direction. The number of codes available for all possible combinations of pitches, with n_{gx} and n_{gy} values ranging from 1 up to a maximum n_g is then

$$c = \sum_{n_{gx}=1}^{n_g} \sum_{n_{gy}=1}^{n_g} \frac{n_o!}{(n_o - n_{gx})! n_{gx}!} \frac{n_o!}{(n_o - n_{gy})! n_{gy}!}. \tag{2.2}$$

The results for the number of codes as a function of tag side length for a square two dimensional tag with different values of n_g, are shown in figure 2.3. It can be seen from this that the maximum encoding capacity of tags 100μm side length is of the order of 10^{21} codes, choosing the limit of n_g in the same manner as in section 2.1.4. Likewise, the maximum achievable value of n_g will be shown to be limited by the presence of unwanted features in the diffraction pattern.

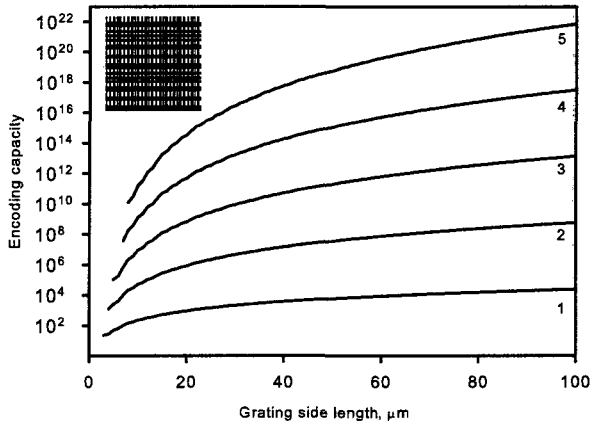

Figure 2.4: Encoding capacity of a square 2-dimensional diffractive barcode tag as a function of the side length of the tag, for different values of k. The value of k is denoted by the number on each curve. Inset shows an example 2-dimensional grating surface.

2.2 Experimental demonstration of high resolution amplitude-grating tags

2.2.1 1-dimensional tags

In order to demonstrate the 1-dimensional tagging concept, a library of chromium gratings was manufactured on a glass substrate using direct write electron beam lithography (fabrication by Kelvin Nanotechnology, Glasgow).

The library of gratings contains almost 7,400 unique barcode tags, 50x50 μm separated by gaps of 200 μm. SEM images of these tags showing a range of different superimposed gratings are presented in figure 2.5. With a nanofabrication minimum feature size δ of about 100nm we have been able to demonstrate tags up to order three (containing three superimposed gratings) that feature no imperfections in grating reproduction. Using the methods of section 2.1.4, we have that $n_g = 75$ for a tag of length 50μm and this superimposing limit thus provides capacity for about

68,000 distinguishable tags. Higher order tags have also been fabricated, but they sometimes show failures in pattern reproduction (figure 2.5 (iv)) and additionally the diffraction patterns for many tags with $n_o > 3$ tend to be unreadable due to unwanted beams produced as a result of the encoding method, which is discussed in more detail in sections 2.3.2 and 3.2.4.

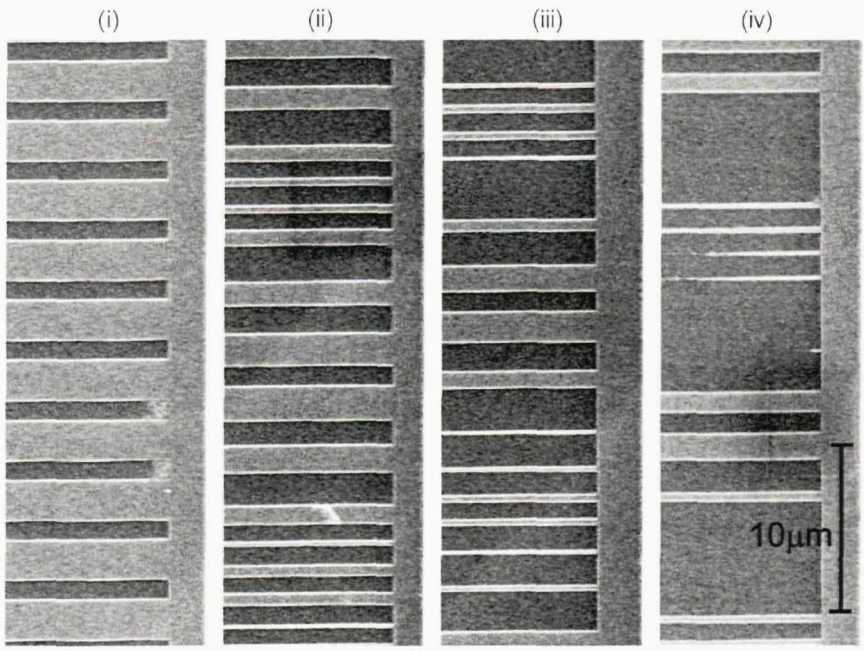

Figure 2.5: SEM images of 1-dimensional barcode tags of different order: (i) single grating tag; (ii) two superimposed gratings; (iii) three superimposed gratings; (iv) four superimposed gratings (note nano-lithography resolution limiting quality of this grating).

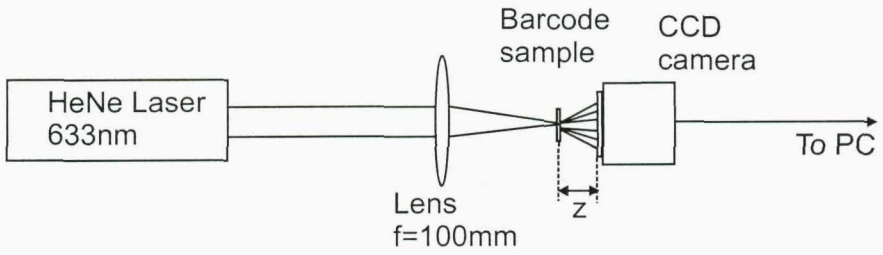

Figure 2.6: Setup used to record the diffraction patterns from metal-on-glass superimposed diffraction grating tags. Light from a helium-neon laser (wavelength 633nm) is focussed by lens of focal length $f = 100$mm onto the grating sample. The resulting diffraction pattern is captured by a CMOS array camera a distance $z = 4mm$ from the grating.

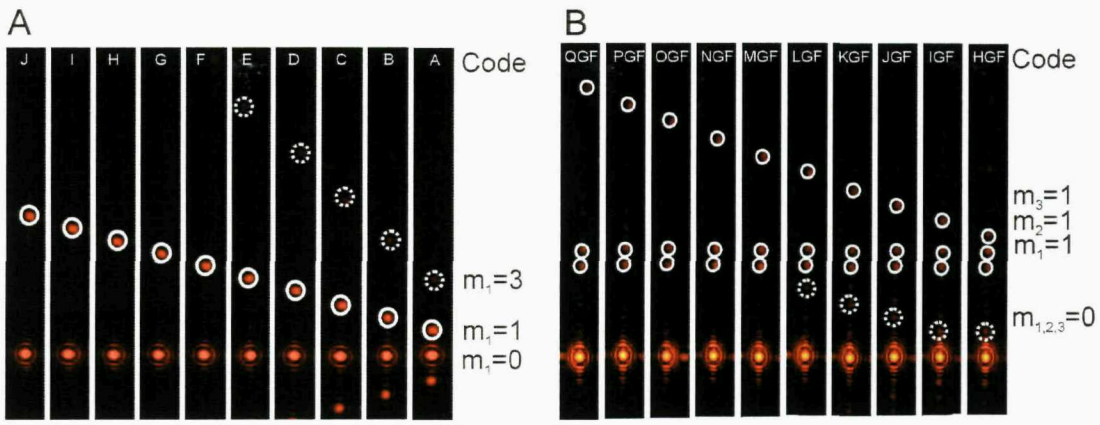

Figure 2.7: Diffraction patterns created by single grating tags (A), and tags containing three different gratings (B). Moving from left to right shows how a progressive decrease in the pitch of one of the gratings changes the diffraction pattern. Third order beams are visible in dotted circles in (A) (second orders do not appear as the gratings have $a/(a-b) = 2$ as explained in section 2.3). Ghost beams are visible in dotted circles in (B).

An example of the diffraction patterns created by these tags is presented in figure 2.7. The gratings were 'read' using the setup shown in figure 2.6; light from a HeNe laser (633nm) incident at normal angle to the sample, after focussing with a lens of focal length $f = 100$mm. The sample is placed a distance f from the focussing lens. The diffraction pattern was captured on a 1280x1024 CMOS array detector (Prosilica EC1280), parallel to the grating and a distance $z = 4mm$ from it. Figure 2.7(A) shows how the diffraction pattern changes with grating pitch; increasing in diffraction angle as the pitch decreases. The series of diffraction patterns (labeled A to J) demonstrates how it is possible to uniquely distinguish between ten different tags containing only a single grating. In the photographs, the first order diffraction spots (marked $m_1 = 1$ as in figure 2.1(A)) are highlighted by the solid circles, while the positions of the much weaker second order diffraction spots ($m_1 = 2$) are indicated by dashed circles.

Figure 2.7(A) shows diffraction patterns from different tags containing three superimposed gratings (patterns HGF to QGF). Here, the first grating diffracts exactly as grating G in figure 2.7(A), while the second grating diffracts as grating F. The third grating differs from pattern to pattern. The first diffraction pattern is from a grating which diffracts as grating H in figure 2.7(A), but then changes step by step to give a higher and higher diffraction angle. The labels assigned to each individual grating in 2.7(A) are used to assign a code to each tag; for example tag HGF

in figure 2.7(B) is formed from the gratings labeled H, G and F in figure 2.7(B). In this way diffraction patterns with up to three superimposed gratings have been resolved. Further increase in the number of superimposed gratings on the tags led to increasing read errors due to the limited minimum feature size available in the grating fabrication process.

2.2.2 Two-dimensional tags

A similar library of 2000 50x50 μm two-dimensional tags was fabricated by the same process used to manufacture the 1-dimensional tags. SEM images of these tags showing a selection of different superimposed gratings are presented in figure 2.8.

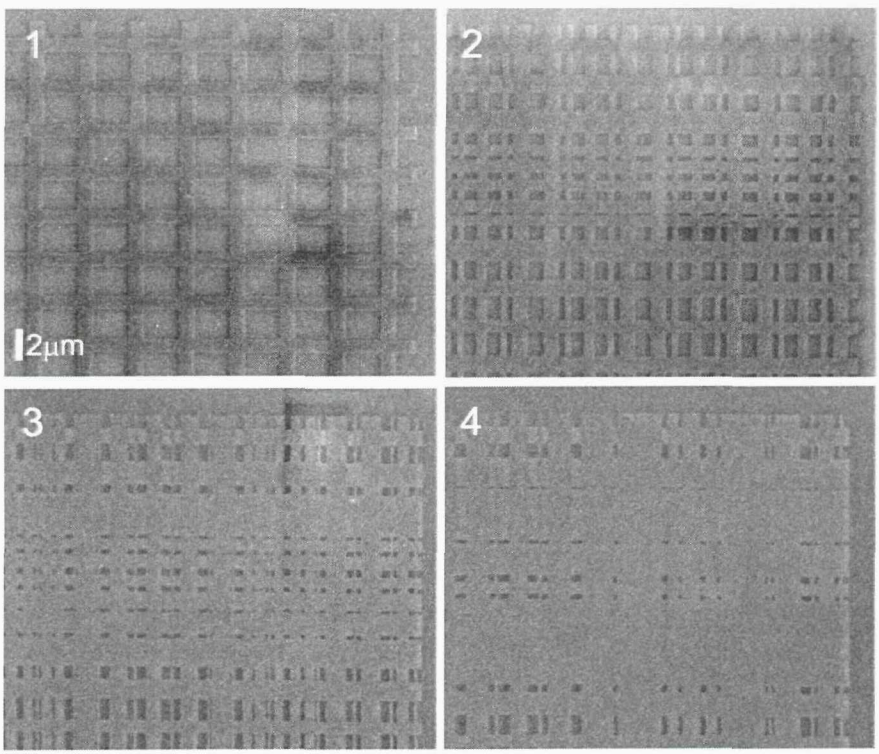

Figure 2.8: SEM images of 2-dimensional tags of different order, with equal numbers of gratings in the two perpendicular directions: (1) single grating tag; (2) two superimposed gratings; (3) three superimposed gratings; (4) four superimposed gratings.

Examples of the diffraction patterns created by these tags are presented in figure 2.9. The gratings were 'read' using a helium-neon laser, and the diffraction pattern projected directly onto the surface of a CMOS array detector, as for the 1D tags.

Figure 2.9 (A) shows how the diffraction pattern changes with grating pitch in each of the perpendicular directions; increasing in diffraction angle as the pitch decreases. The series of diffraction patterns (labeled DA to DD) demonstrates how it is possible to uniquely distinguish between eight different tags containing only a single grating in each perpendicular direction. In the photographs, the first order diffraction spots in the x and y directions ($m_y = 1$ and $m_x = 1$ as defined in figure 1(A)) are highlighted by the solid circles, while the positions of the much weaker second order diffraction spots ($m_y = 2$ and $m_x = 2$) are indicated by dashed circles. Dotted circles indicate 'quadrant' diffracted beams which appear only on 2-dimensional tags. These beams result from the fact that the 2-dimensional gratings are produced by multiplying the transmission functions of two gratings oriented perpendicular to each other: The diffraction pattern from these gratings is thus the convolution of the diffraction patterns of each of the mutually perpendicular gratings. This is discussed in more detail in section 2.3.

Figure 2.9 (B) shows diffraction patterns from different tags containing two superimposed gratings in each of the perpendicular directions (patterns DEDE to DHDE). Here, the first grating in both directions diffracts exactly as grating D in figure 2.7(a). The second grating in the vertical direction has increasing pitch moving from DEDE to DEDH. A similar sequence for the horizontal direction gratings, moving from pattern DEDE to DHDE, demonstrates the ability to independently vary multiple pitches in the two perpendicular directions.

2.2.3 Experimentally obtainable encoding capacities

The encoding capacity of the diffractive encoding technique depends upon separating the beams by the Rayleigh condition (as described in section 2.1.1) and so is affected by the actual beam width. Therefore, measurement of beam-widths from the high resolution metal-on-glass samples enables us to demonstrate how close we may come to being able to obtain the encoding capacities calculated in sections 2.1.1 and 2.1.5.

Figure 2.10 shows the width of the first order diffracted beam at various diffracted angles, for 1-dimensional and 2-dimensional tags. These are seen to be higher than the theoretical widths calculated from equation 2.1, which requires a reduction of our estimate of the obtainable encoding capacity. This increased width is likely to be due to the method used to measure the widths: Since the widths are measured from images taken on a camera, the measured values are very sensitive to inaccuracy in determining system parameters such as the grating to CCD distance. The width

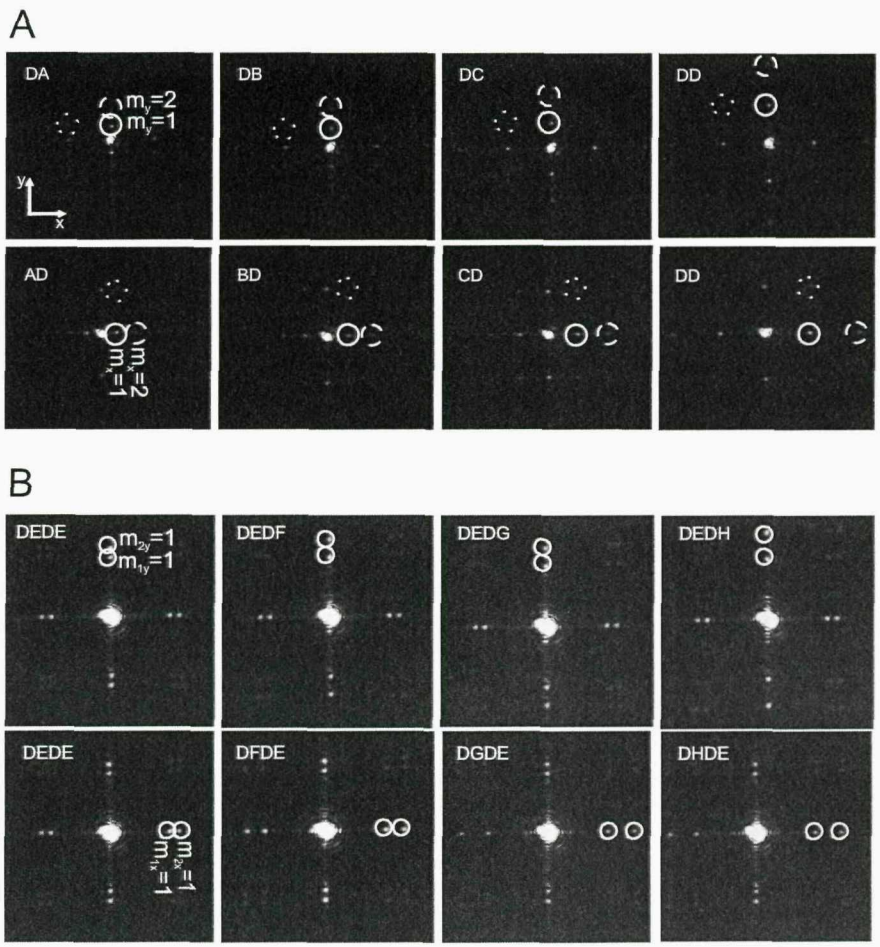

Figure 2.9: Diffraction patterns created by (A) single grating 2-dimensional tags and (B) tags containing two different gratings in each perpendicular direction. Moving from left to right shows how a progressive decrease in the pitch of the vertical (y) grating changes the diffraction pattern. The bottom row illustrates the same change in the pitch of the horizontal x grating. Solid circles indicate positions of 1 of the 4 sets of first order beams, dashed circles indicate second order and dotted circles 'quadrant' beams.

increase is thus system-dependant and could be reduced.

Curves fitted to the data in figure 2.10 may be used in place of equation 2.1, for calculation of the possible diffracted beam positions that may be used for encoding, in the particular system considered here. Following the same method as in section 2.1.1, replacing the analytic value of $\Delta\alpha$ with values calculated from the curves fitted to the data in figure 2.10, an estimate of the values for encoding capacity as a function of grating length is obtained, for various numbers of superimposed gratings, as shown in figure 2.11. While there is an obvious reduction in encoding capacity due to the higher beam width compared to the theoretical ideal situation, there is

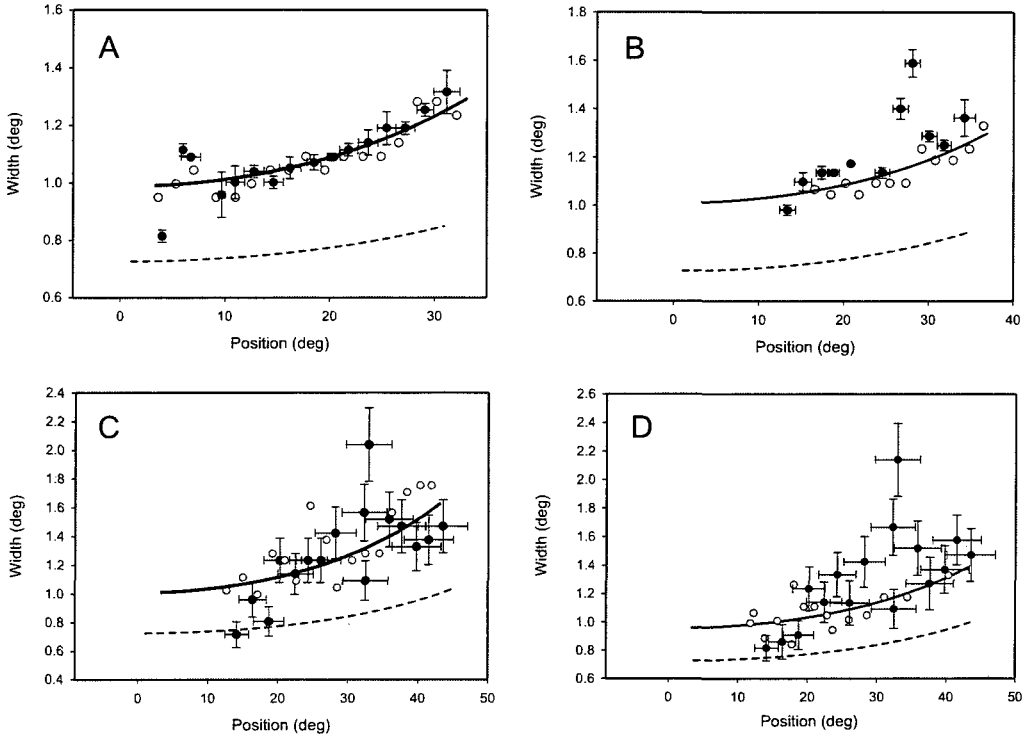

Figure 2.10: Measured beam widths at various angles for 1-dimensional (open circles) and 2-dimensional (black circles) tags illuminated by a beam focussed with a lens of focal length f=100mm. Parts A-D represent 1-4 times superimposed tags, respectively. The dashed line is a plot of theoretical beam width (as described in section 2.1.1) as a function of diffracted angle, for comparison to experimental measurements. Solid lines show fitted curves used to calculate encoding capacities in figure 2.11

still the capacity for very large numbers of codes using this diffractive technique, for example approximately 10^8 on a 100μm 5x superimposed 1-dimensional tag.

2.3 Non-code diffracted beams

2.3.1 Diffracted orders other than $m = 1$

The analysis of the encoding concept given so far assumes that only the first order diffraction spots encoding the data are present. In practice, however, this would only be correct for a grating with a sinusoidal transmission function (figure 2.12(A) inset). Such a grating has only a single frequency Fourier component in addition to the zero frequency, which results in a diffraction pattern containing only zero and first order beams, as shown in figure 2.12(A). The gratings considered here, of the

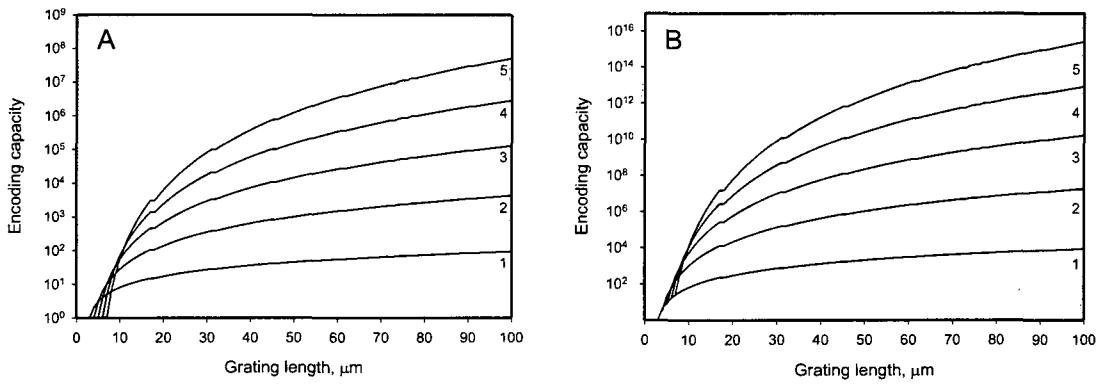

Figure 2.11: Encoding capacity of a diffractive bar-code tag as a function of the length of the tag for different numbers of superimposed gratings, based upon beam widths measured experimentally from metal-on-glass high resolution tags. Graph (A) shows the capacity for 1-dimensional tags and graph (B) the capacity for 2-dimensional tags. The number on each curve corresponds to the number of superimposed gratings.

type shown in figure 2.1, have a step transmission function with period a, as seen in figure 2.12(B and C) insets. In addition to the fundamental Fourier component with period a, there are higher frequency Fourier components which make up such a step function. These components appear as higher order beams ($m_1 > 1$) in the grating's diffraction pattern, shown in figure 2.12(B and C). The relative intensity of the various higher diffracted orders, as calculated from Fraunhofer diffraction theory, depends upon the exact profile of the grating, in particular on the ratio $a/(a-b)$, where b is the width of the transparent grating elements. Each successive higher order is less intense than the previous one, except that some of the higher orders are entirely absent from the diffraction patterns produced by certain grating profiles; for example a grating with $a_1/(a_1 - b_1) = 2$ has no second order ($m_1 = 2$) diffracted beam (figure 7(B)), while a grating with $a_1/(a_1 - b_2) = 3$ has no third order ($m_1 = 3$) beam (figure 2.12(C)).

The higher order beams can be confused with the first order beams, leading to misreading of the tag. It is therefore critical to be able to distinguish the first order diffracted beams from the higher order beams. This can be achieved by use of intensity discrimination of the higher order diffracted beams. The discrimination level is set to the level of the most intense higher order beam. Defining the calculated first order intensity as I_1, this level S can be defined as $S = I_2/I_1$, where I_2 is the intensity of the second order beam. This level S was calculated for ideal rectangular profile gratings with different values of $a/(a-b)$. Gratings with $a/(a-b) = 2$ require the lowest level of threshold, since one needs only to discriminate the third

order beams, as described above: setting $S = 0.05$ eliminates all higher diffraction order beams and provides error-free identification of the tag (see figure 2.13). For all other values, the second order beams have to be discriminated, resulting in the increasing values of S shown in figure 2.13 inset.

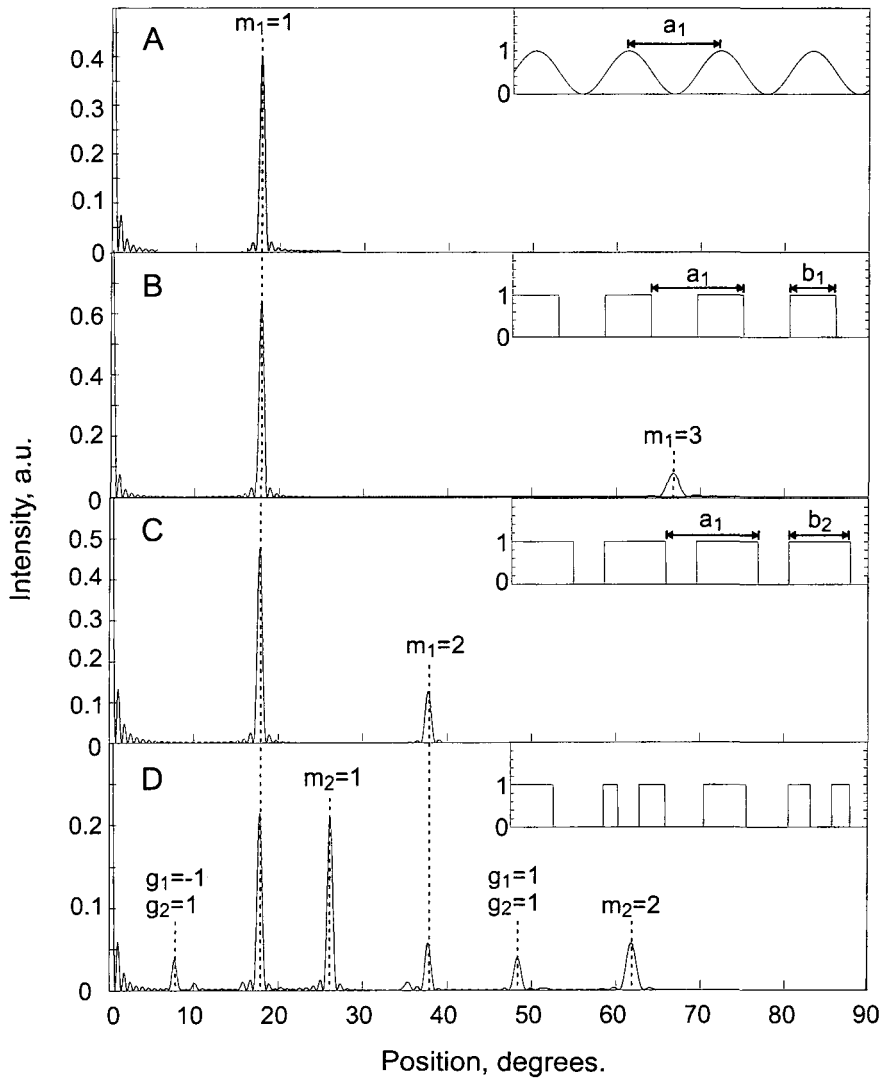

Figure 2.12: Diffracted beams from various grating profiles, calculated by FFT. The grating transmission function is shown in the inset to each graph. A) Sinusoidal transmission function, only first order diffracted beam appears. B) Step transmission function with ratio $a_1/(a_1 - b_1) = 2$. C) Rectangular profile with $a_1/(a_1 - b_2) = 3$. D) Grating with two superimposed pitches a_1 and a_2, both pitches have $a/(a - b) = 3$. In addition to the higher order diffracted beams, ghost beams appear due to superimposing process.

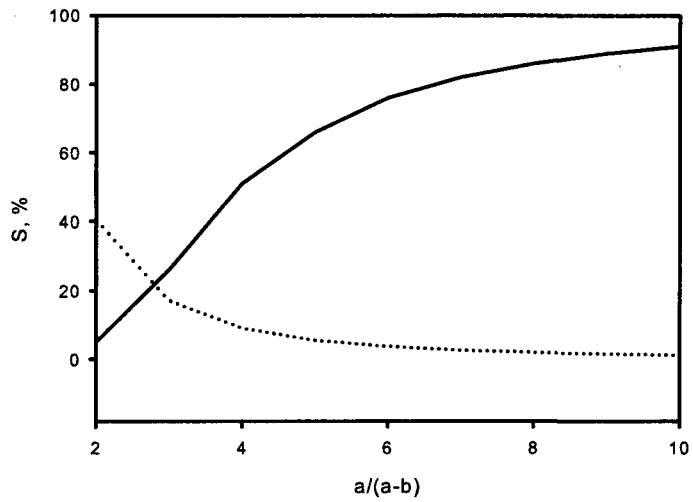

Figure 2.13: The level of intensity discrimination S necessary to ensure higher order elimination (solid curve) and elimination of the ghost and 2-dimensional 'quadrant' beams (dotted curve), for different grating aspect ratios.

2.3.2 'Ghost' orders due to superimposing

In addition to the higher order diffracted beams, when two or more pitches are superimposed, extra 'ghost' beams appear, which may also be confused with code first order beams. This is shown in figure 2.1(D) for two superimposed pitches a_1 and a_2. These beams result from the fact that the superimposed grating profile (figure 2.12(D) inset) is a multiple of the individual grating step functions. Therefore, in addition to the Fourier components of the individual step functions that make up the grating, the superimposed grating profile function has extra Fourier components that arise from the convolution of the individual grating components (figure 2.12(D)). The origin of these beams can be seen from the following analysis: consider a 2-times superimposed grating with transmission function C, consisting of the multiple of the transmission functions A and B of two individual gratings, i.e. $C = AB$. The Fourier transform (and hence the diffraction pattern) of grating C (denoted $FT(C)$ is therefore given by [44]

$$FT(C) = FT(A) \otimes FT(B), \tag{2.3}$$

where $\otimes$ denotes a convolution. The convolution produces a set of beams according to $FT(A)$ about each of the diffracted beams in $FT(B)$. About the zero order, these

produce the code beams from each of the gratings superimposed on the tag, plus the higher order diffracted beams. About the first order diffracted beams, extra 'ghost' beams are produced. From the properties of the convolution operation [44], the intensity of these ghost beams as a fraction of the first order intensity I_1 is equal to the ratio $I_1/I_0 = (\frac{a \sin \frac{b\pi}{a}}{b\pi})^2$ (for derivation, see Appendix A), where I_0 is the zero order intensity, plus a weighting determined by the amplitude and phase of the individual diffraction patterns of A and B at this point. In regions where both individual patterns have a very low light intensity (i.e. away from any of the diffracted orders), the ratio can be considered to be given just by I_0/I_1. These ghost beams can be eliminated using a similar intensity threshold method to that described above for the elimination of diffracted beams with $m > 1$. The resulting threshold for different values of $a/(a-b)$ is shown in figure 2.13. It can be seen from this graph that the thresholds used for higher order elimination will also eliminate the ghost beams for all aspect ratios, except $a/(a-b) = 2$.

By considering equation 2.3 it can be determined that each pair of pitches on a superimposed grating produces a set of ghost beams as a result of the convolution process. The ghosts appear at angular positions that depend upon the spatial frequencies present in the superimposed grating. A pair of gratings superimposed as in figure 2.1(D) individually have spatial frequencies $k_{G1m} = m2\pi/a_1$ and $k_{G2m} = m2\pi/a_2$, which give rise to the diffracted orders shown in figure 2.7(A and B). The superimposed grating has, in addition, spatial frequencies k_{sg} which are linear combinations of these, given by

$$k_{sg} = g_1 k_{G1m} + g_2 k_{G2m}, \tag{2.4}$$

where g_1 and g_2 can have the values $\pm 1, \pm 2, ...$These spatial frequencies produce ghost beams at positions α such that

$$\sin \alpha = \lambda \left(\frac{g_1}{a_1} + \frac{g_2}{a_2} \right), \tag{2.5}$$

which results in a diffraction pattern as in figure 2.12(D). The metal-on-glass superimposed tags shown in figure 2.5 display evidence of these ghost beams (see figure 2.7(B), example ghosts shown in dotted circles). The ghost order positions can be experimentally measured and compared against equation 2.5, as shown in figure 2.14. It can easily be seen that there is very good agreement between this equation and the measured diffracted spot positions.

In addition, the intensities of the ghost beams can be obtained from the FFT sim-

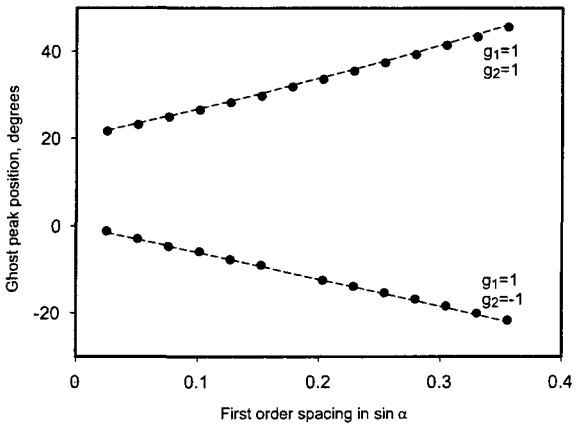

Figure 2.14: Positions of the $g_1 = 1$, $g_2 = 1$ ghost peaks due to a pair of superimposed gratings. The position depends on the angular spacing between the first order beams from the gratings. Points are experimental measurements from the diffraction patterns of the metal-on glass gratings, dashed line is a plot of equation (2) for comparison. The equivalent curves for $g_2 = 1$ are identical, but reflected about 0°.

ulations, in order to determine whether they may be discriminated by a threshold level method, similar to that described for the higher order beams. The simulated intensities of ghost beams $g_1 = g_2 = \pm 1$, which are the most intense, are measured in regions well away from other features of significant intensity in the diffraction pattern. We find that if I_0 is the zero order intensity, I_1 is the first order intensity and I_g the ghost order intensity, the relation $I_1/I_0 = I_g/I_1$ appears to hold, with fluctuations of $\pm 2.4\%$ (these fluctuations are dependant on the relative phase of the field as well as its amplitude, and therefore may be reduced, as will be discussed below). The ratio I_g/I_1 is used as a discrimination level, in a similar manner to the value S used for higher order elimination. It has already been seen in section 2.2.2 that the ratio I_1/I_0 decreases with increasing $a/(a-b)$ (figure 2.13). The ratio I_g/I_1 behaves in the same manner, because of the equivalence $I_1/I_0 = I_g/I_1$, as stated above. As already shown, the higher order intensity increases with increasing $a/(a-b)$. For $a/(a-b) > 2$, the ghost intensities are less than the higher order beam intensities in the regions of the diffraction pattern considered here. Therefore in these regions, the higher order and ghost beams for gratings with $a/(a-b) > 2$ are entirely discriminated by S. Additionally, the side lobes of the zero order (seen near 0° in figure 2.12), cause the ghost beam intensity to increase as its position approaches the zero order. Such ghost beams can be eliminated by having a dis-

crimination threshold that increases close to the zero order. Such a threshold is shown in figure 2.15, for example ghost beam intensities measured from metal-on-glass grating diffraction patterns. The optimal point for both ghost and higher order intensity is $a/(a-b) = 3$ (either side of this value, one or the other increases, see figure 2.13) and we therefore chose this grating profile for subsequent investigation of the superimposed diffraction grating tags. A similar analysis can be performed for other grating profiles.

A more drastic problem occurs when a ghost beam coincides with another ghost, or a higher order beam from one of the other gratings on the tag. The most significant case of coincidence with a higher order beam occurs for $g_1 = g_2 = \pm 1$ ghost beam due to two periods a_1 and a_2, coinciding with a 2nd order beam. This happens when

$$\left(\pm\frac{1}{a_1} + \frac{1}{a_2}\right) = \frac{2}{a_1}, \tag{2.6}$$

where $a_1 > a_2$. For coincidence of two ghost beams in position, the most significant case is for two ghost beams with $g_1 = g_2 = \pm 1$. For any combination of pitches a_1, a_2, a_3 and a_4

$$\left(\pm\frac{1}{a_1} + \frac{1}{a_2}\right) = \left(\pm\frac{1}{a_3} + \frac{1}{a_4}\right), \tag{2.7}$$

where $a_1 > a_2 > a_3 > a_4$.

This effect can create a ghost with an intensity which is a large fraction of the first order intensity (again, this is dependant on the relative phase of the interfering components, see below), which can therefore be extremely hard to discriminate from a code first order beam (see figure 2.15 inset). It is difficult to remove such high intensity ghosts using a threshold method, so tags with high intensity ghosts have to be eliminated from the encoding library. Using equations 2.6 and 2.7, the ghost coincidences for all possible grating combinations and for all different superposition levels can be calculated, and so these tags can be identified and removed from the possible set used for encoding. This gives rise to a set of revised values for the diffractive tag capacity (figure 2.3, dashed curves 2 - 5). It is clear from this that the majority of the tags can still be used for encoding.

Although not studied practically in this thesis, it is possible to change the effect of the combination of ghost orders with other features of the diffraction patterns from the individual gratings on a superimposed tag, by modifying this particular superimposing method. This can be done because the result of interference of features

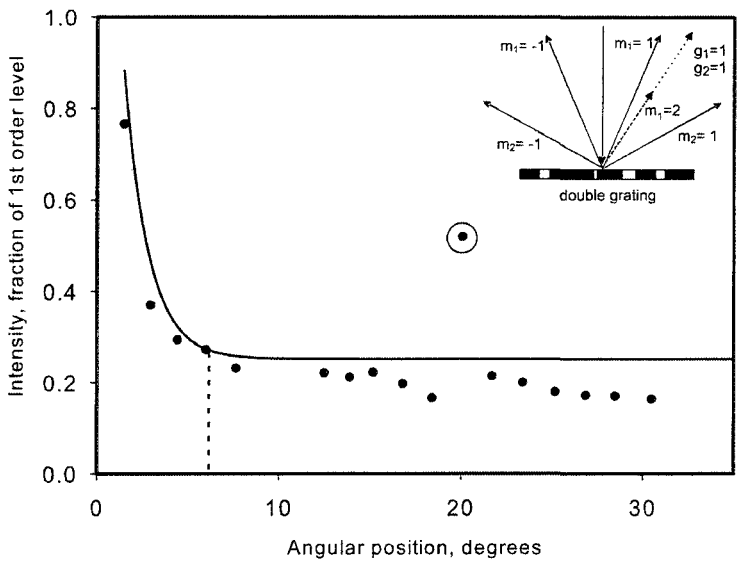

Figure 2.15: The measured intensity of ghost beams at various angular positions for example 2 times superimposed tags with $a/(a-b) = 3$ (black points). The dotted line separates the region where $I_1/I_0 = I_g/I_1$ (right of dotted line) from the region of rising ghost intensity close to the zero order (left of dotted line), due to interference between the ghosts and the zero order subsidiary maxima. The solid line shows an example of a threshold which could discriminate such ghost beams. An example ghost with an intensity that cannot be discriminated by this threshold is indicated by the circled point. Inset shows how such a ghost beam is formed by coincidence in position with a second-order beam.

in the diffraction pattern is dependent not only on the electric field amplitudes, but also the relative phase of the two interfering features. The relative phases of the field due to each grating at a particular point in the detection plane depends on the position of the point, and also on the relative spatial position of the gratings on the tag. Therefore by moving the gratings with respect to each other, the intensity of features produced by interference of ghost beams with other features can be reduced to a minimum level. This is similar to the techniques used in some of the technologies described in chapter 1, such as the binary superimposed Bragg gratings (BSGs).

For 2-dimensional tags, an extra set of diffracted orders appear in the quadrants between the code axes (marked on figure 2.9 (A) by dotted circles). These orders are not on the code axes so in theory would not interfere with the code reading. However, for the reading algorithms that will be considered in chapter 3, we will see that the reading process involves locating these axes (the axis location is not assumed). Therefore these orders may also disrupt the code reading process. The

origin of these beams are due to the convolution process, in a similar manner to the ghost beams described above : a 2D grating with transmission function C consists of the multiple of the transmission functions A and B of two mutually perpendicular gratings i.e. $C = AB$. The intensity of these beams as a fraction of the first order intensity I_1 is therefore equal to the ratio $I_1/I_0 = (\frac{a \sin \frac{b\pi}{a}}{b\pi})^2$, where I_0 is the zero order intensity, plus a weighting determined by the amplitude and phase of the individual diffraction patterns of A and B at this point. Since both individual patterns have very little light at the positions of most of these beams, the ratio can be considered to be given just by I_0/I_1, ignoring the weighting except in regions very close to the zero order. These quadrant beams can be eliminated using a similar intensity threshold method to that described above for the elimination of diffracted beams with $m > 1$. The resulting threshold for different values of $a/(a-b)$ is shown in figure 2.13. It can be seen from this graph that the thresholds used for higher order elimination will also eliminate the extra two dimensional 'quadrant' beams for all aspect ratios, except $a/(a-b) = 2$.

2.3.3 Thresholds and SNR

Throughout this section, the method of thresholding has been used to remove unwanted beams from the diffraction pattern. These unwanted beams, can however (since they are not code beams) be considered as noise, and the threshold is then equivalent to the signal-to-noise ratio (SNR) of the code diffraction pattern. The word "threshold" has been used thus far simply because it describes the method of removing the unwanted noise from the diffraction patter before reading.

The SNR of the grating diffraction patterns determines the limit on the available superimposing levels: as the SNR approaches 1, the gratings can no longer be reliably read. Since more spurious features (ghost beam) appear as more gratings are superimposed on the tag, SNR is inversely proportional to n_g. In our case, as will be discussed in more detail in section 3.2.4, SNR approaches 1 for $n_g = 4$, limiting the encoding method to 3 superimposed gratings for reliable reading.

2.4 Conclusions

In conclusion, the concept of a new optical non-contact tagging technique for microparticles has been demonstrated, based on superimposing large numbers of miniature diffraction gratings on a tag. Various limitations of the method for rectangular

profile gratings have been analysed, such as higher order diffracted beams and ghost beams produced due to the superimposing process, which may be confused with code first order beams. However, it has been shown that in most cases these beams can be eliminated by the use of an intensity threshold method. Using simple combinatorial analysis, the technique was predicted to be capable of creating distinguishable tags containing at least 5 superimposed grating and encoding up to 10^9 tags, each of which is only 100μm long and a few μm wide. To demonstrate this technique a library of 50μm x 50μm tags was manufactured on a glass wafer and the practicality of the superimposed grating tags was confirmed. The simple multiplicative encoding method allows for up to three superimposed gratings, providing capacity for more than 68,000 tags. The available encoding capacity was shown to be limited by inaccuracies in the reading setup, in addition to the limitations provided by the encoding method, which are discussed in more detail in chapter 3. An enormous increase in capacity is possible if two sets of mutually perpendicular gratings are used, creating 'two-dimensional' tags. Combinatorial analysis predicts that up to 10^{21} different two-dimensional barcode tags can possibly be fabricated with up to 5 superimposed gratings in each dimension. A library of two-dimensional tags allowed ones containing at least three superimposed gratings to be resolved, demonstrating an obtainable capacity of the order of 6.2×10^8 codes. The robust nature of the tags, together with the non-contact remote reading capability makes them ideal for a large variety of micro-particle based biochemical, cytological, proteomic and genomic assay applications.

Chapter 3

Encoding for automated assays

In this chapter, the steps required to apply the encoding concept (outlined in the previous chapter) to biochemical assays are outlined. This includes the materials and fabrication details required to manufacture particles compatible with the assay system, and an automated reading algorithm that could be used to identify a particle's code in such a system.

Section 3.1 outlines the type of system which could be used to read diffractively encoded particles in order to perform high throughput assay analysis, together with the requirements for the material from which the particles are fabricated. The concept of phase gratings, manufactured by profiling the surface of the particles, is introduced as being the simplest method for diffractive encoding of particles. Section 3.2 introduces the manufacturing method of nano-imprint lithography for production of encoded particles, and characterize the diffraction patterns from the resulting tags. Finally, section 3.3 presents details of an algorithm for automated reading of the tags, under the conditions likely to be present in a microfluidic assay system.

3.1 Assay system requirements

In order to analyse a bead based assay in a high throughput manner, a microfluidic system must be used. While the exact details and implementation of the microfluidics fall outside the scope of the work presented in this thesis, the requirements of such a system affect the development of tag reading software and hardware, and the material requirements for the tags. We therefore consider here the system requirements, in order to develop these aspects of the diffractive tagging technique for later integration into a microfluidic system. The principle of such a system is

outlined in the schematic in figure 3.1. A mixture of encoded particles which have undergone biochemical binding reactions (such as those described in chapter 1) is pumped into the system. Those which have undergone successful molecular binding are fluorescent and trigger a signal in the fluorescence detector. An impedance detector prompts the diffraction detector to start the reading process (see section 3.3). The diffraction detector is a CCD/CMOS camera; the diffraction pattern is projected directly onto the surface of the camera sensor. The camera takes images of the diffraction patterns obtained from tags, and sends them to a PC for analysis, in order to obtain the code (see section 3.3). The wavelength of the laser used for diffraction measurement should be chosen not to be too close to the absorption peak of the fluorescent dye used to indicate successful molecular binding, so as avoid the possibility of bleaching the dye: in our case we design tags for use with light of wavelength 633nm, well away from the absorption peak of the fluorescent dye Cy3. After identification the particle can, if required, be sorted into a variety of channels, depending on its code and the results of fluorescence detection, for further analysis or chemical processing (example sorting electrodes are shown in figure 3.1(B)). The system of channels and electrodes is manufactured by photolithographic processes, and is contained in a glass chip measuring 20 x 20mm (figure 3.2(A)).

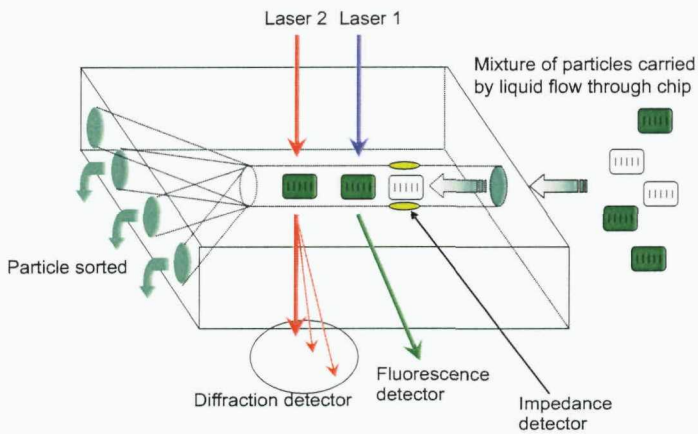

Figure 3.1: Schematic of the kind of microfluidic system that can be used for high throughput analysis of diffraction-encoded micro-particle assays. A mixture of particles enter the system and are analysed for analyte binding and diffractive code, both of which are triggered by impedance detection. The particles are sorted for further analysis on the basis of code and fluorescence signal.

In order to be successfully used for tag detection, the camera must fulfil a number of requirements. It must be able to cope with high intensity incident light (particu-

larly due to the zero order); many CCD sensors are prone to 'bleeding' of signal from saturated pixels into neighbouring pixels. This creates a 'blooming' effect, so that high intensity objects appear much larger than they actually are. This will cause the zero order to interfere with, or obliterate, code beams close to it. The system should therefore use a camera with a CMOS diode-array type sensor, which features an antiblooming ground, moving excess charge away from high intensity pixels to stop it leaking into neighbouring pixels. The size of the sensor must be large enough to fit wide-angle diffraction patterns on at the minimum distance from the gratings, that is required to observe the Fraunhofer diffraction pattern of the tags. To obtain the Fraunhofer diffraction pattern on the camera [44], the distance z between the grating and the camera sensor should satisfy $z \gg kx_{max}/2$. By evaluating the Fresnel diffraction integral at various values of z, we find that at $z \geq kx_{max}/2$ the pattern is equivalent to the Fraunhofer pattern. For our gratings ($x_max \simeq 25\mu$m), this distance is about 3mm.

Electrodes within the microfluidic channel (shown in figure 3.2(C)) keep the particles aligned for reading of the diffraction patterns, although the reading algorithm is able to tolerate some misalignment of the particles (see section 3.3.1). A high frequency electric field is placed across the alignment electrodes. The alignment is accomplished by dielectrophoretic forces (see, for example [84]), which require the tagged particles to have length≠width≠height. A high throughput method for manufacturing large numbers of rectangular blocks is photolithography. This process requires a material which either cross-links (polymerizes) or un-cross-links under exposure to light. The first type is known as a *negative resist* and the second type a *positive resist.* When using a negative resist, as is the case in this work, a layer of material is spun onto a flat substrate (for example glass or silicon), and a mask is used to selectively cross-link rectangular sections of material. After removal of the non-crosslinked material, rectangular particles are left on the substrate, which can then be encoded and subsequently lifted off from the substrate for use in assays.

In addition to the photolithographic properties, the material used must be able to withstand the physical and chemical conditions of the processes required to attach biomolecules to the surface of the particles. The particles must be mechanically stable, in order to withstand pippeting, sonicating and centrifuging accelerations up to 78000 ms^{-2}. The material must be resistant to attack from organic solvents used in the biochemical processes and stable in temperatures up to 50°C. Most importantly, the material must have surface chemistry which is compatible with the attachment of biomolecules to the surface.

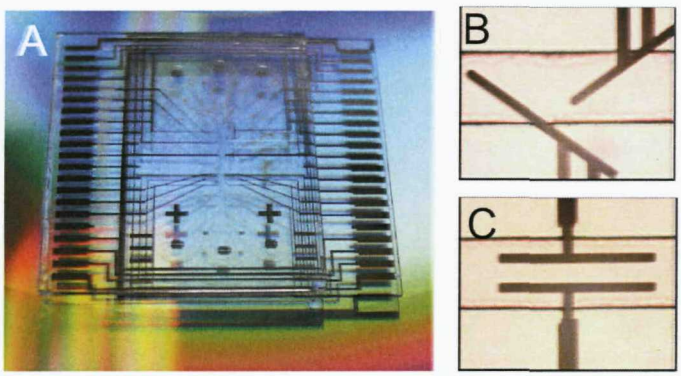

Figure 3.2: (A) An example chip containing a microfluidic channel, through which solutions containing encoded particles can be passed for automated analysis. Electrode connection are seen on the left and righ sides of the chip. After analysis, electrodes (B) force the particles into certain channels, depending upon the analysis results. (C) Parallel electrodes keep the particles aligned during reading of the code, in order to minimise distortion of the diffraction pattern (images courtesy Dr. G. Galitonov).

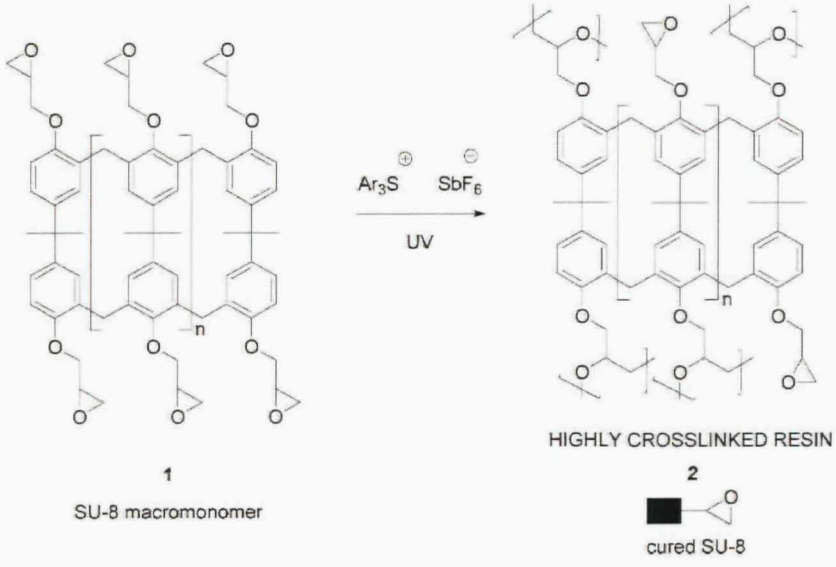

Figure 3.3: Schema of the cross-linking process of SU8. The macromonomer is made of a number of repeating elements (on average 8) containing free expoxide groups. Upon exposure to UV light (wavelength 365nm) in the presence of a photo-initiator, a proportion (depending on the light fluence absorbed during cross-linking) of free epoxide groups open and form bonds to each other, permanently linking the macromonomers together. A number of residual free epoxide groups remain after cross-linking. These free epoxide rings may easily be chemically opened and functionalized for attachment of biological molecules.

Taking the above factors into account, the material chosen for the manufacture of diffractively encoded microparticles was the novolac-epoxy resin SU8, which is well established in the field of microfabrication and micropatterning and is widely used as a negative resist [85, 86, 87]. The structure of the SU8 monomer is shown in 3.3. SU8 is generally dissolved in an organic solvent (for example gamma-butyrolactone), and mixed with a photo-initiator (Ar_3S and SbF_6 mixture). This solution is spun onto a flat substrate and baked to remove the solvent. Upon exposure to UV light of wavelength 365nm, the photoinitiator causes the expoxide groups to form cross-links between the monomers (figure 3.3), resulting in a polymeric material. SU8 performs outstandingly in photolithography, forming flat well-defined microstructures with surface variations as small as ±40nm. After exposure through a mask, SU8 is cured with a post-exposure bake process, forming an extremely thermally stable material, with a decomposition temperature of 380°C [88]. Fully crosslinked SU8 has a tensile breaking strength of approximately 55 MPa [88], comparable to nylon fibres, indicating an ability to withstand high forces without being destroyed. SU8 is also resistant to attack by most organic solvents once crosslinked [89]. In addition, the crosslinked material has residual free epoxide groups on the surface, which are easily functionalized for attachment of biochemical molecules such as oligonucleotides, peptides and antibodies [28, 89, 90, 91, 92, 93]. SU8 also has excellent optical transparancy in the visible region; to demonstrate this, the transmission spectra of flat 17μm thick SU8 plates on a glass substrate were measured using a spectrophotometer, which gave an average transmittance of $99.4 \pm 0.2\%$ for wavelengths 400-700nm (measurement calibrated to the substrate without SU8). All of these properties make SU8 an ideal candidate for diffractively encoded microparticles to be used in bead based assays.

In order to diffractively encode SU8 particles, methods for photolithographically patterning metal onto the SU8 were investigated, in order to produce amplitude gratings similar to those in chapter 2. The manufacturing tests were performed by Dr. Shahanara Banu and the process is outlined schematically in figure 3.4(A). First, SU8 is spun to a thickness of approximately 5μm on a substrate, and selectively cross linked to form bars. The un-crosslinked SU8 is removed with a developer, and gold evaporated to a thickness of approximately 100nm. A positive resist is then spun over the gold coated bars, and patterned to provided a mask in the shape of the required grating. The exposed gold is then etched away, leaving a gold grating on the surface of the bars. Since this process involves many steps and thus is very time consuming, it was abandoned in favour of producing phase gratings using a the one step photolithography process shown in figure 3.4(B). A layer of SU8 is spun onto

a substrate and the bars patterned using the mask shown in figure 3.4(B). This creates grating ridges along the edges of the particles which form a phase grating which diffracts as described in section 1.4.3.

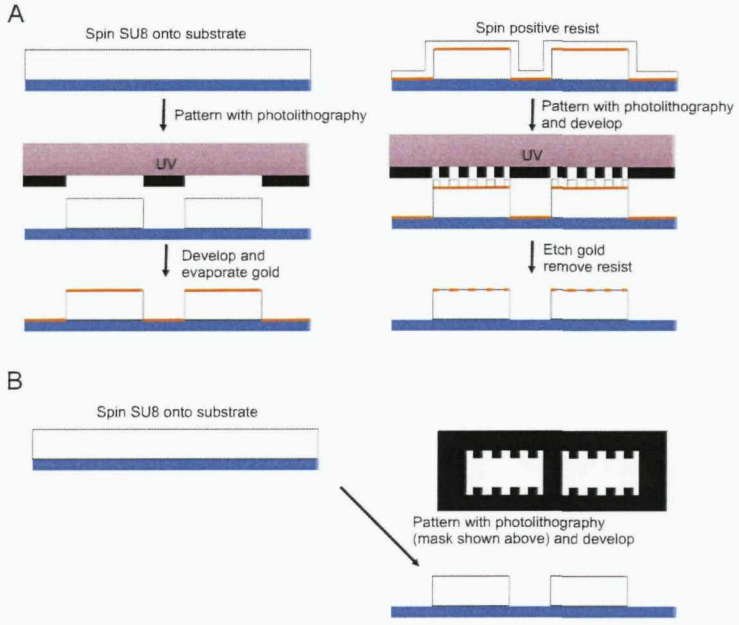

Figure 3.4: Schematic of the procedures for manufacturing (A) amplitude gratings and (B) phase gratings using photolithography.

The photolithography method described above was used to manufacture phase gratings with 4 different periods which were successfully used in real genomic and proteomic assays by members of the 4G group (in particular, Dr. Rohan Ranasighe, Joseph She and Graham Broder) in which the code was detected by distributing the particles on the slide after the assay, and scanning the slide over a reading beam. The code was read using the algorithm described in section 3.3.3, integrated by Dr. Gerasim Galitonov into an overall piece of control software with initial options to detect the fluorescence signal from the chemical components of the assay. In addition to demonstrating the applicability of the encoding technique to its intended application, the assays provided some important data about the number of repeats of each code which need to be read due to fluctuations in the fluorescence signal. More details on this are given in section 3.4. In addition to these static slide-based assays, reading of the codes was succesfully demonstrated in a microfluidic device by Dr. Galitonov, although the full integration with fluorescence required to perform actual fluidic assays still requires some work.

The photolithography method, although successful at producing a very limited

number of periods, was not able to produce large numbers of codes due to the resolution limits of the available lithography devices (resolution limit approximately 2μm).We now move on to describe a manufacturing process which will be shown to be able to reproduce superimposed diffraction gratings as ridge profiles on the surface of SU8, with accuracy adequate to achieve a large number of unique, distinguishable codes.

3.2 Gratings manufactured by nano-imprint lithography

In order to pattern nano-structured encoded superimposed gratings into SU8 as ridge profiles, we use a process known as nano-imprint lithography. In conventional nano-imprint lithography, a high resolution stamp is fabricated in a hard material such as silicon or fused silica using a combination of electron beam lithography and dry etching. Figure 3.5 shows an outline of the basic principle of nano-imprint lithography. The high-resolution stamp is brought into hard contact with soft polymer, transferring the stamp's structures onto the polymer surface. The result is high quality replica of the structures on the stamp, with similar resolution to the original. The process can be repeated many times, providing material transfer from the substrate to the master is minimized using an anti-stick coating. Nano-imprint lithography is therefore ideal for the production of diffractively encoded SU8 micro-tags, which require high quality, high throughput reproduction of many copies of structures with high resolution features.

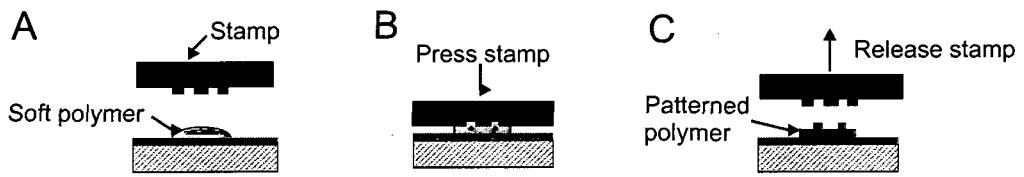

Figure 3.5: Generic outline of the nano-imprint lithography process. A high-resolution structured stamp is brought into contact with a soft polymer, and force applied. The stamp is removed, leaving a high-quality copy of the stamp's structure in the polymer surface.

3.2.1 Imprint ridge depth

In section 2.1.3, the optimum values of ridge depth D for SU8 gratings in air and water were calculated. As we shall see, manufacturing constraints preclude us from using any arbitrary value of D: the nano-imprint process that will be described in the next section can in general only achieve maximum depths of about 500-600nm whilst still adequately resolving features of 100nm width. Gratings superimposed using the simple multiplicative method described in chapter 2 contain some features of 100nm or even less. Therefore, we cannot realistically achieve the optimum value of D for water, whilst maintaining the required feature resolution. However, the chosen a value of $D \approx 600$nm ($D/\lambda = 0.947$) is close to the optimum value for gratings in both air and water, giving $I_0/I_1 = 1.4$ for a single grating in air and $I_0/I_1 = 1.3$ for a single grating in water. It is difficult to guarantee an accurate depth using the process which produced the nano-imprint masters, so the obtained depth deviated somewhat from our originally chosen value. In addition, it will be shown that the features of 100nm or less in size have little effect on the code; most limitation occur due to the interference between wanted and unwanted elements of the diffraction pattern, introduced by the particular coding method used.

The relative intensities of all the diffracted features away from the zero order (e.g. the ratios of first order to second order intensity I_1/I_2 and first order to ghost order intensity I_1/I_g) may also change with different values of D. This will be investigated further in section 3.2.4 alongside experimental results from SU8 encoded tags, together with the variation in the values of I_0/I_1 between different orders on a superimposed tag.

3.2.2 Stamp manufacture

Two types of nano-imprinting stamp were tested. The first was fabricated by e-beam direct-write from silicon carbide, for a simple test of the manufacturing concept. The nano-imprinting stamp was designed as a GDSII mask layout file using dedicated software that allows the user to enter the required grating parameters and then automatically generates the required mask (software written by Dr. Gerasim Galitonov, University of Southampton). The embossing stamp was an area 2 x 2 mm, containing an array of 50 x 50 μm gratings, one of which is shown in figure 3.7(B). The array contained four areas, each of 25 tags with 2 superimposed gratings on the surface. The stamps were manufactured from silicon carbide wafers by Dr. Yifang Chen of the Rutherford Appleton Laboratory. An outline of the pro-

cess is shown in figure 3.6. A 120 nm layer of Poly-methyl-methacrylate (PMMA, molecular weight (MW) = 100k) was spin coated onto the wafer and then baked at 180°C in an oven for 1 hour. A second layer of PMMA (MW = 350k) was then applied under the same conditions. This bilayer resist was essential for the creation of an undercut in the resist profile after lithography to ensure successful lift-off. Electron beam exposure was carried out at 100 kV, using a high resolution vector beam writer (VB6, Leica-Cambridge plc). Standard development of the PMMA in MIBK:IPA (a 1:3 ratio mixture of methyl isobutyl ketone and isopropanol) was undertaken at room temperature. A 30 nm thick chromium layer was deposited by thermal evaporation (Edward evaporator) and the sample soaked in acetone for 20 minutes to lift off unwanted chromium. Etching of the chrome-patterned silicon carbide was performed using an anisotropic dry etch with a mixture of C_2F_6/CHF_3, in an Oxford Plasma Technology System 90 etcher. In this process a plasma of the two gasses reactively removes the silicon carbide. The process is adjusted to make the etch as anisotropic as possible, i.e. creating straight-walled grooves rather than grooves with curved walls. By adjusting the ratio of C_2F_6 to CHF_3, various etched profiles can be achieved. In our case, it was found that a ratio close to 1 produced vertical side-wall profiles as shown in figure 3.7. With this gas mix, the etch rate was approximately 10 nm/minute. After etching, the remaining chromium on the top of the silicon carbide features was removed with a commercial chrome etchant. These stamps were used to imprint barcodes onto flat sections of SU8 for characterisation.

The second type of nano-imprint stamp tested was a nickel stamp moulded from a direct e-beam written silicon master. The advantage of this second process is that the stamp is more robust, and may easily and cheaply be replaced after breakage or severe contamination by moulding a new stamp. This second process therefore lends itself more realistically to mass-manufacture of encoded microparticles. The stamp is the size of a 4" wafer, allowing it to be used in standard wafer processing machines. The layout of encoded tags on the master is different to the silicon carbide master; in this case there is a 4 x 4 mm area of gratings. Within this there are 100 gratings within a 2 x 2mm area, repeated four times to make a 4 x 4mm square. As before, the design was created using the software written by Dr. Galitonov.

The first part of the manufacturing process of the nickel stamp is the creation of the initial silicon mould (silicon mould manufactured by Kelvin Nanotechnology Ltd). This is shown schematically in figure 3.8. First (steps 1 - 4), a raised area 5μm in height and approximately 2 x 2cm in area is created. The purpose of this is to prevent any contaminants disrupting the imprint process, which is likely to happen

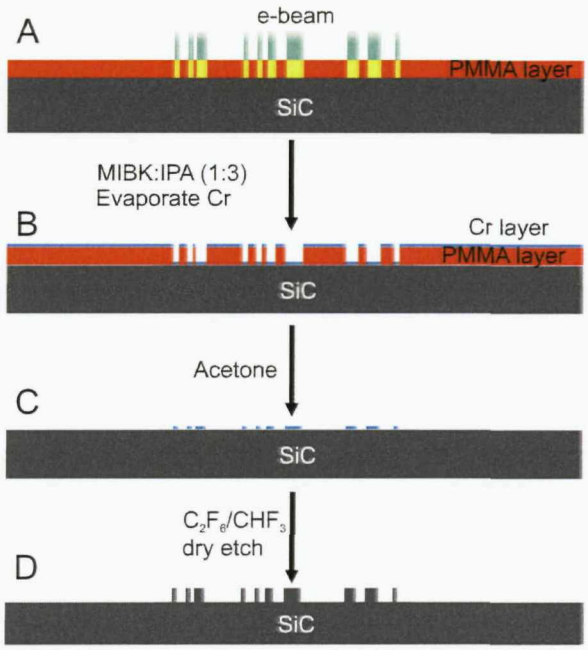

Figure 3.6: Process for manufacturing the SiC nano-imprint master: (A) A layer of PMMA is spun and cured onto the SiC, and the required pattern un-crosslinked by e-beam. Un-crosslinked PMMA is removed with MIBK:IPA and a chrome protective layer is deposited (B). The remaining PMMA removed with acetone leaving a protective chrome layer covering only the required features (C). The unprotected SiC is dry etched away to the required depth, leaving the patterned imprint master (D).

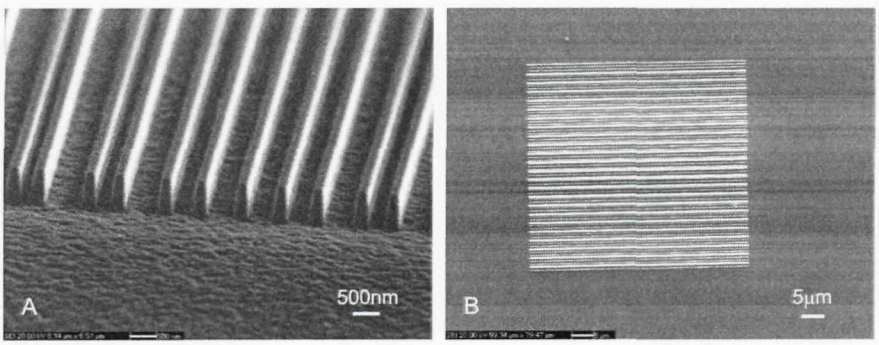

Figure 3.7: SEM images of a SiC nano-embossing master. The high aspect ratio and uniformity of the structures can be seen (A), together with the multiple periods evident in a superimposed grating pattern. Single grating patterns are 50 μm square (B), with many such patterns in an array over a 2 x 2mm area (images courtesy Dr. S. Banu).

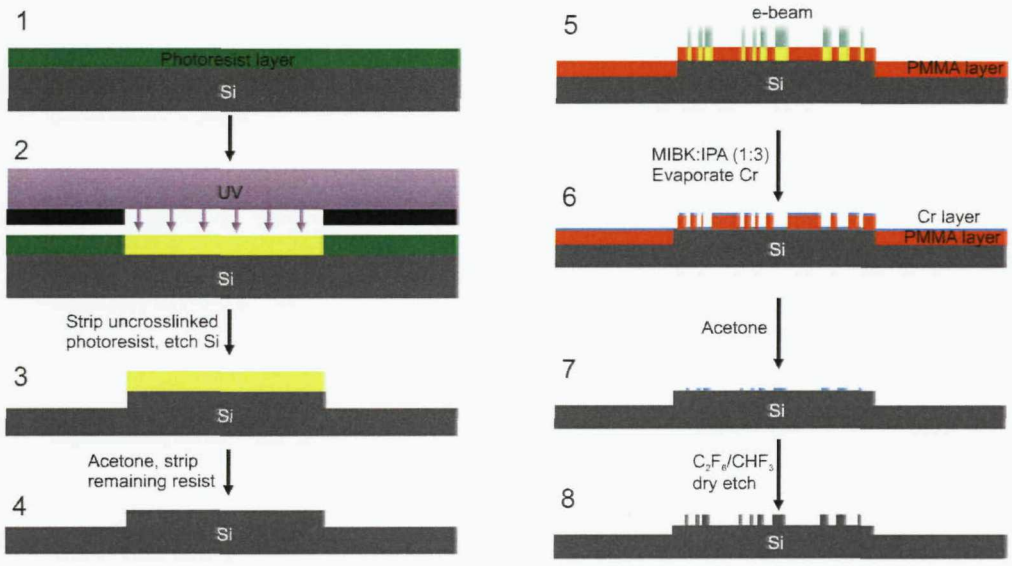

Figure 3.8: Schematic of the process for creating a silicon mould for the manufacture of nickel nano-imprint masters.

over the area of a 4" wafer. The area is created by spinning a layer of negative photoresist onto a 4" silicon wafer (step 1), and exposing it through a mask which crosslinks the resist inside the position of the raised area (step 2). Uncrosslinked resist is then washed away, and the exposed silicon etched to a depth of 5μm. The remaining resist is then removed, leaving a raised area in the centre of the silicon wafer. The pattern of the encoded gratings is then created on top of this raised area (steps 5 - 8) by the same e-beam direct write method used to create the silicon carbide master, as described above.

Once the silicon mould is fabricated, a nickel 'father' mould is created from it by electroforming (all electroforming was carried out by Tecan Ltd using a proprietary process). Nickel is electroplated to a thickness of 300μm over the silicon. The silicon is then completely removed by immersion in potassium hydroxide (KOH), leaving a nickel plate with a reversed copy of the silicon's structure. Nickel is then again plated to a thickness of 300μm over the father mould. This second plate is released from the father mould mechanically, leaving both intact. The father mould is kept and may be used repeatedly, each time creating a nickel copy of the silicon structure which is then used in the nano imprint process. This ability to mould many stamps allows them to be more easily and cheaply replaced than the direct-write silicon carbide stamps. SEM images of the final nickel embossing master are shown in figure 3.10. We can see that the quality of the master produced is similar to that of

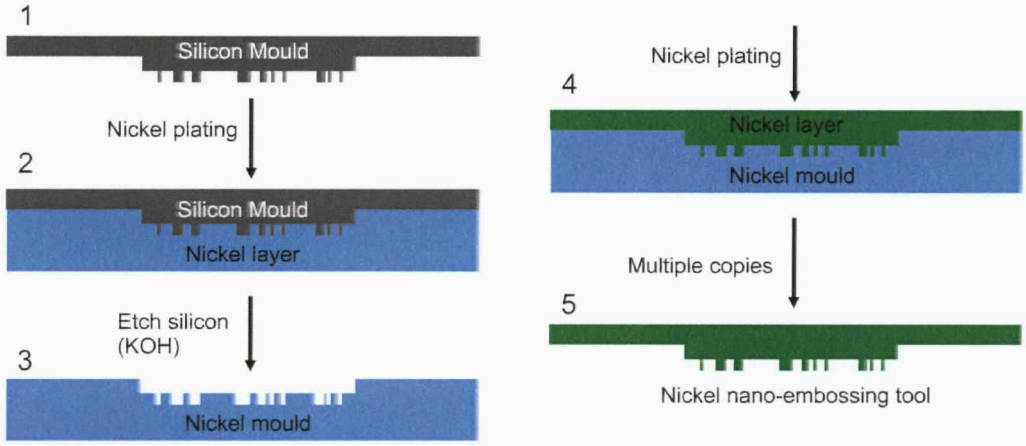

Figure 3.9: Schematic of the process for creating a nickel mould from the silicon mould. The final nickel imprint master is then created from this nickel mould. The nickel mould may be used repeatedly to create many nickel imprint masters.

the silicon carbide master, with some evidence of imperfect reproduction of features less than 160nm in width seen in figure 3.10(3).

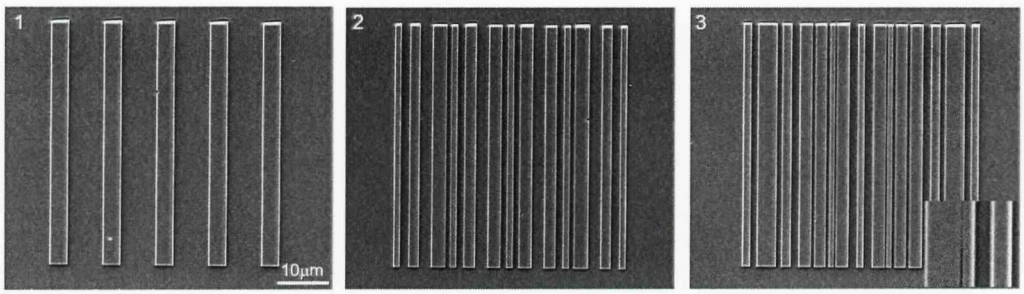

Figure 3.10: SEM image of single (1), 2x superimposed (2) and 3x superimposed (3) gratings on the final nickel nano-imprint master. Inset shows a zoomed in section of the 3x superimposed grating: Note the resolution limit of the process resulting in imperfect reproduction of gaps less than 160nm in width in part (3) inset.

3.2.3 SU8 imprinting process

The manufacture of nano-imprinted SU8 diffractive tags was performed by Dr. Shahanara Banu, a member of the 4G basic technology group. The first imprinting tests were performed using the silicon carbide stamp in a simple home made compression tool, to test the applicability of nano-imprinting to diffractive encoding of SU8. SU8 films were fabricated on boro-silicate float-glass wafers (thickness 700 ± 25 μm,

Schott), which were first spin-coated with a Ti-prime adhesion layer at 3000rpm, followed by baking at 120°C for 2 minutes. A layer of SU8-5 was then spin coated at 2000rpm followed by 1 minute baking at 65° and a further 1 minute at 95°. The final thickness of the SU8 could be adjusted by varying the spin speed; the speed was optimised to 2000rpm to give a film thickness close to 5 μm. After coating the wafer with SU8, the wafer was exposed to light of wavelength 365 nm (I-line of a mercury arc lamp) through a mask, using a MA6 (SUS Microtech) mask aligner, with an optimized exposure dose in the range 60-200 mJ cm^{-2}, depending on the thickness of the SU8. The mask was either blank to fabricate flat films for characterization, or patterned with rectangular blocks for manufacture of bar-shaped particles. After exposure, the wafers were baked at 65°C for 1 minute, and the temperature was then increased for 7.5 minutes at 4°C per minute, to 95°C. The wafers were developed in PGMEA EC solvent (polypropylene-glycol-methyl-ether-acetate, Chestech Ltd, UK.) for 2 minutes with agitation, then thoroughly rinsed with isopropyl alcohol and blow dried.

In order to ensure complete detachment of the stamp after imprinting [11], the stamp was coated with a monolayer of anti-stick agent, trichloro(1H, 1H, 2H, 2H-perfluorooctyl)silane. The stamp was soaked in a solution of 1-2% of the trichlorosilane in ethanol for 30 minutes, rinsed with ethanol and baked in an oven at 120 C for 30 minutes.

Imprinting was performed by pressing the master onto a 2 x 2mm area of wafer containing the pre-fabricated SU8 bars (or flat films for grating characterization), with thicknesses of approximately 5 μm. A home-made press was used, based on a screw clamp arrangement, in which the pressure was adjusted using a torque-wrench. The applied force was calculated from the torque and checked using an electronic balance. The imprinting force was distributed as homogeneously as possible using a piece of PDMS sheet between the stamp and the pressure plate. The stamp was aligned by eye with the substrate and then the assembly was pre-baked. The required force was applied using the torque-wrench, and the system again baked. In order to optimise the imprinting, a range of forces in the range 60-320 N were tested (over the 2 x 2 mm stamp). The baking temperature was ramped from $50 - 100$°C at 4°C min^{-1} for 5 minutes. The stamp was removed manually by levering it off with tweezers, leaving the sample ready for characterisation.

In order to characterize the imprinted patterns, gratings of 50 x 50 μm were fabricated on flat films of SU8. With an imprinting force of 320 N, high quality gratings with high aspect ratio (figure 3.11 (C) and (D)) were obtained, in this case with

feature depths of 650 nm. Patterning bars onto the film by photolithography before imprinting allows us to produce similar high quality imprinted patterns on bars (figure 3.11 (A) and (B)), showing that this technique works well for the production of diffractively encoded microparticles.

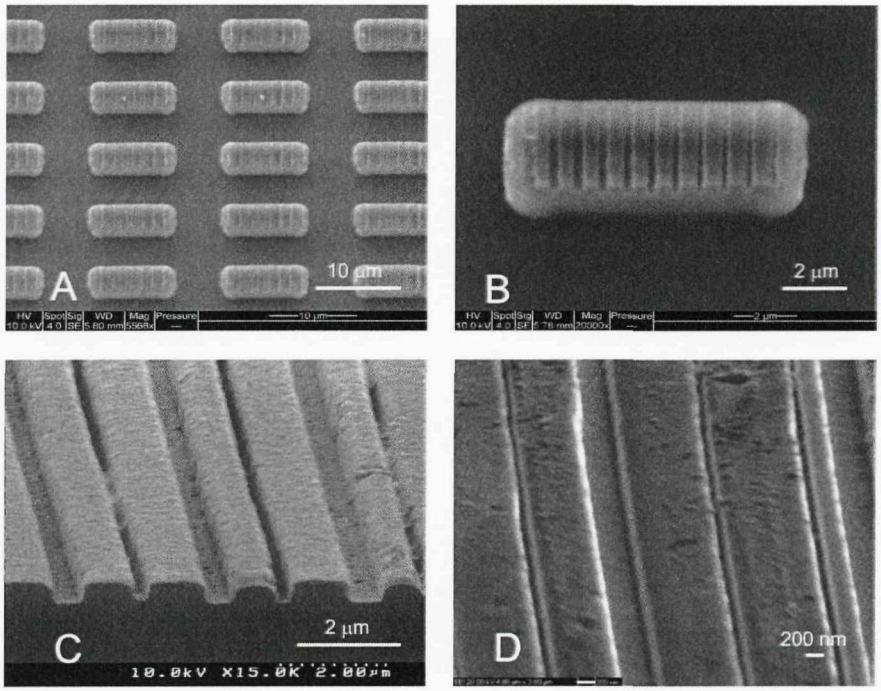

Figure 3.11: SEM images of an array of microbars nano-imprinted using a silicon carbide imprint master(A), with a high quality diffraction grating pattern (B) reproduced on the surface. The depth of the features (C) and uniformity of the profile (C and D) are shown here in patterns imprinted into flat SU8 films. All samples were coated with 5nm gold before imaging (images courtesy Dr. S. Banu).

Once the silicon carbide stamp was shown to produce high quality diffraction gratings, proving that the imprint principle works for manufacture of encoded superimposed grating tags, further imprint tests were made using the nickel imprint masters produced by electroforming. SU8 3005 films were fabricated on glass pretreated as described above. The SU8 was spun to a 5μm layer on the glass by spinning at 500rpm for 5s, followed by spinning at 2500rpm for 30s. The coated glass wafers were then soft baked at 65°C for 5 minutes, followed by 95°C for 30 minutes. As for the silicon carbide stamp, the nickel stamp was coated with silane to ensure detachment of the stamp after embossing. However, in order to allow adhesion of the silane to the stamp, the stamp had first to be coated with evaporated silica (coating by Philips MiPlaza, Netherlands).

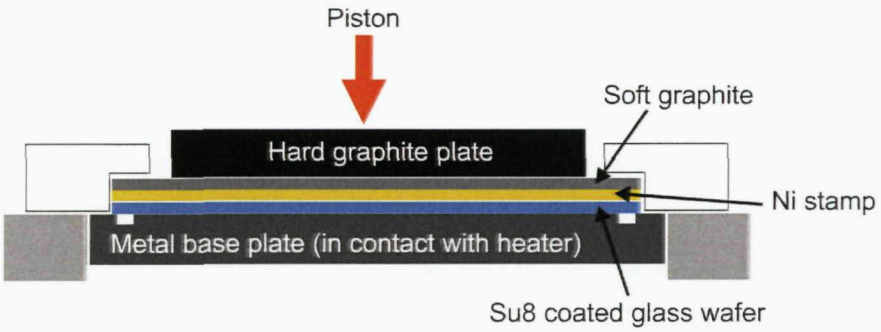

Figure 3.12: Schematic diagram of the stack layout for nano-imprint inside the wafer bonder. The substrate to be embossed is held on a flat plat which is heated to 95°C. The stamp is placed on top of the substrate, and two graphite layers are placed on top of the stamp to evenly distribute the force of the piston. The piston compresses the stack, thus embossing the substrate.

The imprint process was performed under vacuum in an EVG520 wafer bonder. A schematic diagram of the setup inside the bonder is shown in figure 3.12. The SU8 coated substrate is placed on a flat metal base plate which is in contact with a heating element, and the nickel stamp aligned and placed on top of it. A soft graphite plate and a thick hard graphite plate are placed on top of the stamp as a contact surface for the bonder piston, and to evenly distribute the piston pressure over the embossing stamp. The stack is heated to 95°C and the piston brought into contact with the graphite with a force of 1000 N (300 N from stack and 700 N from piston) and the force held for 5 minutes. Due to the raised temperature the imprint is performed at, this process is often referred to as 'hot embossing'. The whole stack including the base plate is then transferred to a mask aligner (EVG620) to expose SU8 with UV light for 30 sec (intensity 10.5-11.0 mW/cm2). The wafer is then baked together with the stamp on a hot plate at 95°C for 10 minutes. After that the wafer is cooled for 2 minutes and the stamp is removed using a knife. SEM images of the resulting gratings are shown in figure 3.13. The results show excellent fidelity with the original master, with the only significant imperfections in the grating structure being the imperfect reproduction of features below 160nm, which was seen on the master (such features are seen in figure 3.13(3).

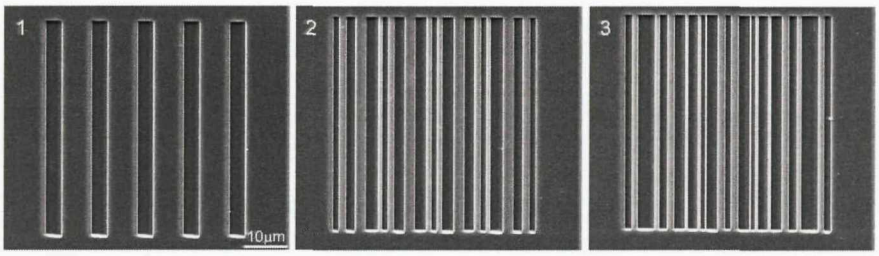

Figure 3.13: SEM images of single grating (1), 2× superimposed (2) and 3× superimposed (3) encoded tags on an SU8 film nano-imprinted using an electroformed nickel imprint master. All samples were coated with 5nm gold before imaging (images courtesy Dr. S. Banu).

3.2.4 Characterization of diffraction from nano-imprinted gratings

To be successful for high capacity encoding, the nano-embossed patterns must have diffraction patterns with characteristics that are similar to those described in chapter 2. That is they must have beam widths, higher order intensities and ghost order intensities close to those for the ideal case. In addition, the diffraction efficiency of the gratings, as considered theoretically in section 1.4.3, should be high enough that the diffracted first orders from the nano-embossed tags are easily distinguishable from any noise present.

The encoding capabilities of the nano-embossed SU8 patterns formed from both types of master were measured using the experimental system described in chapter 2. A helium-neon laser (wavelength $\lambda = 633$ nm) was focused by a lens (focal length f = 100 mm) onto sample plates containing a thin film of SU8 into which 50 × 50μm barcodes had been embossed using the methods described in section 3.2.3. The resulting diffraction pattern was projected onto a CMOS array camera.

The diffraction images recorded for an example set of 5 codes from the sample embossed using the SiC master, each with two superimposed gratings, are shown in figure 3.14. The tags have 2 superimposed gratings, with one pitch remaining constant while the other decreases moving from tag GF to KF. The naming conventions for the tag's code are the same as for figure 2.7. The first order diffracted beams, which constitute the code, are clearly visible and well defined. The figure shows that the code can be easily read by measuring the positions of the first order spots relative to the zero-order beam. The diffraction patterns obtained from the nano-imprinted codes, as shown in figure 3.14, are of high quality and appear

almost identical to those obtained using the gratings made from metal on glass by high resolution e-beam direct write (section 2.2.1).

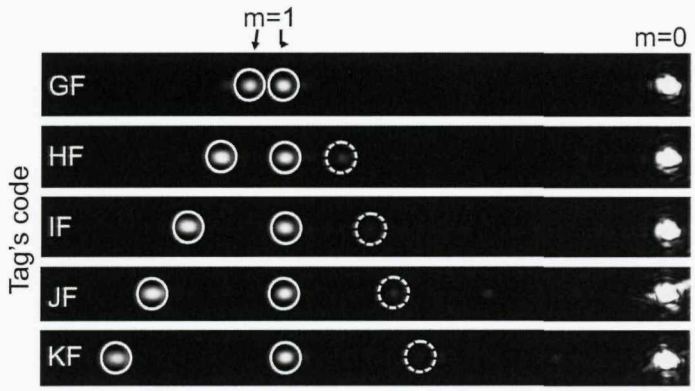

Figure 3.14: Diffraction patterns created by nano-imprinted SU8 tags containing two different gratings, fabricated using a silicon carbide imprint master. First order (m=1) beams are indicated by solid circles, while dotted circles enclose example ghost beams (described in section 2.3.2). Moving from top to bottom shows how a progressive decrease in the pitch of one of the gratings changes the diffraction pattern.

Similar example diffraction patterns from the SU8 tags imprinted using the nickel master are shown in figure 3.15. Figure 3.15(A) shows the diffraction patterns from and example set of 10 single grating barcodes. The pitch of the grating decreases from grating A to grating J. The naming conventions for the tag's code are the same as for figure 2.7. First order (m=1) beams are indicated by solid circles and second order beams by dotted circles. Second order beams are visible because these gratings have $a/(a-b) = 3$, in an attempt to minimise ghost order intensity relative to the first order intensity (see section 2.3.2 for more detailed discussion on this). Figure 3.15(B) shows the diffraction patterns from and example set of 10 tags containing two superimposed gratings. One pitch remains constant, giving a diffracted beam as for grating E in figure 3.15(A), while the other pitch decreases moving from right to left, producing diffracted beams in positions D to N. Both sets of diffraction patterns appear of high quality and similar to the diffraction patterns obtained from the metal-on glass gratings in chapter 2.

We can measure the widths of the diffracted first order beams from the nano-embossed gratings, and compare them to both the widths obtained from the metal-on-glass gratings, and the theoretically expected widths, as in section 2.2.3. The results for the tags created with the silicon carbide stamp are shown in figure 3.16. It

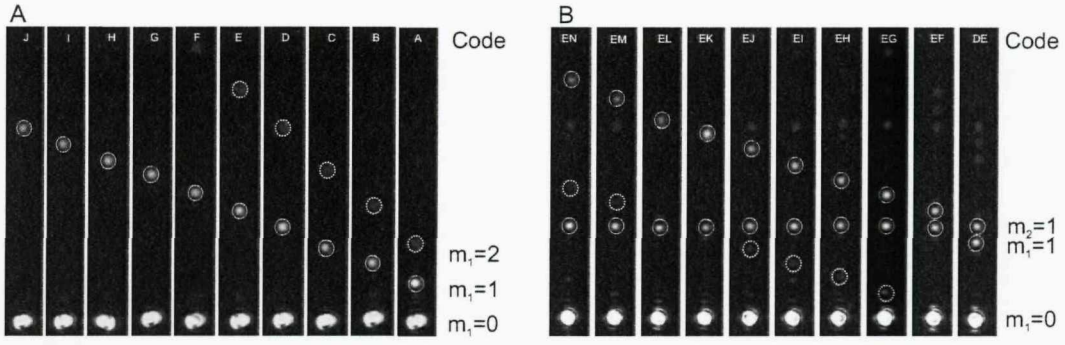

Figure 3.15: Diffraction patterns created by nano-imprinted SU8 tags fabricated using a nickelimprint master. Diffraction patterns created by a single grating tag (A), and tags containing two different gratings (B). Moving from left to right shows how a progressive decrease in the pitch of one of the gratings changes the diffraction pattern. First order (m=1) beams are indicated by solid circles, while second order (m=2) beams in (A) and example ghost beams in (B) are indicated by dotted circles.

can clearly be seen that the beam widths obtained from the nano-embossed gratings are comparable with those from the metal-on-glass gratings. Therefore, the possible encoding capacity of tags manufactured in this way is the same as those shown in figure 2.10. Measuring the intensities of the ghost beams (indicated by dotted circles in figure 3.14) in the regions away from significant other features in the diffraction pattern (as described in section 2.3.2), results in a mean value of of $I_g/I_1 = 0.19 \pm 0.05$. Comparing this to the theoretical value of 0.17 indicates that the ghost beams produced by the nano-embossed tags will successfully be discriminated in the reading process by the kind of threshold level presented in figure 2.15.

The measured beam widths for the nano-embossed SU8 tags created with the nickel stamp are shown in figure 3.17. The plotted points from the SU8 grating are the mean of measurements from the four repetitions of each tag on the master. Error bars indicate the standard deviation of the averaged measurements. Again, the beam widths are seen to be comparable to those measured from the direct-written metal-on-glass gratings, and therefore in a similar way the width increase is mostly due to inaccuracies in measurement of system parameters such as the grating to camera distance. The widths are also similar to those produced by the gratings manufactured using the SiC master, indicating that the nickel master produces similar quality grating profiles. In addition, the low intensity of beams from tags with more superimposed gratings makes the beam width difficult to estimate, causing increased scatter of the beam widths about the level expected due to beam divergence.

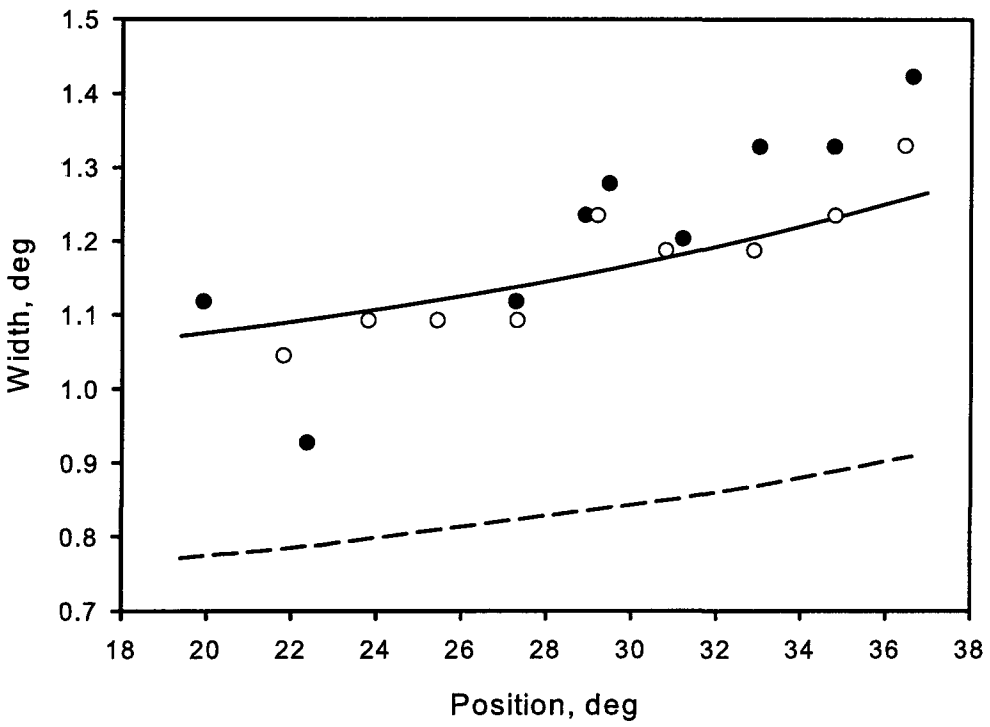

Figure 3.16: Measured beam widths at various angles for metal-on-glass tags (open circles) and nano-imprinted SU8 tags created by the SiC master(black circles), illuminated by a beam focussed with a lens of focal length f=100mm. The dashed line is a plot of theoretical beam width (as described in section 2.1.1) as a function of diffracted angle, for comparison with experimental measurements. Solid line shows fitted curve used to calculate encoding capacities.

The ghost intensities from an example set of SU8 tags containing 2 superimposed gratings were also measured, for comparison with the discrimination method given in figure 2.15. Figure 3.18 shows the ghost intensities from SU8 tags, together with similar measurements from the metal-on-glass tags. The solid line shows the discrimination level used to eliminate the ghost beams and second order beams from the diffraction patterns of the metal-on-glass tags. It is clear that this level successfully discriminates most of the ghost beams from the example SU8 tags. However some ghost beams are not discriminated. In addition, the measured mean value of the second order to first order beam intensity ratio I_2/I_1 is 0.31 ± 0.05, somewhat higher than the expected theoretical value of 0.25 calculated analytically for single gratings with the same aspect ratio as these tags (which have $a/(a-b) = 3$, see figure 2.13). Possible reasons for these higher intensities are considered later in this

section, by comparison to data from FFT simulations.

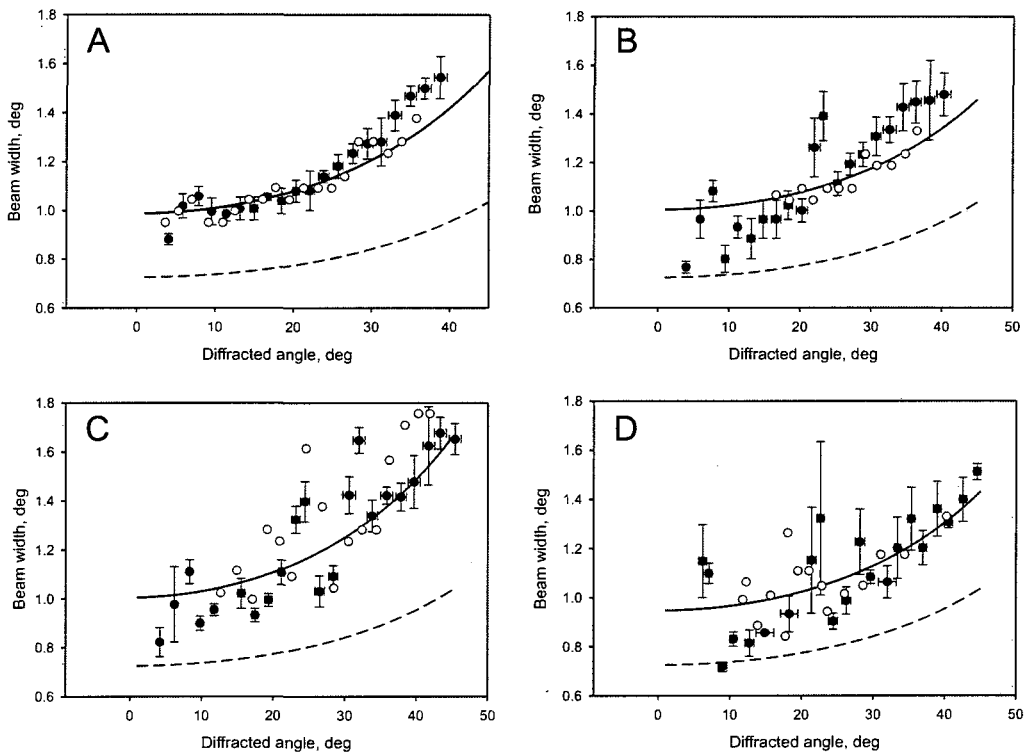

Figure 3.17: Measured beam widths at various angles for metal-on-glass tags (open circles) and nano-imprinted SU8 tags created by the Ni master(black circles) with a single grating (A), 2 superimposed gratings (B), 3 superimposed gratings (C) and 4 superimposed gratings (D) on the surface of the tag. The tags were illuminated by a beam focussed with a lens of focal length f=100mm. The dashed line is a plot of theoretical beam width (as described in section 2.1.1) as a function of diffracted angle, for comparison to experimental measurements. Solid lines show fitted curves used to calculate encoding capacities.

It is important to compare the data from gratings produced with the nickel imprint master to appropriate FFT simulations, in order to indicate the possible cause of differences from values of the diffracted intensities calculated using simple theory of single gratings. As part of this, the effect of manufacturing resolution on the diffraction patterns from the nano-imprinted SU8 tags is investigated. There are three limitations of the master manufacturing process that prevent perfect reproduction of the tags: the spot size of the e-beam write process (in conjunction with the chemistry of the resist), the ability of the plasma etching process to produce vertical sidewalls on the silicon features, and the ability of the nickel plating process to fill very small features with nickel. These effects stop features below a size limit (the manufacturing resolution limit - in our case approximately 160nm) being repro-

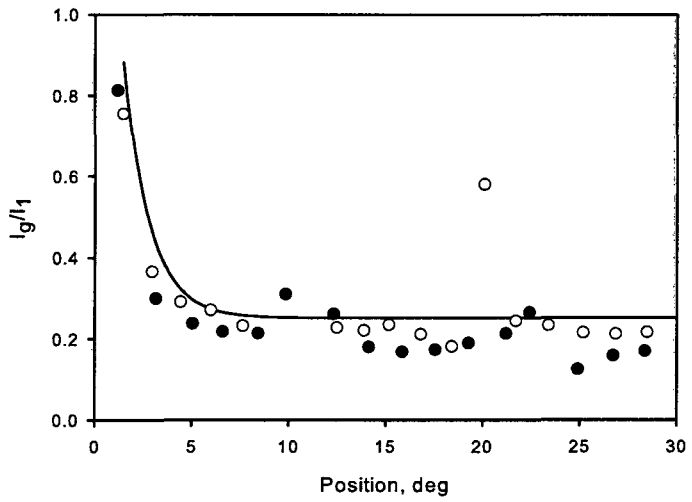

Figure 3.18: The intensity of ghost beams at various angular positions for example 2 times superimposed SU8 tags with $a/(a-b) = 3$ (black points), in a similar manner to figure 2.15. The solid line shows an example of a threshold which could discriminate such ghost beams. Example points measured from the metal on glass grating are shown for comparison (white points).

duced at all on the master. Evidence of this resolution limit affecting the pattern reproduction has already been seen in the SEM images in figure 3.10. Simulating the diffraction patterns of these gratings by FFT and comparing with simulations of perfect gratings, allows us to estimate the effect of limited manufacturing resolution on the grating diffraction patterns. In particular, we would like to investigate whether the variations in ghost and second order intensity observed above could be explained by manufacturing limitations, or whether they are expected from this type of phase grating even in the perfect case.

In order to characterize the quality of ridge depth (D) reproduction from the imprint process, the relative intensities of the zero and first orders were measured and compared to those from FFT simulations similar to those used to calculate figure 2.2. Since the dynamic range of the camera cannot simultaneously display the first and zero orders without the zero order being saturated, a standard silicon photodiode was used to measure the zero and first order intensities. The photodiode was attached to a goniometer centered on the nano-embossed grating sample, enabling it to be moved in an arc over the grating's diffracted angular spectrum. After measuring the zero and first order beam intensities, we need to take account of the extra intensity that will be present in the experimental zero order, due to the fact that

the illuminating spot is 150μm in diameter, compared to the grating dimensions of 50 x 50μm. The half-angle divergence of the illuminating beam (0.49°) is less than the angular half-width of the zero order (0.73°), so that only the zero order intensity is affected. To take account of this, the FFT simulations can be adjusted so that the illuminating light is a Gaussian beam of the appropriate size, rather than a uniform intensity illumination covering only the grating, as used in section 1.4.3. The simulations are performed in 2D, and the diffracted order intensities are summed between the intensity minima surrounding them, in order to correspond to the intensities measured experimentally. For the samples obtained from the SiC stamp, we get a value of $I_0/I_1 = 26.7 \pm 7.5$ which, after taking the extended illumination beam into account, equates to a ridge depth D of $D = 646 \pm 64$nm. From SEM images (taken looking along the ridge of the embossing master), the value of D for the master was directly measured to be $D = 650 \pm 50$nm. We therefore have the expected ridge depth reproduced on the grating surface.

Surface thickness variation affects both the embossing depth and stray light scattered from the surface, resulting in variation of the value of D calculated from the diffraction patterns. Similar measurements of I_0/I_1 for single grating tags embossed from the nickel master yields a value of 6.94 ± 0.77 which is equivalent to an embossing depth of 850 ± 50nm. Direct measurement of the depth from SEM images gives an embossing depth of 890 ± 50nm. It is clear from these measurements that the gratings diffract as expected for their actual embossed depth, but that the master production processes are not capable of producing the required depth (600nm) with very great accuracy. However, the values of I_0/I_1 are sufficiently low for our purposes, allowing the grating to be easily read on the camera used in our system.

In order to characterize the effect of manufacturing resolution on diffraction from phase gratings, FFT simulations of the diffraction patterns were calculated for tags, with all features below 160nm in size removed. Figure 3.19 shows some example diffraction patterns obtained from simulations of perfect and manufacturing-affected gratings. The diffraction pattern from 3x superimposed tag with 160nm resolution shown in figure 3.19(A), appears almost identical to the perfect case shown in figure 3.19(B). Unwanted beams in both cases can be discriminated by a threshold of the form described in section 2.3.2. As the number of superimposed gratings increases, the effect of manufacturing becomes more pronounced, until patterns such as that shown in figure 3.19(C) start to be produced from 5x superimposed gratings. This diffraction pattern appears very different from the perfect case shown in figure 3.19(D), and unwanted ghost beams can no longer be discriminated by the threshold

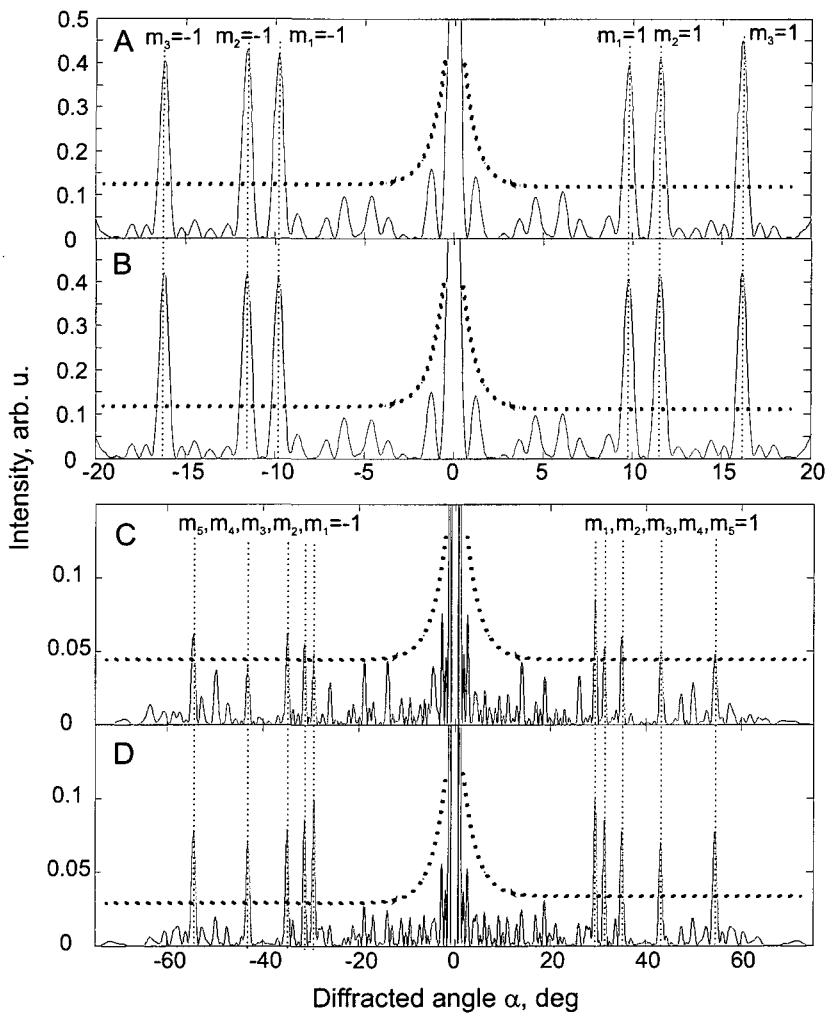

Figure 3.19: Example of simulated diffraction patterns, illustrating the effect of manufacturing limitations. For an example tag, with 3 superimposed gratings, the effect of manufacturing leads to small difference (A) from the perfect case (B). Unwanted beams in both patterns may be discriminated by a threshold of the form described in section 2.3.2 (bold dotted line). As more gratings are superimposed, the negative effects of manufacturing get more pronounced, until most 5x superimposed tags such as the example shown in (C) give very different patterns to the perfect case (D), and a threshold that discriminates ghost beams in (C) (bold dotted line) also eliminates some first orders.

method without removing some first order beams as well.

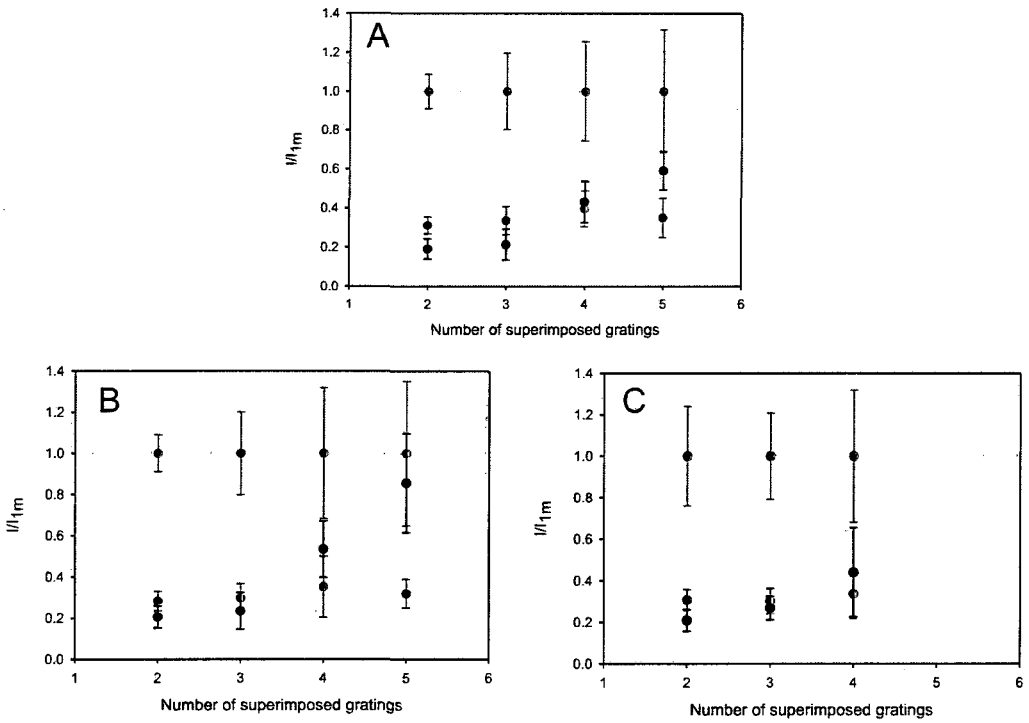

Figure 3.20: The mean values over 25 tags of I_2/I_1 (green points) and I_g/I_1 (black points) for diffraction patterns from simulated perfect tags (A), simulated tags affected by a manufacturing resolution of 160nm (B) and experimental nano-imprinted tags manufactured with the nickel imprint master (C), for different numbers of superimposed gratings. The grey points show the fluctuation of the first order intensity relative to the particular reference first order used for the ratios. Error bars give the standard deviation for each point.

A more detailed simulation of 100 tags (25 each of 2, 3, 4 and 5x superimposed tags) was undertaken to estimate the first order intensities and the ratios I_g/I_1 and I_2/I_1 for tags with an embossing depth of 850nm in air. All tags had one fixed pitch of 3.81μm; the 3, 4 and 5$\times$ superimposed tags, in addition had one fixed pitch of 2.91μm; 4 and 5$\times$ superimposed tags had an additional fixed pitch of 2.11μm; and 5$\times$ superimposed tags had an additional fixed pitch of 1.58μm. All remaining, non-fixed pitches had values which produced diffracted first orders at 25 different positions, spaced by twice the angular width of the diffracted beams, beginning at two beam-widths angular offset from the zero order. All pitches are additionally chosen so that no high intensity ghosts are produced (see section 2.3.2), as such tags would not be used for encoding anyway. The mean first order intensity I_{1m} for each tag was used as a reference intensity for the calculation of I_2/I_{1m} and I_g/I_{1m} for

each tag, which are shown by the green and black points respectively in figure 3.20.

The resulting mean values of I_g/I_{1m} (black points) and I_2/I_{1m} (green points) for tags with 2, 3, 4 and 5 superimposed gratings are shown for perfect tags in figure 3.20(A), and tags with a manufacturing resolution of 160nm in figure 3.20(B). The relative intensity of all other first orders on each tag to the reference first order was also measured, and the mean values of these are shown by the grey points in figure 3.20. The standard deviation of each value, given by the error bars on each point, shows the fluctuation of all the first order intensities about the mean value. We can see that, even for the perfect case, there are fluctuations of all orders, due to the interference of the features from each each individual grating on the tag. These are appear a result of the particular multiplicative encoding method used in this work and, as discussed in section 2.3.2, they magnitude of these fluctuations could be reduced by optimising the relative positions of the superimposed gratings with respect to ecah other, and thus the relative phase of the interfering components. This fluctuation of order intensity appears to become larger with more superimposed gratings, due to the greater probability of features being in proximity, and the larger number of ghost beams.

The values in figure 3.20(B), when compared to those in figure 3.20(A), give an idea of the effect of manufacturing resolution on the tag diffraction patterns. While tags with 2 and 3 superimposed gratings experience very little change due to the limited resolution, those with 4 and 5 superimposed gratings are affected much more dramatically. In general it would appear that more superimposed gratings results in smaller features on the tag and hence a greater effect from limited manufacturing resolution. However, the fluctuations due to the encoding method still appear to be the major limiting factor. The experimental values for 20 tags each with 2, 3 and 4 gratings superimposed on the surface, measured from SU8 tags imprinted using the nickel imprint master, are shown for comparison in figure 3.20(C). As an example, comparing the experimental value of ghost beam $I_g/I_{1m} = 0.21 \pm 0.05$ for a 2 x superimposed tag with the resolution-affected value of $I_g/I_{1m} = 0.20 \pm 0.05$, indicates that the experimental value is in fact exactly as expected. Similarly, there is good agreement between the experimental value of $I_2/I_{1m} = 0.31 \pm 0.05$ and the resolution-affected value of $I_2/I_{1m} = 0.27 \pm 0.05$.

The data from figure 3.20 allows us to estimate how effective the threshold method will be at eliminating the unwanted beams from both perfect and manufacturing-limited tags, which is the reason for measuring the relative intensities of various features of the tags' diffraction patterns. Using the data from the experimental

tags, we can discriminate the higher order beams from tags with 2 or 3 gratings on the surface successfully using a threshold placed at $I/I_{1m} = 0.5$ which is greater than 2.57σ from both the mean first order and mean second order values of I/I_{1m}. Here, σ id the standard deviation of the order intensity, and 2.57σ encompasses 99% of values. Thus we have a 0.5% probability of either a second order or first order crossing the threshold for any one tag. For tags with 4 gratings on the surface, the threshold needs to be at $I/I_{1m} = 0.62$ which is greater than 1σ from both ghost order and first order mean values. This leaves us with a 15% probability of any one tag having an order which crosses the threshold. However, due to the good agreement between the resolution affected simulation and the experimental values, it may be possible to identify the 15% of gratings which lie in this region, and discard them from the set used for encoding. Further investigation needs to be performed to determine whether this is really the case. Looking at the data from the manufacturing-affected simulations, we see that the range of values for ghost and first order beams on 5x superimposed tags coincide extensively. Thus, using an embossing technique with 160nm resolution, we have an absolute limit of 4 superimposed gratings on a tag if tags which cannot be differentiated by the threshold method can be eliminated by simulation, otherwise the limit is 3 superimposed gratings. These limits only apply to the particular multiplicative encoding scheme used here, and phase optimisation (as discussed in section 2.3.2) or alternative encoding methods (such as those reviewed in section 2.1.2) would increase this limit, allowing for higher encoding capacities.

At the end of chapter 2, it was briefly mentioned that the limit on superimposing depends on the obtainable SNR ratio in the tag diffraction patterns. These results indicate real world SNR for this encoding technique of greater than 2 for tags with up to and including three superimposed gratings. For tags with 4 superimposed gratings, 15% of the tags have an SNR less than 1, which marks the point at which some tags cannot be read reliably. Thus we have a limit of 3 superimposed gratings for which all tags have a SNR of greater than 1, and may be reliably read.

3.2.5 Limits on observable diffraction angle

In most real systems (as decribed insection 3.3.2, glass-air interfaces will be present, limiting the observable diffracted angles to around 43°, due to total internal reflection. Figure 3.21 illustrates the encoding capacity for 1-dimensional tags in the system described so far, taking into account real beam widths, the limit of 3-

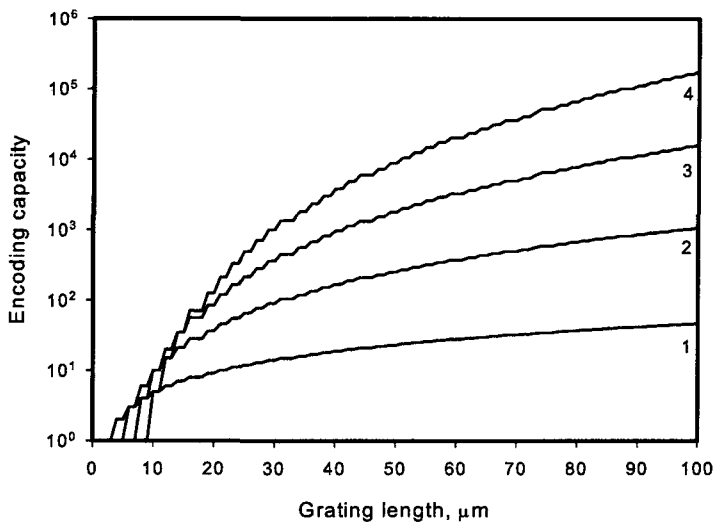

Figure 3.21: Encoding capacity of a 1-dimensional diffractive bar-code tag as a function of the length of the tag for different numbers of superimposed gratings, limited by real beam widths, superimposing limits due to manufacturing and glass/air interfaces. The number on each curve corresponds to the number of superimposed gratings. The 'stepped' appearance of these curves is due to truncation of diffracted beam angles at 90°, as explained in section 2.1.1.

4 superimposed gratings (depending on factors considered in section 3.2.4) which can be distinguished by the threshold method and the 43° diffraction angle limit. This leaves us with capacity for approximately 10^4 codes on a 100μm 1-dimensional 3x superimposed grating. Assuming the same superimposing limit applies to 2-dimensional gratings (although nano-imprinted 2D gratings have yet to be tested), we expect to obtain around 10^8 unique codes on a particle 100 $\times$ 100μm square. These capacities compare reasonably well with the quoted capacities for many of the graphical encoding technologies considered in chapter 1 (which demonstrate capacities of the order of 10^6 codes). However, the graphical encoding technologies have the potential for the number of available codes to be extended to much higher numbers. Therefore, the next chapter will consider a method for which very high encoding capacities are more realistically achievable.

3.3 Reading superimposed grating tags

In order to analyse diffractive tags in a microfluidic system, we need a stable automated reading algorithm that will identify the codes from their diffraction pattern.

In order for such a system to work we need to consider an important effect which we have not covered so far; that tagged particles may not be perfectly oriented with respect to the reading beam. We will then consider the hardware and software required to implement the automated reading of diffractive tags.

3.3.1 Reading misaligned tags

The analysis given so far assumes normal incidence of the reading beam on the tag. In practical chemical and biological implementations these tags will be read in microfluidic devices, where perfect alignment may not always be possible. We therefore have to consider whether we can still recover the pitches on a tag if it is at some non-normal orientation with respect to the reading beam. A tag can rotate about three possible axes, as shown in figure 3.22(A), from which we define three rotation angles η, θ and γ. Non-normal incidence requires a modification of the diffraction equations, so that a beam at diffracted angle α to the z-axis (see figure 3.22(A) for axis definitions) satisfies $a(\sin\eta\cos\theta - \sin(\eta+\alpha)) = m\lambda$. (for derivation, see appendix B), resulting in a distortion of the diffraction pattern.

The results of calculating the diffraction patterns modified by tag rotation are shown in figure 3.22(B, C and D). A grating with a 1μm pitch is chosen to show the variation of α for example $m = +1$ and $m = -1$ orders, due to rotation η (figure 3.22(B)). Rotation by angle η produces reduction of α on one side of the $m = 0$ beam and an increase on the other: this increase in alpha could eventually cause the diffracted first order to move outside the $\pm 90°$ detection range, if η becomes very large. For the other two rotation axes, the diffracted spots change position, but α remains constant. The modified patterns produced by rotations γ and θ have diffraction angles α which are no longer completely in the x-z plane, so we define α_x and α_y to be the diffracted angles seen in the x-z and y-z planes, respectively, in order to show how the pattern appears in angular space. The large dots in figure 3.22 (C and D) show how the first order beams from an example 1μm pitch vary due to these rotations. The small dots are plots of beams with values of α between zero and 90°, in steps of 2°, and illustrate the shape of the modified diffraction patterns over a wide angular range. The open circle in figure 3.22(C and D) shows the position of the $m = 0$ beam. The pattern in figure 3.22 (D) represents how the pattern appears on a flat plane a distance z from and parallel to the unrotated grating (such as the camera sensor in a real system). It is the fact that the rotation θ transforms the grating into a different plane no longer parallel to the observation

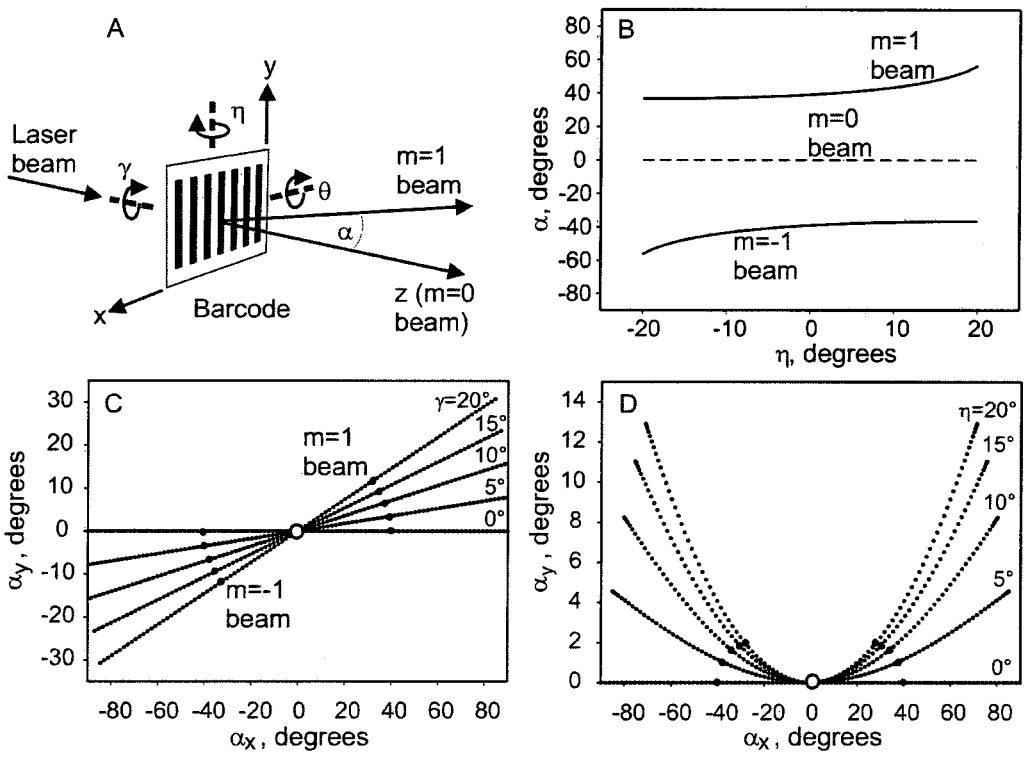

Figure 3.22: Diffraction pattern distortions produced by tag rotation. A) The coordinate system used for distortion analysis. B) Variation of diffracted angle α for example $m = +1$ and $m = -1$ orders from grating with $a = 1\mu$m, due to the rotation η. C) Variation in diffraction pattern orientation for selected values of γ (given above corresponding curve). D) Variation of diffraction pattern shape for selected values of θ (given above corresponding curve).

plane, together with the fact that the observation region is flat and not spherically curved, which introduces the diffraction pattern curvature seen in figure 3.22 (D).

It is, however, still perfectly possible to recover the pitch of a grating from a pattern distorted by tag rotation. To do this, we need to remove the unknown $\cos\theta \sin\eta$ from the diffraction equation. We can do this by measuring the absolute angle of both the $m = 1$ and $m = -1$ diffracted beams with respect to the zero order, denoted α_1 and α_2, respectively. The pitch of the grating can then be reconstructed using

$$a = \frac{2\lambda}{\sin\alpha_2 - \sin\alpha_1}, \tag{3.1}$$

thus the tag can still be identified.

Having described a method for coping with rotation of the tag, it should be

pointed out that extreme rotation angles are not expected. There are alignment electrodes in a microfluidic system, as described in section 3.1, whose purpose is to keep the rotation of encoded particles as small as possible.

3.3.2 Reading system hardware - parameters and limitations

An outline of the hardware used to develop the tag reading system is shown in figure 3.23. A helium-neon laser (wavelength = 633nm) is focused by a lens (focal length f = 100mm) onto a sample plate containing 50 x 50 μm tags. The resulting diffraction pattern is projected onto an 8-bit (256 gray levels) CMOS array camera. The camera streams images through a firewire interface to dedicated reading software, which analyses the diffraction patterns and reads the code on the tag. The code is then stored in a database, and/or output to the user interface. A full microfluidic system would contain additional PC inputs and outputs for reading of the tags' fluorescence and operations such as automated sorting of the tagged particles. Additional optics and laser sources would also be required for fluorescence observation. These extra considerations, however, fall outside the scope of this thesis. To simulate a flow system for the development of the reading software, the metal tags on a flat glass substrate were moved through the reading beam by translating the substrate using an automated, computer controlled translation stage.

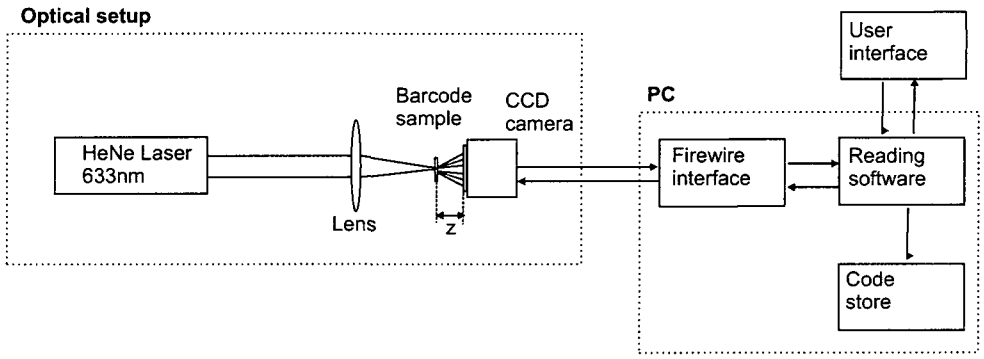

Figure 3.23: An outline of the hardware system used to read superimposed diffraction grating tags.

The optical setup for illuminating the gratings is conceptually very simple, although some component parameters had to be carefully chosen. The wavelength of the reading laser (633nm) is that which was used in the design of the tags. The

focal length of the lens used to illuminate the gratings determines the spot size of the illuminating beam, but also the beam's divergence. A spot approximately the size of the grating is useful in order to keep the zero order intensity to a minimum, as any light which goes around the grating is not diffracted and so adds to the zero order intensity of the tag diffraction pattern. However, a smaller spot has a higher beam divergence which, as explained in section 2.2.3, increases the width of the diffracted first orders, thus reducing the tag encoding capacity. Therefore, the lens chosen must be a compromise between the short focal length required for small spot size, and the longer focal length required for low beam divergence. The chosen focal length of 100mm, producing a spot approximately 3 times the size of the grating is good compromise, keeping a large encoding capacity available (figure 2.11), whilst also allowing gratings to be read without problems caused by the zero order.

The camera used for imaging the diffraction patterns produced by the diffractive tags is the Prosilica EC1280. This camera uses 2/3" 1280 x 1024 8-bit (256 gray levels) CMOS array sensor with anti blooming ground, which is necessary in order to reduce leaking of signal from high intensity pixels into neighbouring pixels. In particular, as described in section 3.1, this reduces spreading of the high intensity zero order over the rest of the diffraction pattern. In addition, it has a multiple slope gain profile for different intensities, integrating low intensity parts of the signal for longer than high intensity parts, which in our case would lead to enhancement of the code beams in the diffraction pattern and reduction of the zero order. The sensor is essentially made of an array of individual diodes, allowing readout from user-definable sections of the sensor, without reading the rest of the pixels, allowing increased frame rates if the diffraction pattern can safely be assumed to be a certain size (for example if only tags producing beam within a certain diffracted angle are in use). The frame rate of this sensor varies from 25fps (full frame) to 120fps (640x480 section of full frame), adequate for readout of many assays. Larger assays may require more sophisticated high speed cameras.

The camera still exhibits some blooming, which together with scattered light from the zero order results in some background noise on the diffraction pattern images. This background light becomes more of a problem with an increasing number of superimposed gratings on the tag. A 1-dimensional tag with n_g superimposed gratings has a first order I_{n_g1} to zero order I_{n_g0} intensity ratio of $I_{n_g1}/I_{n_g0} = I_1/I_0{n_g}^2$, where I_1/I_0 is the ratio for $k = 1$. For a 2-dimensional tag, this ratio becomes $I_{n_g1}/I_{n_g0} = I_1/I_0 n_{g_x}^2 n_{g_y}^2$. As a result, the intensity of the background noise eventually becomes comparable with the first order intensity. The point at which this

happens depends a lot on the system: in our case the superimposing limit is $n_g \simeq 6$ for 1-dimensional tags and for 2-dimensional tags $n_g = n_g \simeq 4$, with square tags of side length 50μm. These limits are higher than the actual limit on superimposing due to the encoding method (see section 3.2.4, of $n_g = 3$, so they have no effect on the real SNR which limits the number of possible superimposed gratings. However, this noise still affects the accuracy with which beam positions and widths can be determined during the reading process even for $n_g = 2$ and $n_g = 3$. The problem may be solved to an extent by making use of the fact that once the position of the zero order has been calibrated, it no longer needs to reach the camera. Therefore a spatial filter consisting of a spot at the size and position of the zero order may be used to prevent the zero order reaching the camera surface, thus reducing problems caused by it.

To obtain the Fraunhofer diffraction pattern on the camera [44], the distance z between the grating and the camera sensor should be greater than 3mm, as discussed in section 3.1. The camera sensor can therefore not be directly attached to the microfluidic chip, which would place it only a few hundred μm from the diffraction grating, but must be outside the chip. This is therefore likely to place a severe limitation on the encoding, in that there will be glass/air interfaces between the grating and the camera, which would limit the diffraction angles to less than 43°, due to total internal reflection. It could be possible to have a cell of index matching oil between the microfluidic chip and the camera, to help reduce this angular limitation on the encoding technique.

3.3.3 Reading software algorithm

A flow diagram of the reading software is shown in figure 3.24. The software was written in MATLAB in order to test the algorithm, resulting in approximately 1 second for the reading of a single frame on a single 2.8GHz processor PC with 768MB RAM, running Microsoft Windows XP Professional. Much faster implementations for the actual flow system would be obtained by using a lower-level language such as C++, although the principle of the algorithm remains the same for all languages.

An example of the results of some of the steps in reading a single grating tag with period $a = 5.6\mu$m is shown in figure 3.25 for visualisation purposes. Initially (step 1), before any tags enter the reading beam, the position of the zero order is calibrated by the user. The incident laser beam is intense enough to saturate the camera, when it is set up for reading tags. Therefore, the zero order position may

be found by using a 'centre-of-mass' method [94], to find the centre point of all saturated pixels. This method takes the coordinates x_i and y_i (coordinates defined in figure 3.25 (A)) of each saturated pixel and works out the coordinates (x_0, y_0) of the central position of all n saturated pixels as $x_0 = \sum x_i/n$ and $y_0 = \sum y_i/n$. Once the position of the zero order has been found and stored, the movement of tags into the reading beam starts. As a tag moves into the beam the intensity of its diffraction pattern increases to a maximum as it becomes centred on the beam, and then decreases. The diffraction pattern at the maximum intensity point is taken from the camera stream to be analysed for reading of the code, and thresholded (step 2) to remove unwanted beams (as described in chapter 2).

Intensity profiles of each horizontal line of pixels are taken (examples shown in figure 3.25 (B & C), respectively) and smoothed using a moving average filter [94] (step 3). The peaks in each profile are located by finding points at which the second differential is negative (steps 4-7). Differentials are approximated using the difference in intensity of each pair of neighbouring pixels. The width of each peak is taken as the distance between the zero values on either side of it; other peaks within this width are taken to be from the same diffracted spot and are labeled as such (steps 8-10). The central peak belonging to a particular spot is found by the centre of mass method, and taken as that particular spot's position (step 11). The software now has the position of every diffracted spot on the camera surface and its distance r from the zero order (figure 3.25 (D)). If there are only 2 spots in the diffraction pattern, the diffracted angle of each is calculated as $\alpha = \arctan(r/z)$, using the pre-measured distance z between the grating and the camera sensor surface. From this the pitch associated with the spot pair is calculated and the code on the tag recovered from a look-up table (steps 12, 13 and 19).

If there are more than 2 spots, once the spot positions have been obtained, the nearest 4 to the zero order are found (steps 12 and 14). The software then needs to take account of a particular problem, associated with the diffraction pattern distortions due to tag rotation described in section 3.3.1. The problem is illustrated in figure 3.26; when the diffraction pattern of a 2-dimensional tag becomes distorted by tag rotation, the spots move away from the x and y axis of the camera. Therefore, the algorithm has to correctly associate the diffracted spots with the appropriate axis, otherwise the 2D tag will be read incorrectly. For an example pattern shown in figure 3.26 (B), figure 3.26 (C) shows the effect due to rotation η (θ gives the same effect, but rotated by 90°), figure 3.26 (D) the effect due to γ and figure 3.26 (E) the effect due to a combination of all three rotations. In all cases, a pair of spots

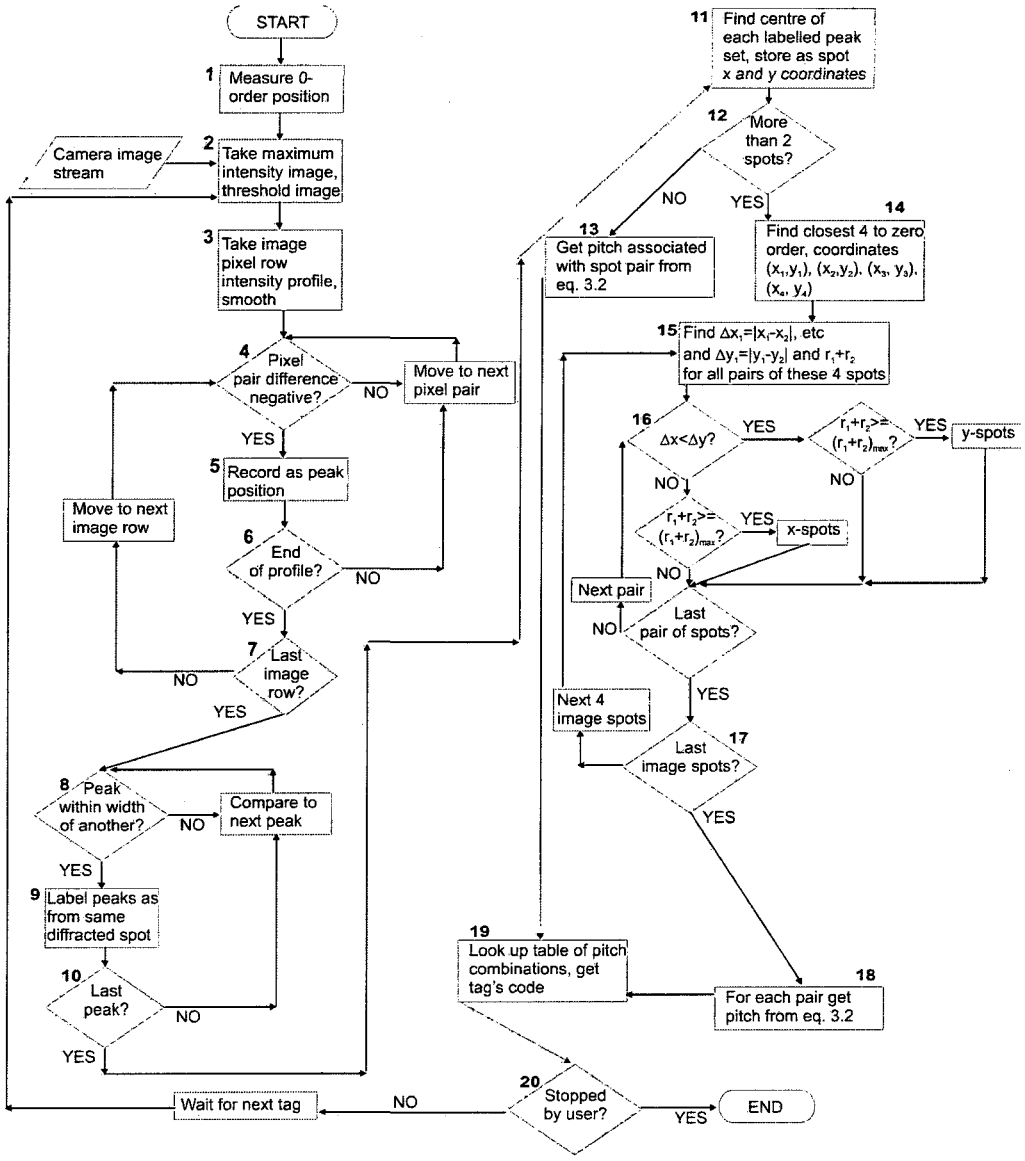

Figure 3.24: An outline of the software algorithm used to analyse the diffraction patterns from superimposed diffraction grating tags, and reconstruct their code.

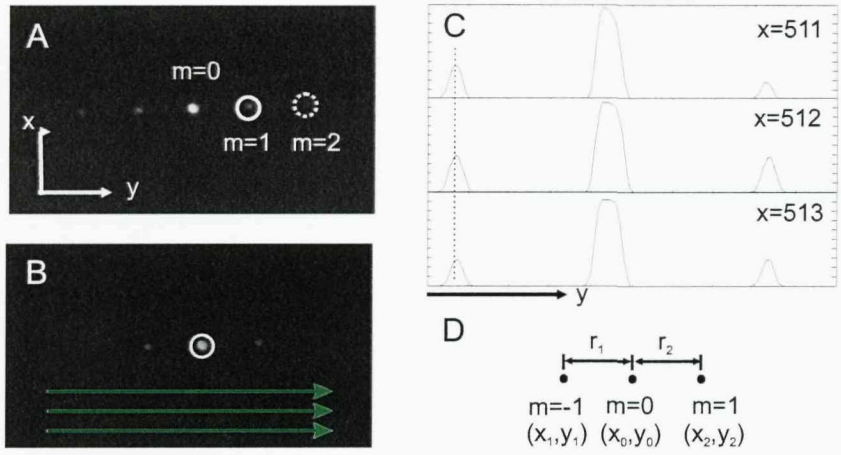

Figure 3.25: (A) A diffraction pattern from a single-grating tag with period $a = 5.6\mu$m, showing the zero ($m = 0$), first ($m = 1$) and second ($m = 2$) order diffracted beams, and image coordinate axis definitions. (B) The diffraction pattern after thresholding to remove the second order beams. The image is scanned to obtain an intensity profile of each image line. (C) Example profiles of 3 image lines on the diffraction pattern. The intensity peaks are identified by differential methods. (D)After step 6 of the algorithm, the software has data on the zero and first order positions. Their separations r_1 and r_2 can be used to reconstruct the grating pitch.

with $\Delta x < \Delta y$ are associated with the y-axis of the tag, and vice-versa (as long as $\gamma < 45°$) and so the spots can be associated with the correct pitch directions on the 2D tag (step 7, figure 3.24). Thus by calculating Δx and Δy for all possible pair combinations of the four spots, we can associate each pair with either the x or y axis. Out of the spots associated with each axis, the actual spot pair that constitute the code is the one that has the maximum distance $r_1 + r_2$ between the two spots. This process is repeated for the next closest spots, until all the spots have been considered (steps 12 and 14-17). The value of the diffracted angle $\alpha = \arctan(r/z)$ for each spot in a pair is then calculated using the pre-measured distance z between the tags and the camera surface. The pitches are recovered from the values of α for each spot pair, using equation 3.1 (step 18). The combination of pitches obtained for the tag is then compared to a look up table of all pitch combinations and their associated codes, and hence the code on the tag is recovered (step 19).

The user may then stop the reading if required (ie at the end of the sample) (step 20). If the process is not terminated by the user, the algorithm then waits for the next tag to enter the reading beam, before repeating the whole reading process.

To estimate the error rate of the reading algorithm, a selection of 10 tags, all

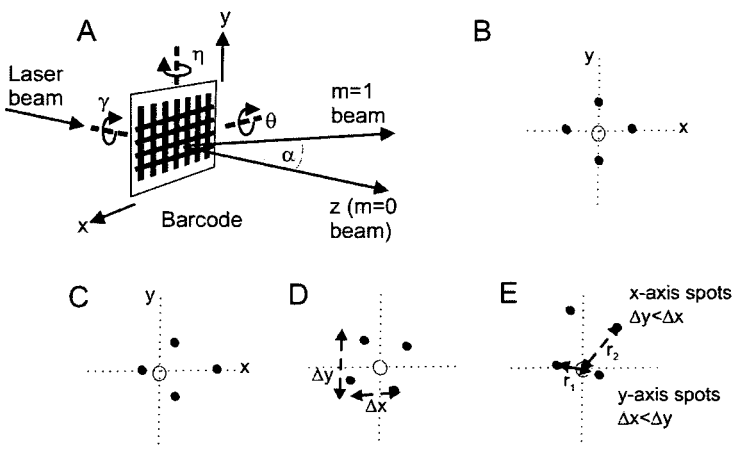

Figure 3.26: Diffraction patterns from a 2-dimensional tag with one grating in each of the perpendicular directions. (A) definitions of the coordinates and rotations used, relative to a 2-dimensional tag. The pattern in (B) has been distorted by rotations η (C), γ (D) and all three rotations (E), causing the spots to move away from the x and y axes of the camera (dotted lines, all parts of figure). The spots can be associated with the correct axes by comparing the quantities Δx and Δy (examples shown in (D)), and r_1 and r_2 (examples shown in (E)).

with first order diffracted angles less than 20°, on a flat substrate were moved past the reading beam on an automated translation stage. The test was performed under no rotation, as rotation is rather difficult to achieve for a large flat substrate containing tags when moving the substrate in this fashion. As each tag was read, it was compared to the tag that should have appeared at the current position of the translation stage's motion. This was repeated 20 times for the 10 tags with no reading errors (out of a total of 200 reads), giving an error rate for the algorithm of 0% under these conditions. As an additional test, a single tag with one 1-dimensional grating on the surface was rotated through all rotation angles by up to 20° for which the algorithm was still correctly able to identify the tag.

3.3.4 Additional error considerations

The reading algorithm above has no error detection/correction implemented for reduced reading error in non-ideal situations. Here sources of reading error that might occur in a real system are briefly considered, together with methods to improve reading accuracy in the presence of such error sources. The first thing to consider is what kind of errors may appear in the reading process, and are they detectable? The

main sources of errors will be stray scattered light from, for example, contamination in the tag's environment. These may form spots on the camera surface which are bright enough to be detected by the reading software even after image thresholding. These could then be marked as first order spots, causing a misreading of the tag. The simplest way to detect whether there are any such spots in the diffraction pattern image is to use the symmetry characteristics of the diffraction pattern; all first orders should have a corresponding pair on the other side of the zero order. Therefore, if there are an odd number of spots, the tag has been read incorrectly, and an error warning can be flagged. Since the problem could occur on both sides of the zero order, a more robust method could be implemented, such as designating one order as an error check, indicating the parity of the code orders.

One advantage that diffractive tags have over all other tag techniques, is that a single code is fundamentally based on the periodicity of the pattern on the tag's surface, rather than the entire structure. Theoretically, then, if a small portion of the tag breaks off (for example during mechanical steps of the chemical processing, such as centrifuging), the code should still be readable. However, if a tag breaks, its length decreases and hence the width of the diffracted beams becomes larger. A certain amount of redundancy then has to be encoded into the tags, by spacing the beams out more, to take into account a certain fraction of the tag being removed. This is done by effectively encoding for a reduced length, lowering the encoding capacity. If breakage occurs reasonably infrequently (for example a few percent of tags) then it may not be worth redundantly encoding. Instead it is accepted that some tags, particularly superimposed tags with beams close together in diffracted angle, will have the possibility to be read incorrectly due to breakage.

3.4 Biological assays with diffractive encoding

The use of diffractively-encoded SU8 particles in real biological assays was recently demonstrated by members of the 4G group [95]. The results from these assays allow us to give an estimate of the number of replicates of each code that must be read in a real biological experiment, and thus the total number of particles that actually have to be included in a real assay experiment. Two types of biochemical assays were performed using diffractively encoded microparticles, by Joseph K. She, Graham R. Broder and Dr. Rohan T. Ranasinghe. The first was a multiplexed DNA hybridisation assay performed using sequences corresponding to a polymorphic locus (N1303K) on the gene encoding the cystic fibrosis transmembrane conductance

regulator (CFTR) protein [96]. This assay aims to identify the single-base mutation (single-nucleotide polymorphism or SNP) that identifies cystic fibrosis. Two codes, identified as 2 and 3, were used in this experiment. Wild type (non-diseased) sequence P2 was bound to code 3 and the mutant sequence, P1, differing by a single nucleotide, was attached to code 2. A hybridization to the complementary strand to P" was then performed. The particles were assayed using conventional flow cytometry. Sorting on the basis of the fluorescence signal, followed by decoding of a representative sample of particles (50 from each fraction) showed that the hybridised population consisted of 96% code 3, with the unhybridised population B consisting of 96% code 2. The mean fluorescence of the mismatched and complementary particles is shown in figure 3.27(c). These results demonstrate that the use of diffractively encoded microparticles permits discrimination of a single mismatch from a Watson-Crick base pair within a short DNA duplex, enabling their use in SNP genotyping applications.

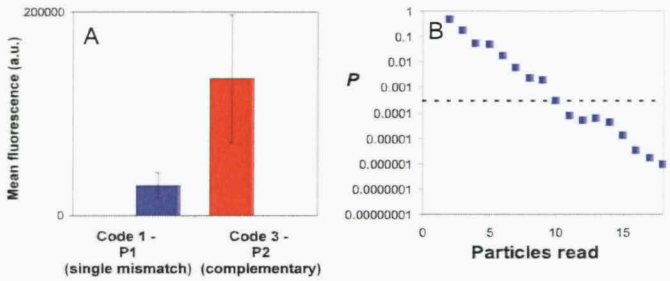

Figure 3.27: Mean fluorescence intensities with standard deviations for representative positive (complementary labelled oligonucleotide present) and negative (complementary labelled oligonucleotide absent) particle sets functionalised with different probes (A) and cumulative P values from positive datasets plotted against read number (B). The 0.03% probability that the difference in mean fluorescence of positive and negative populations could arise by chance is shown by the horizontal dotted line in and B (figure courtesy Dr. R. T. Ranasinghe).

A t-test was used to compare the difference between negative and positive datasets from the DNA hybridisation assay. Cumulative probability (P) values from three positive datasets are plotted against number of particles read, figure 5b and 5d. As expected, as more particles are read, the value of P falls, indicating greater confidence in the difference between datasets. After reading 11 particles, the probability of any of the positive datasets being indistinguishable from the negative dataset is < 0.01 and after reading 16 particles, the probability is < 0.0003. Therefore for

multiplexed platforms where thousands of molecular interactions are assayed, measurement of 15-20 replicates is necessary to satisfy a confidence level of $> 99.97\%$. This level of degeneracy is greater than that necessary for ELISAs, but is comparable to that used in Illumina BeadArrays where 30 replicate beads are used for each oligonucleotide to enable averaging and thorough statistical analysis of results [97]. The degeneracy requires that each coded particle appears in the assay at least 15 times, thus increasing the number of particles that have to be analysed, compared to a single reading of each code.

Having to read this number of replicates for each code obviously has implications for the practical realisation of highly multiplexed assays. Taking the outside range of the number of each code needed to give a $> 99.97\%$ confidence that the code has been assigned the correct judgement on the presence or absence of the fluorescent hybridisation indicator, we need to read 20 times as many codes as the multiplexing level of the assay. Considering, for example, an assay containing 10,000 unique codes, which is obtainable on a 3x superimposed particle 100μm long, 200,000 particles are required to gain the required confidence interval in the fluorescence identification. Assuming the particles are $50 \times 100\mu$m, giving the rectangular shape required by the microfluidic system, the total area of SU8 required to manufacture all of the particles needed for the complete assay is 0.001m^2. Spacing on the manufacturing wafer by their own dimensions to ensure separation after photolithography and lift-off, the area of SU8 required becomes 0.004m^2. This area will fit inside a square 6.4×6.4cm which can be fitted onto a 4" wafer with 1.8cm spare for marks to align the embossing master with the bars. Thus all the particles required for a complete 10,000-plex assay can be manufactured on one wafer in a single embossing step.

3.5 Conclusions

This chapter has considered the steps required to make superimposed diffraction grating tags applicable to assay systems, to be analysed using microfluidic chips. It has been shown that high quality superimposed diffraction gratings may be manufactured in the biologically compatible polymer SU8, by using the high-throughput fabrication method of nano-imprint lithography. Gratings manufactured by this method were shown to give diffraction patterns of comparable quality to those manufactured by e-beam direct write techniques. Therefore, gratings can be mass produced that are both compatible with assay systems and allow for the large encoding capacities given in chapter 2, with some limitations. The encoding method, with

a small contribution from the resolution of the manufacturing process, was shown to limit the number of grating that can be superimposed to 3 (possibly 4 after more investigation), which still allows for 10,000 codes on 100μm particle (when the diffraction angle is limited to 43° due to total internal reflection at glass-air interfaces in the system). Assuming the same superimposing limit applies to 2-dimensional gratings (although nano-imprinted 2D gratings have yet to be tested), it is expected that around 10^8 unique codes can be obtained on a particle $100 \times 100\mu$m square. In addition, the robustness of the reading technique to rotation of the tags with respect to the reading beam has been demonstrated, and a computer algorithm outlined for automated reading of the diffractive tags. The actual number of particles which must be read in an assay experiment has also been estimated, using data from a real biological assay performed by others on diffractively encoded microparticles. Hence, the practicality of high throughput manufacture of the diffractively encoded microparticles has been demonstrated.

Chapter 4

Holographic microparticle encoding

In this chapter we introduce a new diffractive tagging concept, which addresses many of the limitations of the simple superimposed diffraction gratings, that have been investigated in the previous two chapters. This technique involves the writing of encoded holograms into microparticles doped with photochromic dye. We consider the reasons for developing this new technique, methods and dyes for implementing the encoding concept on SU8 microparticles, and an algorithm for reading the encoded holograms.

Section 4.1, considers the advantages of holography and section 4.2 gives a general outline of the formation, reconstruction and properties of encoded holograms written with light into photosensitive materials. Section 4.3, then considers the properties of a specific photosensitive dye that is added to SU8, and methods for manufacturing photosensitive SU8 microparticles. Then, section 4.4 will consider the experimental formation and properties of encoded holograms written into the dye doped SU8. Finally, in section 4.5, an algorithm for reading the codes reconstructed from the holograms will be decribed.

4.1 Rationale for holographic encoding

4.1.1 Introduction to holograms and their encoding advantages

Throughout this chapter, we define holograms as diffractive structures which can be designed to give a specific diffraction pattern. From this definition it is appar-

ent that by creating holographic tags, we have the potential to overcome some of the disadvantages of the superimposed grating tags investigated in the preceding chapters. This will allow us to create a different and potentially improved encoding method for bead based assays.

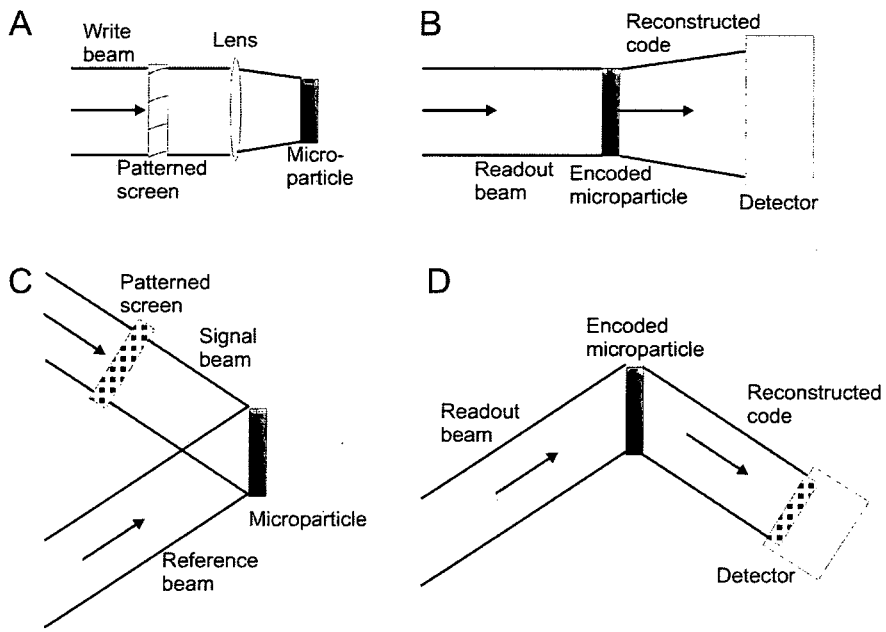

Figure 4.1: Methods of creating holograms in a photochromic material. The hologram surface pattern is precalculated by a computer algorithm and imaged directly onto the surface (A), such that illumination of the material produces the desired code diffraction pattern (B). An alternative method is to pattern a beam with the required code pattern and interfere with another beam on the surface (C). Illuminating the resulting hologram with the original reference beam produces a copy of the code pattern on the reverse side of the hologram (D).

The preceding chapters have described the concept and implementation of a diffractive tagging technique for bead-based assays, based on the use of superimposed diffraction gratings. This technique has been shown to be successful in providing large numbers of unique codes for the identification of microparticles. There are, however, some limitations to this technique, as discussed in chapter 3, which prevent us from obtaining the very large numbers of unique codes that should theoretically be achievable. These include: the high manufacturing resolution required to accurately produce tags with large numbers of superimposed gratings; the very large observation angles required to encompass large numbers of codes; unwanted features such as ghost beams which can affect the reading process and reduce the encoding capacity. In addition, the current nano-imprinted SU8 implementation

creates codes which are permanent and cannot be changed once assigned to a particle (reasons for changing the code will be considered in section 4.1.2), and there is no possibility to introduce binary encoding schemes, for which there exist well-established error-correction mechanisms. It would therefore be ideal to develop a diffractive tagging concept which has the potential to overcome some or all of these limitations.

To create holograms that can encode microparticles, the diffraction pattern desired for encoding purposes is first designed, and a diffractive tag created which will produce this diffraction pattern. By designing the tag's diffraction pattern to fit our requirements, we overcome most of the limitations of the grating tags: we can design tags which in principle produce only the code diffracted beams which we require, that do not require high manufacturing resolution, that produce the entire code within a small angular space, and that allow us to implement binary code schemes which are easily machine readable and open to error detection and correction schemes. Also, by appropriate material choice, the final item on the list of disadvantages of the previous encoding implementation will be overcome: that the code is permanent and may not be changed during experiments. To do this, the hologram should be written into a *photochromic* material. Such materials change their absorption spectrum and/or refractive index upon illumination with light in a certain wavelength band, and revert to their original form upon illumination with light of a different wavelength. While gratings could be written into a photochromic material, writing of holograms was chosen for the various other advantages listed above. There are two methods which can be used to create encoded holograms in a photochromic material, which are schematically outlined in figure 4.1. The first method (figure 4.1(A and B)) is to use a computer algorithm to precalculate a pixellated pattern of absorption constant and/or refractive index, which will give the desired diffraction pattern upon illumination with a plane wave of a certain wavelength. This pattern is written onto a mask, and imaged onto the photochromic material to create the hologram (4.1(A)). When the hologram is illuminated with a plane wave, the desired code diffraction pattern is formed on a detector (4.1(B)). The second method is the more 'classical' method of interference holography. In this method (4.1(C)) one beam is again passed through a screen, this time patterned with the actual code that the hologram should produce. This beam is interfered with a reference beam, creating a complex mixture of diffraction gratings in the photochromic material. When this mixture of gratings (the hologram) is illuminated by a readout beam similar to the original reference beam (4.1(D)), the code pattern is reconstructed

on a detector on the reverse side of the substrate. One advantage of this method is that little or no precalculation is required.

As discussed in chapter 3, the encoded microparticles should be made from the polymer SU8, which is chemically stable, and for which there is a procedure for chemically attaching biomolecules. Therefore a photochromic material needs to be incorporated into SU8 in order to create re-writable holographically encoded microparticles, which are compatible with the necessary biochemistry. Photochromic materials are commonly found as reasonably small organic molecules that may be mixed with polymers in solvent [98, 99, 100], such that they become trapped within the polymer matrix upon polymerization. This will allow the creation of SU8 microparticles with photochromic (and therefore writeable and potentially re-writeable) properties. The reasons for creating re-writeable encoded microparticles are outlined in the next subsection.

4.1.2 Necessity for re-writable tags

In order to justify the creation of re-writeable encoded microparticles, this section will consider the kind of experiment for which it would be necessary to re-write the codes on a set of microparticles. The main reason for having the ability to change the code on a microparticle is to use the particles in *directed combinatorial split-and-mix synthesis* of chemicals. Although this can be accomplished without changing the code, it would require the particles to be sorted after each step, instead of having the code re-written. This requires extra complexity in the microfluidic system, so it is useful to investigate an alternative method. To demonstrate how this works, consider the simple example of creating all possible 2-base DNA strings (oligonucleotides), using all 4 DNA bases A, G, C and T. A schematic outline of the progression of the synthesis is shown in figure 4.2. This synthesis requires $4^2 = 16$ codes, which can be achieved with 4 binary digits (bits). The process begins with blank particles, which are divided equally into four sets. Each set is added to a different reaction vessel, in each of which one of the four bases is attached to the particles. This results in four populations of particles, each one with either A, G, C or T attached to the surface. The particles are encoded with a binary number indicating the base attached to the particle: '0001' indicates A, '0010' indicates G, etc (step 1 in figure 4.2). All of the particles are then mixed into one set and again divided into four. This results in four equal sets of particles, each containing an equal number of particles with A, G, C and T attached to the surface.

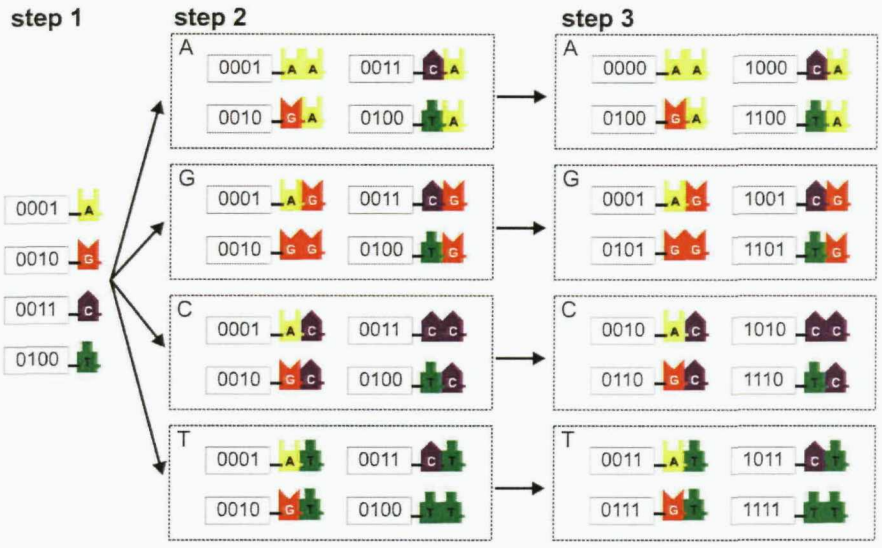

Figure 4.2: The combinatorial split-and-mix synthesis of all 2-base oligonucleotides. In step 1, the particles are functionalized with either A, G, C or T, and encoded to indicate the base attached to them. In step 2, equal amounts of each particle are reacted in order to have one of the four bases added to the oligonucleotide. After reaction (step 3), the particles from each pot are analysed, and the look up table shown in 4.1 used to construct a new unique code for each particle.

Reaction pot	Existing code	New code
A	0001	0000
A	0010	0001
A	0011	0010
A	0100	0011
G	0001	0100
G	0010	0101
G	0011	0110
G	0100	0111
C	0001	1000
C	0010	1001
C	0011	1010
C	0100	1011
T	0001	1100
T	0010	1101
T	0011	1110
T	0100	1111

Table 4.1: Look-up table used to construct the new code for each particle after reaction.

The next step is to add another base to each particle. Each of the four sets is again put into one of the four reaction vessels, each attaching a different base. The result is particles with two-base oligonucleotides AA, AG,... GA, GG..., etc. attached to the surface (step 2, figure 4.2). Now each of the particles are passed through a reading system. First, all of the particles from pot A are passed through, then pot B, etc., so that the reaction that has just taken place on a particle is known. The code on a particle (which signifies the first reaction) is read, and according to this code and the reaction vessel which the particle has just been in, a new code is constructed, e.g. '0000' for AA, '0001' for AG, '0010' for AC, etc, as shown in table 4.1. The old code is then erased, and replaced with the newly constructed code. All the possible 2-base oligonucleotides have now been created, each one attached to a particle containing a code which uniquely identifies it (step 3, figure 4.2). This process can be generally applied to the synthesis of k-base strings of chemicals with n possible bases, which will have n reaction steps, as long as one has k reaction vessels and can write k^n unique codes onto the particles. Once the synthesis is complete, these particles can all be mixed together for further reactions, for example hybridisation to unknown k-base oligonucleotides in a mixture. The hybridized particles can then be identified after reaction in order to identify the unknown sequences.

Having described the motivation behind developing a re-writeable holographic encoding strategy for microparticles, the next section considers the form the code will take, and describe the theoretical basis of a method which will allow use to write this code into photochromic microparticles. This will include a description of the formation of the hologram, as well as the properties of diffraction from it and the encoding capacity.

4.2 Holographic encoding concept

The basic layout of the diffraction pattern from the hologram which is to be used for encoding the microparticles is shown in figure 4.3. The pattern consists of two parts; the first part consists of two orthogonal lines of bright spots, which define a 'code grid', indicated by dotted lines in figure 4.3(A). Each intersection of the dotted lines indicates the position of a code bit. The code is written onto this grid as a binary string, by either placing a bright spot at a bit position to indicate a '1' bit, or leaving the bit position blank to indicate a '0' bit. An example depicting the 16-bit code 0110 1011 1111 1001 is shown in figure 4.3(B). Similar square arrays of bright and dark regions have become a standard method for encoding in large scale

volume holographic memories [80].

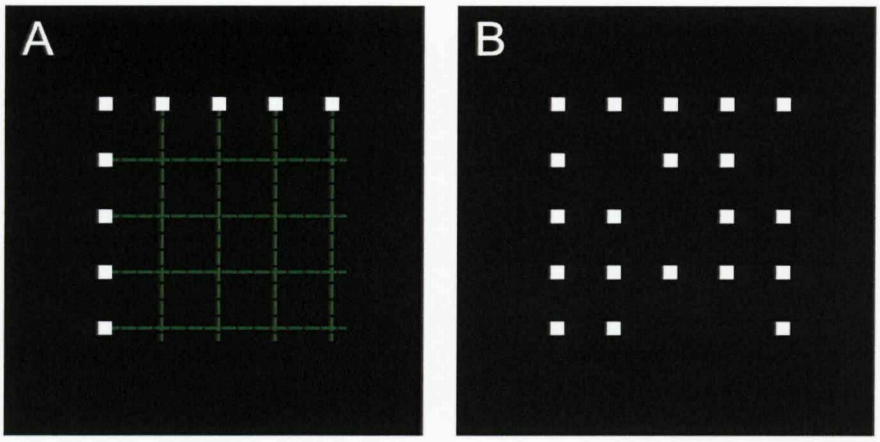

Figure 4.3: The diffraction pattern to be used to encode microparticles. (A)Two orthogonal lines of spots define a code grid, upon which spots may be placed to represent a '1' bit. Grid spaces left blank indicate a '0' bit. (B)An example depicting the code 0110 1011 1111 1001.

The two orthogonal grid defining spot lines are present as a reference frame for automatic computer reading of the code: once this frame is found, the code grid can be constructed in the computer's memory, and each position on it analysed for the presence or absence of a spot. The binary code represented by the array is thus reconstructed. More details on an algorithm for reading the codes are given in section 4.5.

4.2.1 Fourier Holography

Having described the form of the microparticle diffraction patterns, a method for forming a hologram on SU8 is now required, which will produce such a diffraction pattern. As briefly considered in section 4.1.1, there are two principal methods of doing this; an interference holography method, and the precalculation of the hologram by a computational algorithm, such as those already reviewed in chapter 1.

The method that was chosen for forming holographically encoded microparticles, as briefly considered in section 4.1.1, is a standard interference holography method. This method was chosen over the CGH methods, due to the fact that the holograms may be easily written into photochromic microparticles directly, with no pre-calculation required. This particular implementation of interference holography

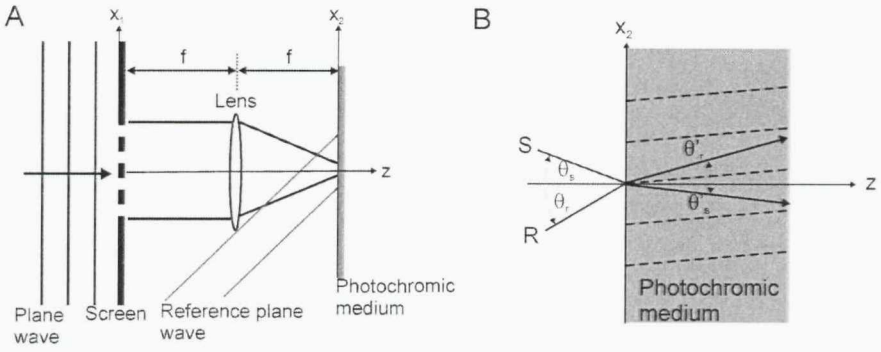

Figure 4.4: (A) Setup for forming a Fourier hologram. A plane wave of wavelength λ is passed through a patterned screen and focussed through a lens of focal length f onto the photochromic medium. A reference plane wave, also of wavelength λ, is incident on the medium in the same place, forming an interference pattern between the two. (B) The geometry of interference between a single plane wave from the screen Fourier transform S, and the reference plane wave R.

is generally termed *Fourier holography*. To describe the formation and diffraction properties of holograms created using this method we will follow the analyses given in references [101], [102] and [103]. A schematic outline of a generic writing setup for this method is shown in figure 4.4(A). A unit amplitude plane wave of wavelength λ is passed through a patterned screen (referred to as the 'object'; in our case the pattern is the code we require for particle identification, as described above) with transmittance $t(x_1, y_1)$, where the y_1-axis is perpendicular to the plane of figure 4.4. The wavelength is chosen to be one which will cause a change in the transmission properties of the photochromic material to be used for recording the hologram. A lens of focal length f is placed a distance f from the screen, and the photochromic material placed an equal distance in front of the lens. The electric field distribution $E(y_2, z_2)$ (where y_2 is again perpendicular to the plane of figure 4.4) of the light incident on the substrate due to the light passing through the screen is given by [44].

$$E(x_2, y_2) = 1/i\lambda f \int\int_{-\infty}^{\infty} t(x_1, y_1) \exp\left[-2\pi i/\lambda f(x_1 x_2 + y_1 y_2)\right] dx_1 dy_1 \qquad (4.1)$$

which is simply a scaled Fourier transform of the object pattern. This distribution is usually referred to as the 'signal' beam, as it contains the information about the object's transmittance. This indicates the reason for having the lens at distance f from both the object and photochromic material: this arrangement pro-

duces the exact Fourier transform of the object transmittance, which is equivalent to converting each object point to a plane wave. This allows the hologram to be reconstructed with no abberation, even if the reconstruction wavelength or angle are different to those of the reference beam [101]. Also incident on the material is a unit amplitude plane wave, also of wavelength λ, at incidence angle θ_r. This plane wave is termed the 'reference' beam, and its field at the substrate is given by $U(x_2, y_2) = \exp[-2\pi i/\lambda(x_2 \cos\theta_r + y_2 \sin\theta_r)]$. Both fields propagate into the medium, interfering and causing a change in transmission properties throughout the volume of the photochromic medium. For simplicity in the following analysis, we use the fact that the signal field in equation 4.1 is a sum of a series of plane waves. Therefore the interaction of one of these plane waves with the reference plane wave is considered, which will then be applicable to the other plane waves making up the signal beam. The geometry of such an interaction is shown in figure 4.4(B). A signal plane wave is incident on the photochromic medium at angle θ_s to the z-axis, and thus propagates in the medium with angle $\theta'_s = \arcsin(n \sin\theta_s)$, where n is the bulk refractive index of the photochromic medium. Similarly, the reference plane wave is incident on the medium at angle θ_r, and so propagates with angle $\theta'_r = \arcsin(n \sin\theta_r)$ in the medium. Therefore, within the photochromic medium, the field due to the signal plane wave is given by $U_s(z, y_2) = \exp[-(2\pi i/\lambda)(z \cos\theta'_s + y_2 \sin\theta'_s)]$ and that due to the reference wave is given by $U_r(z, y_2) = \exp[-(2\pi i/\lambda)(z \cos\theta'_r + y_2 \sin\theta'_r)]$. The intensity $I(z, y_2)$ of light in the medium is then

$$I(z, y_2) = |U_s(z, y_2) + U_r(z, y_2)| = 2 + 2\cos\phi \tag{4.2}$$

where, for simplicity of notation, we have introduced $\phi = (\mathbf{k}_s - \mathbf{k}_r) \cdot \mathbf{r}$. Here $\mathbf{r}$ is the vector to point (z, y_2). The photochromic material response to the incident light will be proportional to I, so that, assuming for the moment that only the transmission T of the material changes in response to illumination, the resulting hologram has transmission

$$T(z, y_2) = T_0 + 2B\cos\phi \tag{4.3}$$

where B is a constant incorporating exposure time and the material response to illumination, and T_0 is the constant transmission offset over the whole hologram. This result constitutes a sinusoidal grating with grating wavevector $\mathbf{K} = \mathbf{k}_s - \mathbf{k}_r$. Lines of minimum transmission from equation 4.3 bisect the angle between the reference and signal plane waves, and are shown as dotted lines in figure 4.4(B).

The total transmission of the hologram formed from the patterned screen will be the sum of a number of these terms representing each plane wave in the Fourier transform of the screen pattern. This analysis applies only to media in which the holograms formed have low diffraction efficiency (i.e. less than around 5% [102]), as it has been assumed that the intensity remains constant as the light propagates through the hologram (a non-depletion approximation). If diffraction efficiency is high, a significant fraction of the writing beams will be diffracted out of the medium as the light propagates, and a more rigorous coupled-wave theory based on Maxwell's equations must be used [102]. The material used experimentally in this chapter will be shown in section 4.4 to give holograms with a diffraction efficiency of less than 1%, permitting the use of this simple theory.

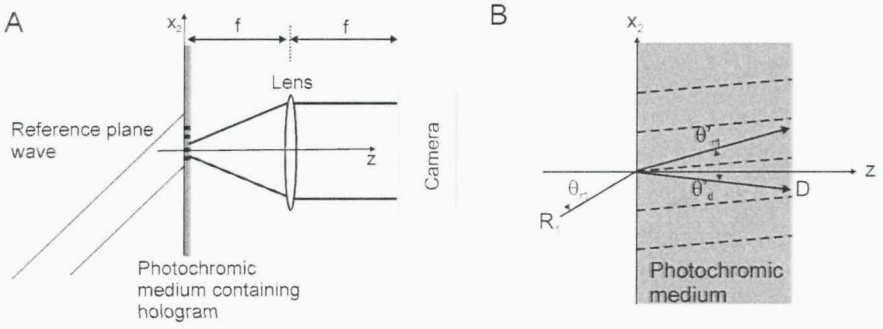

Figure 4.5: (A) Setup for reading a Fourier hologram of the type written using the setup in figure 4.4. A reference plane wave, of wavelength λ, is incident on the medium in the same configuration as in the writing process. Diffraction from the hologram is focussed by a lens onto camera, forming an image of the original screen pattern. (B) The geometry of formation of a diffracted plane wave from interaction of the reference plane wave with the hologram.

To read the hologram, a setup of the kind shown schematically in figure 4.5(A) is used. A reference plane wave R_1 of wavelength λ is incident on the hologram at angle θ_{r1} and propagates in the medium with angle $\theta'_{r1} = \arcsin(n \sin \theta_{r1})$. The plane wave scatters from the absorption variations in the hologram, forming a diffracted field of plane waves D propagating at angle θ'_d in the photochromic medium. The full characteristics of this diffracted field are obtained by calculating the Kirchhoff integral for the readout wave and the transmittance given by equation 4.3 which is considered in detail in reference [103]. The resultant diffracted field of the $\pm$1st orders is given by

$$U_{d\pm}(z, y_2) = CF \sec\theta'_d \mathrm{sinc}\{(kT/2\cos\theta'_d)[\pm\cos(\theta'_d - \theta'_r) \mp \cos(\theta'_d - \theta'_s) + p\cos(\theta'_d - \theta'_{r1}) - p]\} \quad (4.4)$$

where p is the ratio of writing wavelength to reading wavelength, T is the thickness of the photochromic medium, and $F = [\mp\sin(\theta'_d - \theta'_r) \pm \sin(\theta'_d - \theta'_s) + p\sin(\theta'_d - \theta'_{r1})]$. Equation 4.4 can be used to determine hologram formation and readout geometries which maximise the diffracted first order intensity. An important geometry which maximises the value of $U_{d\pm}(z, y_2)$ and hence the diffracted first order intensity [103], is that for which $\theta_{r1} = \theta_r$ and $\theta_d = \theta_s$, with $p = 1$. Therefore, by recording a hologram using the setup in figure 4.4 and then illuminating it with a plane wave of the same wavelength and incidence angle as the original recording reference wave, each plane wave originally in the object beam will be reconstructed in the diffracted beam. For our case, the result is that the Fourier transform of the code patterned onto the object beam will be reconstructed from the hologram. In fact, due to the exact Fourier transform performed by the writing lens, the Fourier transform of the code is correctly reconstructed with no aberration by a readout beam of a different wavelength and incident angle, albeit angularly displaced and reduced in intensity, as we shall consider in section 4.2.3. A lens of focal length f performs the inverse Fourier transform of the diffracted field (i.e. the inverse operation to equation 4.1), resulting in the reconstruction of the code pattern which was on the object screen. The code pattern may then be observed by CCD camera for automated reading of the codes. Such a geometry will be considered in the rest of the theoretical analysis, and this geometry will be used experimentally for writing holographic codes into microparticles.

4.2.2 Hologram size and encoding capacity

The encoding capacity of the binary array concept described in section 4.2, depends on the required size of the hologram and the number of bits that can fit into the observable image space. The observable space clearly depends on the camera surface area used to observe the hologram during reconstruction. In order to correctly reconstruct the code image from the hologram written into a particle, enough of the Fourier transform of the code must be written into the particle to record all of the required information about the position of the bits in the code. To begin with, consider the code pattern as a square array of square spots of side length b

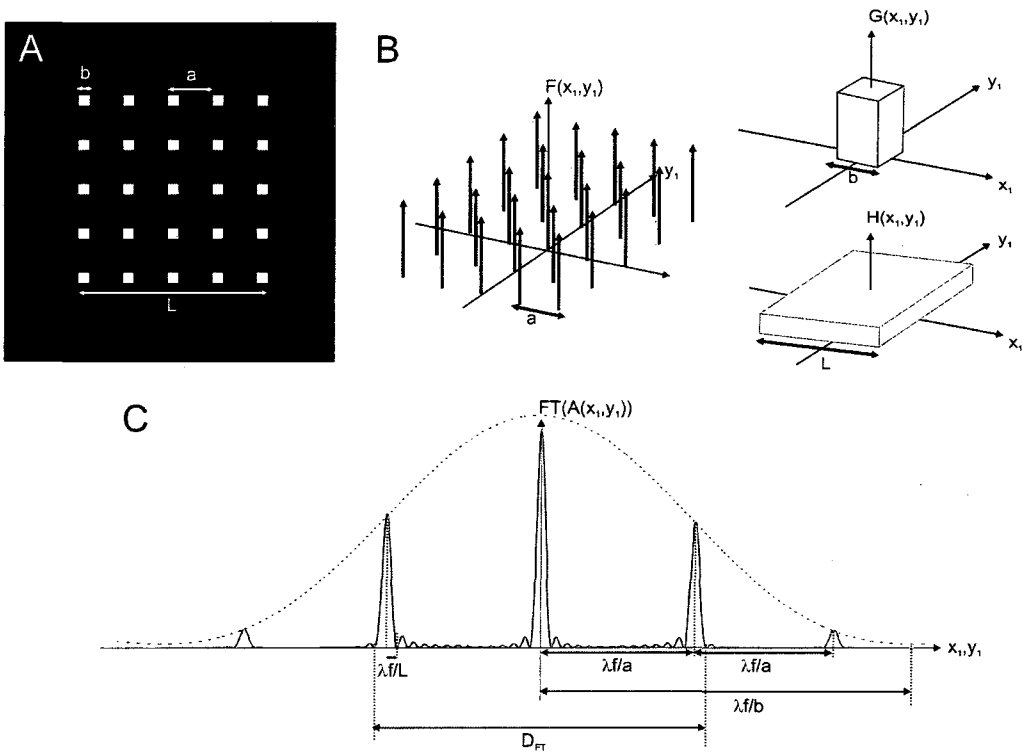

Figure 4.6: (A)An example code pattern featuring a square array of bright squares of side length b and separation a. (B) The array may be considered as a convolution of an infinite array of delta functions F with separation a with a square function G which defines the code spot size, and square function H which defines the size of the entire array. From this, the form of the Fourier transform of the code when projected onto a substrate as in figure 4.4 may be deduced (C), allowing us to easily estimate the minimum hologram size D_{FT} for given values of a, b and f.

and centre-to-centre spacing a, with total array length L (see figure 4.6(A)). Note that throughout this chapter a, b and L refer to paramaters of the image written into/recovered from a hologram, not the hologram itself. Using the geometry of figure 4.4, this array is represented for the moment as a transmittance function $t(x_1, y_1)$. The field $U(x_2, y_2)$ of this projected through a lens of focal length f onto a flat substrate, as in figure 4.4, is given by equation 4.1. Aside from a constant factor, this is the Fourier transform of the aperture function into frequency space $(x_2/\lambda f, y_2/\lambda f)$. The function $A(x_1, y_1)$ may be represented as

$$A(x_1, y_1) = F(x_1, y_1) \otimes G(x_1, y_1) \times H(x_1, y_1), \tag{4.5}$$

where $\otimes$ denotes a convolution, $F(x_1, y_1)$ is an infinite 2D array of delta-functions spaced by a in the x_1 and y_1 directions, $G(x_1, y_1)$ is a square function where $G = 1$

for $-b/2 \leq x_1, y_1 \leq b/2$ and $G = 0$ elsewhere, and $H(x_1, y_1)$ is a square where $H = 1$ for $-L/2 \leq x_1, y_1 \leq L/2$ and $H = 0$ elsewhere (F and G are shown in figure 4.6(B)). The Fourier transform of $A(x_1, y_1)$, denoted $FT(A)$, may then be written as $FT(A) = FT(F)FT(G) \otimes FT(H)$ [44], where

$$FT(F) = a^2 \text{comb}\left(\frac{ax_2}{\lambda f}\right) \text{comb}\left(\frac{ay_2}{\lambda f}\right) \tag{4.6}$$

$$FT(G) = b^2 \text{sinc}\left(\frac{bx_2}{\lambda f}\right) \text{sinc}\left(\frac{by_2}{\lambda f}\right) \tag{4.7}$$

$$FT(H) = L^2 \text{sinc}\left(\frac{Lx_2}{\lambda f}\right) \text{sinc}\left(\frac{Ly_2}{\lambda f}\right). \tag{4.8}$$

Here $\text{comb}\left(\frac{ax_2}{\lambda f}\right) \text{comb}\left(\frac{ay_2}{\lambda f}\right)$ denotes an infinite array of delta functions spaced by $\lambda f/a$ in the x_1 and y_1 direction, as defined in [44]. The form of the function $FT(A)$ may therefore easily be deduced by considering the functions above, without the need to fully calculate it, and is shown in figure 4.6(C) - the Fourier transform of the square array function is a series of peaks whose maxima are spaced by $\lambda f/a$ in the x_1 and y_1 directions, with zero-to-zero widths $\lambda f/L$, enveloped by a sinc function that falls to zero at $\pm\lambda f/b$. In order to have enough information to correctly reproduce the positions of the spots in the square array, the hologram on the particle must at least contain the first peaks of the Fourier transform, i.e. the smallest dimension D of the particle to be encoded should be greater than $D_{FT} = 2(\lambda f/a + \lambda f/L)$. Figure 4.7 shows the hologram size vs a for different values of f, with $\lambda = 532$nm. This wavelength was chosen, as it is the one which will be used experimentally (see sections 4.3 4.4). The values demonstrate the particle sizes that can be encoded with this technology, depending on the values of f and a we can achieve experimentally.

As stated above, the encoding capacity of a hologram depends on the bit spacings (as shown in figure 4.7), and the size of the observable image space. Assuming the only lens in the imaging system is the FT lens, the observable image space is limited by the sensor size of the camera used to observe the reconstructed code hologram. As an example, the encoding capacity of different hologram sizes was calculated for a number of values of f, when a standard 2/3" (active area 8.5 x 6.8 mm) camera sensor is used to observe the reconstructed code. The bits reconstructed from each size of hologram are spaced by a distance a using values from figure 4.7 for the particular value of f being considered. The largest rectangular array of bits spaced by a that fit into the sensor area was calculated, and a reference row

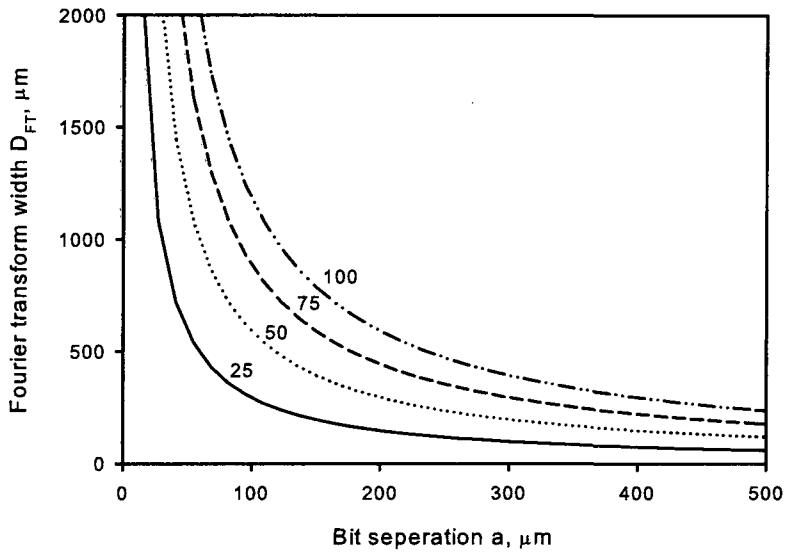

Figure 4.7: The width D_{FT} of the code Fourier transform as a function of the separation between code bits, for different values of f. The values of f are given above each curve in mm

and column of bits (as described in section 4.2) removed. The remaining n bits are available for encoding, and the number of unique binary codes available using these bits is 2^n. The resulting encoding capacities are shown in figure 4.8. The 'stepped' appearance of the graph results from the fact that all code spot arrays must contain an integer number of spots in each dimension of the array. Therefore, the capacity only increases when the hologram FT size allows a higher number of spots to fit in the image area, creating a step in the encoding capacity, which then remains constant until one more spot will fit in the image area in either dimension. It is clearly seen that a very large number of codes are available, with 10^{32} codes available from a particle 100μm in size with $f = 50mm$, and 10^{150} codes available on a 100μm particle when $f = 25mm$. Thus large numbers of particles can be uniquely encoded, with diffraction patterns that are contained within an easily observable image space.

There are a number of caveats that may prevent such high encoding capacities from being obtained. Firstly the value of a can never be exact; it is prone to an inaccuracy due to the finite resolution of the method use to display the object code mask. For the spatial light modulator that will be used in the experimental section 4.4, the resolution is the pixel pitch, which in our case is 13.68μm. Thus all values of

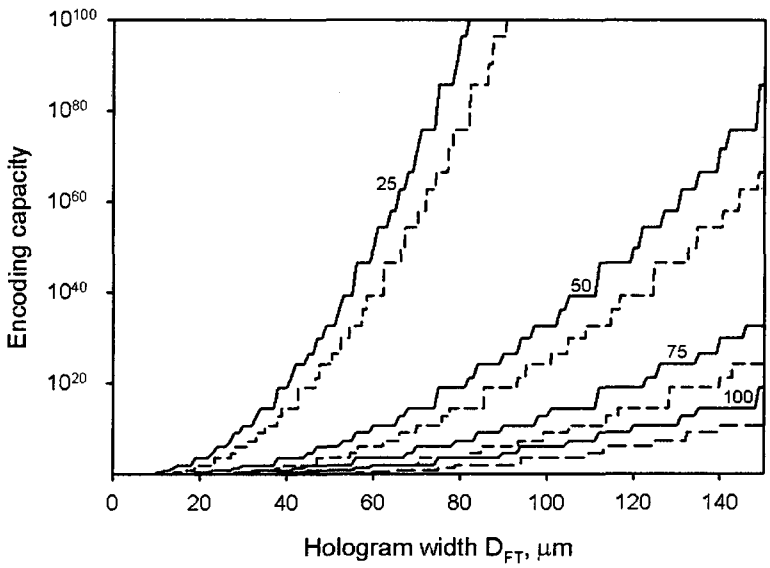

Figure 4.8: The encoding capacity of different hologram sizes, for various values of f, when the reconstructed code is observed on a standard 2/3" camera sensor. Solid lines show the fundamental encoding capacity, dashed lines show the capacity after taking account of more realistic system parameters. The values of f are given above each pair of curves in mm.

a have a tolerance of $\pm 13.68\mu$m, resulting in some code spots having a larger period than intended. The result is a reduced encoding capacity, because allowance must be made for a dots spaced by a larger value of a to be contained within the sensor dimensions. There are additional effects which can change the apparent dot spacing in the image diffracted from the hologram including the fact that the laser light has an uncertainty in wavelength $\Delta\lambda$ and is diverging (i.e. is not actually a perfect plane wave. A typical value of $\Delta\lambda$ for a DPSS (Diode-pumped solid-state) laser such as that used for the experiments described in section 4.4 is $\Delta\lambda \approx 1$nm. The reduced encoding capacity taking into account these effects is shown by the dashed lines in figure 4.8, giving around 10^{24} code on a 100μm particle with $f = 50$mm.

There are a number of effects that will still further reduce the encoding capacity; one which will have a very large effect is the use of a smaller camera sensor. There may be reasons to place a limit on the shortest focal length used, as a lens closer to the sample will collect more of the light scattered from the sample surface. Preliminary tests on experimental holograms suggest that the focal length limit lies between $f = 50mm$ and $f = 25mm$, for the particular materials studied. Additionally, we

may want code diffraction patterns which are much smaller than the sensor size, to make sure the patterns stay within the sensor when the particles are not perfectly aligned to the readout beam. Such effects of angular rotation of the holograms are considered in the next section.

4.2.3 Angular sensitivity of diffraction from SU8 holograms

In addition to providing information about the conditions which give a maximum intensity reconstructed image from a hologram, equation 4.4 allows an analysis of the effect that angular rotation of a hologram has on its diffraction pattern. This will be important for the application of encoded holograms to automated flow-based reading systems, where there is a possibility of the encoded particle not being perfectly normal to the reading beam, as already considered for superimposed grating tags (see section 3.3.1). Much like gratings, the diffracted angles within the hologram are expected to change if the hologram rotates. However since the hologram is written throughout the volume of the material, rather than just on the surface, there will be other effects arising from the violation of the Bragg law. Equation 4.4 can be used to calculate the diffracted intensity for different values of θ_{r1}, which is equivalent to a rotation of the hologram about the y axis. The intensity variation depends on a number of parameters, notably θ_s, θ_r, write wavelength, read wavelength and thickness T of the hologram material. The effect of these parameters on the diffracted intensity for different θ_r is investigated in the following, using typical parameters which we will later use in the experimental investigation of holograms in SU8. It will turn out to be useful to record holograms with light of wavelength $\lambda = 532$nm and read with light of wavelength $\lambda' = 633$nm due to the properties of the photochromic dye that will be used (see section 4.3.1). Typical SU8 films will have thickness in the range 5 - 35μm.

Figure 4.9(A) shows the effect of changing θ_{r1} on the hologram diffracted first order intensity, for a selection of values of θ_r and θ_s, with $T = 35\mu$m. There is a peak in intensity at the Bragg angle, when $2sin\theta_{r1}\lambda/(sin\theta_s - sin\theta_r) = \lambda'$. For values of θ_{r1} either side of this peak, the diffracted intensity falls off in a sinc^2-function form. The width of the sinc function decreases with increasing θ_r and θ_s. Therefore the larger the incident angles of the recording beam, the smaller the rotation of the hologram that can be tolerated, before the hologram intensity drops to an unacceptable level. In addition to the intensity reduction, the diffracted angle of the hologram image also changes with changing θ_{r1}, as shown in figure 4.9(B). This adds a limitation

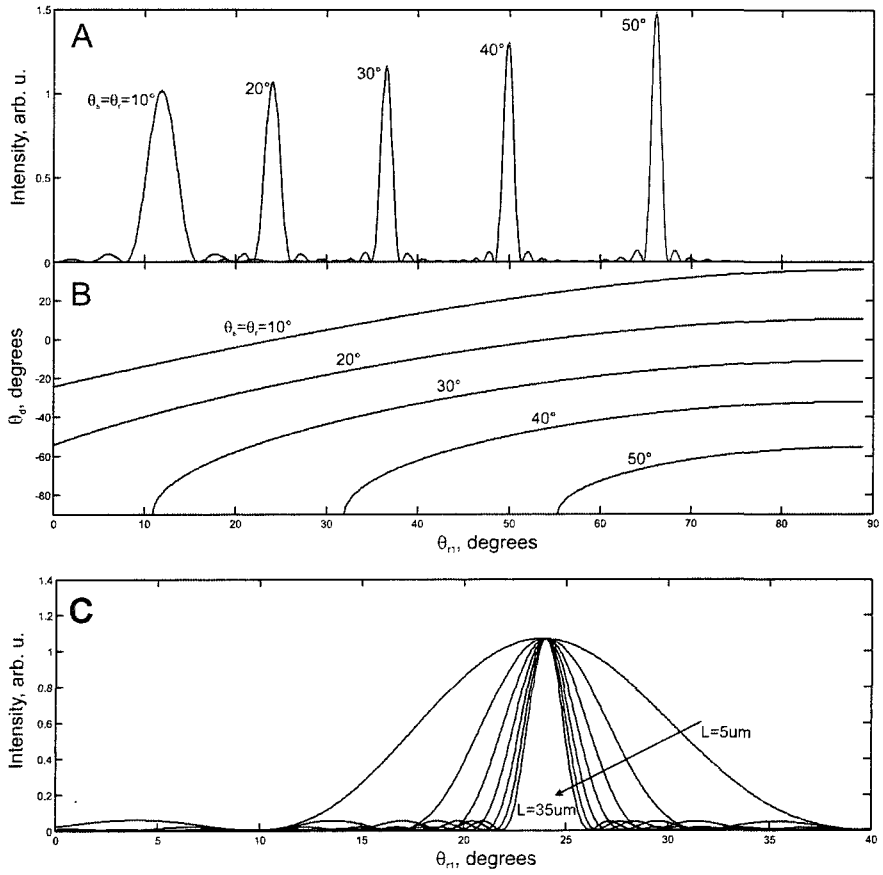

Figure 4.9: (A)Diffracted first order intensity for a hologram formed from two plane waves, as in figures 4.4 and 4.5, for different values of θ_{r1}. The effect is shown for a number of values of θ_s and θ_r, denoted next to each curve. Increased efficiency with increased θ_s and θ_r results from the greater total material volume in the hologram. (B)The diffracted angle corresponding to each value of θ_{r1}, for different values of θ_r and θ_s as denoted next to each curve, with writing wavelength of 532nm and reading wavelength of 633nm. (C)Diffracted first order intensity for a similar hologram with $\theta_r = \theta_s = 20°$, for values of L ranging from 5 - 35μm. Values of T increase in 5μm steps in the direction of the arrow. All figures where calculated by inputting the appropriate parameters into equation 4.4.

which is specific to the setup in use: at some point the hologram will move outside the reconstruction lens/camera.

In addition to the effect of θ_r and θ_s on the hologram angular sensitivity, the thickness T of the hologram has some effect. Figure 4.9(C) shows the variation of hologram intensity with varying θ_{r1}, for different values of T ranging from 5μm to 35μm in steps of 5μm, with a fixed value of $\theta_r = \theta_s = 20°$. From this it is clear that the thicker the hologram is, the smaller the rotation that can be tolerated. The calculated hologram rotation θ_{ex} that causes the diffracted intensity to fall to zero,

for changing θ_r, with $\theta_s = 0$ and with different fixed values of T, is shown in figure 4.10.

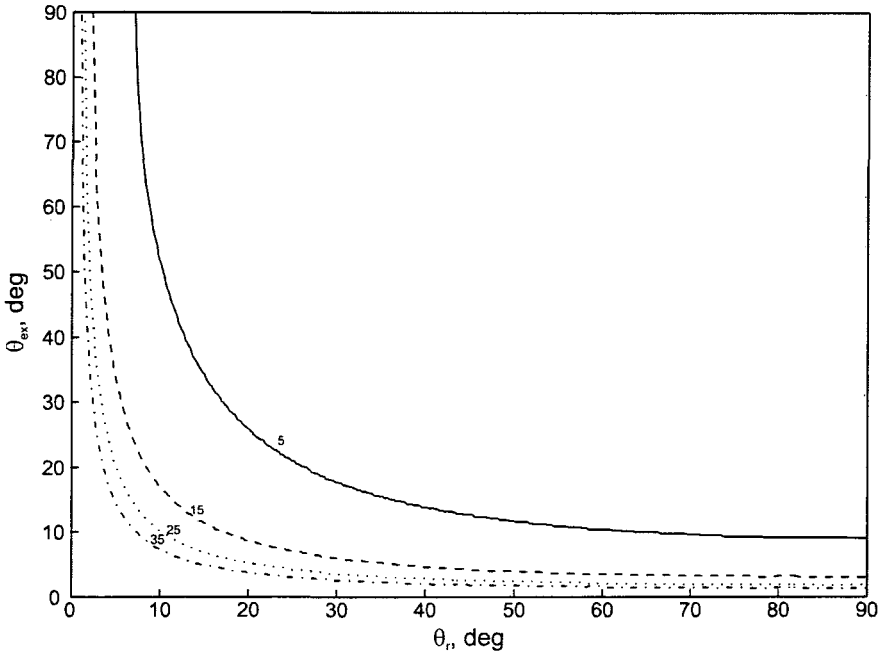

Figure 4.10: The rotation θ_{ex} of a hologram required to extinguish the diffracted image, for different values of θ_r and selected values of hologram thickness T. The number above each curve indicates the value of T in μm.

For the parameters that are used experimentally, i.e. $T \approx 35\mu$m and $\theta_r - \theta_s > 20°$, figure 4.10 shows that we can only tolerate rotations of less than $\pm 3°$. To allow for such a rotation, the size of the code image space must be reduced to leave an empty border of approximately 2mm for a value of $f = 50mm$, in order to allow for movement of the code without it going outside the sensor area. This places the most severe limitation yet on the encoding capacity, reducing it by a factor of 10^{10} from the values in figure 4.8, giving around 10^{14} codes on a 100μm particle when $f = 50$mm. However, this is still a very large number of codes. Moving the camera would eliminate the need for this border, if it could be accomplished fast enough to read the code in a high throughput system.

Possible intensity variations in the code pattern should also be considered, caused by the movement of the hologram and associated with the differing optimum diffracted angle of the different plane waves which make up the diffraction from the hologram. If the hologram contains only the first and second order beams from the Fourier transform, in addition to the zero order, the maximum plane wave angle diffracted

from the hologram will be $\theta_{d0} \pm \arctan[2(a+L)/f]$, where θ_{d0} is the diffracted angle of the zero order of the diffracted code Fourier transform. For values of a up to 500μm which have been considered so far, the θ_{r1} position of the intensity peaks differ by a maximum of 0.5%.

4.2.4 Summary

To summarise this theoretical section: A method of creating holograms in a photochromic material has been considered in detail. This method can create holograms which, when illuminated, will reproduce binary code in the form of an array of spots. The fundamental encoding capacities of these holograms depend on the spacing of spots in the code array, and the focal length f of the writing FT lens. For $f = 50mm$ around 10^{32} unique codes are available on a 100μm hologram. There is considerable angular sensitivity associated with these holograms , due the fact that they are written throughout the volume of the material, and are therefore subject to Bragg selectivity. For typical experimental parameters of SU8 microparticles, the maximum rotation of the hologram which can be tolerated is $\pm 3°$. In allowing for the movement of the diffracted image from a code hologram due to a 3° rotation, the encoding capacity of a 100μm hologram with $f = 50mm$ reduces to about 10^{14} codes.

The next section considers the materials and fabrication techniques necessary to manufacture SU8 particles suitable for holographic encoding. These materials and processes will set the values of some of the parameters that were used in the above calculations, in particular the values of λ and λ' given above, and also the value of L.

4.3 Photochromic dyes and sample preparation

4.3.1 Dye photochemistry

Holographic storage in polymer materials has attracted a lot of attention for many years, particularly for application to holographic compact discs [79, 104, 105]. The most successful commercial implementations have concentrated on writing holograms into photopolymerizable materials [105], forming 'write-once read many' holographic memories. However, substantial research efforts in the last 20 years have concentrated on the use of organic photochromic molecules dispersed in polymer

matrices [98, 99, 100, 107], for application to re-writable holographic storage devices. Of these, the most promising materials are the diarylethene derivatives, first studied by Masahiro Irie and his group [106, 107]. These organic dyes can undergo a photo-induced conversion between two states with different absorption spectra. Both states of these dyes are extremely thermally stable, meaning that in dark conditions written holograms can, for some dyes of this type, remain for many months [108]. Some diarylethene derivatives can also be cycled from one form to the other and back many thousands of times [107], allowing rewritable storage to be implemented using these materials.

The photochromic dye used in this thesis is the commercially available diarylethene dye 1,2-Bis(2,4,5-trimethyl-3-thienyl)-cis-1,2-dicyanoethene (TCI-Europe), which has previously been characterized for its photochromic properties in the polymer matrices of PMMA and PVA [107]. Although other diarylethene derivatives are available, this is the only one that was found to be soluble in either of the two solvents commonly used for SU8; either gamma-butyrolactone or cyclopentanone. The possible photochemical reactions of the dye molecule are shown in figure 4.11. Upon illumination with UV light in the 300-400nm wavelength band the molecule in form (i) may undergo a *conrotatory cyclization* to form (ii), a *disrotatory cyclization* to form (iii), or a *cis-trans isomerization* to form (iv). The reactions that are interesting for this application are the cyclization reactions, as these are the ones for which the molecule's absorption spectrum changes (the cis-trans isomerization competes with the cyclization processes, and its importance will be considered in section 4.4).

The allowed cyclization reactions of a molecule are determined by the Woodward-Hoffmann rules [109], which are based on the symmetry of the highest occupied molecular orbital (HOMO; the highest energy electron orbital which contains any electrons). For molecules containing double bonds, these are known as π-orbitals. The Woodward-Hoffmann rules for this dye state that the molecular symmetry allows the disrotatory cyclization to take place in the ground state of the molecule, and the conrotatory reaction in an excited state of the molecule (i.e. the disrotatory reaction can be brought about only by heat, and the conrotatory reaction by light). For a more complete discussion, one may calculate [110] the energies of the π orbitals for the initial and final forms of the molecule for both cyclization types. By considering the symmetry of the orbitals in the initial form and final form, one can draw a *state correlation diagram* [112] showing how electrons will redistribute from the form (i) orbitals to the form (ii) orbitals. Such diagrams for the conrotatory and disrotatory cyclizations of 1,2-Bis(2,4,5-trimethyl-3-thienyl)-cis-1,2-dicyanoethene are

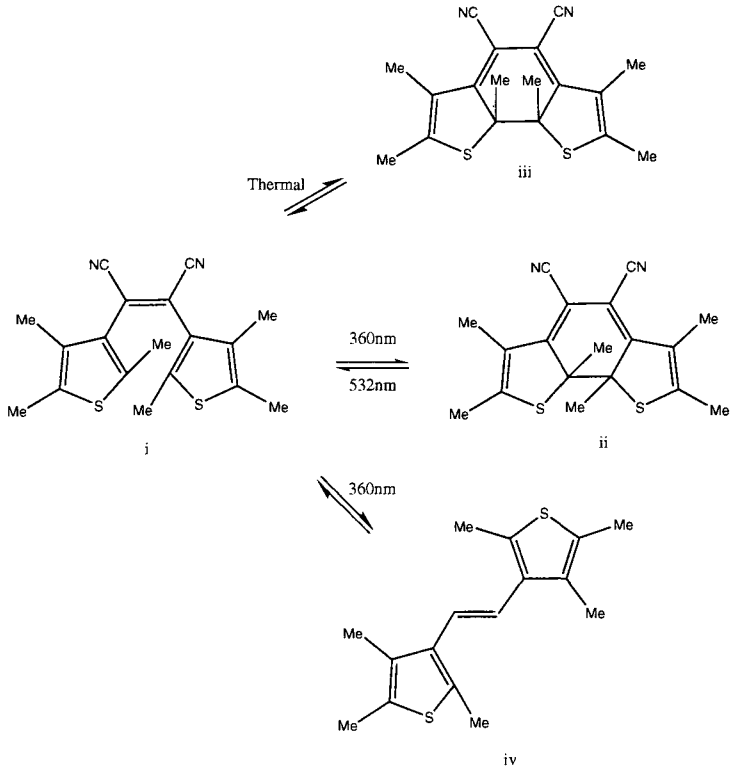

Figure 4.11: The photochemical reactions of 1,2-Bis(2,4,5-trimethyl-3-thienyl)-cis-1,2-dicyanoethene.

shown in figures 4.12(1) and 4.12(2), respectively. Dotted lines in these figures indicate the expected correlation from pure symmetry considerations; solid lines show more realistic correlations, as electron-electron repulsion prevents states of the same symmetry from crossing. Although the disrotatory reaction could theoretically be allowed by heating, in reality the large energy difference between the ground states of the two forms makes it extremely unlikely. This has been shown experimentally by the fact that the disrotatory cyclization does not appear to occur even at temperatures around 300°C [110].

Having seen that the disrotatory cyclization to all intents and purposes does not take place, only the conrotatory cyclization can be used to transform the molecule from the open ring to the closed ring form. As seen in figure 4.12(2), there is an extremely large energy barrier between the two forms in the ground state, prohibiting the cyclization. However, in the S_2 excited state, no such barrier exists, allowing the cyclization to occur. Thus the molecule can be cyclized by use of light which will excite the molecule to the S_2 state. The reverse, ring-opening, process also

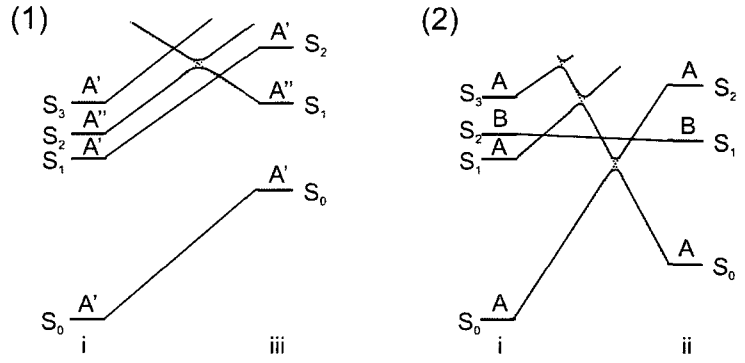

Figure 4.12: State correlation diagrams for (1) the disrotatory cyclization from form (i) to form (iii) and (2) the conrotatory cyclization from form (i) to form (ii). Here A', A", A and B represent the orbital symmetries as defined in [112]. Figure modified from [110] Figures 1 and 2.

easily takes place in the S_2 excited state, albeit requiring a lower energy (longer wavelength of light) to excite the molecule. Thus using two wavelengths of light, we can transfer the molecule reversibly between forms (i) and (ii). The yield of each form (modelled for free molecules) upon illumination with UV light is 30% form (ii), and 70% excited state of form (i). Of the molecules in the excited state of form (i), 50% decay to form (i) ground state and 50% to form (iv) ground state [111]. Since form (iv) cannot cyclize, around 35% of molecules are "lost" in each photocyclization .Thermally (i.e. in the molecular ground state), the closed-ring form is reasonably unlikely to transfer to the open ring form, because of the same energy barrier that prevents the cyclization. However, since the closed-ring ground state has a higher energy than the open-ring ground state, the barrier for thermal reversion of the closed ring form is lower, making the closed ring form slightly less thermally stable than the open ring form. Nevertheless, the closed ring form can be expected to remain for some time at room temperature, or perhaps even higher temperatures [110]. This is a useful property, as the codes written into particles need to remain for the duration of any biochemical experiment they are used in, without being thermally erased.

The molecule in form (i) (open-ring form) has an absorption band mainly in the UV region of the electromagnetic spectrum (see figure 4.13 dashed line). Illuminating the molecule with light within this absorption band transfers the molecule into its excited state. This allows the conrotatory cyclization to take place as described above, changing the molecule to form (ii) (closed ring form). The closed ring form has an additional absorption band in the visible region, for wavelengths from around

500-600nm (see figure 4.13 solid line). The change may be reversed by irradiating the molecule with visible light within this visible absorption band.

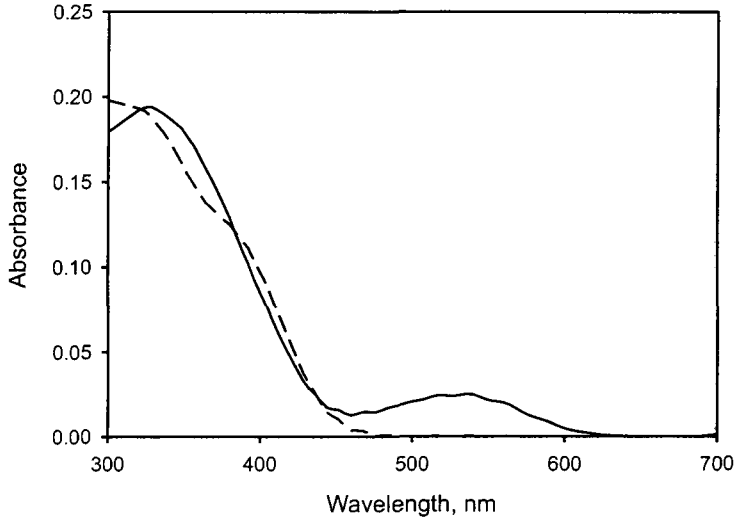

Figure 4.13: The absorption spectra of the open ring (dashed line) and closed ring (solid line) forms of the photochromic diarylethene dye 1,2-Bis(2,4,5-trimethyl-3-thienyl)-cis-1,2-dicyanoethene in cross-linked SU8.

4.3.2 Manufacture of dye-doped SU8 films and microparticles

In order to manufacture SU8 microparticles doped with the photochromic dye, it was first necessary to optimise the steps for cross-linking the dye-doped SU8. First the appropriate SU8 solution had to be chosen from the available standard solutions; the dye was found to dissolve most readily in the SU8-2000 series resists, which are solutions in cyclopentanone. Next, the exposure time required to cross-link the SU8 needed to be optimised, as the dye prevents the SU8 cross-linking within standard exposure time of approximately 10s. This arises from the fact that, as we have seen in section 4.3.1, the dye absorbs UV in the 300-400nm wavelength region. Since light of wavelength 365nm is required to initiate the polymerization of SU8, the dye prevents the SU8 cross-linking under standard process conditions: a much longer exposure time is required. To optimize the UV exposure time 5% wt dye was mixed with SU8-2015 solution in cyclopentanone. A 0.7mm thick boro-silicate float glass substrate (Schott Borofloat) was pre-treated with a Ti-prime adhesion promoter (Microchem Corp.) spun onto the substrate at 3000rpm, and the substrate

baked at 120°C for 2 minutes. The SU8 was then spun at 8000rpm to a flat plate of thickness 8μm on the glass substrate, and baked for 1 min at 65°C followed by 3 min at 95°C. To create a flat surface to minimise distortion to the written holograms, the plate was then left to relax for 2 hours at room temperature (23°C). A number of samples were exposed for a variety of times to UV light (wavelength 365nm) through a mask patterned with 500 x 1500 μm rectangles. After exposure the samples were developed in EC solvent (Microposit) for 1 min. The exposure time was increased until rectangular dye-doped SU8 microparticles remained on the substrate after development. An exposure time of 8 min was found to give fully cross-linked microparticles (compared to a typical time for a similar layer wihtout dye of about 12s). The exposure was performed in 48 intervals of 10s each, with a dark time of 20s after each interval, in order to prevent the sample heating up during the long exposure. After exposure the SU8 was baked on a hotplate with the temperature ramped from 50 to 95°C at 2°C min^{-1}, and left to cool on the switched off hotplate, in order to minimise distortions of the particle surfaces due to thermal stress.

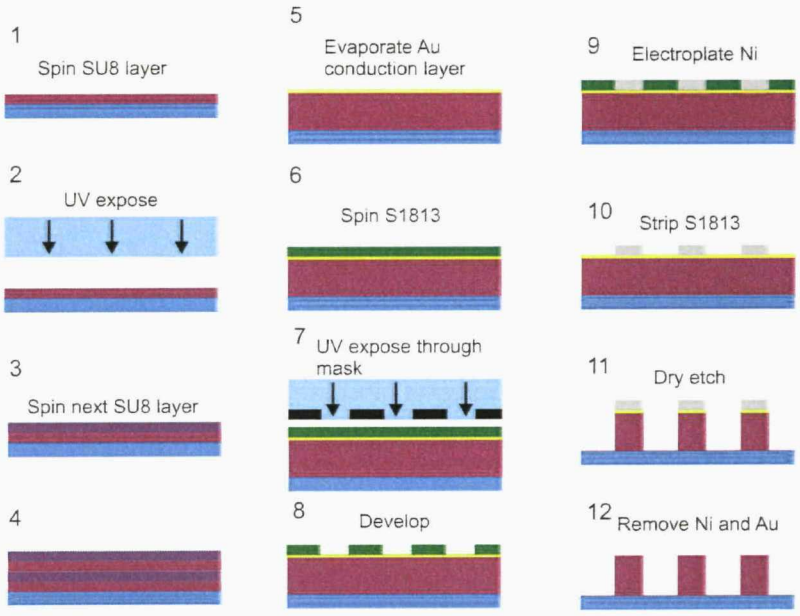

Figure 4.14: Schematic of the process used to manufacture the photochromic dye doped SU8 microparticles.

It was found that to create holograms with a reasonable signal-to-noise ratio, much more dye must be used than was present in the 8μm layers described above (essentially increasing the value of B in equation 4.3). Since the particles need to

be thicker from a structural point of view anyway (due to their relatively large size compared to thickness), it was decided to achieve this by creating structures which were fabricated from multiple 8μm layers. This process involves spinning and cross-linking a layer of dye-doped SU8, spinning and crosslinking another layer on top of this etc, to create a layered structure. In our case we observed that an adequate hologram signal to noise ratio was obtained from a structure with 4-layers. Flat plates of multi-layered SU8 were created by this method (represented schematically by steps 1-4 in figure 4.14). While a similar increase in hologram signal could have been obtained by creating a single thick layer of SU8, or adding more dye to a single 8μm layer, it was decided not to do this, because of the very long UV exposure times that would be required to cross-link the SU8.

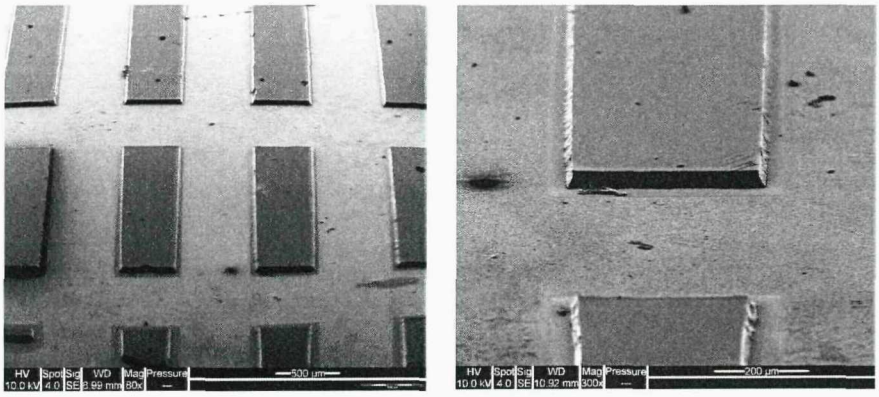

Figure 4.15: SEM images of 500 x 1500 x 35μm microparticles on glass substrate after completion of the manufacturing process.

Initially, manufacture of multilayered particles was attempted by patterning each layer photolithographically, before spinning the next layer. However, this was found to result in particles with a curved surface profile. This is partly due to the different total baking times of each layer causing thermal stress and thus curving, and partly due to the effect of spinning SU8 over pre-formed structures. It was therefore decided to form the particles by dry etching. A schematic of the final optimised process for forming photochromic dye-doped SU8 microparticles in shown in the schematic in figure 4.14. This part of the process was carried out by Dr. Shahanara Banu. First, 50nm aluminium is evaporated onto the glass substrate as a sacrificial layer to allow later release of the particles from the surface, prior to pre-treatment. Then (steps 1-4) a four layer flat plate of SU8 is manufactured, as described above. A chrome adhesion layer followed by a gold conduction layer is evaporated onto the SU8 (step 5) and 2.8μm of the positive photoresist S1828 is spun at 5000rpm on top of the gold

and thermally cured at 95°C for 35min (step 6). This is then exposed to UV light of wavelength 365nm and intensity 14 mW cm^{-2} for 11s, through a mask that defines the shape of the particles. Exposed areas of resist are washed away with MF319 solvent (aqueous solution of tetramethylammonium hydroxide, Microchem Corp.), leaving holes defining areas where the particles will be. Nickel is electroplated into the holes by use of the conduction layer (step 9). Electroplating was carried out in a Watt's bath [113] containing an aqueous solution of nickel sulphate ($NiSO_4.7H_2O$, concentration 267g/L), nickel chloride ($NiCl_2.6H_2O$, concentration 100g/L)and boric acid (H_3BO_3, concentration 35g/L). The sample forms the cathode and a blank nickel plate the anode of the electrochemical system. Nickel ions are deposited onto the sample from the nickel compounds in the solution. To obtain a nickel thickness of 5μm, the current density was set to 1 mA cm^{-2} and the plating carried out for 14 minutes 16 s. After electroplating, the S1828 is removed with acetone. Exposed gold was removed by ion-beam milling in an Oxford Instruments Ionfab 300 plus for 15min, using argon ions at a flow rate of 6 cm^3 min^{-1}. The exposed SU8 was dry-etched away using an Oxford Plus Plasma etcher. The machine parameters were set as defined in a previous publication [114]; gas flow rates of 60 cm^3 min^{-1} for O_2, 3 cm^3 min^{-1} for SF_6, and a chamber pressure of 150 millitorr. After the dry etch, the nickel protection layer was removed by immersing the sample in 30% aqueous ferric chloride ($FeCl_3$) solution at 70°C for 30 seconds. The resulting particles were well defined, as seen in the example SEM images shown in figure 4.15, and flat to within ±50nm as measured on a stylus profiler.

4.4 Writing encoded holograms into SU8

4.4.1 Holograms written into SU8 films

In order to write holograms into the photochromic SU8, the whole sample is initially exposed to a broadband mercury UV source (intensity 20mW cm^{-2} measured at a wavelength of 365nm) for 30mins, to transfer the dye into form (ii). Encoded holograms are written into the photochromic dye-doped SU8 using a standard holographic setup for forming Fourier transform holograms, the basic principles of which were considered in section 4.2.1. A schematic of the setup used is shown in figure 4.16(A). Light from a frequency doubled diode-pumped Nd:YVO_4 laser (wavelength $\lambda = 532$nm, near to the peak of the visible absorption band of form (ii) of the dye) is split equally into two beams. One beam (the 'signal beam') is expanded 10 times

by lenses L1 and L2, and spatially filtered by the pinhole P between the two lenses. The signal beam is then reflected from a spatial light modulator (Texas Instruments DMD (R)), which patterns the beam with the required code. The patterned beam is focussed through a lens L3, to create the Fourier transform (FT) of the code pattern on the SU8 film. The other laser beam (the 'reference beam') is reflected directly onto the same place on the photochromic sample. The signal and reference beams are incident at angles $11 \pm 1°$ and $35 \pm 1°$ to the sample normal, respectively. The hologram was illuminated with a 633nm laser beam from 3mW He-Ne laser during writing, which is incident at angle $27 \pm 1°$, in order to be Bragg-matched to the hologram for maximum reconstruction intensity and minimal distortion of the reconstructed hologram (see section 4.2.3 for more detail). This wavelength was chosen to allow easy monitoring of the hologram diffraction as the writing progressed, due to the different diffracted first order angle produced by this wavelength. The diffraction pattern reconstructed from the hologram is focussed by a second FT lens (L4) onto a CMOS camera sensor (1280 x 1024 pixels, Prosilica EC1280) in order to view the reconstructed image. The reconstructed image develops to a maximum intensity before the hologram begins to erase due to multiple interference patterns building up from substrate reflections [115]. The time taken for the reconstructed image to reach maximum intensity in our case was approximately 6s with a total power in both writing beams of 0.1 mW. This corresponds to an absorbed energy of 0.6 mJ being required to form a maximum intensity encoded hologram.

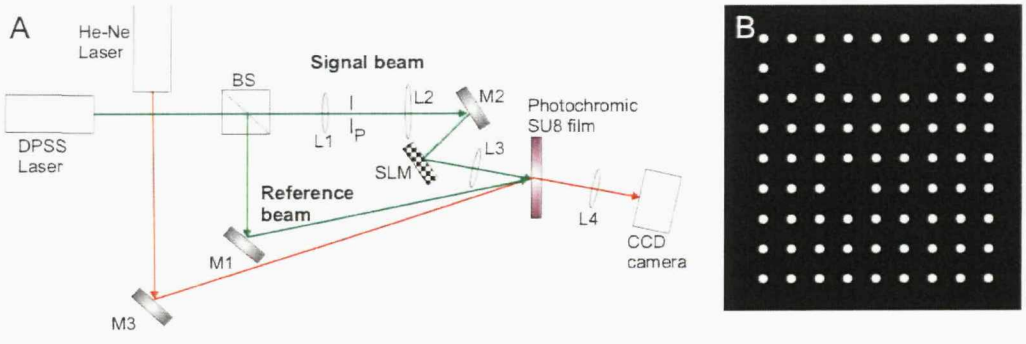

Figure 4.16: (A) Schematic of the setup used to write encoded holograms into dye-doped SU8 microparticles. DPSS: frequency doubled diode pumped Nd:YVO_4 laser, HeNe: Helium-neon laser, BS: beamsplitter, M: mirror, L: lens, SLM: spatial light modulator. (B) Example of a code pattern written onto the signal beam using the SLM, indicating the grid-defining spots (indicated by dotted lines) and the code spots (indicated by shaded square).

An example of the kind of code patterns written onto the signal beam using

the SLM is shown in figure 4.16(B). White spots represent points at which light is reflected onto the sample, the rest of the beam being reflected away from the sample. The top row and leftmost column of spots constitute a reference frame which defines the code grid for the benefit of an automated reading algorithm, as discussed in section 4.2. The rest of the spots represent a binary number which uniquely identifies the SU8 particle: a bright spot at a code grid position indicates a '1' bit and the absence of a bright spot at a particular grid position indicates a '0' bit. The example in figure 4.16(B) represents the binary string 01000011 11111111 11111111 11111111 11011111 11111111 11111111 11111111. The spacing between the grid positions in this case was 220 μm. This spacing, together with the focal length f of the FT lens, determines the size of the Fourier transform of the pattern on the SLM, and thus the size of the hologram. In this case a value of $f = 50$mm was used for ease of arrangement of the setup, which together with the chosen value of code grid spacing resulted in FT size of 400μm, allowing the hologram to be written onto the 500μm SU8 particles.

After writing, the hologram is reconstructed by illuminating with the 633nm laser beam used to monitor the writing process. The diffraction pattern reconstructed from the hologram is focussed by a second FT lens onto a CMOS camera sensor (1280 x 1024 pixels, Prosilica EC1280) in order to view the reconstructed code. As an example, the diffraction pattern reconstructed from a hologram written using the pattern in figure 4.16(B) is shown in figure 4.17. The hologram was written into a flat plate of dye-doped SU8, in order to characterize the capabilities of the material to form encoded holograms. The pattern in figure 4.17(A) shows that the required code pattern has successfully been reproduced with minimal distortion. Cross sections through a row of entirely 1 bits (figure 4.17(B)) and a row containing both 1 and 0 bits indicates the high contrast between bright and dark regions of the encoded diffraction pattern from the hologram. The mean signal to noise ratio (SNR) of 1 bit intensity to 0 bit intensity in diffraction patterns from holograms written using this method is 5.9 ± 1.2. This value of SNR determines how well the holograms can be read using a threshold method similar to the superimposed gratings. As we shall see, in the case of holograms, random scattered light from the SU8 surface seems to be the main source of noise, rather than unwanted diffraction pattern features, as in the case of the gratings. The hologram is erased by the reading light, requiring 15mins of constant illumination with a power of 1mW to erase the hologram to the point where the hologram signal-to-noise ratio becomes too low for the reading algorithm described in section 4.5. Due to the lower power of

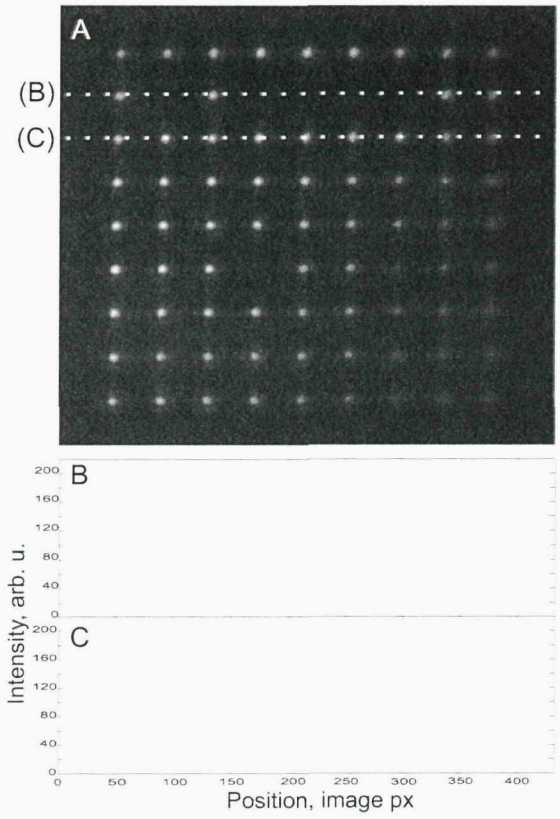

Figure 4.17: (A)An example camera image of a code reconstructed from an encoded hologram written into diarylethene doped SU8. (B)A cross section through a row of entirely 1 bits (row indicated on (A) by correspondingly labelled dotted line. Comparing this cross-section with one taken through a row containing a mixture of 0 and 1 bits (C) indicates the obtainable signal to noise ratio between 0 and one bits.

the reading light, together with the lower dye absorption at the reading wavelength, this erasure is much slower than erasure by the writing laser.

In order to be successfully used for a biological assay, the written hologram must remain readable throughout the duration of the experiment (typically up to a few days). We have seen that form (ii) of the diarylethene dye returns to form (i) upon illumination with light of wavelength 532nm. In addition, form (ii) can decay to form (i) by thermal relaxation (section 4.3.1), although the thermal lifetime is expected to be reasonably long. This thermal decay will cause the diffracted light from the hologram to reduce in brightness over time, eventually making the hologram unreadable. In order to characterize the thermal decay of the dye in the SU8 matrix, a hologram was written into a flat plate of dye-doped SU8, as

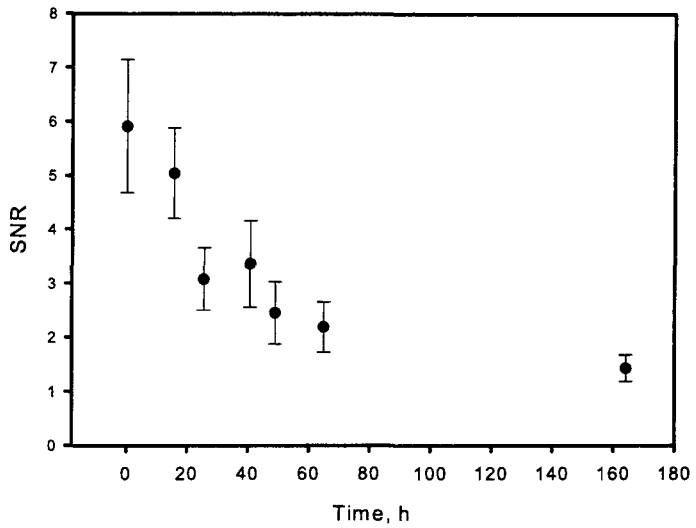

Figure 4.18: Signal to noise ratio of hologram vs time kept in the dark at room temperature.

described above, and the image reconstructed for enough time to take an image with the camera (approximately 1 second). The hologram was left in the dark at 20°C for 4 days, reconstructing the hologram at various time intervals. A graph of hologram SNR over time is shown in figure 4.18. This shows that the hologram SNR reduces by approximately 60% after 70 hours (2.9 days), giving a remaining SNR of 2.3. Since, as seen in section 4.5, we have an algorithm which can read holograms with SNR> 2, the hologram is still readable after almost 3 days storage at room temperature.

Section 4.1.2 discussed an additional property that would be desirable in our holographic encoded microparticles. This is that, for certain applications such as combinatorial synthesis, it would be advantageous to be able to erase and rewrite the holograms encoding the particles. Diarylethene dyes have previously been characterized as being rewritable [107]; when in form (ii) the dye may be returned to form (i) and back to form (ii) repeatably. In order to test the rewritability of holographically encoded SU8 particles, 10 holograms were written into particles as described above. After recording the reconstructed image from the holograms, the sample was illuminated with 532nm light to erase the holograms. The sample was then re-illuminated with UV light to return the dye to form (ii) and the same holograms written into it again. This process was repeated a number of times, and the resulting SNR for each write is presented in figure 4.19. The write number starts with 1 as the first write

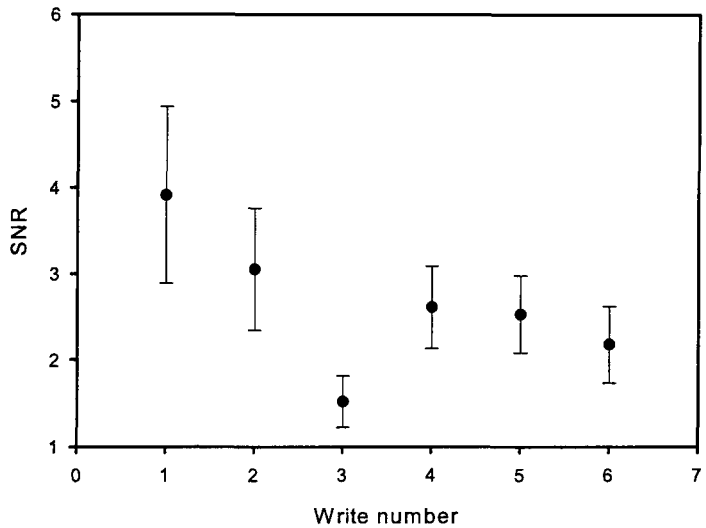

Figure 4.19: Signal to noise ratio of a hologram vs number of write/ erase cycles. '1' corresponds to the first write with no erasure. Writes 1-3 were performed within three hours of each other. The sample was left for 48 hours and then writes 4-6 performed within 3 hours of each other, indicating the partial recovery of the fatigued dye over time.

before any erasure. These results show that two successive different holograms may be written into the SU8, before chemical fatigue causes the hologram SNR to fall below 2, rendering it unreadable by the software described in section 4.5. Leaving the hologram in the dark for 48 hours at room temperature restores 70% of the 1st hologram SNR, allowing the particle to be written two more times to produce readable holograms. This partial restoration of the hologram intensity suggests that at least part of the fatigue mechanism is a cis-trans isomerization of the open-ring form of the dye to 1,2-Bis(2,4,5-trimethyl-3-thienyl)-trans-1,2-dicyanoethene, in accordance with previous observations [107]. This extra isomerization is illustrated in figure 4.11 by the transformation of form (i) to form (iv). Only the cis isomer may undergo the cyclization necessary for the absorption spectrum change, which allows holograms to be written into the material: a proportion of the dye transforming to the trans isomer will therefore reduce the diffraction efficiency of the resulting holograms. The isomerization is reversible, with the trans form relaxing thermally to the cis isomer over 48 hours, restoring the hologram intensity to 70% of the initial value. However, further investigation will have to be performed to discover whether this is actually the case.

4.4.2 Holograms written into SU8 particles

To demonstrate the writing of holograms into particles, a wafer of $1500 \times 500 \times 35\mu$m particles was manufactured on an aluminium coated glass substrate, as described in section 4.3.2. The large size was chosen for demonstrating the writing of holograms into particles, in order to facilitate aligning the particles with the writing beams. Further work in this area would concentrate on using the system with smaller particles. The particles were lifted from the wafer by sonicating for 2 hours in the standard aluminium etch solution MF319 (Microchem Corp.). The MF319 was diluted out with de-ionised water, and the particles pipetted onto a glass slide, where they were left to dry in order to prevent movement during hologram writing. Holograms of a 4×4 spot array (spot spacing 490 μm)were written into the particles using the setup shown in figure 4.16(A). An example hologram reconstructed from a particle by the method described in section 4.4.1 is shown in figure 4.20(A), together with a cross section indicating the signal to noise ratio in figure 4.20(B).

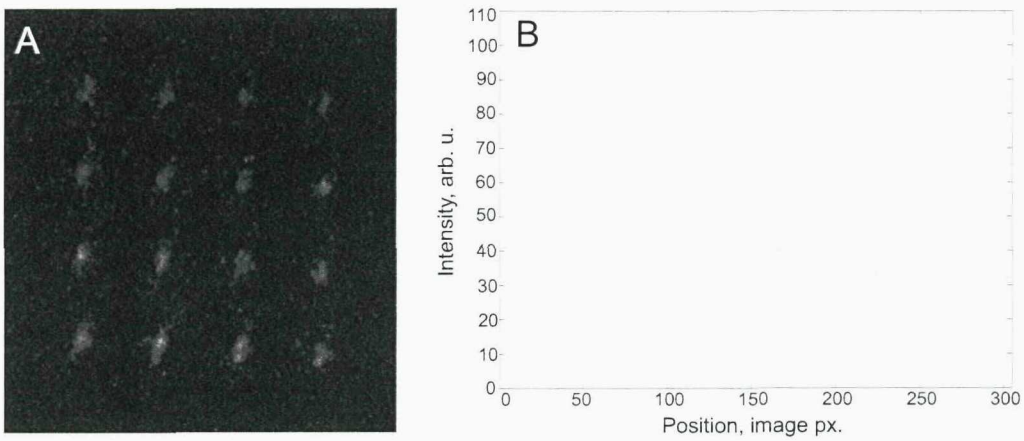

Figure 4.20: (A) An image of the reconstructed diffraction pattern from a hologram written into a $1500 \times 500 \times 35\mu$m SU8 particle. Image is contrast enhanced for clarity. (B)A cross section through the image indicates the pattern signal-to-noise ratio.

The mean signal to noise ratio of the pattern in figure 4.20 ($\pm$ standard deviation) is 1.9 ± 0.3. From figure 4.20 it is clear that the patterns reconstructed from the lifted-off particles are noisier and less intense than those reconstructed from flat SU8 films, which is most likely caused by the harsher fabrication and lift-off conditions of the particles compared to the flat films. However, the encoding principle has been shown to work on dry-etched SU8 particles with a reasonable signal-to-noise ratio of the resulting hologram diffraction patterns. Further work can now concentrate on

improving the signal-to-noise ratio and fabricating smaller encoded particles with large encoding capacities.

4.5 Reading encoded holograms

4.5.1 Reading optics and hardware

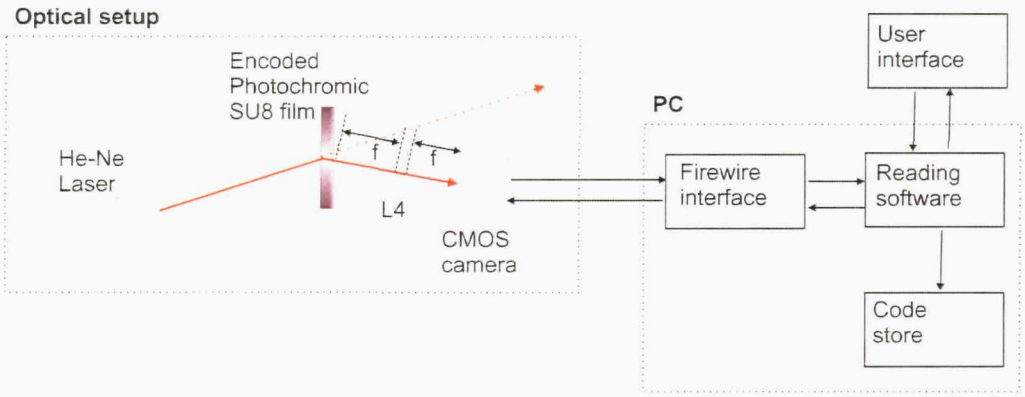

Figure 4.21: Schematic layout of the reading hardware. The optical part of the setup is identically to the monitoring part of the setup that was shown in figure 4.16(A). The reconstructed diffraction pattern from the hologram is collected by a CMOS camera and fed via a firewire interface to a PC running dedicated analysis software.

The reading optical setup has already been seen in figure 4.16(A), as it is integrated into this larger setup. The reading part consists of the components shown in figure 4.21. A laser beam from a helium-neon laser (wavelength 633nm) is incident on the encoded hologram. The beam is Bragg-matched to the hologram so that its angle of incidence produces the maximum intensity diffracted image (as explained above). This beam diffracts from the hologram, and the diffracted light is collected by a lens of focal length f set at distance f from the hologram. The lens focusses the light onto a CMOS camera sensor which is set at distance f from the lens, producing the code pattern on the camera sensor. The camera is connected by a firewire (IEEE 1394) interface to a PC, which runs dedicated custom software to analyse the image on the camera sensor, and reconstruct the tag's code. The details of the software are outlined in the next subsection.

4.5.2 Decoding algorithm

The reconstructed diffracted code from the hologram is read using dedicated reading software, which analyses the image on the CMOS camera in order to identify the code. It was found that differential methods of peak identification, such as those described in section 3.3.3, are relatively unsuccessful in correctly reading holograms, due to the large effect of surface perturbations on the uniformity of the code spots. This often resulted in the identification of more than one code spot when there should only be one. In principle the differential method would read a hologram from a very high quality surface, but it is prudent to reduce the effect of surface perturbations as much as possible, in order to reduce the reading error rate. Therefore, an algorithm based on a different image analysis technique was developed, and is described in this section.

A flow diagram of the algorithm is shown in figure 4.22. The image is first filtered with a Gaussian filter, to remove the substantial proportion of the random noise in the image (caused by unwanted scatter from the sample)(step 4 of algorithm). The software thresholds the image, and equalizes the image brightness histogram (steps 2 and 3). The histogram equalization process divides the brightness histogram into 'dark' and 'bright' parts, and forces bright parts to brighter values and dark parts to darker values [94]. The aim of this is make the code image more uniform in brightness and reduce the background light. The image is then binarized so that all features above the threshold become white, and all features below threshold become black (step 5). The connected components method [94] is then used to independently label all white features in the image and find their position (steps 6 and 7). The connected components method is outlined in figure 4.23. The aim is to find regions of white pixels that are independent of each other (i.e. regions of white pixels surrounded by black pixels). An example 5 x 9 pixel image of white (1) regions surrounded by a black (0) region, is shown in figure 4.23(A). The image is scanned from the top down. Each time a non-zero pixel is encountered at position (x, y), its neighbouring pixels are analysed in the manner shown in figure 4.23(B). If all the neighbours are zero, a new label is assigned to the pixel. If any neighbour is non-zero, the label of that neighbour is used for the current pixel. In this way a labeled image such as the one in 4.23(C) is formed. Here 'label collision' has occurred, that is each of the white regions has pixels with more than one label assigned. The whole image is scanned again, and any neighbouring pixel pairs with non-zero and non-equivalent labels are assigned the lowest of their two label values. After the first such pair has been analysed, all pixels with the higher of the two values are switched to the lower

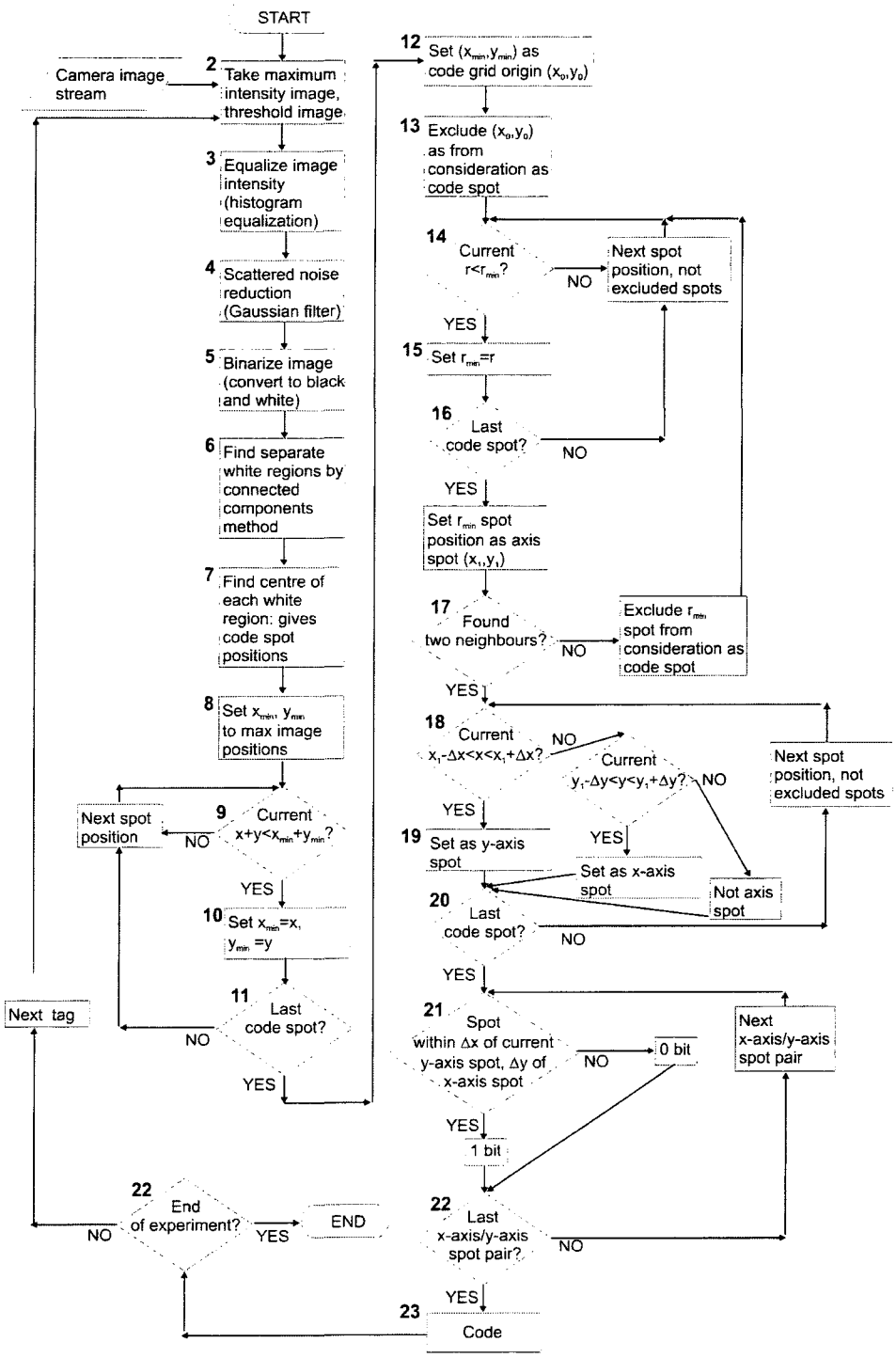

Figure 4.22: Flow diagram of a decoding algorithm for micro-particles encoded with holographic binary arrays which uniquely identify the particle.

one: in our case the algorithm converts all '3' pixels to '2' and all '5' pixels to '4'. Thus there are two independent regions that are now identifiable by their labels, as shown in figure 4.23(D). Finding their 'centre-of-mass', as decribed in section 3.3.3, results in a position for each region.

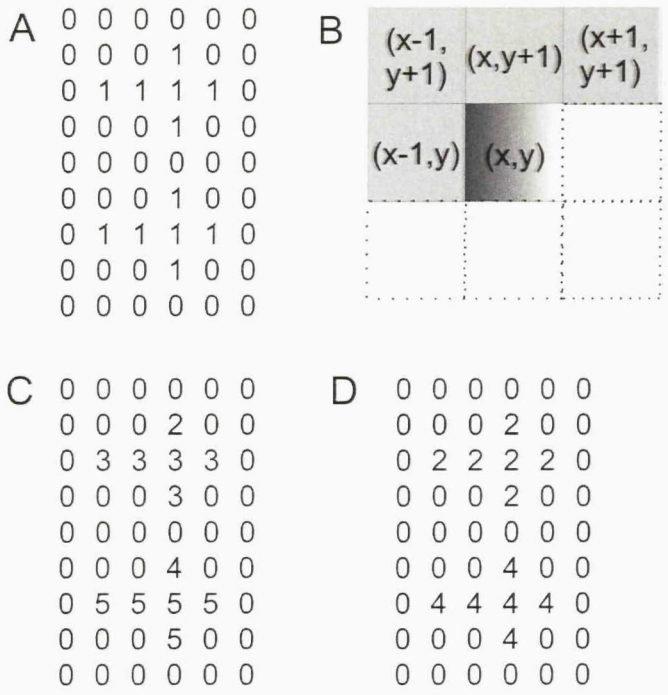

Figure 4.23: An outline of the connected components method: an image consisting of bright (1) and dark(0) regions (A) is scanned from the top down. The neighbours $(x-1, y)$, $(x-1, y+1)$, $(x, y+1)$ and $(x+1, y+1)$ of each pixel at coordinates (x, y) are analysed (C). If all neighbours are zero the pixel is assigned a new label, otherwise the pixel is assigned the label of a neighbour (C). Scanning again for neighbouring label pairs results in independent regions which are uniquely labeled (D).

Once the positions of all the bright spots in the image have been identified, recovering the code is a matter of identifying the spots' spatial arrangement. First, the grid-defining 'axis spots' must be found. To begin with, the axis origin spot at position (x_0, y_0) is found (steps 9-12), by identifying the spot with the minimum value of the sum $x + y$ for its (x, y) coordinates. The nearest neighbour spots (the two spots with minimum distance r_{min} from (x_0, y_0); distance of point (x, y) from (x_0, y_0) defined as $r^2 = (x - x_0)^2 + (y - y_0)^2$) within a tolerance Δx of x_0 is then labeled as the first y-axis spot, and that within Δy of y_0 is labeled as the first x-axis spot (steps 14-16). This sets the direction of the x and y axes. Spots within the same tolerances of these are then labelled as the next axis spots and so on, always

referring positions back to the previous spot (steps 18-20). Once the axis spots are identified, each grid position is analysed by looking within δy of an x-axis spot's y-coordinate and δx of an y-axis spot's x-coordinate. If a spot feature is present, this grid position is taken as a 1 bit, otherwise a 0 bit is assigned to the grid position. By analysing each possible x and y axis spot combination, the binary code identifying the particle is built up (steps 21-23). In an automated system, the experiment is either ended, or the algorithm starts again, ready to identify the next particle. The software successfully reconstructs the code of all holograms with SNR$\geq$2, otherwise identifying the code as unreadable. Reading of 50 holograms written into a flat SU8 plate resulted in correct reading of 96% of the holograms and correct identification of the remaining 4% as unreadable.

4.5.3 Error correction

The use of a binary encoding method, as mentioned at the start of this chapter allows the use of standard binary error-correction and detection schemes. A number of schemes have been developed for digital radio and cable transmissions [116], which allow the decoder to detect whether or not the binary sequence has been corrupted during transmission. Corruption in this case means that a '0' bit has been switched by noise to a '1', or vice-versa. In this case, the scattering of light from contaminants or surface imperfections may cause such a switch, and in order to have a safeguard against this, we can implement error correction schemes in our encoding.

The basic principle of an error correction scheme is to set aside a fraction of the code bits for encoding information about the structure of the code. The simplest scheme is a single 'parity check' bit. One bit of the code is set aside as a check bit, and given the value '1' if there are an even number of '1' bits in the code, and '0' if there are an odd number of '1' bits. If one bit of the code is switched in value by noise, the code will change from having an odd number to having an even number of '1' bits (or vice-versa), and the parity check bit will enable us to detect if this has happened, allowing us to discard this code. Such a scheme can of course only detect an odd number of errors. Since the holographic codes are arranged in a square array, however, there is a much more robust scheme that can easily be implemented. This is shown schematically in figure 4.24; a parity check bit is placed on each row and column of the code, together with a corner check bit for detecting errors in the parity bits themselves. All single bit errors can not only be detected using this scheme, but also corrected, so that the code can be recovered. Double and triple bit errors

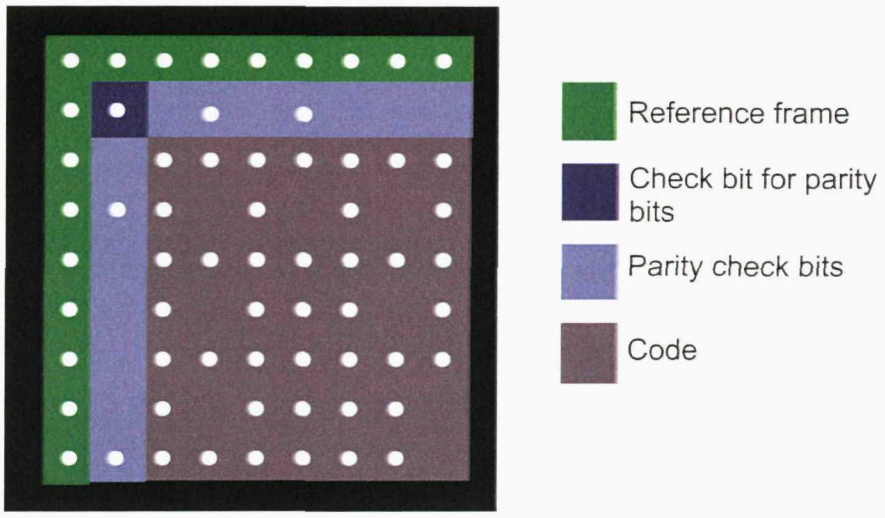

Figure 4.24: Layout of a code which includes a parity check on each row and column of the code. This scheme can detect and correct all single bit errors, and detect but not correct all double and triple bit errors.

will be detected, but the code cannot be corrected, so a particle with such a code must simply be rejected from the experiment. The detection, however, avoids the more serious problem of a mis-read. Any more than three bits in error will result in a misread code, however the parity bits increase the robustness of the encoding scheme.

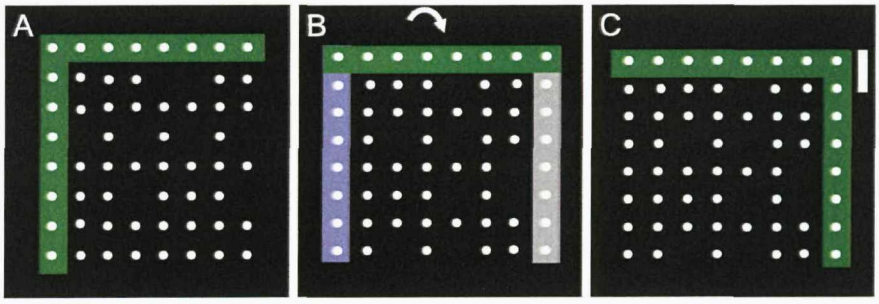

Figure 4.25: An example of the effect of large code rotations and a solution to the problem. (A)An example of a code spot array, with the axis spots highlighted in green. (B)The code array from (A) rotated by 90° in the direction of the arrow. The axis spots *should* be those highlighted in green and grey, however they are incorrectly identified as those highlighted in green and blue, leading to a misreading of the tag. (C)The addition of a rectangle which identifies the top of the array allows the axis spots on the rotated pattern to be correctly identified.

A second source of error is rotation of the tag about the axis normal to its largest

surface, resulting in rotation of the entire code array, so that the array appears tilted compared to the images seen so far. The most extreme problem is rotation by $> 90°$, so that the wrong sets of spots are identified as the axis spots, as shown in figure 4.25(A), resulting in a (most likely unidentifiable) misreading of the code. This could potentially be solved by making sure the bottom row and rightmost column of the (correctly oriented) code part are never made up entirely of one digits, so that the reference frame may be used to identify the orientation. This would however require not using some codes. A method which allows all codes to be used involves introducing an asymmetric feature into the code pattern, to identify the top of the code. An example of such a feature is shown in 4.25(B). This feature is a reactangle of larger size than the code spots, which is thus easily identifiable as the orientation identification feature. The connected components method outlined in section 4.5.2 can easily identify the size of the white regions in the image; the largest region can then be labeled as the orientation indicator, identifying the top of the code array.

The final source of error which should be considered is breakage of the particle, so that part of it is missing. As already considered in reference to the superimposed grating tags (see section 3.3.4), diffraction based methods of microparticle encoding rely on the periodicity of the patterns on the particle, rather than the absolute features as is the case for most other microparticle encoding techniques considered in chapter 1. Thus even if part of the pattern is removed by damage, the periodicity remains, so that the code can still be reconstructed. However, if part of the tag is broken, reducing its size, each code spot will appear wider in the reconstruction. If, as considered so far in theoretical calculations, a hologram is created from only the first peaks of the code Fourier transform, the width of each spot is already equal to the distance between spots. Therefore, any widening of the spots could start to make neighbouring spots hard to distinguish from each other. To prevent this, both the first and second code Fourier transform peaks could be contained within the the hologram. This will allow robustness of the encoding against tag breakage, albeit at the expense of substantially reducing the encoding capacity.

4.6 Conclusions

A second novel diffraction-based method of encoding polymer microparticles has been presented. This method is based on the writing of holograms into the particles, that produce code images upon illumination. The particles are manufactured by a dry-etch process from the epoxy photo-resist SU8, to which biochemical molecules

can successfully be attached. It has been demonstrated that the inclusion of a photochromic diarylethene dye in the SU8 allows encoded holograms to be written into the material. Holograms written into a flat SU8 plate have a mean signal-to-noise ratio of 5.9 on the initial write, and remain for more than 3 days at room temperature, allowing ample time for biological experiments to be performed. A dedicated computer decoding algorithm for the codes has been demonstrated. The holograms may be re-written once within a short time, whilst still remaining readable by the computer decoding algorithm. Holograms written into particles have been demonstrated, with a lower mean SNR of 1.9 ± 0.3, although care taken with factors which may reduce the surface quality of the particles compared to flat plates mean that there is the possibility of increasing this SNR value. 8-bit holograms have been successfully demonstrated on flat SU8 plates, which have an encoding capacity of 10^{19} unique codes.

Chapter 5

Conclusions and further work

5.1 Conclusions

In conclusion, the concept of a new optical non-contact tagging technique for microparticles has been demonstrated, based on superimposing large numbers of miniature diffraction gratings on a tag. The particular superimposing method used was a simple binary AND, or multiplicative approach, with no optimisation of the expected diffraction pattern. Various limitations of the method for rectangular profile gratings have also been analysed, such as higher order diffracted beams and ghost beams produced due to the superimposing process, which can be confused with code first order beams. However, we have shown that in most cases these beams can be eliminated by the use of an intensity threshold method. Simple combinatorial anlysis predicts that the technique is capable of creating distinguishable tags containing at least 5 superimposed grating and encoding up to 10^9 tags, each of which is only 100μm long and a few μm wide. To demonstrate this technique we manufactured a library of 50μm x 50μm tags on a glass wafer and confirmed practicality of the superimposed grating tags. With the particular encoding method used it has been possible to resolve tags containing at least three superimposed gratings, providing capacity for more than 68,000 tags. An enormous increase in capacity is possible if two sets of mutually perpendicular gratings are used. Combinatorial analysis shows that up to 10^{21} different barcode tags can possibly be fabricated with such two-dimensional superimposed gratings up to order five. A chip library of such 2-dimensional tags allowed tags containing at least three superimposed gratings to be resolved, demonstrating an obtainable capacity of the order of 6.2×10^8 tags. The robust nature of the tags, together with the non-contact remote reading capability makes them ideal for a large variety of micro-particle based biochemical, cytological,

proteomic and genomic assay applications.

The steps required to make superimposed diffraction grating tags applicable to assay systems, to be analysed using microfluidic chips, have been considered. It has been shown that high quality superimposed diffraction gratings may be manufactured in the biologically compatible polymer SU8, by using the high-throughput fabrication method of nano-imprint lithography. Gratings manufactured by this method were shown to give diffraction patterns of comparable quality to those manufactured by e-beam direct write techniques.Therefore gratings can be mass produced, that are both compatible with assay systems and allow for the large encoding capacities given in chapter 2, with some limitations. The encoding method, with a small contribution from the resolution of the manufacturing process was shown to limit the number of gratings that can be superimposed to 3 (possibly 4 after more investigation), which still allows for 10,000 codes on 100μm particle (when the diffraction angle is limited to 43° due to total internal reflection at glass-air interfaces in the system). Assuming the same superimposing limit applies to 2-dimensional gratings (although nano-imprinted 2D gratings have yet to be tested), around 10^8 unique codes can be obtained on a particle $100 \times 100\mu$m square. In addition, the robustness of the reading technique to rotation of the tags with respect to the reading beam has been demonstrated, and outline given of a computer algorithm for automated reading of the diffractive tags. The actual number of particles which must be read in an assays experiment has also been estimated, using data from a real biological assay performed by others on diffractively encoded microparticles. Hence, the practicality of high throughput manufacture of the diffractively encoded microparticles has been demonstrated.

A second novel diffraction-based method of encoding polymer microparticles has been presented. This method is based on the writing of holograms into the particles, that produce code images upon illumination. The particles are manufactured by a dry-etch process from the epoxy photo-resist SU8, to which biochemical molecules can successfully be attached. It has been demonstrated that the inclusion of a photochromic diarylethene dye in the SU8 allows encoded holograms to be written into the material. Holograms written into a flat SU8 plate have a mean signal-to-noise ratio of 5.9 on the initial write, and remain for more than 3 days at room temperature, allowing ample time for biological experiments to be performed. A dedicated computer decoding algorithm for the codes has been demonstrated. The holograms may be re-written once within a short time, whilst still remaining readable by the computer decoding algorithm. Holograms written into particles have been

demonstrated, with a lower mean SNR of 1.9 ± 0.3, although care taken with factors which may reduce the surface quality of the particles compared to flat plates mean that there is the possibility of increasing this SNR value. 8-bit holograms on flat SU8 plates have been successfully demonstrated, which have an encoding capacity of 10^{19} unique codes.

5.2 Further work

5.2.1 Superimposed diffraction grating-encoded microparticles

Although it has been demonstrated that superimposed diffraction gratings can be manufactured successfully and with high quality in SU8 by nano-imprint methods, further work in this area must concentrate on developing a microfluidic reading system, and using the codes for highly multiplexed assays. As mentioned in chapter 1, the nature of the collaborative project within which the work for this thesis was done, means that these aspects have already begun to be developed by other people. The microfluidic systems have already been developed and tested with low-resolution diffractive codes defined by photolithography. These tests have indicated that it is possible to capture and analyse the diffraction pattern from a particles moving in a continuous flow stream. The next step is to manufacture large numbers of particles nano-imprinted with many different codes, in order to rigorously test the reading algorithm in a flow system. Data, such as alignment capabilities and maximum flow speeds, must be obtained to characterize the practical limitations of the system for high throughput analysis.

Further analysis of the codes must be performed to determine whether the limit of the number of superimposed gratings can be extended above 3, by predicting and eliminating codes which will not be correctly read using the threshold method of eliminating the higher order beams. The minimum spacing of first orders between different codes should also be more rigourously determined to ensure that reading errors rates for the codes are as low as possible. This requires manufacture of a large number of repetitions of a set of embossed codes, in order to more fully characterize variations in first order beam width, beam position and intensity (relative to both the zero order and higher order beams) variations between samples. In addition, the use of a more optimised method for superimposing the gratings should be studied, in order to reduce the effect of unwanted diffraction pattern features, and thus increase

the reliability and available encoding capacity of the technique.

The most important test of the technology is demonstrating its use in highly multiplexed biological assays. This has already been started with demonstration of up to 4-plex assays, using low resolution photolithographically defined diffractive microparticles. An important future step is to design assays which require much higher (of the order of hundreds or thousands) multiplexing, which can make use of large numbers of different codes. The most significant test of the encoding technology will be the ability to perform high throughput, error-free analysis of such an assay in a microfluidic system.

5.2.2 Holographically encoded microparticles

It has been demonstrated that microparticles of SU8 doped with a photochromic dye can be manufactured, and encoded holograms can be written into them. Having done this, and shown that the dye can support holograms whose diffracted images have a signal-to-noise ratio more than adequate for encoding purposes, further work should concentrate on reducing the particle size, whilst still maintaining large encoding capacities. It has been shown that this is theoretically possible with the right combination of writing lens focal length and spacing spots in the code.

The dye currently in use maintains a hologram in a readable form for up to 3 days. There are many variants of the diarylethene-type dyes, and further investigation should focus on whether any of these can retain readable holograms for even longer. In addition, investigating whether any of these dyes can support more hologram rewrites than the one use in this thesis would be advantageous for many applications.

The third focus of further research in this area should be the integration of the whole holographic technology with a microfluidic system. This includes the alignment of the particles for reading, which is more critical than for the grating codes, due to the volume nature of the holograms. The integration should also include the writing of the particles inside the fluidic system, which presents something of a challenge in that to form holograms, the particle must be stopped and held still for the duration of the hologram writing. This could be accomplished by use of electric forces, or perhaps by doping the SU8 with magnetic nanoparticles in order to hold the microparticles in place with magnetic field, in a manner similar to the fluorescent photo-bleached tags [37]. The reading algorithm also needs to be properly tested with respect to error rates when reading flowing holographically encoded particles. The technology must also be demonstrated in use in multiplexed assays.

In addition to using dyes to dope SU8, there is substantial scope for investigation of writing holograms into the surface of the SU8 itself, by using a UV laser in the holographic system to pattern holograms be crosslink the SU8 selectively with the hologram interference pattern. It may also be possible to create imprint stamps from the SU8 structured via this method, by plating with nickel for example, allowing the holographic SU8 structures to be copied by imprinting. It would also be fruitful to investigate the use of other photosensitive polymers for forming the hologram, particularly if re-writeable polymers can be found. Further investigation into the use of computer generated holograms would also be useful, particularly if an algorithm for generating hologram diffracted images off-axis from the zero order is used.

Due to the volume nature of the holograms, and thus their wavelength selectivity, there exists the possibility of using common white light sources rather than a laser source to read the holograms. There may also exist the potential to integrate a sensing technology based on chemical changes to the polymer making up the microparticle, in a similar manner to that described in [82, 83]. This could potentially allow the hologram itself to be used for detection of analyte binding during reactions.

Appendix A

Derivation of first to zero order intensity ratio

The first to zero order intensity ratio, I_1/I_0 of a grating with parameters a, b and N as defined in section 2.1.1 is derived as follows. The angular intensity spectrum $I(\alpha)$ of light of wavelength λ and wavevector $k = 2\pi/\lambda$ diffracted by such a grating is given by [43]

$$I(\alpha) = C\left(\frac{\sin\beta}{\beta}\right)^2\left(\frac{\sin N\chi}{sin\chi}\right)^2 \tag{A.1}$$

where C is a constant $\chi = (ka/2)sin\alpha$ and $\beta = (kb/2)sin\alpha$. Using equation 1.1, for the zero order ($m = 0$), we have that $\sin\alpha = 0$ and therefore $\chi = \beta = 0$. Applying L'Hospital's rule [117],

$$\lim_{\beta\to 0}\frac{\sin\beta}{\beta} = \lim_{\beta\to 0}\cos\beta = 1 \tag{A.2}$$

and

$$\lim_{\chi\to 0}\frac{\sin N\chi}{\sin\chi} = \lim_{\chi\to 0}\frac{\cos N\chi}{\cos\chi} = N. \tag{A.3}$$

Therefore, inputting these values into equation A.1, the zero order intensity I_0 is

$$I_0 = CN^2. \tag{A.4}$$

Similarly, for the first order ($m = 1$), we have that $\sin\alpha = \lambda/a$ and so $\chi = \pi$ and $\beta = \pi b/a$. Applying L'hospital's rule again,

$$\lim_{\chi \to \pi} \frac{\sin N\chi}{\sin \chi} = \lim_{\chi \to \pi} \frac{\cos N\chi}{\cos \chi} = N. \tag{A.5}$$

Inputting the values of β and α given above into equation A.1 therefore gives the expression for the first order intensity I_0 as

$$I(\alpha) = CN^2 \left(\frac{a \sin(\pi b/a)}{\pi b} \right)^2. \tag{A.6}$$

Finally, dividing equation A.6 by equation A.4 gives the expression for I_1/I_0 as

$$I(\alpha) = \left(\frac{a \sin(\pi b/a)}{\pi b} \right)^2. \tag{A.7}$$

Appendix B

Derivation of rotated grating diffraction angles

The equation for the diffracted angle of the mth order from a grating with period a, for which the readout light is not incident normally but at some arbitrary angle η to the grating normal, is derived using the geometry shown in figure B.1. Using similar methods as used to derive equation 1.1, orders must appear at angles $\eta + \alpha$ to the grating normal (and hence angles α to the diffracted zero order) for which the path difference between waves diffracted from either end of one period is equal to $m\lambda$, where m is an integer. From figure B.1, it can be seen that this occurs when α satisfies

$$a(\sin\eta - \sin(\eta + \alpha)) = m\lambda. \tag{B.1}$$

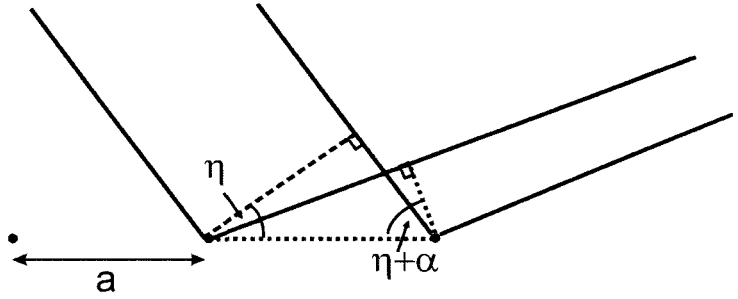

Figure B.1: Geometry for deriving the diffraction equation for a plane wave of wavelength λ incident at angle η to the grating normal, into a diffracted order at angle α to the diffracted zero order (and hence angle $\eta + \alpha$ to the grating normal)

The additional rotation angle θ introduces a modification due to the plane of

diffraction moving from normal to the grating, to a plane at angle θ to the grating normal. This modification is found using the standard definition of spherical polar coordinates [118], and the resulting diffraction equation is

$$a(\sin\eta\cos\theta - \sin(\eta + \alpha)) = m\lambda. \tag{B.2}$$

References

[1] Kindt, T.J., Goldsby, R.A., Osborne, B.A., "Kuby Immunology", 6th Edition, W.H. Freeeman and Company (2007)

[2] Wiese, R., Belosludtsev, Y., Powdrill, T., Thompson, P. and Hogan, M., Clin. Chem. 47 (2001) 1451

[3] Fall, B.I., Eberlein-Konig, B., Behrendt, H., Niessner, R., Ring, J. and Weller, M.G., Anal. Chem 75 (2003) 556

[4] Kato-Maeda, M., Gao, Q. and Small, P.M., Cell. Microbiol. 3 (2001) 713

[5] Lockhart, D.J., and Winzeler, E.A., Nature 405 (2000) 827

[6] Jayapal, M. and Melendez, A.J., Clin. Experim. Pharmacol. Physiol. 33 (2006) 496

[7] Bibikova,M., Lin, Z., Zhou, L., Chudin, E., Garcia, E.W., Wu, B., Doucet, D., Thomas, N.J., Wang, Y., Vollmer,E., Goldmann, T., Seifart, C., Jiang, W., Barker, D.L., Chee, M.S., Floros, J. and Fan, J-B., Genome Res. 16 (2006) 383

[8] Pang, S., Smith, J., Onley, D., Reeve, J., Walker, M. and Foy, C., J. Immunol. Methods 302 (2005) 253.

[9] Whiteford, N., Haslam, N., Weber, G., Prugel-Bennett, A., Essex, J.W., Roach, P.L., Bradley, M. and Neylon, C., Nucleic Acids Res. 33 (2005) e171

[10] Wilson, R., Cossins, A. R. and Spiller, D. G., Angew. Chem. Int. Ed. 45 (2006) 6104.

[11] Morgan, E., Varro, R., Sepulveda, H., Ember, J.A, Apgar, J., Wilson, J., Lowe, L., Chen, R., Shivraj, L., Agadir, A., Campos, R., Ernst, D., and Gaur, A., Clin. Immunol. 110 (2004) 252

[12] http://www.luminexcorp.com/technology/index.html

[13] Kellar, K.L, Douglass, J.P., J. Immunol. Methods 279 (2003) 277

[14] Hurley, J.D., Engle, L.J., Davis, J.T., Welsh, A.M. and Landers, J.E., Nucleic Acids Res. 32 (2004) e186

[15] http://www.fda.gov/bbs/topics/NEWS/2008/NEW01770.html

[16] Jaiswal, J. K., and Simon, S. M., Trends Cell Biol. 14 (2004) 497.

[17] Ma, Q., Wang, X., Li, Y., Shi, Y. and Su, X., Talanta 72 (2007) 1446

[18] Mattheakis, L. C., Dias, J. M., Choi, Y., Gong, J., Bruchez, M. P., Liu, J. and Wang, E., E. Anal. Biochem. 327 (2004) 200.

[19] Medintz, I.L., Uyeda, H.T., Goldman, E.R., and Mattoussi, H., Nature Materials 4 (2005) 435

[20] Han, M., Gao, X., Su, J.Z. and Nie, S., Nature Biotechnol. 19 (2001) 631

[21] Dabbousi, B.O., Rodriguez-Viejo, J., Mikulec, F.V., Heine, J.R., Mattoussi, H., Ober, R., Jensen, K.F. and Bawendi, M.G., J. Phys. Chem. B 101 (1997) 9463

[22] Dejneka, M.J., Streltsov, A., Pal, S., Frutos, A.G., Powell, C.L., Yost, K., Yuen, P.K., Muller, U., and Lahiri, J., Proc. Natl. Acad. Sci. USA 2 (2003) 389

[23] Nicewarner-Pena, S.R., Griffith Freeman, R., Reiss, B.D., He, L., Pena, D.J., Walton, I.D., Cromer, R., Keating,C.D., Natan, M.J., Science 294 (2001) 137

[24] Reiss, B. D., Griffith Freeman, R., Walton, I. D., Norton, S. M., Smith, P. C., Stonas, W. G., Keating, C. D. and Natan, M. J., J. Electroanal. Chem. 522 (2002), 95.

[25] Keating, C. D. and Natan, M. J., Adv. Mater. 15 (2003) 451

[26] Sha, M.Y., Walton, I.D., Norton, S.M., Taylor, M., Yamanaka, M., Natan, M.J., Xu, C., Drmanac, S., Huang, S., Borcherding, A., Drmanac, R. and Penn, S.G., Anal. Bioanal. Chem. 384 (2006) 658

[27] World Patent number WO0016893

[28] Evans, M., Sewter, C. and Hill, E., Assay Drug Dev. Technol. 1 (2003) 1

[29] Zhi, Z.-L., Morita, Y., Hasan, Q. and Tamiya, E., Anal. Chem. 75 (2003) 4125

[30] Zhi, Z.-L., Murakami, Y., Morita, Y., Hasan, Q. and Tamiya, E., Anal. Biochem. 318 (2003) 236

[31] Zhi, Z.-L., Morita, Y., Yamamura, S. and Tamiya, E., Chem. Commun. (2005) 2448

[32] Pregibon, D. C., Toner, M. and Doyle, P. S., Science 315 (2007) 1393

[33] Hoffmann, D., OBrien, J., Brennan, D., Loughran, M., Sensors and Actuators B 122 (2007) 653

[34] Wood, D.K., Braun, G.B., Fraikin, J.-L., Swenson, L. J., Reichb, N. O. and Cleland, A. N., Lab Chip 7 (2007) 469

[35] Derveaux, S., De Geest, B.G., Roelant, C., Braeckmans, K., Demeester, J. and De Smedt, S.C., Langmuir 23 (2007) 10272

[36] Derveaux, S., Stubbe, B.G., Roelant, C., Leblans, M., De Geest, B.G., Demeester,J., and De Smedt, S.C., Anal. Chem. 80 (2008) 85

[37] Breckmans, K., De Smedt, S. C., Roelent, C., Leblans, M., Pauwels, R. and Demeester, J., Nature Mat. 2 (2003), 169.

[38] Su, X., Zhang, J., Sun, L., Koo, T., Chan, S., Sundararajan, N., Yamakawa, M. and Berlin, A., Nano Lett. 5 (2005) 49.

[39] Bravo-Vasquez, J.P., and Fenniri, H., Sensors and Actuators B 125 (2007) 357

[40] Fenniri, H., Chun, S., Ding, L., Zyrianov, Y. and Hallenga, K., J. Am. Chem. Soc. 125 (2003) 10546

[41] Qin, L., Banholzer, M.J., Millstone, J.E., and Mirkin, C.A., Nano Lett. 7 (2007) 3849

[42] Qin, L., Park, S., Huang, L. and Mirkin, C.A., Science 309 (2005) 113

[43] Hecht, E., "Optics", 4th International Edition, Addison Wesley (2002)

[44] Goodman, J.W., "Introduction to Fourier Optics", McGraw-Hill (1968)

[45] Born, M. and Wolf, E., "Principles of Optics", 7th (Expanded) Edition, Cambridge University Press (1999)

[46] Silver, S., J. Opt. Soc. Am. 52 (1962) 131

[47] Duana, K., Lu, B., Opt. Laser Technol. 37 (2005) 193

[48] Ishio, H., Minowa, J. and Nosu, K., J. Lightw. Technol. LT-2 (1984) 448

[49] Avrutsky, I.A., Ellis, D.S, Tager, A., Anis, H. and Xu, J.M., IEEE J. Quantum Electron. 34 (1998) 729

[50] Jayaraman, V., Chuang, Z-M. and Coldren L.A., IEEE J. Quantum Electron. 29 (1993) 1824

[51] Tohmori, Y., Yoshikuni, Y., Tamamura, T., Ishii, H., Kondo, Y. and Yamamoto, M., IEEE Photon. Technol. Lett. 5 (1993) 126

[52] Ishii, H., Tanobe, H., Kano, F., Tohmori, Y., Kondo, Y. and Yoshikuni, Y., IEEE J. Quantum Electron. 32 (1996) 433

[53] Yasaka, H., Sanjoh, H., Ishii, H., Yoshikuni, Y. and Oe, K., J. Lightwave Technol. 15 (1997) 334

[54] Mahnkopf, S., Kamp, M., Forchel, A. and Marz, R., Appl. Phys. Lett. 82 (2003) 2942

[55] Winzer, P.J., Proc. IEEE, 94 (2006) 952

[56] Eardly, P.L., Wisely, D.R., Wood, D. and McKee, P., IEEE Proc.-Optoelectron. 143 (1996) 365

[57] Keller, P. and Gmitro, A.F., Appl. Opt 31 (1992) 5517

[58] Waddie, A.J., Randle, Y.R., Symington, K.J., Snowdon, J.F. and Taghizadeh, M.R., IEEE J. Select. Topics Quantum Electron. 9 (2003) 557

[59] Yeh, S.L., Lo, R.C. and Shi, C.Y., Appl. Opt. 43 (2004) 858

[60] Dammann, H. and Klotz, E., Opt. Act. 24 (1977) 505

[61] Dames, M.P., Dowling, R.J., McKee, P. and Wood, D., Appl. Opt. 30 (1991) 2685

[62] Hutchins, R., Yang, H., Morris, J.E. and Feldman, M.R., Appl. Opt. 36 (1997) 2313

[63] Paterson, C. and Smith, R.W., Appl. Opt. 38 (1999) 6152

[64] Rippoll, O., Kettunen, V. and Herzig, H.P., Opt. Eng. 43 (2004) 2549

[65] Skeren, M., Richter, I. and Fiala, P., J. Mod. Opt. 49 (2002) 1851

[66] Makowski, M., Sypek, M., Kolodziejczyk, A. and Mikula, G., Opt. Eng. 44 (2005) 125805

[67] Clark, M. and Smith, R., Opt. Commun. 124 (1996) 150

[68] Seldowitz, M.A., Allebach, J.P. and Sweeney, D.W., Appl. Opt. 26 (1987) 2788

[69] Chhetri, B.B, Yang S. and Shimomura, T., Appl. Opt. 39 (2000) 5956

[70] Georgiou, A., Wilkinson, T.D., Collings, N. and Crossland, W.A., J. Opt. A: Pure Appl. Opt. 10 (2008) 015306

[71] Abookasis, D., Batikoff, A., Famini, H. and Rosen, J., Appl. Opt. 45 (2006) 4617

[72] Luo, B., Wang, C., Du, J., Ma, C., Guo, Y. and Yao, J., Microelectron. Eng. 83 (2006) 1368

[73] Leger, J.R., Swanson, G.J. and Veldkamp, W.B., Appl. Opt. 26 (1987) 4391

[74] Sinzinger, S., Opt. Commun. 209 (2002) 69

[75] Ohtsubo, J. and Fujimoto, A., Opt. Rev. 14 (2007) 266

[76] Yuan, X.-C., Tao, S.H., Cheong, W.C., Chen, Y.W., Lim, M.S., Moh, K.J. and Ho, A.T.S., Opt. Eng. 43 (2004) 2493

[77] Yaqoob, Z. and Riza, N.A., IEEE Photon. Technol. Lett. 16 (2004) 954

[78] Burr, G. W., Jefferson, C. M., Coufal, H., Jurich, M., Hoffnagle, J. A., Macfarlane, R. M. and Shelby, R. M., Opt. Lett. 26 (2001) 444

[79] Dubois, M., Shi, X., Erben, C., Longley, K. L., Boden, E. P. and Lawrence, B. L., Opt. Lett. 30 (2005) 1947

[80] Hesselink, L., Orlov, S.S., and Bashaw, M.C., Proc. IEEE 92 (2004) 1231

[81] http://www.smartholograms.com/

[82] Marshall, A.J., Blyth, J., Davidson, C. A. B. and Lowe, C. R., Anal. Chem. 75 (2003) 4423

[83] Marshall, A.J., Kabilan, S., Blyth, J. and Lowe, C. R., J. Phys.: Condens. Matter 18 (2006) S619

[84] Hughes, M.P., Nanotechnology 11 (2000) 124

[85] Shaw, J. M., Gelorme, J. D., LaBianca, N. C., Conley, W. E. and Holmes, S. J., IBM J. Res. Dev. 41 (1997) 81

[86] Lorenz, H., Despont, M., Fahrni, N., Brugger, J., Vettiger, P. and Renaud, P. Sensors Actuators A 64 (1998) 33

[87] Lorenz, H., Despont, M., Fahrni, N., LaBianca, N., Renaud, P. and Vettiger, P., J. Micromech. Microeng. 7 (1997) 121

[88] Feng, R. and Farris, R.J., J. Micromech. Microeng 13 (2003) 80

[89] Cavalli, G., Banu, S., Ranasinghe, R.T., Broder, G.R., Martins, H.F.P., Neylon, C., Morgan, H., Bradley, M. and Roach, P.L., J. Comb. Chem. 9 (2007) 462.

[90] Chang-Yen, D. A. and Gale, B. K. Lab Chip 3 (2003) 297

[91] Preininger, C. and Sauer, U. Sensors Actuators B 90 (2003) 98

[92] Preininger, C., Bodrossy, L., Sauer, U., Pichler, R. and Weilharter, A., Anal. Biochem. 330 (2004) 29

[93] Preininger, C., Sauer, U., Dayteg, J. and Pichler, R. Bioelectrochemistry 67 (2005) 155

[94] Sonka, M., Hlavac, V. and Boyle, R., "Image Processing, Analysis and Machine Vision", International Thomson Computer Press (1993)

[95] Broder, G.R., Ranasinghe, R.T., She, J.K., Banu, S., Birtwell, S.W., Cavalli, G., Galitonov, G.S., Holmes, D., Martins, H.F.P., Neylon, C., Zheludev, N., Roach, P.L. and Morgan, H., Anal. Chem., in press (2008) doi: 10.1021/ac7018574

[96] Osborne, L.; Santis, G.; Schwarz, M.; Klinger, K.; Dork, T.; McIntosh, I.; Schwartz, M.; Nunes, V.; Macek, M.; Reiss, J.; Highsmith, W. E.; McMahon, R.; Novelli, G.; Malik, N.; Burger, J.; Anvret, M.; Wallace, A.; Williams,

C.; Mathew, C.; Rozen, R.; Graham, C.; Gasparini, P.; Bal, J.; Cassiman, J. J.; Balassopoulou, A.; Davidow, L.; Raskin, S.; Kalaydjieva, L.; Kerem, B.; Richards, S.; Simonbouy, B.; Super, M.; Wulbrand, U.; Keston, M.; Estivill, X.; Vavrova, V.; Friedman, K. J.; Barton, D.; Dallapiccola, B.; Stuhrmann, M.; Beards, F.; Hill, A. J. M.; Pignatti, P. F.; Cuppens, H.; Angelicheva, D.; Tummler, B.; Brock, D. J. H.; Casals, T.; Macek, M.; Schmidtke, J.; Magee, A. C.; Bonizzato, A.; Deboeck, C.; Kuffardjieva, A.; Hodson, M.; Knight, R. A. Hum. Genet. 89 (1992) 653.

[97] Novak, J. P.; Miller, M. C.; Bell, D. A. Biol. Direct 2006, 1, DOI 10.1186/1745-6150-1-18.

[98] Chen, Y., Wang, C., Fan, M., Yao, B and Menke, N., Opt. Mater. 26 (2004) 75

[99] Meng, X., Zhu, W., Guo, Z., Wang, J. and Tian, H., Tetrahedron 62 (2006) 9840

[100] Sankar, D., Palanisamy, P.K., Manickasundaram, S. and Kannan, P., Opt. Mater. 28 (2006) 1101

[101] Caulfield, H.J. (Ed.), "Handbook of Optical Holography", Academic Press (1979)

[102] Collier, R.J., Burckhardt, C.B. & Lin, L.H., "Optical Holography", Academic Press (1971)

[103] Leith, E.N., Kozma, A., Upatnieks, J., Marks, J. and Massey, N., Appl. Opt. 5 (1966) 1303

[104] Gallego, S., Ortuo, M.F., Neipp, C., Fernndez, E., Belndez, A. and Pascual, I., Opt. Express 15 (2007) 9308

[105] Horimai, H., Tan, X., and Li, J., Appl. Opt. 44 (2005) 2575

[106] Irie, M. and Mohri, M., J. Org. Chem. 53 (1988) 803

[107] Irie, M., Jap. J. Appl. Phys. 28 (1989) Supplement 28-3 215

[108] Luo, S., Chen, K., Cao, L., Liu, G., He, Q., Jin, G., Zeng, D. and Chen, Y., Opt. Express 13 (2005) 3123

[109] Woodward, R.B. and Hoffman, R., J. Am. Chem. Soc 87 (1965) 395

[110] Nakamura, S. and Irie, M., J. Org. Chem. 53 (1988) 6136

[111] Frederick, J.H., Fujiwara, Y., Penn, J.H., Yoshihara, K. and Petek, H., J. Phys. Chem. 95 (1991) 2845

[112] Longuet-Higgins, H.C. and Abrahamson, E.W., J. Am. Chem. Soc. 87 (1965) 2045

[113] Schlesinger, M. and Paunovic, M. (Eds.), "Modern Electroplating", Wiley (2000)

[114] Hong, G., Holmes, A.S. and Heaton, M.E., Microsyst. Technol. 10 (2004) 357

[115] Meerholz, K., Mecher, E., Bittner, R. and De Nardin, Y., J. Opt. Soc. Am. B 15 (1998) 2114

[116] Lin, S. and Costello, D.J., "Error Control Coding", 2nd Edition, Pears Education International (2004)

[117] Weisstein, E.W. "L'Hospital's Rule" from MathWorld - A Wolfram Web Resource, http://mathworld.wolfram.com/LHospitalsRule.html

[118] Weisstein, E.W. "Spherical Coordinates" from MathWorld - A Wolfram Web Resource, http://mathworld.wolfram.com/SphericalCoordinates.html

Publication list

Parts of this work have been published in the following:

Journal papers

Graham R. Broder, Rohan T. Ranasinghe, Joseph K. She, Shahanara Banu, Sam W. Birtwell, Gabriel Cavalli, Gerasim S. Galitonov, David Holmes, Hugo F. P. Martins, Cameron Neylon, Nikolay Zheludev, Peter L. Roach, and Hywel Morgan, "Diffractive micro-barcodes for encoding of biomolecules in multiplexed assays", *Anal. Chem.* **80**, 1902-1909 (2008)

S. W. Birtwell, G. S. Galitonov, N. I. Zheludev and H. Morgan, "Superimposed Nano-structured Diffraction Gratings as High Capacity Barcodes for Biological and Chemical Applications", *Opt. Commun.* **281**, 1789-1795 (2008)

S. Banu, S. Birtwell, G. Galitonov, Y. Chen, N. Zheludev and H. Morgan "Fabrication of diffraction-encoded micro-particles using nano-imprint lithography", *J. Micromech. Microeng.* **17**, S116-S121 (2007)

G. S. Galitonov, S. W. Birtwell, N. I. Zheludev and H. Morgan, "High capacity tagging using nanostructured diffraction barcodes", *Opt. Express* **14**, 1382-1387 (2006)

Conference presentations

S. Birtwell, G. Galitonov, H. Morgan and N. Zheludev, "Diffraction bar-codes as high capacity optical microtags for chemical and biological applications" Optics and Photonics Division conference at Photon 06, Manchester, UK, 4 - 7 Sep 2006.

S Banu, S Birtwell, G Galitonov, A Whitton, Y Chen, N Zheludev and H Morgan, "Nano-Imprinting Lithography-A Novel Way to Fabricate Diffractive Barcoded Particles" MME 2006, Southampton, UK, 3 - 5 Sept 2006

S. Banu, S. Birtwell, Y. Chen, G. Galitonov, H. Morgan and N. Zheludev, "High Capacity Nano-optical Diffraction Barcode Tagging for Biological and Chemical Applications" NSTI Nanotech 2006, Boston, Massachusets, May 7 - 11 2006 (Technical Proceedings of the 2006 NSTI Nanotechnology Conference and Trade Show, vol. 1, pp. 34 - 37)

D. Holmes, A. Whitton, G. Cavalli-Petraglia, G. Galitonov, S. Birtwell, S. Banu, N. Zheludev, and H. Morgan "Optical and impedance detection of DNA hybridisation on barcoded micro particles in a microfluidic device" 2006 NSTI Nanotech / Conference on Nano Electronics & Photonics, Boston, Massachusetts, USA, 7 - 11 May 2006 (Technical Proceedings of the 2006 NSTI Nanotechnology Conference and Trade Show, vol. 2, pp. 666 - 669)

S. Banu, S. Birtwell, G. Galitonov, D. Holmes, N. Zheludev, and H. Morgan, "Microfabricated barcodes for particle identification", 16th MME MicroMechanics Europe Workshop, Goteborg, Sweden, 04 - 06 Sep 2005 (Proc. of 16th MME MicroMechanics Europe Workshop, pp. 252-255).